Characterizing the Response of the Cascadia Margin Gas Hydrate Reservoir to Bottom Water Warming Along the Upper Continental Slope

Final Scientific/Technical Report

October 1, 2013 – March 31, 2017

Principle Authors: Evan A. Solomon
H. Paul Johnson
Marie S. Salmi
Theresa L. Whorley

Report Issued: November 2017

DOE Award No.: DE-FE0013998

Submitted by:
Evan A. Solomon

University of Washington
School of Oceanography
Box 355351
Seattle, WA 98195-5351
e-mail: esolomn@uw.edu
Phone number: (206) 221-6745

Prepared for:
United States Department of Energy
National Energy Technology Laboratory

Disclaimer

TABLE OF CONTENTS

EXECUTIVE SUMMARY

In October 2013, the University of Washington initiated a study funded through DOE-NETL entitled: Characterizing the response of the Cascadia margin gas hydrate reservoir to bottom water warming along the upper continental slope. The objective of this project is to understand the response of the WA margin gas hydrate system to contemporary warming of bottom water along the upper continental slope. Through pre-cruise analysis and modeling of archive and recent geophysical and oceanographic data, we (1) inventoried bottom simulating reflectors along the WA margin and defined the upper limit of gas hydrate stability, (2) refined margin-wide estimates of heat flow and geothermal gradients, (3) characterized decadal scale temporal variations of bottom water temperatures at the upper continental slope of the Washington margin, and (4) used numerical simulations to provide quantitative estimates of how the shallow boundary of methane hydrate stability responds to modern environmental change. The results of the pre-expedition analysis of historic bottom water temperatures and the simulations of the response of the upper limit of gas hydrate stability to intermediate water warming on the Washington margin have been published (Hautala et al., 2014). The work on characterizing regional heat flow was published in *Journal of Geophysical Research* (Salmi et al., 2017), and a synthesis of seep distribution along the Washington margin was published in *Geochemistry Geophysics Geosystems* (Johnson et al., 2015). These pre-cruise results provided the context for a systematic geophysical and geochemical survey of methane seepage along the upper continental slope from 48° to 46°N during a 10-day field program on the *R/V Thompson* from October 10-19, 2014. This systematic inventory of methane emissions along this climate-sensitive margin corridor and comprehensive sediment and water column sampling program provided data and samples for Phase 3 of this project that focused on determining fluid and methane sources (deep-source vs. shallow; microbial, thermogenic, gas hydrate dissociation) within the sediment, and how they relate to contemporary intermediate water warming. This work was summarized in a paper for the 9th International Conference on Gas Hydrates (Whorley et al., 2017) and is in preparation for submission to *Earth and Planetary Science Letters* (Whorley et al., *in prep.*). This project supported two graduate student theses (Salmi and Whorley) and two undergraduate students (Miller and Fay).

During the 2014 research expedition, we discovered nine seep sites between ~470 and 520 m water depth, within the zone of predicted methane hydrate retreat over the past 40 years. We imaged 22 bubble plumes with heights commonly rising to ~300 meters below sea level with one reaching near the sea surface. Some of the seep sites are controlled by local margin structure, mainly extensional faults and ridges. We collected 22 gravity cores and 20 CTD/hydrocasts from the 9 seeps and at background locations (no acoustic evidence of seepage) within the depth interval of predicted downslope retreat of the methane hydrate stability zone. Approximately 300 pore water samples were extracted from the gravity cores, and the pore water was analyzed for salinity, pH, alkalinity, acetylene, n-butane, ethane, ethylene, methane, methyl acetylene, propane, propylene, Cl, Br, NH_4, SO_4, Na, K, Ca, Mg, Li, B, Sr, and Ba concentrations, as well as for $\delta^{18}O$, δD, and $\delta^{13}C$-DIC stable isotope ratios. Bottom water samples were also analyzed for C_1-C_4 hydrocarbon concentrations and noble gas ratios. This comprehensive geochemical dataset was used to characterize the fluid and gas source(s) at each of the seep sites surveyed.

Hydrocarbons heavier than methane were below the detection limit (<0.5 ppmv) in both pore water and bottom water samples, suggesting any gas hydrate present is Structure I methane hydrate. The

pore water data shows decreasing chloride concentrations downcore at several sites with measured values as low as 170 mM (30% seawater value), and the sulfate-methane transition zone occurs between 50-80 cm below seafloor. Collectively, the pore water solute, noble gas, and isotope ratios suggest the pore water freshening is not the result of methane hydrate dissociation, but rather the dominant source of pore water freshening at these seep sites is clay dehydration at sediment depths where temperature exceeds 60 ^{o}C. Analysis of a suite of chemical geothermometers brackets the temperature of the fluid source(s) between 100-200 ^{o}C. Based on the geochemical dataset, active methane hydrate precipitation is occurring at the seep site that is about 10 m deeper than the upper limit of methane hydrate stability. The other seeps are fed by a range of fluid and gas sources and do not have a significant geochemical signature of methane hydrate dissociation; the majority of these seeps contain fluid sourced from relatively shallow sediment depths (the upper few hundred meters of the sediment column), whereas two consist of fluids from sources >2 km below the seafloor. Only a few of the gravity cores collected have pore water profiles that are in steady-state, suggesting a dynamic sedimentary and biogeochemical system at the upper continental slope along the entire Washington margin.

The primary results of this project are: 1) Bottom simulating reflector-derived heat flow values decrease from 95 mW/m^2 10 km east of the deformation front to ~60 mW/m^2 60 km landward of the deformation front, with anomalously low values of ~25 mW/m^2 on a prominent mid-margin terrace off central Washington.

2) The temperature of the incoming sediment/ocean crust interface at the deformation front ranges between 164-179 ^{o}C off central Washington, and the 350 ^{o}C isotherm at the top of the subducting ocean crust occurs 95 km landward of the deformation front. Differences between BSR-derived heat flow and modeled conductive heat flow suggest mean upward fluid flow rates of 0.4 cm/yr across the margin, with local regions (e.g. fault zones) exhibiting fluid flow rates up to 3.5 cm/yr.

3) A compilation of 2122 high-resolution CTD, glider, and Argo float temperature profiles spanning the upper continental slope of the Washington margin from the years 1968 to 2013 show a long-term warming trend that ranges from 0.006-0.008 ^{o}C/yr. Based on this long-term bottom water warming, we developed a 2-D thermal model to simulate the change in sediment temperature distribution over this period, along with the downslope retreat of the methane hydrate stability field. Over the 43 years of the simulation, the thermal disturbance propagated 30 m into the sediment column, causing the base of the methane hydrate stability field to shoal ~13 m and to move ~1 km downslope.

4) A preliminary analysis of seafloor observations and mid-water column acoustic data to detect bubble plumes was used to characterize the depth distribution of seeps along the Cascadia margin. These results indicate high bubble plume densities along the continental shelf at water depths <180 m and at the upper limit of methane hydrate stability along the Washington margin.

5) The goal of the 2014 research expedition on the *R/V Thompson* was to test whether there is active methane hydrate dissociation along the upper continental slope of the Washington margin in response to contemporary warming. Sampling focused on the depth range of simulated retreat of the methane hydrate stability field based on the record of bottom water warming. The majority of the seeps cored during the field program contained abundant authigenic carbonate indicating that they are locations of long-lived seepage rather than emergent seep systems related to methane hydrate dissociation. Despite the evidence for enhanced methane seepage at the upper limit of

methane hydrate stability along the Washington margin, we found no unequivocal evidence for active methane hydrate dissociation as a source of fluid and gas at the seeps surveyed. The pore fluid and bottom water chemistry shows that the seeps are fed by a variety of fluid and methane sources, but that methane hydrate dissociation, if occurring, is not widespread and is only a minor source (below the detection limit of our methods).

Collectively, these results provide a significant advance in our understanding of the thermal structure of the Cascadia subduction zone and the fluid and methane sources feeding seeps along the upper continental slope of the Washington-sector of the Cascadia margin. Though we did not find unequivocal evidence for methane hydrate dissociation as a source of water and methane at the upper pressure-temperature limit of methane hydrate stability at present, continued warming of North Pacific Intermediate Water in the future has the potential to impact the methane hydrate reservoir in sediments at greater depths along the slope. Thus, this study provides a strong foundation and the necessary characterization of the background state of seepage at the upper limit of methane hydrate stability for future investigations of this important process. This project has resulted in fourteen conference abstracts and papers as well as eight peer-reviewed publications to date, with an additional manuscript close to submission and several others planned in the near future.

PUBLICATIONS RELATED TO THIS PROJECT

Conference Abstracts and Papers

Solomon, E.A., Kowalski, L.[**], Whorley, T.L.[*], 2017. Chronic downward flow of seawater in bacterial mats at Hydrate Ridge – mechanisms and biogeochemical significance, Goldschmidt 2017, Paris, France, August 13-18, 2017.

Whorley, T.L.[*], Solomon, E.A., Philip, B.T.[*], Torres, M.E., Johnson, H.P., 2017. Investigating the response of methane hydrates to modern bottom water warming along the upper continental slope of the Cascadia margin, Paper, 9th International Conference on Gas Hydrates, Denver, CO, USA.

Solomon, E.A., Kowalski, L.[**], Whorley, T.L.[*], 2017. Chronic downward flow of seawater in bacterial mats at Hydrate Ridge – mechanisms and biogeochemical significance, Extended Abstract, 9th International Conference on Gas Hydrates, Denver, CO, USA.

Whorley, T.L.[*], Solomon, E.A., Torres, M.E., Johnson, H.P., Berg, R.D.[*], Philip, B.T.[**], 2016. Evaluating water and methane sources at the upslope limit of methane hydrate stability along the Washington margin, Gordon Conference on Natural Gas Hydrate Systems, 29 Feb – 3 March, 2016, Galveston, TX.

Solomon, E.A., 2016. Characterizing the response of the Cascadia margin gas hydrate reservoir to contemporary bottom water warming. University of Washington, Tacoma – Environmental Science Seminar, May 23, 2016.

Embley, R.W., Merle, S.G., Raineault, N., Baumberger, T., Seabrook, S.A., Johnson, H.P., Trehu, A.M., Lupton, J.E., Thurber, A.R., Hammond, S.R., Solomon, E.A., Salmi, M., 2016. Numerous bubble plumes mapped and new seeps characterized on the Cascadia margin. AGU Fall Meeting, Abstract OS41A-1939.

Whorley, T.L.[*], Solomon, E.A., Torres, M.E., Johnson, H.P., Berg, R.D.[*], Philip, B.T.[**], 2015. Evaluating active methane hydrate dissociation along the Washington margin in response to bottom water warming, AGU Fall Meeting, San Francisco, CA, Abstract OS23B-2015.

Salmi, M.S.[*], Harris, R.N., Johnson, H.P., Solomon, E.A., 2015. High resolution thermal model of the Washington margin of the Cascadia subduction zone, AGU Fall Meeting, San Francisco, CA, Abstract T21D-2870.

Graw, M.F.[*], Solomon, E.A., Treude, T., Pohlman, J., Colwell, F.S., 2015. Towards biogeochemical modeling of anaerobic oxidation of methane: Characterization of microbial communities in methane-bearing North American continental margin sediments, AGU Fall Meeting, San Francisco, CA, Abstract OS33A-1993.

Johnson, H.P., Miller, U.K.[**], Salmi M.S.[*], Solomon, E.A., 2015. Analysis of bubble plume distributions to evaluate methane hydrate decomposition on the Cascadia margin, AGU Fall Meeting, San Francisco, CA, Abstract OS23B-1990.

Solomon, E.A., 2014. New perspectives on CO_2 and CH_4 cycling in gas hydrate-bearing continental margin sediments, University of Washington, Earth and Space Sciences Colloquium, June 5, 2014.

Solomon, E.A., 2014. Investigating climate-sensitive gas hydrate deposits and seafloor hydrocarbon seeps: methane sources, transport, and sinks. Scripps Institution of Oceanography Earth Sciences Seminar, May 5, 2014.

Solomon, E.A., 2014. Response of the Washington Margin Gas Hydrate Reservoir to Warming North Pacific Intermediate Water, Art Institute of Seattle, March 6, 2014.

Salmi, M.[*], Johnson, H.P., Solomon, E.A., Harris, R.N., 2014. Heat flow survey on the

Washington margin of the Cascadia subduction zone. AOGS 11th Annual Meeting, Sapporo, Japan.

* Denotes graduate student
** Denotes undergraduate student

Journal Publications

Whorley, T.L.*, Solomon, E.A., Philip, B.T.*, Johnson, H.P., *in prep*. Investigating the response of methane hydrates to modern bottom water warming along the upper continental slope of the Cascadia margin, *Earth Planet. Sci. Lett.*

Salmi, M. S., H.Paul Johnson, Robert Harris, 2017. Thermal environment of the southern Washington region of the Cascadia Subduction Zone, *J. Geophys. Res. Solid Earth*, 122, 5852-5870.

Miller, U.K., H.Paul Johnson, *submitted.* An evolutionary sequence of carbonate deposition on the Cascadia Margin, *J. Geophys. Res.*

Johnson, H.Paul, J. Gomberg, S. Hautala, M. Salmi, 2017. Sediment gravity flows triggered by remotely generated earthquake waves, *J. Geophys. Res. Solid Earth*, 122, 4584-4600.

Philip, B.T.**, Denny, A.R.*, Solomon, E.A., Kelley, D.S., 2016. Time-series measurements of bubble plume variability and water column methane distributions above Southern Hydrate Ridge, Oregon, *Geochem. Geophys. Geosyst.*, 17, 1182-1196.

J. Gomberg, P. Bodin, J. Bourgeois, S. Cashman, D. Cowan, K. Creager, B. Crowell, A. Duvall, A. Frankel, F. Gonzalez, H. Houston, H. Paul Johnson, H. Kelsey, U. Miller, E. Roland, D. Schmidt, L. Staisch, J. Vidale, W. Wilcock, E. Wirth, 2016. Planning for a subduction zone observatory", Eos, Trans of AGU, May 2016; DOI: 10.1029/2016EO052635

Johnson, H.P., Miller, U.K.**, Salmi, M.S.*, Solomon, E.A., 2015. Analysis of bubble plume distributions to evaluate methane hydrate decomposition on the upper continental slope, *Geophys. Geochem. Geosyst.*, 16, 3825-3839, doi:10.1002/2015GC005955.

Hautala, S.L., Solomon, E.A., Johnson, H.P., Harris, R.N., Miller, U.K.**, 2014. Dissociation of Cascadia margin gas hydrates in response to contemporary ocean warming, *Geophysical Research Letters*, 41, 8486-8494.

INTRODUCTION AND MOTIVATION

Gas hydrates are stable at moderate pressures and low temperatures, and are ubiquitous in sediments at continental margins worldwide. Considering their widespread occurrence, they represent one of the largest reservoirs of organic carbon on Earth, with estimates of the amount of carbon stored in the global gas hydrate reservoir ranging from ~550 to 6.6×10^4 GtC (e.g. Kvenvolden, 1988; Milikov, 2004; Klauda and Sandler, 2005; Archer et al., 2009; Piñero et al., 2013). Globally, an estimated 99% of the methane hydrate reservoir is in continental margin sediments along continental slopes, with the remaining 1% in high-latitude permafrost-bearing sediments (Collett et al., 2009; Ruppel, 2011). The majority of the methane hydrate reservoir occurs at mid- to low-latitudes at concentrations of ~1-5% of the pores of fine-grained clays, but can exceed 20-80% in some settings (e.g. sands and fractured clays; Boswell and Collett, 2006; 2011).

Due to the positive geothermal gradient in marine sediments, methane hydrates exist as a stable phase only within the upper few hundred meters of continental slope sediments. The upper limit of methane hydrate stability depends on bottom water temperature and is generally near or below 500-meter water depth at lower latitudes for Structure I gas hydrate. The susceptibility of methane hydrate to warming ocean water depends on the magnitude and duration of the warming, the depth of the reservoir beneath the seafloor, and the thermal diffusivity of the sediments. As a result, shallow methane hydrates at the upper limit of stability on continental margins and associated with sub-sea permafrost on circum-Arctic shelves are the most susceptible to contemporary ocean warming. Compared to thinning permafrost on Arctic shelves, continental slope methane hydrates at the upper limit of stability represent a larger fraction of the global gas hydrate reservoir (Ruppel, 2011), have a wider distribution, and are located at shallower depths within the sediment column. The close proximity of upper slope methane hydrates to actively circulating seawater promotes hydrate dissociation over relatively short timescales in response to modest seawater warming at intermediate depth; periods of tens of years vs. 10^2 to 10^3 years for other climate-sensitive deposits (e.g. Ruppel, 2011).

Considering there is contemporary bottom water warming along many continental margins worldwide, studies of the upper slope methane hydrate reservoir response to warming provides an opportunity to investigate the dynamics of methane hydrate dissociation at present. Documenting the vulnerability and behavior of this climate-sensitive portion of the global gas hydrate reservoir to ocean warming provides a foundation to better understanding how methane hydrate systems responded to environmental change in the past and how they will evolve in the future. Determining whether methane hydrate dissociation along continental margins is occurring as a result of contemporary bottom water warming is also important in the context of the global ocean-atmosphere inventory of greenhouse gases. This hydrate-derived flux could potentially contribute to ocean acidification through microbial oxidation of methane, initiation of slope instability, and contributes to the emission of methane-derived CO_2 from the ocean to the atmosphere.

This project focused on the upper limit of gas hydrate stability along the Washington-segment of the Cascadia margin. The Washington margin has recently been the focus of an impressive array of scientific initiatives and programs including Earthscope, the Plate Boundary Observatory, the Ocean Observatories Initiative (OOI), GeoPRISMS, the ARRA Cascadia Initiative, the COAST 2-D multi-channel seismic survey in 2012, and an NSF-funded heat and fluid flux survey in 2013. Because of this high level of scientific activity, many of the parameters associated with the distribution and stability of methane hydrates are already well-characterized.

These critical contextual features include (1) high resolution swath bathymetry over almost the entire margin and adjacent abyssal depths, (2) abundant MCS profiles that have located and identified Bottom Simulating Reflectors (BSRs) associated with hydrates over most of the Washington margin, and (3) well-located sites of methane emissions that are positioned along the margin in both shallow and deep-water, with several that correspond to the "feather-edge" limit of gas hydrate stability in the NE Pacific (~500 m water depth). Furthermore, a compilation of 2122 high-resolution CTD, glider, and Argo float temperature profiles spanning the upper continental slope of the Washington margin from the years 1968 to 2013 show a long-term warming trend that ranges from 0.006-0.008 ^{o}C/yr since 1970 (Hautala et al., 2014). The full suite of these observations; (a) BSRs demonstrating a large-scale hydrate reservoir in the margin sediments, (b) methane plume emissions from critical depth intervals, and (c) significant historical intermediate-depth bottom water warming, combine to make the Washington margin a rich target area to examine the response of methane hydrate to environmental changes.

The objective of this project was to understand the response of the Washington margin gas hydrate system to the contemporary warming of bottom water along the upper continental slope. Through pre-cruise analysis and modeling of archive and recent geophysical and oceanographic data, we (1) mapped the distribution of methane hydrate along the central and northern Washington margin based on BSRs from archive multi-channel seismic data, (2) used these BSRs to refine margin-wide estimates of heat flow and geothermal gradients, (3) used the new heat flow distribution to estimate the temperature at the plate boundary fault from the deformation front to the coastline at the Washington sector of the Cascadia subduction zone, (4) provided a rigorous characterization of bottom water temperature temporal variations at the upper continental slope, and (5) used numerical simulations to provide quantitative estimates of how the shallow boundary of gas hydrate stability responds to modern environmental change. These pre-cruise results provided the context for a systematic geophysical and geochemical survey of methane seepage along the upper continental slope from 48° to 46°N during a 10-day field program on the *R/V Thompson* from October 10-19, 2014. The integrated geophysics and geochemistry cruise results provided locations of new seep sites in the zone of methane hydrate retreat predicted from our earlier numerical simulations of methane hydrate dissociation in response to bottom water warming. The results of the field program also provided a rigorous geochemical evaluation regarding the source of fluid and methane emissions at these locations, and an informed evaluation of whether there is significant methane hydrate dissociation in response to contemporary bottom water warming. These results are described in the following sections of this report.

References

Archer, D., Buffett, B., Brovkin, V., 2009. Ocean methane hydrates as a slow tipping point in the global carbon cycle, PNAS, 106(49), 20596–20601.

Boswell, R., Collett, T. S., 2006, The gas hydrates resource pyramid, Fire in the Ice Newsletter, U.S. DOE – Office of Fossil Energy, Fall 2006, 5-7.

Boswell, R., Collett, T. S., 2011. Current perspectives on gas hydrate resources, Energy and Environmental Science, 4, 1206-1215.

Collett, T. S., A. H. Johnson, C. C. Knapp, and R. Boswell, 2009, Natural Gas Hydrates: A Review, in T. Collett, A. Johnson, C. Knapp, and R. Boswell, eds., Natural gas hydrates—Energy resource potential and associated geologic hazards: AAPG Memoir 89, p. 146– 219.

Hautala, S.L., Solomon, E.A., Johnson, H.P., Harris, R.N., Miller, U.K.**, 2014. Dissociation of Cascadia margin gas hydrates in response to contemporary ocean warming, *Geophysical Research Letters*, 41, 8486-8494.

Klauda, J. B., Sandler, S. I., 2005. Global distribution of methane hydrate in ocean sediment, Energy and Fuels, 19 (2), 459-470.

Kvenvolden K.A. 1988. Methane hydrate — A major reservoir of carbon in the shallow geosphere?, Chemical Geology, 71, 41-51.

Milikov, A. V., 2004. Global estimates of hydrate-bound gas in marine sediments: how much is really out there?, Earth-Science Reviews, 66, 183-197.

Piñero, E., Marquardt, M., Hensen, C., Haeckel, M., Wallmann, K., 2013. Estimation of the global inventory of methane hydrates in marine sediments using transfer functions, Biogeosciences, 10, 959-975.

Ruppel, C. D., 2011. Methane Hydrates and Contemporary Climate Change, Nature Education Knowledge, 3 (10):29.

PRE-EXPEDITION RESULTS

Bottom Simulating Reflector Distribution and Regional Heat Flow

Introduction

This work relates to Tasks 2-4 in our original proposal. The results presented in this section were a significant portion of Marie Salmi's Ph.D. thesis at the University of Washington and were published in *Journal of Geophyscial Research Solid Earth*; the citation is below:

Salmi, M. S., H.P. Johnson, Harris, R.N., 2017. Thermal environment of the southern Washington region of the Cascadia Subduction Zone, *J. Geophys. Res. Solid Earth*, 122, 5852-5870.

Tectonic Setting

The Cascadia Subduction Zone (CSZ) extends 1100 km along strike from Mendocino, California, USA to Vancouver Island, Canada and is known to produce infrequent but high magnitude megathrust earthquakes [Atwater and Hemphill-Haley, 1997; Atwater, 2010; Goldfinger et al., 2012]. The CSZ subducting plate interface is unusually seismically quiet for an active subduction zone, with only limited numbers of earthquakes observed at the northern and southern terminations and offshore southern Oregon [Trehu et al., 2008, 2015; Morton and Bilek, 2014]. This accretionary margin is the result of the Explorer, Gorda, and Juan de Fuca oceanic plates subducting beneath the North American plate. The Juan de Fuca, the largest of these oceanic plates, subducts at a rate of 35 to 41 mm yr^{-1} with crustal ages ranging between 6 and 10 Ma at the deformation front [Wilson, 1993]. There is no distinguishable trench due to Late Pleistocene glacial sediment fill from the adjacent continental margin [Heaton and Hartzell, 1987; Calkins et al., 2011]. Sediment thickness seaward of the deformation front varies between 2 and 3 km. The incoming plate has one of the highest known basement temperatures of any subduction zone due to young age of the plate and the thermal isolation by rapid sediment accumulation rates [Davis et al., 1990; Wilson, 1993].

The Washington State portion of the CSZ comprises an accretionary wedge with distinct lower and upper margins, consisting of landward verging folds and faults [McNeill et al., 1997; Adam et al., 2004] atypical for an active subduction zone. Regions undergoing extension with westward dipping normal and listric faults are present on the middle and upper margin offshore Grays Harbor in areas shallower than 1000 meters water depth [McNeill et al., 1997]. The extensional faulting forms a distinctive mid-slope terrace feature within the Grays Harbor area (Figure 1) related to fluid over-pressurization at depth [McNeill et al., 1997].

Heat flow data along the CSZ margin is relatively sparse with limited thermal studies offshore Vancouver Island [Davis et al., 1990; Hyndman et al., 1993; Yuan et al., 1996; 1999], Oregon [Trehu et al., 1995; Zwart et al., 1996], and Washington [Booth-Rea et al., 2008]. In this study we analyze Multi-Channel Seismic (MCS) reflection data acquired during the MGL1212–COAST (Cascadia Open-Access Seismic Transects) survey collected on the R/V Langseth [Holbrook et al., 2012]. This cruise provided seismic imaging of the southern portion of the Washington Margin consisting of nine closely-spaced (~ 8 km) lines extending 25 km seaward of the deformation front to the edge of the continental shelf, approximately perpendicular to the margin. Two additional N-S lines provide along-strike data that overlap the nine E-W lines. BSRs imaged within the MCS profiles are interpreted in terms of temperature

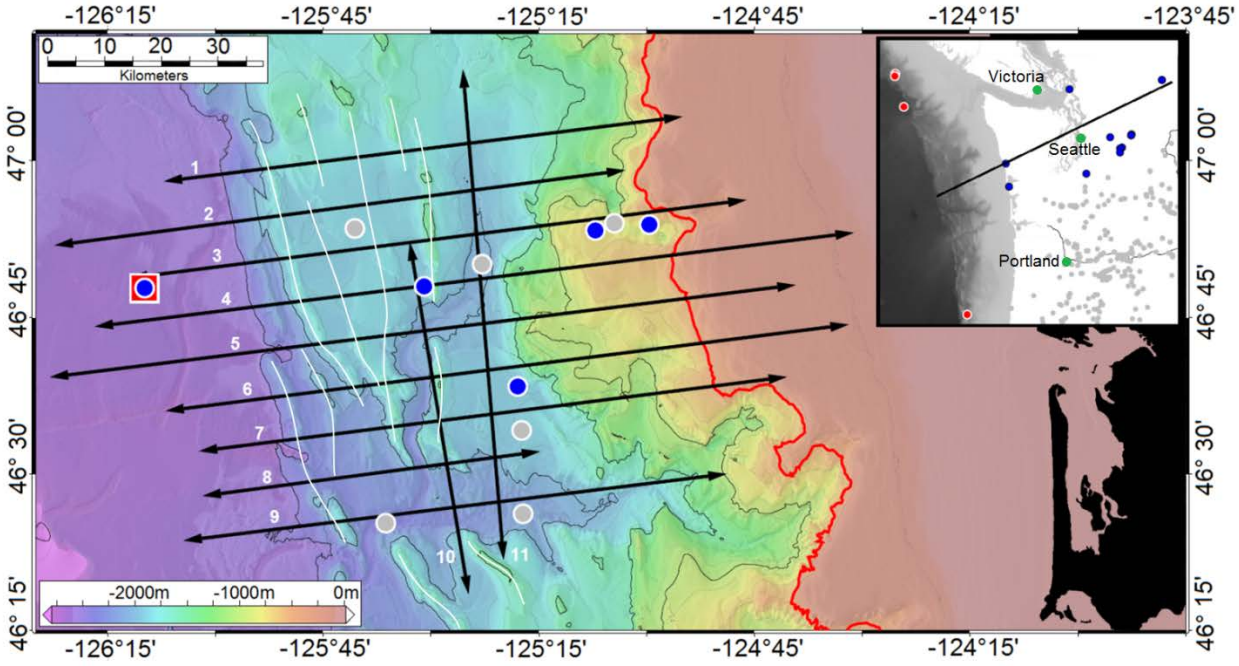

Figure 1: Location of COAST 2012 Multi-Channel Seismic profiles (black lines) with their corresponding line numbers (white text). White lines trace prominent anticlinal ridges visible in the MCS. LDEO OBSs (Blue circles) deployed during the 2012-2013 year within the Langseth survey area were equipped with thermistors. CTD cast location (red square) was used for BSR seafloor temperature calculations and sediment cores (grey circles) were used for BSR heat flow sedimentation correction. Inset displays IODP/ODP borehole (Red dots) and continental heat flow measurements (grey dots) including those used in the current study (blue dots). Green dots mark major metropolitan cities.

and provide a high-resolution 3-D view of heat flow variations across the accretionary wedge. The primary goal of this study is to provide an increased understanding of the thermal environment of a 100 km along-strike portion of the CSZ offshore Southern Washington using analysis of high-resolution BSR data. The BSR heat flow data was corrected for bathymetry and sedimentation accumulation rate, and incorporated MCS derived thermal conductivity values. BSR estimates of heat flow are then compared to a finite element model derived for each of the 9 perpendicular MCS lines to estimate temperatures at the top of the oceanic basement. Areas of misfit between the BSR data and the numerical model are interpreted in terms of fluid discharge.

Heat Flow Estimates From Bottom Simulating Reflectors

The COAST MCS profiles (Figure 1) were acquired using a single 8 km long streamer deployed at a water depth of 15 meters for all odd numbered lines (1, 3, 5, 7, 9 and 11) and 9 meters depth for all even lines (2, 4, 6, 8, and 10), collecting data at 2 millisecond sample rate. A total of 36 individual airguns were used, resulting in a total of 6600 cubic inches of source volume. All MCS lines were processed shipboard using ProMax seismic software [https://www.landmark.solutions/SeisSpace-ProMAX]. The seismic profiles used to calculate the BSR depths were generated using a two-dimensional velocity structure for each line determined

through pre-stack time migration. This study primarily used shipboard processed seismic profiles as the consistently processed data existed for all MCS lines.

Solid hydrate is an ice-like phase with lattice vacancies filled with predominately methane molecules that forms in regions of high pressure and low temperature [Henry and Clennell, 1999; Malinverno et al., 2008]. BSRs within the sediment column mark the boundary between solid hydrate above and free gas below, indicating the lower limit of hydrate stability zone [Davis et al., 1990; Kvenvolden, 1993]. We identified BSRs using the following criteria: 1) the reflector horizon crosses surrounding sediment stratigraphy; 2) the horizon roughly mimics the seafloor bathymetry; and 3) the acoustic wave forms a negative polarity horizon [Davis et al, 1990]. Requirements for BSR formation include upward diffuse fluid flow and relatively high gas concentrations within the sediment pore space [Haacke et al., 2008; Yuan et al., 1999].

Heat flow (Q) is derived from BSRs based on the following equation,

$$Q = K \frac{T_{BSR} - T_{SF}}{Z_{BSR}}, \quad (1)$$

where T_{BSR} and T_{SF} are the temperatures (°C) at the BSR and seafloor respectively, Z_{BSR} is BSR depth below seafloor, and K is bulk sediment thermal conductivity. As with prior studies, we assume that after correcting for the effects of bathymetry and sedimentation, the thermal gradient between the seafloor and BSR is constant and that the accretionary wedge is in a thermal steady state.

To determine Z_{BSR}, the seafloor and BSR two-way travel time (TWTT) from the MCS profiles were recorded by the 2D horizon tracking module within the software program OpendTect [http://www.opendtect.org/]. TWTT is recorded for every Common Depth Point (CDP) within the individual survey profiles. To convert TWTT to depth, the velocity profile within the upper 500 meter of the sediments is determined using the method from Hyndman et al., [1993] and seismic velocity profiles collected during the 2012 Langseth cruise (Figure 2) using the relationship,

$$Z_{BSR} = 0.776\Delta t + 2.33x10^{-4}\Delta t^2, \quad (2)$$

where Δt is time difference between the seafloor and the BSR, both in seconds of TWTT. Based on the MCS source frequency, the TWTT vertical resolution is between ±3 to ±5 meters and accounting for uncertainties in the velocity, the depth estimate uncertainty is approximately ±13 m.

We estimate the average thermal conductivity, K, between seafloor and Z_{BSR} using the relationship provided by Davis et al. [1990] for the Vancouver Island Margin located 250 km north of our survey area which accounts for the increase in thermal conductivity with depth due to porosity loss. Comparison of the Z_{BSR} derived K to thermal conductivity measurements from Ocean Drilling Program (ODP) 889/890 boreholes offshore Vancouver Island and Oregon shows a correlation to within ±10% and are assumed to be similarly reliable for the near surface Cascadia margin sediments [Davis et al., 1990; Ganguly et al., 2000]. Heat flow is calculated using the average K between seafloor and Z_{BSR} [Ganguly et al., 2000; Riedel and Shankar, 2012]. Seafloor temperatures, T_{SF}, at the seawater/sediment interface are determined using a Conductivity Temperature Depth (CTD) cast taken west of the deformation front (Figure 1) by the R/V Thompson in 2012, within the same region and time period as the COAST cruise. CTD casts have commonly been used for previous BSR heat flow studies for determining seafloor temperatures [He et al., 2007; Riedel et al., 2010]. Based on ocean bottom seismometers (OBS) equipped with temperature sensors deployed during the survey cruise time period (July 12-24, 2012), the seafloor temperature can vary ±0.3°C from that estimated by the CTD cast [Toomey et al., 2014].

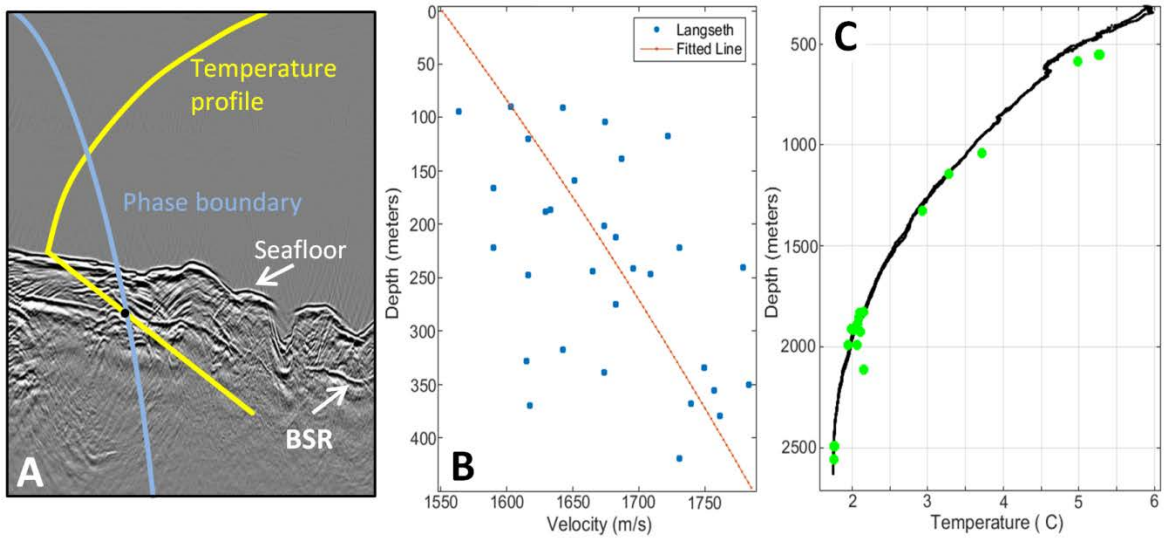

Figure 2: Method and parameters used to calculate BSR heat flow. A) BSR temperature is calculated knowing the depth of the seafloor and BSR using the methane hydrate phase stability curve (blue line). B) Seismic velocity (Vp) to meters below seafloor relationship from the Langseth pre-stack time migrated velocity profiles. Data points represent velocity picks over anticlinal ridges within the lower accretionary margin. Orange line is the best fit of the data. See text for equation. C) Temperature profile determined by CTD cast (Figure 1). Green dots are seafloor temperatures, measured 5 centimeters above the seafloor derived from Thermal Blankets

BSR depth within the sediment column is a function of both pressure and temperature. If the pressure can be estimated, then the phase relationship between gas and hydrate can be used to determine T_{BSR}. Previous studies based on borehole and seismic profiles find that *in situ* pressures within the sediment column are neither purely lithostatic nor hydrostatic, but fall between these two end members [Hyndman et al., 1993; Screaton et al., 2002; Saffer and Tobin, 2011]. Based on these previous BSR heat flow studies, we assume a 50% ratio of hydrostatic to lithostatic pressure at the BSR depth [Hyndman et al., 1993; Saffer, 2015]. This assumption differs from previous work on the Cascadia Subduction Zone that applied either fully hydrostatic [Hyndman et al., 1992; Ganguly et al., 2000] or fully lithostatic pressure [Golmshtok et al., 2000], a difference that can account for roughly 3 mW m^{-2} difference in BSR heat flow. For this study, *in situ* pressure is calculated using the following equation [Haacke et al., 2008],

$$P(Z_{BSR}) = \frac{1}{2}\left[Lg\phi_0(\rho_f - \rho_s)\left(1 - e^{-Z_{BSR}/L}\right) + g\rho_s Z_{BSR} + g\rho_f Z_w + g\rho_f (Z_{BSR} + Z_w)\right]. \quad (3)$$

Pressure (P) is based on Z_{BSR} and is calculated assuming a porosity compaction length (L) of 1.2 km [Hyndman et al., 1993], gravity (g) of 9.81 m s^{-2}, grain density (ρ_s) of 2.65x10^3 kg m^{-3} [Shi et al., 1998], and seafloor porosity (ϕ_o) of 0.55. Water density (ρ_f) varied based on *in situ* pore fluid temperature [Lienhard and Sharqawy, 2009], salinity of 33.5 g kg^{-1}, and seafloor depth (Z_w) and Z_{BSR}. We assume a pure methane gas composition [Davis et al., 1990; Kastner et al., 1995] and pore-water salinity at the BSR depth similar to ocean salinity of 33.5 g kg^{-1} [Riedel et al., 2006; Liu and Fleming, 2006; Kastner et al., 1995]. BSR pressure and salinity provides a BSR temperature using an empirically derived stability relationship [Tishchenko et al., 2005]. Seafloor depths used to estimate water column pressure are determined from swath bathymetry corrected with eXpendable BathyThermograph (XBT) derived sound velocities, collected during

the COAST cruise. Estimated overall uncertainty for the pressure was ±0.15 MPa, corresponding to a BSR temperature uncertainty of ±0.06 °C.

Bathymetric Correction

Seafloor bathymetry variations perturb the geothermal gradient, with local bathymetric highs decreasing the heat flow and depressions increasing the heat flow. To determine the isotherm distribution in the margin sub-surface, we apply a correction to the heat flow measurements [Ganguly et al., 2000; Harris et al., 2010; Li et al., 2013; Figure S1]. Seafloor bathymetry was derived from 50 meter gridded Langseth EM122 bathymetry with gaps filled using the 100 meter resolution Global Multi-Resolution Topography [GMRT; Ryan et al., 2009].

The horizontal dimension of the seafloor area used for the bathymetric correction was determined as 10 times the Z_{BSR} (Figure S2). To estimate the thermal gradient correction at the BSR depth due to abrupt changes in bathymetry, a 3-D map of seafloor temperatures was constructed by extracting temperatures corresponding to the seafloor depths from the CTD cast (Figure 2). The thermal offset associated with individual BSR measurements were determined by continuous propagation of the temperature using the discrete Fourier Transform method to account for localized bathymetric variability. The resulting gradient corrections were then applied to the geothermal gradient. The overall average bathymetric correction was +7.5 mW m^{-2} with predominantly large bathymetric corrections concentrated around areas of sharp topographic relief including anticlinal ridges and steep canyon walls.

Sediment Accumulation Correction

The rapid sediment accumulation rates present on the Washington margin, ranging up to 44 cm kyr^{-1} [Barnard, 1978], produce a transient decrease in the surface heat flow value [Hutchison, 1985; Kaul et al., 2000]. Correcting for recent sedimentation requires both the interval of the deposition and the sediment accumulation rate, which varies widely along a continental margin due to erosive turbidite channels and distance from fluvial inputs. Sediment accumulation rates for the Cascadia accretionary wedge were determined using six age-dated piston cores with lengths ranging from 1.78 to 5.28 meters [Barnard, 1978; Figure 1] applied over an interval of 10,500 years (Table S1). The low density of sampling sites required the accumulation rates to be averaged into zones, which included anticlinal ridges, sedimented 'ponds', and turbidite channels. These corrections were applied to the heat flow values using the solution to the thermal growth model [Martin et al., 2004; Equation 4]:

$$Q_{BSR} = Q_B \left[1 - \frac{1}{2} \left[\begin{array}{c} \left(1 + \frac{v_s t_s}{Z_{BSR}}\right) erfc\left(\frac{Z_{BSR}+v_s t_s}{2\sqrt{\kappa t_s}}\right) \\ -\left(1 - \frac{v_s t_s}{Z_{BSR}}\right) e^{\left(\frac{-v_s Z_{BSR}}{\kappa}\right)} erfc\left(\frac{Z_{BSR}-v_s t_s}{2\sqrt{\kappa t_s}}\right) - 2\frac{v_s t_s}{Z_{BSR}} \end{array} \right] \right]. \quad \textbf{(4)}$$

The required parameters include the sediment accumulation rate (v_s, in meters $year^{-1}$), depth of the BSR below seafloor (Z_{BSR}, meters), and sediment accumulation time interval (t_s, years). A sediment thermal diffusivity (κ) of 1.15×10^{-7} m^2 s^{-1} was determined *in situ* within the mid-slope terrace of the COAST Line 4 at 1049 meters water depth [Homola et al., 2015]. Q_B is the bathymetrically corrected heat flow, resulting in Q_{BSR}, the basal heat flow with effects of sediment accumulation removed. Based on the uncertainties associated with the BSR heat flow calculation (Supplemental Material), the calculated uncertainty of the BSR heat flow is

approximately ±10%, similar to previous estimates [Davis et al., 2003; Marcaillou et al, 2006], with a maximum of ±18% for areas of rapid bathymetric variations.

Localized Heat Flow Behavior

BSRs were identified within 10 of the 11 Langseth MCS lines, resulting in a total of 40,232 individual heat flow determinations within the survey area (Figure 3). No BSRs were observed within the deformation front or beneath the most seaward anticlinal ridge. The westward limit of detected BSRs was observed along Line 4, beneath the second anticlinal ridge landward of the deformation front. Seafloor depths where BSRs are identified range from 2310 meters within sediment ponds between anticlinal ridges up to 710 meters along Line 4. No BSRs were observed near the calculated methane hydrate stability water depth of 500 meters at this latitude of the Cascadia margin [Johnson et al., 2015]. Of the two Langseth MCS lines oriented parallel to the deformation front (Figure 1), Line 11 has no detectable BSRs due to poor imaging of the sub-seafloor, although the adjacent Line 10 has better data quality and BSRs are observed along much of the profile. The data gap along Line 10 between Lines 2 and 3 was caused by an air gun shutdown due to the presence of large mammals within the area (Figure 3A). BSRs are primarily located (51% of total picks) within exposed anticlinal ridges and within the prominent mid-slope terrace (21%) (Figure 3A), while several buried anticlinal ridges in Lines 1, 2, and 5-7 contain BSRs located above buried structures, such as diapirs or anticlinal ridges. There is a general lack of observable BSRs within the inter-ridge sediment ponds and turbidite channels.

BSR heat flow values show a generally decreasing trend landward from the deformation front, an expected result due to the plate convergence rate and the thickening overlying sediment wedge. Within the lower accretionary wedge, heat flow drops sharply from around 90 mW m^{-2} to 70 mW m^{-2} and then continues to decrease landward at a similar rate as observed in the lower wedge (Figure 3B). An abrupt and systematic decrease in heat flow of approximately 12 mW m^{-2} occurs approximately 43 kilometers east of the deformation front, the furthest landward extent of the mid-slope terrace (Figure 3B). Another distinct feature within the heat flow profiles is an increase in heat flow exceeding 20 mW m^{-2} over a prominent sharp anticlinal ridge located 30 to 35 km from the deformation front within Lines 1- 5 (Figure 3A). Low heat flow values present on the eastern upper margin segment of Line 4 are distinct from other profiles in the same region (Figure 3B).

Subduction Thermal Model

A finite element model (FEM) was constructed to represent a 2-D slice of the subduction zone replicating the thermal and geological conditions for each of the 9 across-strike MCS profiles. This FEM produces surface heat flow values that can be compared with heat flow estimates derived from BSRs and continental heat flow values. We use the algorithm of Wang et al. [1995] previously used in many subsequent heat flow studies [e.g., Harris and Wang, 2002; Harris et al., 2010; Cozzens and Spinelli, 2012]. The FEM uses an 8-node construction with a corresponding thermal element defined by estimated thermal parameters governed by the following equation (Equation 5),

$$0 = \nabla \cdot (K_m \nabla T) - \rho c v \cdot \nabla T + Q_R, \quad (5)$$

where ρc is volumetric thermal capacity, K_m is bulk material thermal conductivity, v is material velocity, T is modeled temperature, and Q_R is radiogenic heating. The thermal model was iterated until the thermal environment reached steady state.

The thermal model internal structure was determined by assigning zones corresponding to physical/geological units of the CSZ such as the depth and thickness of the downgoing Juan de Fuca plate [Flueh et al., 1998; Parsons et al., 1999] and the location and shape of the Siletz terrane; an oceanic basaltic complex accreted onto the North American plate [Blackwell et al., 1990; Parsons et al., 1999; Wells et al., 2014; Wong, 2005]. Unfortunately, little is known of the *in situ* state of the Siletz rock properties but data based on published laboratory, seismic velocities, and exhumed subducted crust are used instead.

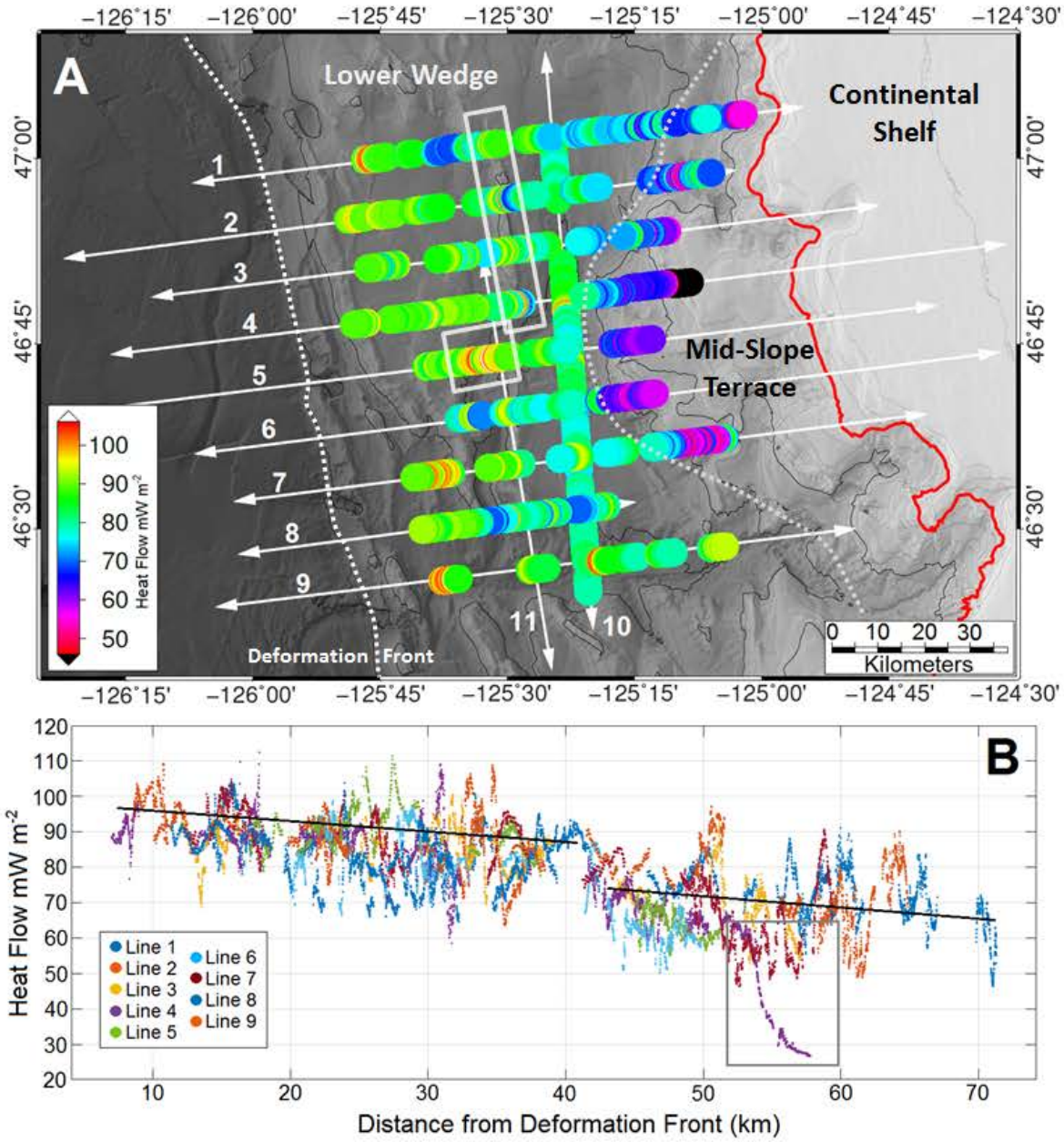

Figure 3: A) BSR heat flow measurements (circles) along the 11 MCS lines (white solid lines). Deformation front, lower and mid-slope defined by dashed grey lines. The 500 meter upper limit of hydrate stability is indicated by a solid red line. B) All heat flow profiles are indexed asdistance from the deformation front. General heat flow trends are traced by black lines.

The geometry of the FEM (Figure 4) is defined through node location, providing the internal physical structure of the model. The young (8.5 Ma) lithosphere of the Juan de Fuca plate has not yet reached thermal equilibrium, therefore isotherms at the western boundary and lithosphere thickness are assigned a full theoretical thickness of 95 km [Stein and Stein, 1992]. This assignment allows the plate and upper mantle geotherms to evolve with age based on a modified half space cooling model. MCS profiles collected from the Juan de Fuca Spreading Ridge to the Cascadia margin offshore Washington suggest a relatively constant crustal thickness of 6.5 km [Han et al., 2016]. The COAST Langseth seismic profiles indicate that the sediment thickness at the deformation front varies between 2.5 and 2.9 km, values which were incorporated into the corresponding thermal models for each MCS line. We assigned a 1° slope for the incoming oceanic plate just west of the deformation front due to the pre-subduction bending of the incoming plate [Han et al., 2016]. The plate continues to subduct at a shallow angle of 5° beneath the outer accretionary wedge, increasing to 10° at the mid-accretionary wedge 60 km from the deformation front, and continuing to increase to 15° as the oceanic plate separates from the continental plate [Flueh et al., 1998; Parsons et al., 1999; Han et al., 2016].

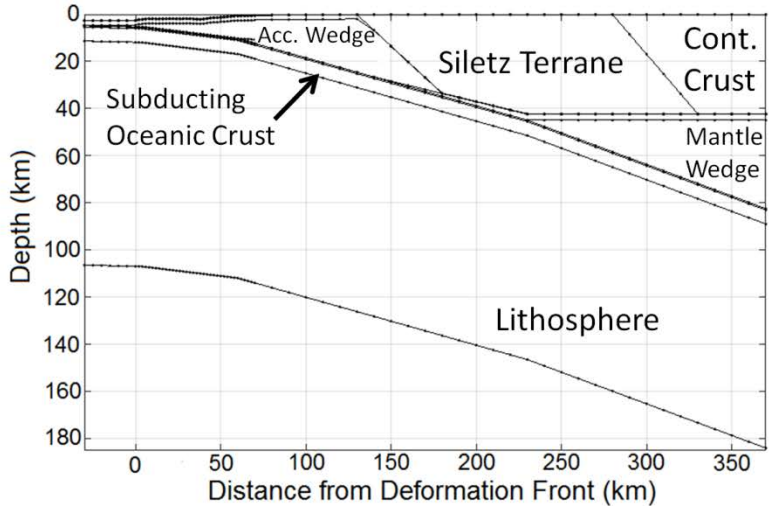

Figure 4: Thermo-physical units of the finite element model based on active and passive seismic profiles.

The western boundary of the Siletz terrain at the Washington Coast marks the transition from accretionary wedge sediments to the basaltic Siletz backstop which further extends to the eastern edge of Puget Sound for this latitude [Parsons et al., 1999]. Incorporated seafloor depths were estimated from bathymetry within the GMRT database [Ryan et al., 2009] and extrapolated to a 2 km horizontal grid to fit the mesh resolution of the model. The incoming oceanic plate was assigned a horizontal velocity of 40 mm year^{-1} [Clague, 1997; McNeill et al., 1997] and adjusted as the plate subduction angle increased (Figure S3). Estimated mantle wedge circulation beneath Puget Sound was determined based on the subduction rate of the incoming oceanic crust (Figure S3). The North American continental plate has an estimated thickness of 42 ± 6 km [McCrory et al., 2014]. Slight ambiguities in the assumed model geometry account for a potential heat flow variability of ±3.5 mW m^{-2} at the deformation front and ±1 mW m^{-2} in the Puget Sound Basin, corresponding to uncertainties of the plate interface of ±4.7°C and ±22°C respectively.

Boundary conditions for the numerical model are calculated using the same thermal properties assigned to the thermal model (Table 1). The top (seafloor and land topography) and bottom boundaries are set to constant temperatures of 2°C and 1450°C, respectively [Stein and

Table 1. Model Thermal Parameters

Name	Thermal Conductivity ($W\ m^{-1}K^{-1}$)	Published Ranges	Thermal Capacity ($J\ m^{-3}K^{-1}$)	Radiogenic Heat ($\mu W\ m^{-3}$)
Heat flow zone	1.1[A]	1.15[F]	$2.6x10^6$	0.6[I,J]
Continental Crust	2.50[B]	2.75[H]	$3.3x10^6$ [H]	0.2
Siletz terrain	1.59[C]	1.8[N];2.0[F]; (1.37;2.25)[L]	$3.3x10^6$ [H]	0.02[K]
Upper Sediment	Range[*]	--	$2.6\ x10^6$	0.6[I,J,F]
Main Sediment	2	--	$2.6\ x10^6$	0.6[I,J,F]
Lower Sediment	2.3	--	$3.0\ x10^6$	0.6[I,J,F]
Transition	2.9[H]	--	$3.3x10^6$	0.02
Mantle	3.1[H]	2.9[2],3.14[M]	$3.3x10^6$ [H]	0.02[H]
Oceanic Crust -2A	2.9[N,EF]	--	$3.3x10^6$ [N,J,F] $2.6x10^6$ [H]	0.01[K]
Oceanic Crust - 2B+C	2.9[N,E,F]	--	$3.3x10^6$ [N,J,F]	0.01[K]
Lithosphere	3.25	--	$3.3x10^6$ [N,J]	0.02[H]

A: Davis et al., 1990
B: McKenzie et al., 2005
C: Blackwell et al., 1990; Wong, 2005
D: Wang et al., 1993
E: Wang and Davis, 1992
F: Hyndman and Wang, 1993
G: Davis and Villinger, 1992
H: Wada et al., 2008
I: Lewis et al., 1988
J: Wang et al., 1995
K: Oleskevich et al., 1999; Wong, 2005
L: McKenna and Blackwell, 2002
M: Parsons and Sclater, 1977
N: Cozzens, 2011

Stein, 1992]. A 500 meter thick thermal zone, utilizing thermal parameters that match the average BSR variables (Table 1), was incorporated into the top of the model to calculate surface heat flow. The landward boundary conditions consist of a continental geothermal gradient parameterized with a heat flow of 60 mW m^{-2} and an adiabatic gradient of 0.3°C km^{-1} through the mantle wedge [Blackwell et al., 1990; Hyndman and Wang, 1993]. The seaward boundary geotherm, located 30 km seaward of the deformation front, was calculated using the program SlugSed [Hutnak and Fisher, 2007]. This finite element model simulates the thermal evolution

of the oceanic plate in 2D and includes the thermal impact of the rapid sediment accumulation as the oceanic plate ages. Thermal diffusivity was adjusted within the SlugSed model to closely match heat flow values obtained using two thermal blankets deployed by the ROV Jason II west of the deformation front [Salmi et al., 2014; Johnson et al., 2013]. All other parameters within SlugSed were kept identical to the FEM. The plate is assumed to be 7.75 Ma old at the western edge of the model, with continuous spreading producing an oceanic plate age of 8.5 Ma at the deformation front [Wilson, 1993].

Radioactive decay due to heat production (Q_R) within the sediments will increase surface heat flow. Estimates of radiogenic heating were assigned to each sub-surface structure using *in situ* measurements and published models (Table 1). Radiogenic heat production for the Siletz terrain, composed largely of oceanic basalt, is assumed to be 0.02 μW m^{-3} [McKenna and Blackwell, 2002; Wong, 2005]. The assigned effective coefficient of friction of 0.03 along the subduction thrust is consistent with previous published values [Wang et al., 1995; Wada and Wang, 2009; Harris et al., 2010]. Thermal conductivity was determined using a porosity model that varies both as a function of depth due to variable sediment compaction and across-strike to account for large porosity changes within the sediment column. Excluding the top two kilometers of accretionary wedge sediments, thermal conductivity values for each thermo-physical unit are reported in Table 1. A variation of 10% in model thermal conductivity (see Supplemental Material) can offset offshore heat flow values near the deformation front by ±12 mW m^{-2} and alter plate temperatures by ±0.5°C at the deformation front increasing to ±10°C near the mantle tip.

Seismic velocity analyses reveal a general across-strike variation in velocities that are attributed to porosity changes and the thermal conductivity values used in the model were assumed to be a direct function of these porosities. To capture the landward decrease in porosity within the thermal model, the nodes within the top 2 km of the accretionary wedge were assigned values of thermal conductivity based on their position within the margin. The 2 kilometer depth limit was based on the depths within the MCS shipboard profiles that had identifiable reflectors. Bulk thermal conductivity (K_m) for each node with the top 2 km was calculated using the geometric mean of water (K_w) and sediment (K_s) thermal conductivities: $K_m = {K_w}^{\emptyset} {K_s}^{(1-\emptyset)}$ where porosity (ϕ) was defined using $\emptyset = \emptyset_o e^{-z/L}$, which accounts for porosity reduction with increasing sediment depth (z) due to sedimentation compaction [Athy, 1930; Kinoshita, 1994]. The surface porosity Φ_o is assigned a value of 0.55 and composite thermal conductivity is calculated based on a grain thermal conductivity of 2.5 W $m^{-1}K^{-1}$ [Grevemeyer and Villinger, 2001] and water thermal conductivity of 0.6 W $m^{-1}K^{-1}$. Previous studies of the porosity scaling parameter (L) have found variations in compaction lengths exists along the margin cross-strike, with a value of L = 1.5 for the incoming plate sediments, L = 1.0 for the lower margin and L = 2.5 for the mid-slope terrace [Hyndman et al., 1993].

In comparison to the Vancouver Island margin, the high resolution seismic velocity structure of COAST MCS Line 5 [Fortin, 2015] shows similar porosity length scales and a sharp transition from 1.3 to 2.7 km from the lower to middle/terrace portion of the wedge, but only a very slight +0.1 km change from the incoming sediments to the lower wedge (Figure S4). For our model calculations, we assigned L values of 1.3, 1.2, and 2.7 km to the incoming sediment, the lower wedge and the remaining continental margin, respectively.

Uncertainty in the thermal model due to geometry and thermal properties (see Supplemental Material) show that surface heat flow variability ranges from ±8 to ±16 mW m^{-2} for the lower accretionary wedge surface heat flow, primarily due to the large unknowns in thermal

conductivity. This leads to a maximum plate temperature uncertainty of ±7°C at the deformation front, which reaches ±32°C at the mantle tip located 230 km east of the deformation front at a depth of 41 km.

Thermal Model Results

Individual thermal models for the accretionary wedge were constructed for all 9 MCS profiles oriented perpendicular to the subduction zone strike. Each model used distinct seafloor bathymetry and thermal conductivities, as described above, to emulate variations within each profile (Figure 5). The terraced shape of the Washington accretionary wedge has a pronounced effect on calculated heat flow values that was not considered by previous Cascadia thermal models. Sediment thickness on the incoming plate ranged from 2540 meters on Line 7 to 2910 meters on Line 3 and was accounted for in the thermal models. The general north-south trend in sediment thicknesses arises from the regional distribution of Pleistocene sediment fans on the Juan de Fuca plate (Figure 1), which includes the Nitinat Fan to the north and the Astoria Fan to the south [Gutscher et al., 2001].

Modeled surface heat flow (Q_{model}) decreases systematically landward toward the Puget Sound Basin (Figure 5) due to the subduction of the relatively cooler oceanic plate that initially depresses isotherms within the overlying continental plate prior to reaching the warm back-arc mantle within the Puget Sound basin. Model values of seafloor heat flow on the incoming oceanic plate immediately west of the deformation front have an average value of 110 ± 1.1 mW m^{-2}. At approximately 75 km landward of the deformation front, most heat flow profiles have decreased to values near 53 mW m^{-2} coinciding with the seaward edge of the Washington continental shelf. Continuing eastward, heat flow decreases to 39 mW m^{-2} at the Washington coastline 135 km east of the deformation front, and falls to values near 21 mW m^{-2} beneath Olympia, Washington. Heat flow values from the FEM compare closely to onshore heat flow measurements from drilled wells located within 100 km north and south of the subducting plate dip profile [Blackwell et al., 1990; Figure 5; Figure 1- inset]. Heat flow values located within the lower margin, less than 20 km from the deformation front, display a pronounced trend where general heat flow values decrease faster in the northern lines compared to the southern lines (Figure 5). Line 9 is an exception to this trend within the first 5 km, due to the influence of a large isolated anticlinal ridge located directly landward of the deformation front (Figure 1).

Modeled Temperature at the Plate Interface

The subducting Juan de Fuca plate has a poorly imaged decollement along the subducting plate fault plane and it is assumed for the purpose of this study that the sediment-crust interface is the plate boundary [Davis and Hyndman, 1989; Booth-Rea et al., 2008]. Modeled temperatures along the crust/sediment interface at the deformation front for the nine closely spaced MCS lines range between 164°C to 179°C (Figure 6). It should be noted the modeled temperatures are near the range of uncertainty. Incoming plate boundary temperatures appear positively correlated with the thickness of the incoming sediment package (Figure 6) and represent a source of along-strike thermal variability for the updip limit of the seismogenic zone. Our thermal models predict that the 350°C plate boundary temperature occurs 94 km east of the deformation front and the decollement temperature reaches 450°C at 155 km from the deformation front (Figure 6).

The location of the seismogenic zone, where tectonic stress is stored along the megathrust fault, depends, at least in large part, on thermally mediated processes [Hyndman et al., 1993; Cozzens and Spinelli, 2012]. In older models, the updip limit of the seismogenic portion of the fault zone was determined by the smectite-illite transition temperatures between 100°-150°C [Hyndman and Wang, 1993; Moore and Saffer, 2001]. However, recent studies have identified other chemical and physical processes such as porosity and diagenetic alterations that also alter the friction along the decollement in the temperature range of 60° to 150°C [Saffer and Marone, 2003; Lauer and Saffer, 2015]. The development of chemical diagenesis along the downgoing plate interface and within the overlying sediments depends strongly on the temperature and pressure environment. Thermal modeling of the COAST dataset indicates a plate boundary temperature range of 164°C to 179°C at the deformation front. This isotherm distribution would place the smectite-illite thermal transition zone well within the overlying sediment column, rather than located at the sediment-igneous plate boundary. A smecitite-illite transition that lies within the overriding sediment package has implications with how the deformation front and accretionary wedge may deform and shift during a megathrust earthquake.

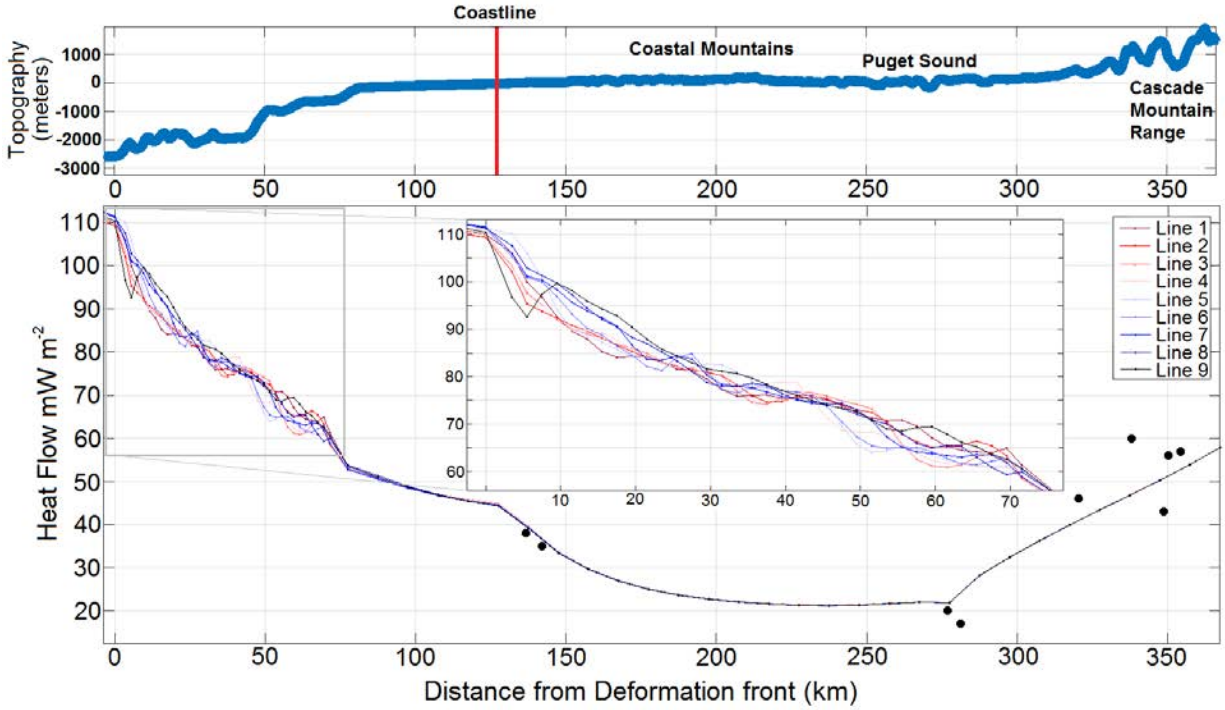

Figure 5: Large scale view of model derived surface heat flow profiles from the incoming Juan de Fuca plate to east of the Cascade Mountains. Topographic profile (top) indicates major geographical locations. Co-located black dots mark continental heat flow measurements [Blackwell et al., 1990].

Based on chemical and physical properties of the relevant rock composition, the down-dip limit of the seismogenic zone has been suggested to correlate with the 350°C isotherm due to the brittle-ductile transition [Hyndman et al., 1993, Oleskevich et al., 1999; Hyndman, 2013]. A higher temperature range of 350°C to 450°C for the fault interface has been assigned as a transition zone, where earthquakes will not originate but a megathrust fault can still slip if initiated further updip [Hyndman et al., 1997]. It has been suggested the significant presence of quartz within the overlying oceanic derived Siletz terrane at the fault zone could elevate this transition zone temperature as high as 550°C [McCrory et al., 2014]. Based on our 150° to 350°C

temperature bounds, the proposed fully-locked seismogenic zone is roughly 100 km wide along the southern Washington portion of the Cascadia Margin and we identify this location as fully offshore. This result compares well with the previous thermal model constructed by Hyndman and Wang, 1995 (Figure 6), despite different lithostatic and incoming plate parameter assumptions.

Comparison of modeled thermal boundaries to the geodetic model locking zones from Wang et al., [2003] and shows that our thermally defined boundaries of 300°C and 450°C are located within the same regions as their zones of 100% and 75% locking. However, our thermal boundaries are slightly narrower in the northern section of the survey area (Lines 1 - 4) and diverge landward from the geodetic model further south (Lines 5 – 9). Geodetic modeling by Schmalzle et al., [2014] that assume the outer portion of the accretionary wedge is fully locked show a similar locking distribution to Wang et al., [2013] but appear more parallel to the coast, closer to our modeled isotherms. The general agreement between model derived isotherms and geodetically determined locked percent argue for the importance of using both methods to determine seismogenic risk of subduction zones.

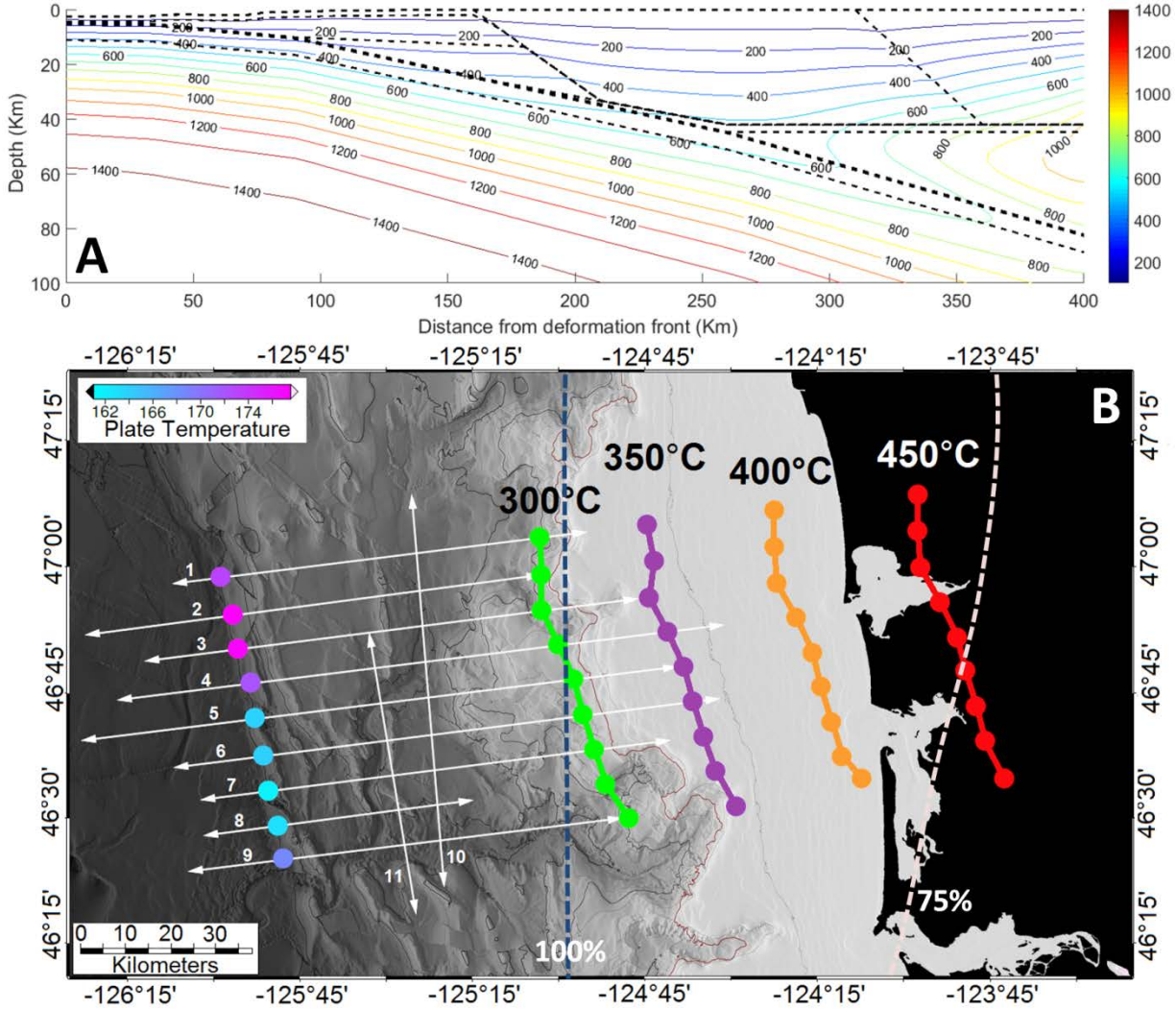

Figure 6: A) Modeled isotherm profile for MCS Line 5. B) Temperature of Juan de Fuca plate sediment interface at the deformation front (circles) for all 9 profile lines, see color bar for scale. The 300°, 350°, 400°,

and 450°C isotherms for the plate sediment interface are marked with connected circles. The COAST survey profiles are marked by white lines. Dashed line marks the fully locked (dark blue) and the 75% locked (white) plate interface based on geodetic modeling [Wang et al., 2003].

Fluid Advection

Upward fluid advection within the lower accretionary margin produced from sediment compaction or escape from within the igneous plate explains the observed BSR heat flow departures from the models. Previous studies showing a similar overall increase in heat flow within the central portion of the lower wedge (Figure 3A) has been interpreted as evidence for substantial sub-surface diffuse fluid flow on the Vancouver Island margin based on Darcy fluid modeling of the accretionary wedge [Davis et al., 1990; Wang et al., 1993].

To estimate upward fluid advection, we first assume that most fluid is initially produced from sources below the upper 500 meters of the sediment column and flows vertically into the near seafloor BSR zone [Le Pichon, 1991]. Fluid movement can be estimated using Equations 6 and 7 below [Bredehoeft and Papadopulos, 1965; Hutnak and Fisher, 2007],

$$\frac{T_2 - T_1}{T_p - T_1} = \frac{e^{(\beta Z_{BSR}/Z_p)} - 1}{e^{\beta} - 1} \quad (6)$$

$$\beta = \frac{v_z c_f \rho_f Z_P}{K_m} \quad (7)$$

using seafloor temperature (T_1), BSR temperature (T_2), water volumetric thermal capacity ($c_f \rho_f$) and modeled temperature (T_p) at ~500 meter sediment depth (Z_p). The resulting fluid flow estimates (v_z) ranged locally from weak down flow of fluid to a maximum fluid flow approaching +3.5 cm yr^{-1}. The median fluid flow for the study area was +0.4 cm yr^{-1}, based on the offset between BSR and model values. Comparison to previous estimates of fluid advection include +1.6 mm yr^{-1} based on standard porosity compaction [Le Pichon, 1991], measured fluid advection within the Oregon coast of +3.2 cm yr^{-1} [Zwart et al., 1996] and localized maximum values that approach +1 m yr^{-1} [Han and Suess, 1989], our estimates lie within the previous estimates of margin fluid flow.

Conclusions

Bottom simulating reflectors derived from 11 multi-channel seismic profiles identify key variations in heat flow values within the southern Washington section of the Cascadia Subduction Zone. These new MCS profiles detected gas hydrate deposits extending across-strike, ranging from 7 km east of the deformation front to the shoaling seafloor depth of 700 meters on the upper margin. After corrections for bathymetry and sedimentation, heat flow values follow a generally declining trend beginning approximately 95 mW/m^2 and decreasing to near 60 mW/m^2 at a 60 km distance from the deformation front. Abnormally low heat flow in the Line 4 MCS profile within a prominent mid-wedge terrace indicates recent large-scale slumping and listric fault rotation within an area permeated with abundant extensional normal fault zones visible in the COAST MCS profiles.

Thermal models corresponding to the nine across-strike MCS lines were constructed using variable accretionary wedge thermal conductivity values and thicknesses of the incoming sediment. Modeled decollement temperatures at the deformation front produced incoming oceanic plate interface temperatures ranging from 164°C to 179°C. These temperatures locate the updip limit of the seismogenic zone at the deformation front and identify a source of along-strike

thermal variability. The downdip limit of the seismogenic zone at 350°C occurs west of the coastline at 94 km from the deformation front. These boundaries resolve a narrow 100 km wide seismogenic zone that is completely off-shore Washington State. Predicted plate sediment interface isotherms of 300°C and 450°C co-locate with the boundaries of 100 % and 75% locking respectively based on geodetic models.

Comparison between measured and numerically modeled BSR heat flow identify localized but substantial departures that reflect vertical fluid advection occurring throughout the lower accretionary wedge terrace sediments. Differences between the BSR data and model estimates produce a fluid flow mean value of +0.4 cm yr^{-1} for the entire survey area, with localized fluid flow extremes approaching +3.5 cm yr^{-1}.

References

Abers, G. A., L. S. MacKenzie, S. Rondenay, Z. Zhang, A. G. Wech, and K. C. Creager (2009), Imaging the source region of Cascadia tremor and intermediate-depth earthquakes, Geology, 37, 1119–1122, doi: 10.1130/G30143A.1.

Adam, J., D. Klaeschen, D, N. Kukowski, and E. Flueh (2004), Upward delamination of Cascadia Basin sediment infill with landward frontal accretion thrusting caused by rapid glacial age material flux, Tectonics, 23, TC3009, doi: 10.1029/2002TC001475.

Athy, L.F. (1930), Density, porosity, and compaction of sedimentary rocks, Am. Assoc. Petrol. Geol. Bull., 14, 1–24.

Atwater, B. F. (2010), Evidence for Great Holocene Earthquakes along the Outer Coast of Washington State, Science, **236**(4804), 942–944, doi: 10.1126/science.236.4804.942.

Atwater, B. F., and E. Hemphill-Haley (1997), Recurrence intervals for great earthquakes of the past 3,500 years at northwest Willapa Bay, Washington, Prof. Paper 1576, US Geological Survey, Menlo Park, CA.

Barnard, W. D. (1978), The Washington Continental Slope: Quaternary Tectonics and Sedimentation. Mar. Geol. 27, 79–114.

Blackwell, D. D., J. L. Steele, S. Kelley, and M. A. Korosec (1990), Heat flow in the State of Washington and Thermal Conditions in the Cascade Range, J. Geophys. Res, 95, B12, 19495-19516.

Booth-Rea, G., D. Klaeschen, I. Grevemeyer, and T. Reston (2008), Heterogeneous deformation in the Cascadia convergent margin and its relation to thermal gradient (Washington, NW USA), Tectonics, 27, TC4005, doi: 10.1029/2007TC002209

Bredehoeft, J. D., and I. S. Papadopulos (1965), Rates of Vertical Groundwater Movement Estimated from the Earth's Thermal Profile, Water Resources Res., 1, 325–328.

Calkins, J. A., G. A. Abers, G. Ekström, K. C. Creager, and S. Rondenay (2011), Shallow structure of the Cascadia subduction zone beneath western Washington from spectral ambient noise correlation, J. Geophys. Res, 116, B07302, doi: 10.1029/2010JB007657

Chand, S., and T. A. Minshull (2003), Seismic constraints on the effects of gas hydrate on sediment physical properties and fluid flow: a review, Geofluids, 3, 275–289, doi: 10.1046/j.1468-8123.2003.00067.x.

Clague, J. J. (1997), Evidence for large earthquakes at the Cascadia Subduction Zone. Rev. Geophys., 35(4), 439-460, doi: 10.1029/97RG00222.

Cozzens, B. D. (2011), A wider seismogenic zone at Cascadia due to hydrothermal circulation in subducting ocean crust, M.S. Thesis, Dpartment of Earth and Environmental Science, New Mexico Institute of Mining and Technology, Socorro, New Mexico, USA.

Cozzens, B. D., and G. A. Spinelli, (2012), A wider seismogenic zone at Cascadia due to fluid circulation in subducting oceanic crust, Geology, 40(10), 899–902, doi: 10.1130/G33019.1

Daigle, H., E. J. Screaton, (2015), Evolution of sediment permeability during burial and subduction, Geofluids, **15**, 84–105, doi: 10.1111/gfl.12090.

Davis, E. E., and R. D. Hyndman (1989), Accretion and recent deformation of sediments along the northern Cascadia subduction zone, Geol. Soc. Am. Bull, 101, 1465–1480.

Davis, E. E., and H. Villinger (1992), 2. Tectonic and Thermal Structure of the Middle Valley Sedimented Rift, Northern Juan de Fuca Ridge, in Proceedings of the Ocean Drilling Program, Initial Reports, 139, College Station, TX.

Davis, E. E., R. D. Hyndman, and H. Villinger (1990), Rates of Fluid Expulsion Across the Northern Cascadia Accretionary Prism: Constraints From New Heat Flow and Multichannel Seismic Reflection Data, J. Geophys. Res., 95, 8869–8889, doi: 10.1029/JB095iB06p08869.

Davis, E. E., K. Wang, K. Becker, R. E. Thomson, and I. Yashayaev (2003), Deep-ocean temperature variations and implications for errors in seafloor heat flow determinations, J. Geophys. Res., 108(B1), 2034, doi: 10.1029/2001JB001695.

Fisher, A. T., E. E. Davis, and K. Becker (2008), Borehole-to-borehole hydrologic response across 2.4 km in the upper oceanic crust: Implications for crustal-scale properties, J. Geophys. Res., 113, B07106, di: 10.1029/2007JB005447

Flueh, E. R., M. A. Fisher, J. Bialas, J. R. Childs, D. Klaeschen, N. Kukowski, T. Parsons, D. W. Scholl, U. ten Brink, A. M. Trehu, and N. Vidal (1998), New seismic images of the Cascadia subduction zone from cruise SO108 — ORWELL, Tectonophysics, 293, 69–84, doi: 10.1016/S0040-1951(98)00091-2.

Fortin, J., S. Stanchits, S. Vinciguerra, Y. Guegun (2011), Influence of thermal and mechanical cracks on permeability and elastic wave velocities in a basalt from Mt. Etna volcano subjected to elevated pressure, Tectonophysics, 503, 60-74, doi: 10.1016/j/tecto.2010.09.028.

Fortin, W. F. J. (2015), Extracting physical parameters from marine seismic data: New methods in seismic oceanography and velocity inversion (Order No. 3722992). Available from ProQuest Dissertations & Theses Global. (1728153007).

Ganguly, N., G. D. Spence, N. R. Chapman, and R. D. Hyndman (2000), Heat flow variations from bottom simulating reflectors on the Cascadia margin, Mar. Geol., 164, 53–68, doi: 10.1016/S0025-3227(99)00126-7.

Gao, Dawei, Kelin Wang, Earl E. Davis, Yan Jiang, Tania L. Insua, and Jiangheng He. "Thermal state of the Explorer segment of the Cascadia subduction zone: Implications for seismic and tsunami hazards." *Geochemistry, Geophysics, Geosystems* (2017).

Goldfinger, C., C. H. Nelson, A. E. Morey, J. E. Johnson, J. R. Patton, E. Karabanov, J. Gutierrez-Pastor, A. T. Eriksson, E. Gracia, G. Dunhill, R. J. Enkin, A. Dallimore, and T. Vallier, (2012), Turbidite Event History - Methods and Implications for Holocene Paleoseismicity of the Cascadia Subduction Zone, U. S. Geol. Surv. Prof. Pap. 1661-F Profession, 170 pages.

Golmshtok, A. Y., A. D. Duchkov, D. R. Hutchinson, and S. B. Khanukaev (2000), Heat flow and gas hydrates of the Baikal Rift Zone, Int. J. Earth Sci, 89, 193–211, doi:10.1007/s005319900071.

Gutscher, M., D. Klaeschen, E. Flueh, and J. Malavieille (2001), Non-Coulomb wedges, wrong-way thrusting, and natural hazards in Cascadia, Geology, 29, 379–382, doi: 10.1130/0091-7613(2001)029<0379

Grevemeyer, I., and H. Villinger (2001), Gas hydrate stability and the assessment of heat flow through continental margins, Geophys. J. Int., **145**, 647–660, doi: 10.1046/j.0956-540x.2001.01404.x

Haacke, R. R., G. K. Westbrook, and M. S. Riley (2008), Controls on the formation and stability of gas hydrate-related bottom-simulating reflectors (BSRs): A case study from the west Svalbard continental slope, J. Geophys. Res., 113, B05104, doi: 10.1029/2007JB005200

Hacker, B. R., G. A. Abers, and S. M. Peacock (2003), Subduction factory 1. Theoretical mineralogy, densities, seismic wave speeds, and H2O contents, J. Geophys. Res., 108, 1–26, doi:10.1029/2001JB001127

Han, M. W., and E. Suess (1989), Subduction-induced pore fluid venting and the formation of authigenic carbonates along the cascadia continental margin: Implications for the global Ca-cycle, Palaeogeogr. Palaeoclimatol. Palaeoecol., 71, 97–118, doi: 10.1016/0031-0182(89)90032-1

Han, S., S. M. Carbotte, J. P. Canales, M. R. Nedimović, H. Carton, J. C. Gibson, and G. W. Horning (2016), Seismic reflection imaging of the Juan de Fuca plate from ridge to trench: new constraints on the distribution of faulting and evolution of the crust prior to subduction, Journal of Geophysical Research: Solid Earth, 121(3), 1849–1872, doi:10.1002/2015JB012416

Harris, R. N., and K. Wang (2002), Thermal models of the Middle America trench at the Nicoya Peninsula, Costa Rica. Geophys. Res. Lett., 29(21), doi: 10.1029/2002GL015406.

Harris, R. N., G. A. Spinelli, C. R. Ranero, I. Grevemeyer, H.Villinger, and U. Barckhausen (2010), Thermal regime of the Costa Rican convergent margin: 2. Thermal model of the shallow Middle America subduction zone offshore Costa Rica, Geochemistry Geophys. Geosystems, 11, Q12S29, doi: 10.1029/2010GC003273

Harris, R. N., J. A. Conder, and A. Heuret (2014), The thermal structure of the subduction thrust within accretionary and erosive margins, Tectonophysics, 633, 221–231, doi: 10.1016/j.tecto.2014.07.009

He, T., G. D. Spence, M. Riedel, R. D. Hyndman, and N. R. Chapman (2007), Fluid flow and origin of a carbonate mound offshore Vancouver Island: Island: Seismic and heat flow constraints, Mar. Geol., 239(1–2), 83–98, doi:10.1016/j.margeo.2007.01.00

Heaton, T. H., and S. H. Hartzell (1987), Earthquake hazards on the Cascadia subduction zone, Sci. New Ser., 236(4798), 162–168, doi: 10.1126/science.236.4798.162

Henry, P., and M. Ben Clennell (1999), Formation of natural gas hydrates in marine sediments 2. Thermodynamic calculations of stability conditions in porous sediments, J. Geophys. Res., 104, 23005–23022, doi: 10.1029/1999JB900167

Holbrook, W.S., Kent, G., Keranen, K., Johnson, P., Trehu, A., Tobin, H., Caplan- Auerbach, J., and Beeson, J. (2012), Cascadia fore arc seismic survey: Open- access data available: Eos (Transactions, American Geophysical Union), 93, 521–522, doi:10.1029/2012EO500002.

Homola, K., H. P. Johnson, and C. Hearn (2015), In situ measurements of thermal diffusivity in sediments of the methane-rich zone of Cascadia Margin, NE Pacific Ocean, Elem. Sci. Anthr., 3, doi:10.12952/journal.elementa.000039.

Hutchison, I. (1985). The effects of sedimentation and compaction on oceanic heat flow. Geophys. J. R. Astron. Soc. 82: 439–459.

Hutnak, M., a. T. Fisher, L. Zühlsdorff, V. Spiess, P. H. Stauffer, C. W. Gable, and L. Zuhlsdorff (2006), Hydrothermal recharge and discharge guided by basement outcrops on 0.7-3.6 Ma seafloor east of the Juan de Fuca Ridge: Observations and numerical models, Geochemistry, Geophys. Geosystems, 7, Q07O02 , doi 10.1029/2006GC001242.

Hutnak, M., and A. T. Fisher (2007), Influence of sedimentation, local and regional hydrothermal circulation, and thermal rebound on measurements of seafloor heat flux,. J. Geophys. Res., 112, B12101, doi: 10.1029/2007JB005022

Hyndman, R. D. (2013), Downdip landward limit of Cascadia great earthquake rupture, J. Geophys. Res. Solid Earth, 118, 5530–5549, doi:10.1002/jgrb.50390

Hyndman, R. D., and K. Wang (1993), Thermal Constraints on the Zone of Major Thrust Earthquake Failure: The Cascadia Subduction Zone, J. Geophys. Res., 98, 2039–2060, doi:10.1029/92JB02279

Hyndman, R. D., J. P. Foucher, M. Yamano, and A. Fisher (1992), Deep sea bottom-simulating-reflectors: calibration of the base of the hydrate stability field as used for heat flow estimates. Earth Planet. Sci. Lett., 109, 289–301, doi:10.1016/0012-821X(92)90093-B

Hyndman, R. D., K. Wang, T. Yuan, and G. D. Spence (1993), Tectonic Sediment Thickening, Fluid Expulsion, and the Thermal Regime of Subduction Zone Accretionary Prisms: The Cascadia Margin off Vancouver Island, J. Geophys. Res., 98, 21865–21876, doi: 10.1029/93JB02391

Hyndman, R. D., M. Yamano, and D. A. Oleskevich, (1997), The seismogenic zone of subduction thrust faults, Isl. Arc, **6**(3), 244–260, doi: 10.1111/j.1440-1738.1997.tb00175.x.

Ingebritsen, S. E., and T. Gleeson (2015), Crustal permeability: Introduction to the special issue, Geofluids, 15, 1–10, doi:10.1016/j.jvolgeores.2010.07.023

Johnson, H. P., Solomon, E. A., Harris, R. N., Salmi, M. S., and Berg, R. D. (2013), Heat Flow and Fluid Flux in Cascadia's Seismogenic Zone. Eos, Transactions American Geophysical Union, 94(48), 457-458.

Johnson, H. P., U. K. Miller, M. S. Salmi, and E. A. Solomon (2015), Analysis of bubble plume distributions to evaluate methane hydrate decomposition on the continental slope, Geochem. Geophys. Geosyst., 16(11), 3825–3839, doi:10.1002/ 2015GC005955.

Kastner, M., K. A. Kvenvolden, M. J. Whiticar, A. Camerlenghi, and T. D. Lorenson (1995), 10. Relation between Pore Fluid Chemistry and Gas Hydrates Associated with Bottom-Simulating Reflectors at the Cascadia Margin, Site 889 and 892, Proc. Ocean Drill. Program Sci. Results, 146, 175–187.

Kaul, N., A. Rosenberger, and H. Villinger, (2000), Comparison of measured and BSR-derived heat flow values, Makran accretionary prism, Pakistan, Mar. Geol., 164, 37–51, doi: 10.1016/S0025-3227(99)00125-5

Kinoshita, M. (1994), Estimation of grain thermal conductivity in the turbidite sediment of the Juan de Fuca Ridge. *In* Mottl, M.J., Davis, E.E., Fisher, A.T., and Slack, J.F. (Eds.), *Proc. ODP, Sci. Results*, 139: College Station, TX, 553–558. doi:10.2973/odp.proc.sr.139.250.1994

Kvenvolden, K. A. (1993) Gas hydrate—Geological perspective and global change: Reviews of Geophysics, 31, 173–187, doi:10.1029/ 93RG00268.

Lauer, R. M., and D. M. Saffer (2015), The impact of splay faults on fluid flow, solute transport, and pore pressure distribution in subduction zones: A case study offshore the Nicoya Peninsula, Costa Rica, Geochemistry Geophys. Geosystems, 16, 1089–1104, doi: 10.1002/2014GC005638

Le Pichon, X., P. Henry, and K.-N. S. Crew, (1991), Water budgets in accretionary wedges: a comparison,. Phil. Trans. R. Soc., 335, 315–330, doi: 10.1098/rsta.1991.0138

Lewis, T. J., W. H. Bentkowski, E. E. Davis, R. D. Hyndman, J. G. Souther, and J. A. Wright (1988), Subduction of the Juan de Fuca Plate: Thermal consequences, J. Geophys. Res., 93, 15207–15225, doi: 10.1029/JB093iB12p15207

Li, L., X. Lei, X. Zhang, and G. Zhang (2012), Heat flow derived from BSR and its implications for gas hydrate stability zone in Shenhu Area of northern South China Sea, Mar. Geophys. Res., 33, 77–87, doi: 10.1007/s11001-012-9147-3

Li, H., T. He, and G. D. Spence, (2013), North Cascadia heat flux and fluid flow from gas hydrates: Modeling 3-D topographic effects, J. Geophys. Res. Solid Earth, 119, 99–115, doi: 10.1002/2013JB010101

Lienhard, J.H. and M. H. Sharqawy (2009), Seawater Properties Software for Matlab, http://web.mit.edu/seawater/#Downloads

Liu, X., and P. B. Flemings, (2006), Passing gas through the hydrate stability zone at southern Hydrate Ridge, offshore Oregon, Earth Planet. Sci. Lett., 241, 211–226, doi: 10.1016/j.epsl.2005.10.026

Malinverno, A., M. Kastner, M. E. Torres, and U. G. Wortmann, (2008), Gas hydrate occurrence from pore water chlorinity and downhole logs in a transect across the northern Cascadia margin (Integrated Ocean Drilling Program Expedition 311), 113, 1–18, doi: 10.1029/2008JB005702

Marcaillou, B., G. Spence, J. Collot, and K. Wang, (2006), Thermal regime from bottom simulating reflectors along the north Ecuador – south Colombia margin: Relation to margin segmentation and great subduction earthquakes, 111, 1–16, doi: 10.1029/2005JB004239

Martin, J. T. and R. P. Lowell, (2000), Precipitation of quartz during high-temperature, fracture-controlled hydrothermal upflow at ocean ridges: Equilibrium versus linear kinetics, Journal of Geophysical Research, **105(**B1), 869-882, doi: 10.1029/1999JB900342

Martin, V., P. Henry, H. Nouzé, M. Noble, J. Ashi, and G. Pascal, (2004), Erosion and sedimentation as processes controlling the BSR-derived heat flow on the Eastern Nankai margin, Earth Planet. Sci. Lett., **222**, 131–144, doi: 10.1016/j.epsl.2004.02.020

McCrory, P. A., R. D. Hyndman, Blair, and J. L. Blair, (2014), Relationship between the Cascadia forearc mantle wedge, nonvolcanic tremor, and the downdip limit of seismogenic rupture, Geochemistry, Geophys. Geosystems, 15, 1071–1095, doi: 10.1002/2013GC005144

McKenna, J. R., and D. D. Blackwell, (2002), Shallow Thermal Conditions in the Central and Southern Cascadia Subduction Zone. Unpublished Paper can be found online at: http://cascadiageo.org/documentation/literature/cascadia_papers/cszthermal.pdf

McKenzie, D., J. Jackson, and K. Priestley (2005), Thermal structure of oceanic and continental lithosphere, Earth Planet. Sci. Lett., 233, 337–349, doi: 10.1016/j.epsl.2005.02.005

McNeill, C., A. Piper, C. Goldfinger, L. D. Kulm, and S. Yeats (1997), Listric normal faulting on the Cascadia continental margin Coast Range, J. Geophys. Res., 102, 12123–12138, doi: 10.1029/97JB00728

Morton, E. A., and S. L. Bilek (2014), Preliminary Event Detection of Earthquakes Using the Cascadia Initiative Data, Seismological Research Letters, 86(5), doi:10.1785/0220150098

Moore, J. C., and D. Saffer (2001), Updip limit of the seismogenic zone beneath the accretionary prism of southwest Japan: An effect of diagenetic to low-grade metamorphic processes and increasing effective stress, Geology 29, 183–186, doi: 10.1130/0091-7613(2001)029<0183:ULOTSZ>2.0.CO;2

Oleskevich, D. A., R. D. Hyndman, and K. Wang (1999), The updip and downdip limits to great subduction earthquakes: Thermal and structural models of Cascadia, south Alaska, SW Japan, and Chile, J. Geophys. Res. 104, 14965-14991, doi: 10.1029/1999JB900060

Parsons, B., and J. G. Sclater (1977), An analysis of the variation of ocean floor bathymetry and heat flow with age, J. Geophys. Res., 82, 803–827, doi: 10.1029/JB082i005p00803

Parsons, T., R. E. Wells, M. A. Fisher, E. Flueh, and U. S. ten Brink (1999), Three-dimensional velocity structure of Siletzia and other accreted terranes in the Cascadia forearc of Washington, J. Geophys. Res, 104, 18015-18039, doi: 10.1029/1999JB900106

Riedel, M., E. C. Willoughby, M. A. Chen, T. He, I. Novosel, K. Schwalenberg, R. D. Hyndman, G. D. Spence, N. R. Chapman, and R. N. Edwards (2006), Gas hydrate on the northern Cascadia Margin: regional geophysics and structural framework, Proc. Ocean Drill. Program Sci. Results, 311, 1-28, doi:10.2204/iodp.proc.311.109.2006

Riedel, M., A. M. Tréhu, and G. D. Spence (2010), Characterizing the thermal regime of cold vents at the northern Cascadia margin from bottom-simulating reflector distributions, heat-probe measurements and borehole temperature data, Mar. Geophys. Res., 31, 1–16, doi: 10.1007/s11001-010-9080-2

Riedel, M., and U. Shankar (2012), Combining impedance inversion and seismic similarity for robust gas hydrate concentration assessments - A case study from the Krishna-Godavari basin, East Coast of India, Mar. Pet. Geol., 36, 35–49, doi: 10.1016/j.marpetgeo.2012.06.006.

Rogers, A. M., T. Walsh, W. J. Kockelman, and G. R. Priest. 1996. Assessing Earthquake Hazards and reducing Risk in the Pacific Northwest. Prof. Paper 1560, US Geological Survey, Menlo Park, CA.

Rotman, H. M. M., and G. A. Spinelli. 2014. Remarkably consistent thermal state of the south central Chile subduction zone from 36 ˚ S to 45 ˚ S, Journal of Geophysical Research: Solid Earth, 119(4), 3503-3516, doi:10.1002/2013JB010811

Ryan,W. B. F., S.M. Carbotte, J. O. Coplan, S.O'Hara, A. Melkonian,V. Ferrini, A. Goodwillie, F. Nitsche, J. Bonczkowski, and R. Zemsky (2009), Global multi-resolution topography synthesis, Geochem. Geophys. Geosyst., 10, Q03014, doi: 10.1029/2008GC002332.

Salmi, M. S., H. P. Johnson, M. A. Tivey, and M. Hutnak, (2014), Quantitative estimate of heat flow from a mid-ocean ridge axial valley, Raven Field, Juan de Fuca Ridge: Observations and inferences, J. Geophys. Res. Solid Earth, 119, doi: 10.1002/2014JB011086

Saffer, D. M., and C. Marone (2003), Comparison of smectite- and illite-rich gouge frictional properties: application to the updip limit of the seismogenic zone along subduction megathrusts, Earth Planet. Sci. Lett., 215, 219–235, doi: 10.1016/S0012-821X(03)00424-2

Saffer, D. M. (2015), The permeability of active subduction plate boundary faults, Geofluids, 15, 193–215, doi: 10.1111/gfl.12103

Saffer, D. M., and H. J. Tobin (2011), Hydrogeology and Mechanics of Subduction Zone Forearcs: Fluid Flow and Pore Pressure, Annu. Rev. Earth Planet. Sci., 39, 157–186, doi: 10.1146/annurev-earth-040610-133408

Screaton, E., D. Saffer, P. Henry, and S. Hunze (2002), Porosity loss within the under thrust sediments of the Nankai accretionary complex: Implications for overpressures, Geology, 30, 19–22, doi: 10.1130/0091-7613(2002)030<0019

Shi, Y., C. Wang, M. G. Langseth, M. A. Hobart, and R. Von Huene (1988), Heat Flow and Thermal Structure of the Washington-Oregon accretionary prism - A study of lower slope, Geophys. Lett., 15, 1113–1116, doi: 10.1029/GL015i010p01113

Spinelli, G. A., and A. T. Fisher (2004), Hydrothermal circulation within topographically rough basaltic basement on the Juan de Fuca Ridge flank, Geochemistry Geophys. Geosystems, 5, Q02001, doi: 10.1029/2003GC000616

Spinelli, G. A., and K. Wang (2008), Effects of fluid circulation in subducting crust on Nankai margin seismogenic zone temperatures, Geology, 36, 887, doi: 10.1130/G25145A.1

Spinelli, G. A., and K. Wang (2009), Links between fluid circulation, temperature, and metamorphism in subducting slabs, Geophys. Res. Lett., 36, L13302, doi:10.1029/2009GL038706

Stein, C. A., and S. Stein (1992), A model for the global variation in oceanic depth and heat flow with lithospheric age, Nature, 359, 123–129, doi:10.1038/359123a0

Tishchenko, P., C. Hensen, K. Wallmann, and C. Shing (2005), Calculation of the stability and solubility of methane hydrate in seawater, 219, 37–52, doi: 10.1016/j.chemgeo.2005.02.008

Trehu, A. M., G. Lin, E. Maxwell, and C. Goldfinger (1995), A seismic reflection profile across the Cascadia subduction zone offshore central Oregon: New constraints on methane distribution and crustal structure. J. Geophys. Res. Solid Earth, 100, 15101–15116, doi: 10.1029/95JB00240

Tréhu, A. M., J. Braunmiller, and J. L. Nabelek (2008), Probable low-angle thrust earthquakes on the Juan de Fuca–North America plate boundary, Geology, 36, 127-130, doi: 10.1130/G24145A.1

Tréhu, A. M., J. Braunmiller, and E. Davis (2015), Seismicity of the Central Cascadia Continental Seismicity of the Central Cascadia Continental Margin near 44.5 ° N : A Decadal View, Seismol. Res. Lett., 86(3), 819-829, doi:10.1785/0220140207

Tobin, H. J., and D. M. Saffer (2009), Elevated fluid pressure and extreme mechanical weakness of a plate boundary thrust, Nankai Trough subduction zone, Geology, 37, 679–682, doi: 10.1130/G25752A.1

Toomey, D. R., R. M. Allen, A. H. Barclay, S.W. Bell, P. D. Bromirski, R. L. Carlson, X. Chen, J. A. Collins, R. P. Dziak, B. Evers, et al. (2014), The Cascadia Initiative: A sea change in seismological studies of subduction zones, Oceanography, 27, 138–150, doi:10.5670/oceanog.2014.49.

Torres, M. E., B. M. A. Teichert, A. M. Trehu, W. Borowski, and H. Tomaru (2004), Relationship of pore water freshening to accretionary processes in the Cascadia margin: Fluid sources and gas hydrate abundance, Geophys. Res. Lett., 31, L22305, doi:10.1029/2004GL021219

Wada, I., K. Wang, J. He, and R. D. Hyndman (2008), Weakening of the subduction interface and its effects on surface heat flow, slab dehydration, and mantle wedge serpentinization, J. Geophys. Res., 113, B04402, doi: 10.1029/2007JB005190

Wada, I., and K. Wang (2009), Common depth of slab-mantle decoupling: reconciling diversity and uniformity of subduction zones, Geochemistry, Geophysics, Geosystems, 10, Q10009, doi: 10.1029/2009GC002570.

Wang, K., and E. E. Davis (1992), Thermal effects of marine sedimentation in hydrothermally active areas, Geophys. J. Int., 110, 70–78, doi: 10.1111/j.1365-246X.1992.tb00714.x.

Wang, K., R. D. Hyndman, and E. E. Davis (1993), Thermal Effects of Sediment Thickening and Fluid Expulsion in Accretionary Prisms: Model and Parameter Analysis., J. Geophys. Res., 98, 9975–9984, doi: 10.1029/93JB00506

Wang, K. L., T. Mulder, G. C. Rogers, and R. D. Hyndman (1995), Case for very low coupling stress on the Cascadia subduction fault, J. Geophys. Res., 100, 12907–12918, doi: 10.1029/95JB00516

Wang, K., R. Wells, S. Mazzotti, R. D. Hyndman, and T. Sagiya (2003), A revised dislocation model of interseismic deformation of the Cascadia subduction zone, J. Geophys. Res., 108, 1–13, doi: 10.1029/2001JB001227

Wang, K., and Y. Hu (2006), Accretionary prisms in subduction earthquake cycles: The theory of dynamic Coulomb wedge, J. Geophys. Res., 111, B06410, doi: 10.1029/2005JB004094

Wells, Ray, David Bukry, Richard Friedman, Doug Pyle, Robert Duncan, Peter Haeussler, and Joe Wooden (2004), Geologic history of Siletzia, a large igneous province in the Oregon and Washington Coast Range: Correlation to the geomagnetic polarity time scale and implications for a long-lived Yellowstone hotspot, Geosphere, 10(4), 692-719, doi: 10.1130/GES01018.1

Wilcock, W. S. D., and A. McNabb (1996), Estimates of crustal permeability on the Endeavour segment of the Juan de Fuca mid-ocean ridge, Earth Planet. Sci. Lett., 138, 83–91, doi: 10.1016/0012-821X(95)00225-2

Wilson, D. S. (1993), Confidence intervals for motion and deformation of the Juan de Fuca Plate, J. Geophys. Res., 98, 16053–16071, doi: 10.1029/93JB01227

Yamano, M. (2003), Extremely high heat flow anomaly in the middle part of the Nankai Trough, Phys. Chem. Earth, 28, 487–497, doi: 10.1016/S1474-7065(03)00068-8

Yuan, T., R. D. Hyndman, G. D. Spence, and B. Desmons (1996), Seismic velocity increase and deep-sea gas hydrate concentration above a bottom-simulating reflector on the northern Cascadia continental slope, J. Geophys. Res., 101, 13655–13671, doi: 10.1029/96JB00102

Yuan, T., G. D. Spence, R. D. Hyndman, T. a. Minshull, and S. C. Singh (1999), Seismic velocity studies of a gas hydrate bottom-simulating reflector on the northern Cascadia continental margin: Amplitude modeling and full waveform inversion, J. Geophys. Res., 104, 1179–1191, doi: 10.1029/1998JB90002

Zuhlsdorff, L., V. Spieb, C. Hubscher, H. W. Villinger, A. Rosenberger, V. Spieß, C. Hubscher, H. W. Villinger, and A. Rosenberger (2000), Implications for focused fluid transport at the northern Cascadia accretionary prism from a correlation between BSR occurrence and near-sea-floor reflectivity anomalies imaged in a multi-frequency seismic data set, Int. J. Earth Sci., 88, 655–667, doi: 10.1007/s005310050295

Zwart, G., J. C. Moore, and G. R. Cochrane (1996), Variations in temperature gradients identify active faults in the Oregon accretionary prism, Earth Planet. Sci. Lett., 139, 485–495, doi: 10.1016/0012-821X(95)00244-7

Contemporary Bottom Water Warming Along the Upper Slope of the Washington Margin and Modeling the Response of the Methane Hydrate Stability Field

Preface

This work relates to Tasks 5-6 in the original proposal. The results described in this chapter were published in *Geophysical Research Letters*; the citation is below:

Hautala, S.L., Solomon, E.A., Johnson, H.P., Harris, R.N., Miller, U.K., 2014. Dissociation of Cascadia margin gas hydrates in response to contemporary ocean warming, *Geophysical Research Letters*, 41, 8486-8494.

Introduction

Gas hydrates represent one of the largest reservoirs of organic carbon on Earth [Boswell and Collett, 2011]. As the upper limit of gas hydrate stability deepens in response to ocean warming, the additional flux of hydrate-derived methane could contribute to ocean acidification, oxygen consumption in the water column, and upper continental slope instability, as well as potentially increased emissions of CH_4 and methane-derived CO_2 to the atmosphere (e.g. Revelle, 1983). Recent studies of gas hydrate dynamics associated with contemporary warming have focused on the Arctic [Berndt et al., 2014; Westbrook et al., 2009; Thatcher et al., 2013; Reagan et al., 2011; Biastoch et al., 2011], with less attention given to the vulnerability of the much larger methane reservoir present at lower latitudes.

Gas hydrates are stable under conditions of low temperature and high pressure, and they typically exist within the top few hundred meters of continental slope sediments. The depth where the gas hydrate stability field pinches out and vanishes (typically along the upper continental slope; termed the feather edge of gas hydrate stability) is dependent on bottom water temperature and local geothermal gradients, and represents one of the most climate-sensitive boundaries in the global gas hydrate reservoir [Boswell and Collett, 2011; Ruppel, 2011]. Upper continental slope gas hydrates are more sensitive to warming than other deposits because of their proximity to transient seawater temperatures at the seafloor, allowing dissociation on relatively short timescales - a few decades compared to 10^2 to 10^3 years for other climate-sensitive reservoirs such as those associated with thinning Arctic permafrost [Berndt et al. 2014; Ruppel, 2011]. Recent field and modeling studies show that part of the methane released to the Arctic Ocean at the upper continental slope off West Svalbard may be due to ongoing gas hydrate dissociation in response to bottom water warming [Berndt et al., 2014; Westbrook et al., 2009; Thatcher et al., 2013; Reagan et al., 2011].

Although lower latitude hydrates represent a large percentage of the global methane inventory, there are few studies on the vulnerability of these systems to warming of water at the seafloor (e.g. Kennett et al., 2003). A recent study considered the response of the Carolina Rise hydrate system in the North Atlantic to seawater temperature changes caused by a probable Holocene Gulf Stream shift, with implications for continued future warming (Phrampus and Hornbach, 2012). The degree of seafloor ocean warming directly impacting gas hydrate systems will depend on regional currents and water masses. In particular, circulation affecting the eastern Pacific margins is fundamentally different than for the western North Atlantic. The methane

hydrate-rich Washington margin has a dense set of archived water column data (Fig. 1) that records systematic warming over the last four decades at the depth of upper continental slope gas hydrates. Using a sediment model with an upper boundary condition tightly constrained by these observations, we find that warming of the North Pacific at the depth corresponding to intermediate water is likely to have a substantial impact on the Cascadia margin gas hydrate reservoir. This finding has worldwide implications for other upper continental slope reservoirs that are typically bathed in intermediate and lower thermocline waters.

Methods

A. Water Column Temperature Data

High-resolution CTD, glider and ARGO float temperature profiles extending to a depth of at least 200 m were extracted at observed levels from the World Ocean Database 2013 (National Oceanographic Data Center) for the region 124.5°W to 127.5°W and 46.5°N to 48.5°N (Fig. 1). Available data spans the years 1968 to 2013. We added several CTD casts from an August 2013 field program in the immediate vicinity of methane bubble plume sites to the data from the NODC archive. If only pressure was available in the NODC archive, temperature sampling depth was estimated using the TEOS-10 Gibbs Seawater Oceanographic Toolbox [McDougall and Barker, 2011] at the latitude of the profile, otherwise reported depth values were retained. Entire profiles containing clearly erroneous values, i.e., negative temperatures or temperature values > 16°C or < 4°C at 200 m, were eliminated, as were profiles taken within Juan de Fuca Canyon. The remaining 2122 open-ocean temperature profiles were linearly interpolated to 10 m depth intervals ranging from 50 to 1000 m. To remove bias from an uneven seasonal sampling distribution (for example, at 480 m depth, monthly-average temperature varies over the year by 0.27°C with warmest values in August), long-term monthly average values were subtracted from the data.

To quantitatively estimate the local rate of seawater warming in the presence of sampling biases related to geographical temperature gradients and substantial decadal variability, we performed a multivariate linear regression (Fig. 2). In addition to the dependency of interest (sampling year), other independent variables for the multivariate linear regression are latitude, water depth estimated by linearly interpolating the 0.5′ SRTM30 PLUS bathymetry data [Sandwell and Smith, 2009; Becker et al., 2009] at each sampling location, and the monthly Pacific Decadal Oscillation (PDO) index [Zhang et al., 1997; Mantua et al., 1997] from the Joint Institute for the Study of the Atmosphere and Ocean website at the University of Washington. Unlike Fig. 2a, interannual to decadal variability visually dominates the regional-average time-series in the upper ocean (not shown) and the correlation between temperature and the Pacific Decadal Oscillation (Fig. 2c) is large and positive, as expected [Zhang et al., 1997; Mantua et al., 1997]. The PDO index during the months of our observations ranges from -2.23 to +2.83, with values over +2.0 sampled only between 1983-1998 and with negative indices sampled since 2010 (Fig. 2b). A sensitivity study (see online supplementary materials) was conducted to understand how various assumptions impact the regression-derived warming trend at 480 m. Of particular interest are cases where slightly different subsets of the data are used: data collected only over the slope, data collected only since 1980, adding data within the Juan de Fuca canyon, and excluding ARGO and glider data. Sensitivity calculations using different methodological choices yield a warming trend that ranges from +0.0061 to +0.0080 °C yr^{-1} and agree within error bars with our best estimate shown in Fig. 2b, c.

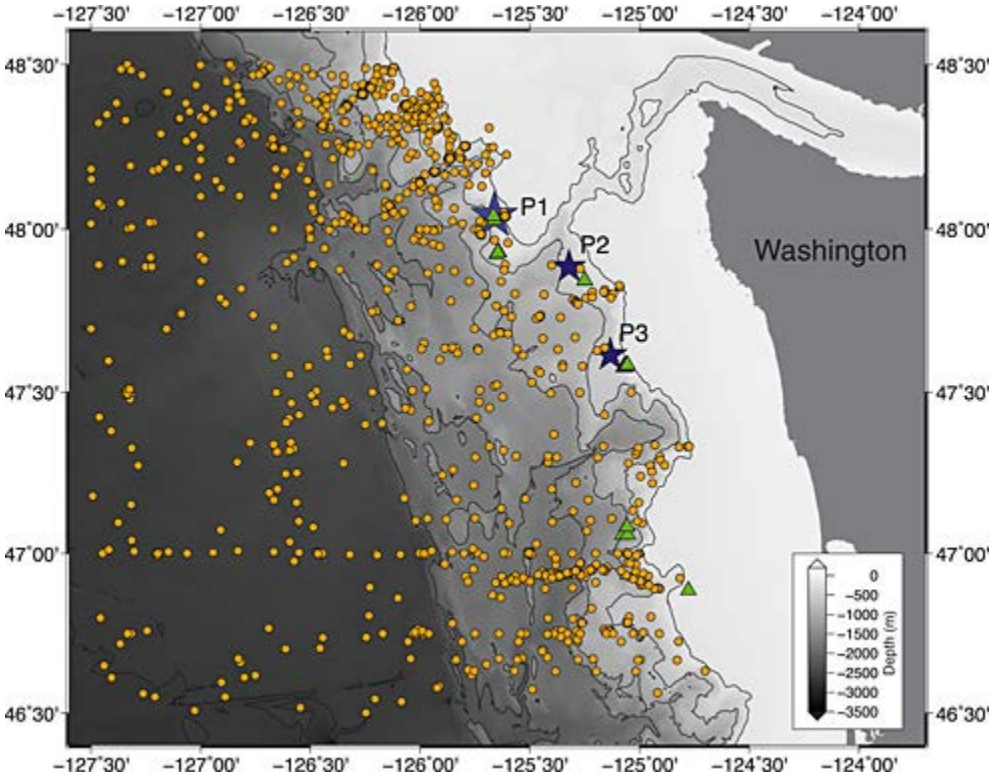

Figure 1. Map of data locations. Bathymetry of the Washington continental slope from GeoMapApp with locations of compiled vertical profiles of conductivity-temperature-depth (CTD) observations shown as orange dots. The locations of bathymetric transects P1–P3 are denoted by blue stars (the length of transects is quite short at the map scale), and the locations of known methane seep sites are denoted by green triangles. The contours for water depth are set at 300 m, 500 m, and then every 500 m.

B. Sediment Thermal Model

To evaluate the response of the gas hydrate reservoir to the observed warming trend, we first estimate the temperature at the seafloor at a given location and year that is solely associated with long-term climate variation (i.e., under neutral PDO conditions), using the regression coefficients shown in Fig. 2 and differences in latitude, water depth, and year from average values for the compiled data (47.9798^{o} N, 1291 m, and 1992, respectively). We focus on three individual bathymetric transects across the Washington margin with differing topography at the up-slope limit of gas hydrate stability (Fig. 1). Temperature at the seafloor is estimated from the regression along these transects at the beginning (1970) and end (2013) of the observation period, resulting in a change of +0.29°C at 480 m water depth (Fig. 2b).

A 2-D thermal model is used to simulate the change in sediment temperature distribution over this time period (Fig. 3) along with volume of the gas hydrate stability zone, its downslope retreat, and the associated mass of gas hydrate affected by bottom water warming (Supp. Figs. 1-4). This model is based on a finite element heat flow model with prescribed initial and boundary conditions [Wang et al., 1995]. Model cells have dimensions of 100 m horizontally and 2 m vertically in the upper 100 m of the sediment column, increasing to 20 m between 100-200 mbsf. The base of the model is sufficiently deep to avoid boundary effects and we prescribe a constant

basal heat flux of 60 mW m^{-2} based on nearby heat flow data derived from Bottom Simulating Reflectors [Booth-Rea et al., 2008]. Thermal conductivity and heat capacity are constant throughout the model domain with values of 0.92 W m^{-1} K^{-1} and 2.52×10^{6} J km^{-3}. These parameters yield a thermal diffusivity of 3.8×10^{-7} m s^{-2}, consistent with observed values (see Supplementary Information). At each location along the bathymetric transects, the upper boundary condition for the sediment column is set by the PDO-neutral 1970 temperature estimate. The initial condition is a steady-state heat flux matching this upper boundary condition. Transient solutions are calculated with an interval of one year. The base of the gas hydrate stability zone is computed assuming Structure I gas hydrate and hydrostatic conditions [Tishchenko et al., 2005]. The latent heat of gas hydrate dissociation was not included in our simulations, producing a maximum estimate for the total volume of sediment affected by a vertical shift in the gas hydrate stability zone.

C. Projected Seafloor Temperature

Projections of seafloor temperature are based on global average surface air temperature projections from the Intergovernmental Panel on Climate Change (IPCC) AR4 report [Meehl et al. 2007]. We first extrapolate the observed temperature trend in our data, as determined by the regression analysis, backward in time to 1950. We consider a simple extrapolation of the observed trend forward in time to 2100 to be a conservative scenario, noting that such behavior resembles IPCC emissions-stabilized projections and that the local observed trend at 480 m depth (+0.0068°C per year) is considerably smaller than the global average air temperature trend over the rest of this century using even the most optimistic (emissions-reducing) scenario, RCP2.6 in AR5 (+0.0105°C per year). The highest emissions A1F1 scenario in AR4 shows a global warming of +4.0°C in 2090-2099 relative to 1980-1999, an average warming trend of +0.0381°C per year. Note that the highest emissions scenario, RCP8.5, in AR5 yields a similar average warming trend of +0.0389°C per year [Stocker et al., 2013]. Local subsurface water values projected for 2100 are estimated from these global-average surface air temperature projections through scaling them by the ratio of the warming trend observed in our data at 480 m to the reported global-average AR4 trend in measured air temperature since 1950 (+0.013°C per year).

D. Warming Trend Sensitivity study

We explored the effect of several alternate choices of methodology in computing the warming trend (Table S1). In most cases, we feel that our decisions, such as using water depth rather than longitude, accounting for the seasonal cycle, and excluding Juan de Fuca canyon data, should improve the accuracy of the estimate. However, the large difference in the estimated warming trend between CTD-only and combined CTD, glider and float data sets warrants more explanation. At the time of our download, there was no CTD data available in the NODC archive in this region for 2010-2013. As seen in Fig. 2a, three-year regional averages are low relative to surrounding years during 2009-2011 when they rely heavily on float and glider data (Fig. 2a). Thus when the trend is estimated using CTD data only, it increases substantially. However, CTD data from our August 2013 cruise to gas hydrate vent sites is included in the data set, and its average value is significantly lower than the three-year regional-average data point shown in Fig. 2a for 2012. Also, the PDO index at sampling times was consistently negative during this period (Fig. 2b). Thus rather than an instrumental bias, we hypothesize decadal variability, particularly as it impacts the offshore region sampled by the glider/float data (see the difference between slope-

and deep-water data in Fig. 2a) as the responsible factor for the relatively low three-year regional-averages from 2009-2011. Finally, we note that the CTD-only and "best" estimates agree within their error bars, as do all other runs in this sensitivity study.

Best estimate	*0.0068 ± 0.0009*
Alternate Methodological Choice	**°C per year**
Longitude used rather than water depth for offshore coordinate	0.0070 ± 0.0009
Quadratic terms allowed	0.0068 ± 0.0009
Seasonal cycle not removed	0.0070 ± 0.0009
Juan de Fuca canyon data not excluded	0.0067 ± 0.0009
Exclude glider and float data	0.0080 ± 0.0011
Temperature converted from ITS-68 to ITS-90 for data prior to 1990	0.0068 ± 0.0009
Data restricted to the slope, taken as 200-1000 m water depth	0.0077 ± 0.0018
Data restricted to the upper slope, taken as 200-600 m water depth	0.0067 ± 0.0038
Data restricted to 1977 and later	0.0076 ± 0.0012
Data restricted to 1980 and later	0.0069 ± 0.0013
Regression using ENSO MEI* rather than PDO index	0.0061 ± 0.0008

Table S1. Summary of the warming trend at 480 m and its 95% confidence level error bars under variations in several assumptions of the regression calculation. *Multivariate ENSO Index, Wolter, K. and M. S. Timlin (1998), Measuring the strength of ENSO events – how does 1997/98 rank? *Weather* **53**: 315-324, data downloaded from ESRL website.

Observed long-term warming in the Cascadia water column

Water column warming observed in the CTD data shown in Fig. 1 is summarized in Fig. 2. In Fig. 2a, we highlight the regional average record of water column warming at 480 m, corresponding to the up-slope limit of gas hydrate stability in 1970. Latitudinal and offshore temperature gradients determined from the regression analysis (Fig. 2c) are consistent with large-scale circulation. Below 200 m, isotherms tilt downward approaching the shelf, reflecting some northward flow down to at least 1000 m above the slope [Hickey, 1979]. With its core at ~200 m, the California Undercurrent is associated with an intensification of this northward flow into a jet, bringing relatively saline water from the tropical eastern Pacific to the entire subarctic continental slope [Thomson and Krassovski, 2010]. The change in sign of the offshore gradient above the undercurrent indicates the transition to coastal upwelling. Below the near-surface

waters, we observe weak long-term warming above the core of the undercurrent, likely reflecting opposing temperature tendencies at a given depth from climate change and an observed dynamical shoaling of constant potential density surfaces [Mienvielle and Johnson, 2013].

The magnitude and statistical significance of the warming trend increases with depth below the undercurrent, reaching a maximum between 300-600 m depth (Fig. 2c) at a rate that is

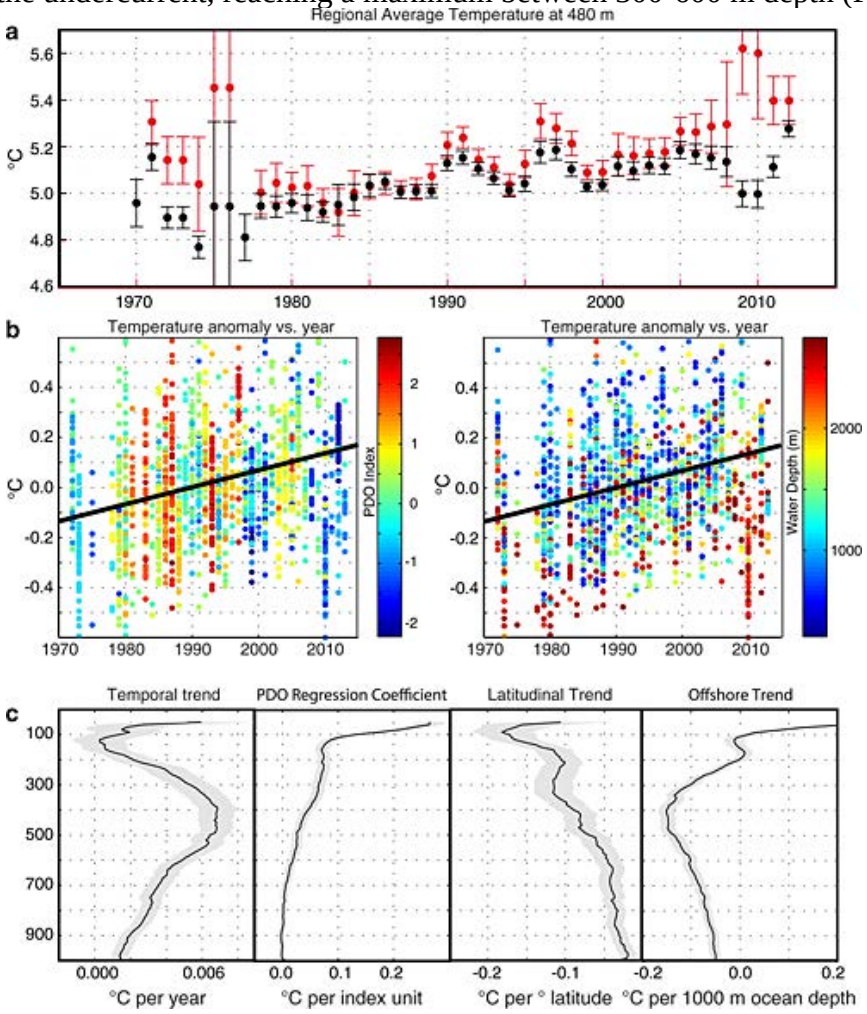

Figure 2. (a) Open-ocean warming record off the Pacific Northwest for water depths greater than 200 m. The black symbols show the 3 year average temperatures, centered on the year shown on the *x* axis, at 480 m for the data shown in Figure with *t* test 95% confidence level error bars. The red symbols show the averages and error bars using only data from water depths between 200 and 1000 m. (b) Raw temperature anomaly, defined by subtracting the long-term regional monthly average value, at 480 m versus year of observation and color coded by PDO index and water depth. The solid line shows the warming trend of 0.0068 ± 0.0009°C yr^{-1}, estimated from a multivariate linear regression (see Methods). The adjusted R^2 at this depth is 0.22. (c) Regression coefficients for each of the four independent variables as a function of depth, with 95% confidence interval error estimates shaded gray.

comparable to the global average temperature trend at similar depth and latitude [Rhein et al. 2013]. The percentage of equatorial source water over the continental slope declines below the undercurrent core to less than 30% by 500 m depth off Oregon [Thomson and Krassovski, 2010].

In 2013, water at 300-600 m depth sampled at the upper continental slope had potential density (σ_θ) between 26.78 to 27.09 kg m^{-3}, averaging 26.97 σ_θ at 480 m. (Note: in the absence of any salinity change, the estimated warming of 0.29°C at this depth would have lowered the potential density by 0.04 kg m^{-3}.) The primary water mass in this density range is North Pacific Intermediate Water (NPIW), with a characteristic low-salinity end-member established in the far western Sea of Okhotsk [Reid, 1965; Talley, 1993]. NPIW is traditionally defined only within the subtropical gyre, where it is associated with a characteristic salinity minimum. However, after crossing the Pacific a fraction of the water in the NPIW density range turns northward following the counterclockwise subarctic gyre. At Ocean Station P (50°N, 145°W), western subarctic gyre water contributes over 50% of the water mass mixture at 26.7 σ_θ [Whitney et al, 2007].

The transit time via ocean currents from the open-ocean western to eastern Pacific subarctic gyre is approximately one to two decades for 26.7 to 27.2 σ_θ [Ueno and Yasuda, 2003]. Temperature changes can also occur via isotherm shifts associated with geostrophic adjustment of ocean circulation to atmospheric forcing, particularly on the margin where coastal waves can efficiently transmit circulation changes. On the Washington margin, deepening isopycnals below the core of the California Undercurrent suggest that the warming we observe may, in part, reflect the geostrophic signature of increasing transport in the undercurrent [Mienvielle and Johnson, 2013]. A change in the mixing ratio between Sea of Okhostk water and Oyashio Current water could also result in a temperature trend in the NPIW [Kouketsu, et al. 2010]. However, over the long term, sea surface warming in water mass formation regions will be communicated throughout the remote ocean interior. Recent studies show that since the 1950s, Sea of Okhotsk water in the NPIW density range has warmed at rates higher than we observe off the Washington margin [Itoh, 2007; Nakanowatari et al., 2007]. A recent study [Johnstone and Mantua, 2014] finds that the sea-surface warming along the eastern rim of the subarctic gyre over the last century is correlated to an atmospheric sea-level pressure trend, with a leading mode that resembles the PDO spatial pattern. However, the effects of atmospheric dynamical forcing decline rapidly with depth, consistent with the decline of PDO-correlated variability in Fig. 2c. Furthermore, the atmospheric pressure trend would be expected to be associated with cooling in the western Pacific [e.g., Mantua et al., 1997]. Warming over several decades has also been observed at locations spanning the subarctic Pacific in the NPIW density range [Whitney et al., 2007; Koutketsu, 2010; Nakanowatari et al., 2007]. At Ocean Station P, warming on both depth levels and potential density surfaces is evident, with maximum values of just over +0.01°C yr^{-1} at 26.7 to 26.9 σ_θ and a trend of +0.008 °C yr^{-1} at 27.0 σ_θ for the period 1956-2006 [Whitney et al., 2007].

Impact of seafloor warming on the methane hydrate reservoir

Over the 43 years of our simulation, the thermal disturbance generated by warming of water in contact with the seafloor propagates 30 m into the sediment column (Fig. 3), causing the base of the gas hydrate stability field to shoal by ~13 m (Supp. Fig. 3), with a horizontal downslope retreat of ~1 km. The horizontal distance the GHSZ retreats offshore is proportional to the upper margin slope (Supp. Fig. 1, 2, and 4). These estimates do not consider advection of seawater or the latent heat of gas hydrate dissociation. The latent heat of dissociation would act to stabilize gas hydrate, whereas gas ebullition drives seawater circulation that would warm the sediment column further enhancing the rate of gas hydrate dissociation (e.g. Tryon et al., 2002; Solomon et al., 2008). Thus, these are conservative first-order estimates based solely on

conduction of heat. To estimate the volume and mass of gas hydrate that could dissociate, we assume a 5-m thick sulfate reduction zone in 1970, with gas hydrate occurring only below this depth. Assuming an average porosity of 0.63 in the upper 15 m [Riedel et al., 2006], and an average gas hydrate saturation of 5% of the sediment pore space, approximately 129-164 m^3 of gas hydrate per meter of margin could dissociate. Thus, warming along the Washington upper

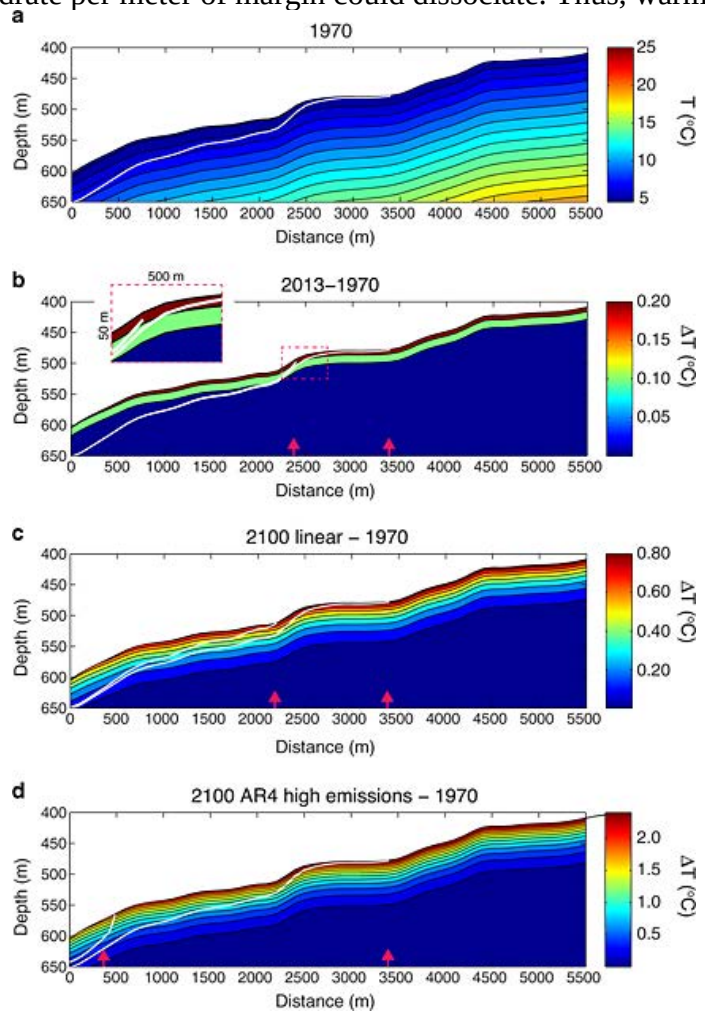

Figure 3. Sediment thermal simulations for bathymetric transect P1. (a) Initial subseafloor temperature distribution in 1970 based on the regression (see Methods) and a basal heat flow of 60 mW/m^2 [*Booth-Rea et al.*,]. The white line is the base of the gas hydrate stability zone (BGHSZ) in the sediment column for Structure I gas hydrate and hydrostatic pressure following the methods outlined in *Tishchenko et al.* [2005]. (b) The simulated change in sediment temperature between 1970 and 2013 and the corresponding shift in the BGHSZ. The BGHSZ shoals over a broad area in response to warming, accompanied by a retreat of its landward edge (indicated by red arrows). (c) Simulated change in sediment temperature between 1970 and 2100 based on the linear extrapolation of seafloor temperature. The upper white line is the BGHSZ in 2100. (d) Simulated change in sediment temperature between 1970 and 2100 based on the high-emission AR4 projection. The upper white line is the BGHSZ in 2100, and the lower white line is the BGHSZ in 1970.

continental slope between 1970-2013 has the potential to dissociate 0.12 to 0.15 Gg of gas hydrate per meter assuming a Structure I hydrate density of 9×10^5 g m^{-3} (Table 1). We consider these estimates to be only first-order since the sulfate-methane transition zone (SMTZ) depends

on the background methane flux and could be either thicker or thinner than assumed. Furthermore, the depth of gas hydrate first occurrence depends on pore water methane concentrations being at least equal to methane hydrate solubility. This depth is dependent on the rate of *in situ* methanogenesis, methane flux from below, sedimentation rate, and compaction [Davie and Buffett, 2001], and is often substantially deeper than the SMTZ. The thickness of the SMTZ and first occurrence of gas hydrate in this region lack field constraints.

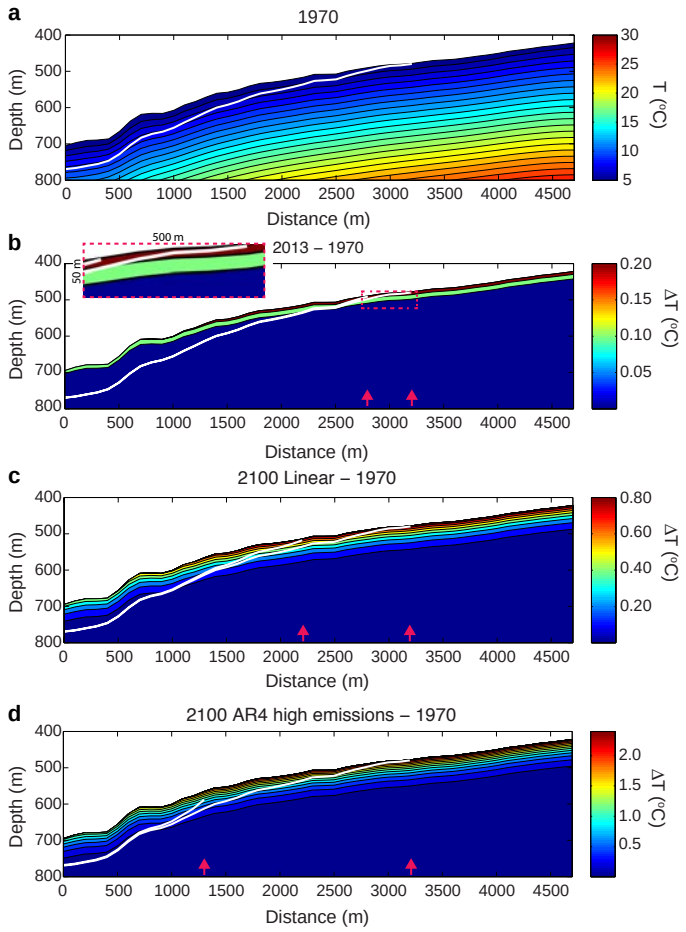

Supplementary Figure 1. Sediment thermal simulations for bathymetric transect P2. a. Initial subseafloor temperature distribution in 1970 based on the regression (see Methods) and a basal heat flow of 60 mW/m [Booth-Rea et al., 2008]. The white line is the base of the gas hydrate stability zone (BGHSZ) in the sediment column for Structure I gas hydrate and hydrostatic pressure following the methods outlined in Tischenko (2005). b. The simulated change in sediment temperature between 1970 and 2013 and corresponding shift in the BGHSZ. The BGHSZ shoals over a broad area in response to warming, accompanied by a retreat of its landward edge (indicated by red arrows). c. Simulated change in sediment temperature between 1970 and 2100 based on the linear extrapolation of seafloor temperature. The upper white line is the BGHSZ in 2100. d. Simulated change in sediment temperature between 1970 and 2100 based on the high-emissions AR4 extrapolation. The upper white line is the BGHSZ in 2100 and the lower white line is the BGHSZ in 1970.

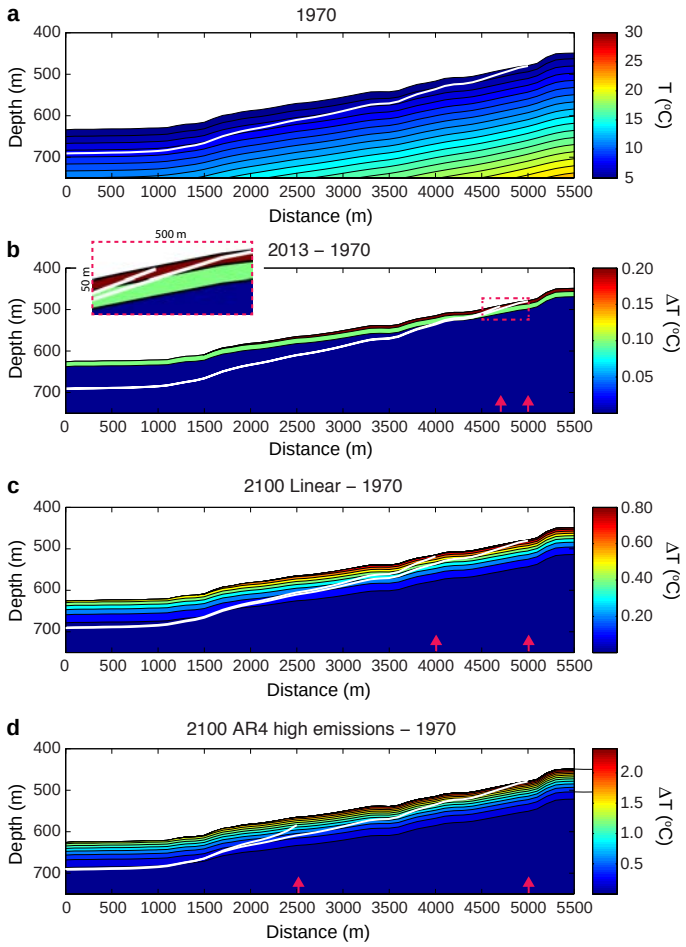

Supplementary Figure 2. Sediment thermal simulations for bathymetric transect P3. a. Initial subseafloor temperature distribution in 1970 based on the regression (see Methods) and a basal heat flow of 60 mW/m [Booth-Rea et al., 2008]. The white line is the base of the gas hydrate stability zone (BGHSZ) in the sediment column for Structure I gas hydrate and hydrostatic pressure following the methods outlined in Tischenko (2005). b. The simulated change in sediment temperature between 1970 and 2013 and corresponding shift in the BGHSZ. The BGHSZ shoals over a broad area in response to warming, accompanied by a retreat of its landward edge (indicated by red arrows). c. Simulated change in sediment temperature between 1970 and 2100 based on the linear extrapolation of seafloor temperature. The upper white line is the BGHSZ in 2100. d. Simulated change in sediment temperature between 1970 and 2100 based on the high-emissions AR4 extrapolation. The upper white line is the BGHSZ in 2100 and the lower white line is the BGHSZ in 1970.

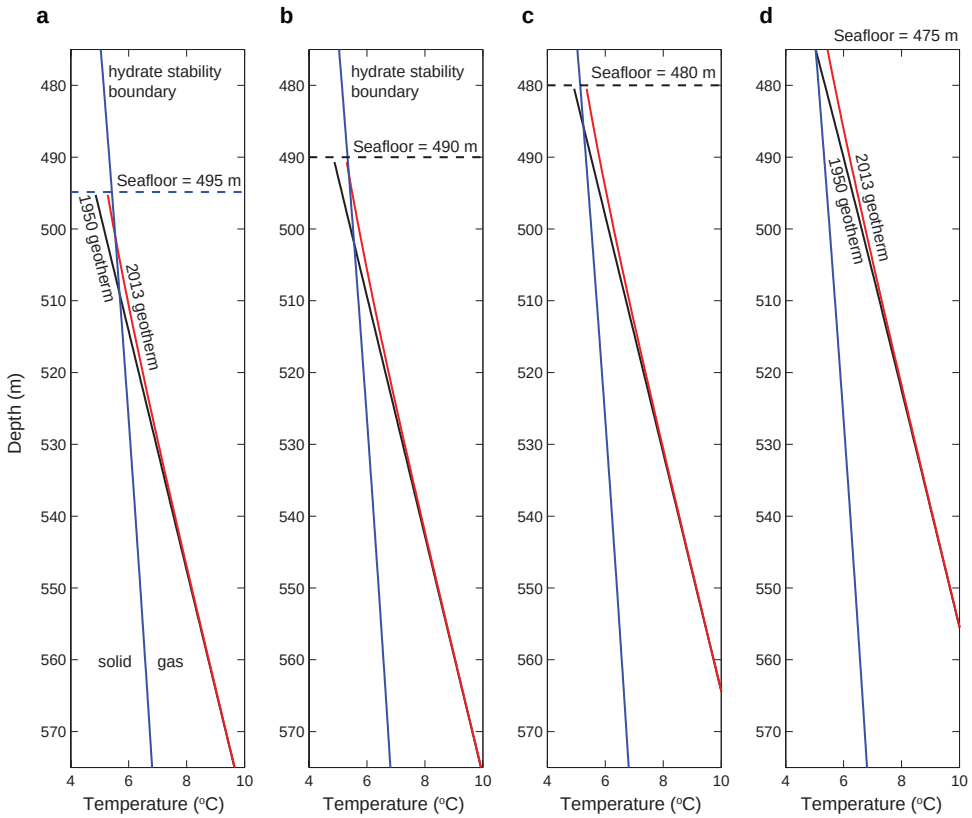

Supplementary Figure 3. Shift in the gas hydrate stability field as a function of seafloor depth along transect P2 between 1950 and 2013 for a. seafloor depth = 495 m, b. seafloor depth = 490 m, c. seafloor depth = 480 m, and d. seafloor depth = 475 m. The blue line represents the gas hydrate stability boundary. The 1950 and 2013 geotherms are shown as the black and red lines, respectively. The black dashed line represents the seafloor in each panel.

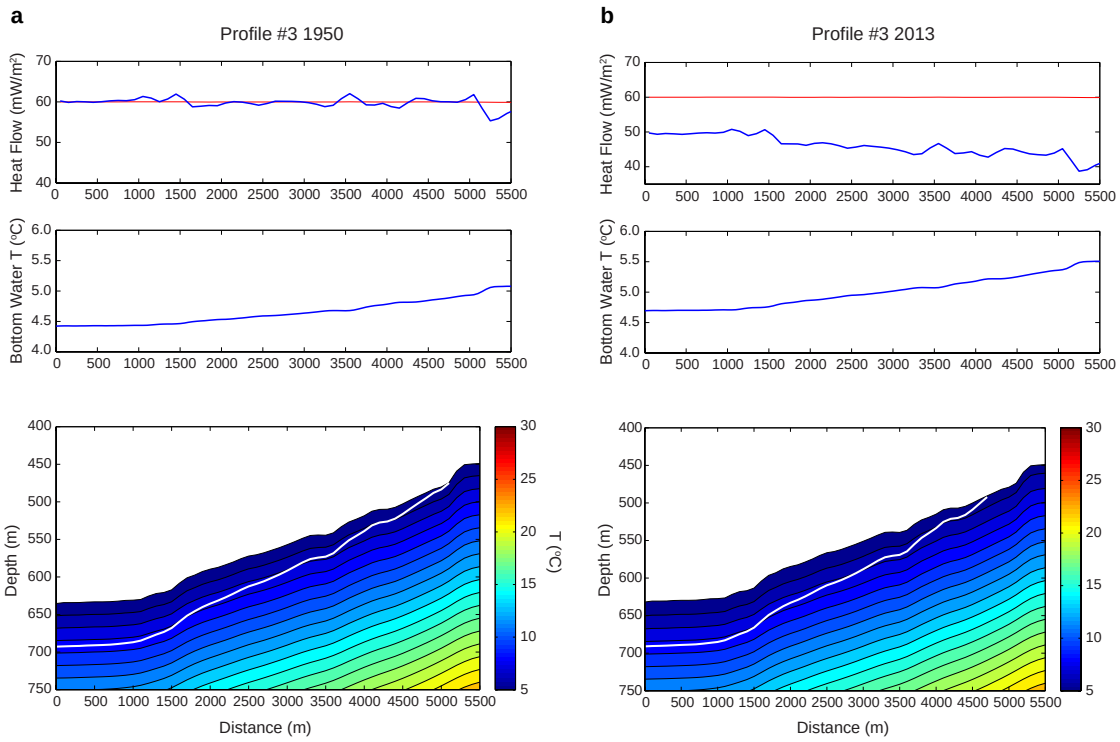

Supplementary Figure 4. Heat flow at the seafloor, estimated seafloor temperature, and subseafloor temperature distribution along transect P3 in a. 1950 and b. 2013. The white line represents the BGHSZ.

Taking the average mass of dissociated gas hydrate per meter of margin based on the three transects, we estimate that the total mass of hydrate potentially annually dissociating along the 253 km length of the Washington sector of the Cascadia margin is ~32.4 Tg. This hydrate-derived methane flux is approximately 500 times the background "passive flux" to the SMTZ over the same area, assuming an upward pore fluid advection rate of 2 mm yr^{-1} and methane concentrations in equilibrium with methane hydrate below the SMTZ [Hyndman and Davis, 1992]. Due to the lack of field constraints along the WA upper continental slope, we cannot estimate the fraction of the methane released due to gas hydrate dissociation that is consumed via anaerobic oxidation of methane in the sediments, or the fraction that bypasses this filter and is emitted to the water column. However, from northern Washington to northern Oregon, the presence of bubble plumes at the retreating upslope limit of gas hydrate (470-530 m water depth; Supp. Fig. 5), suggests that a portion of the methane released by contemporary warming may be emitted to the water column, as observed in the Arctic [Berndt et al., 2014; Westbrook et al., 2009; Thatcher et al., 2013].

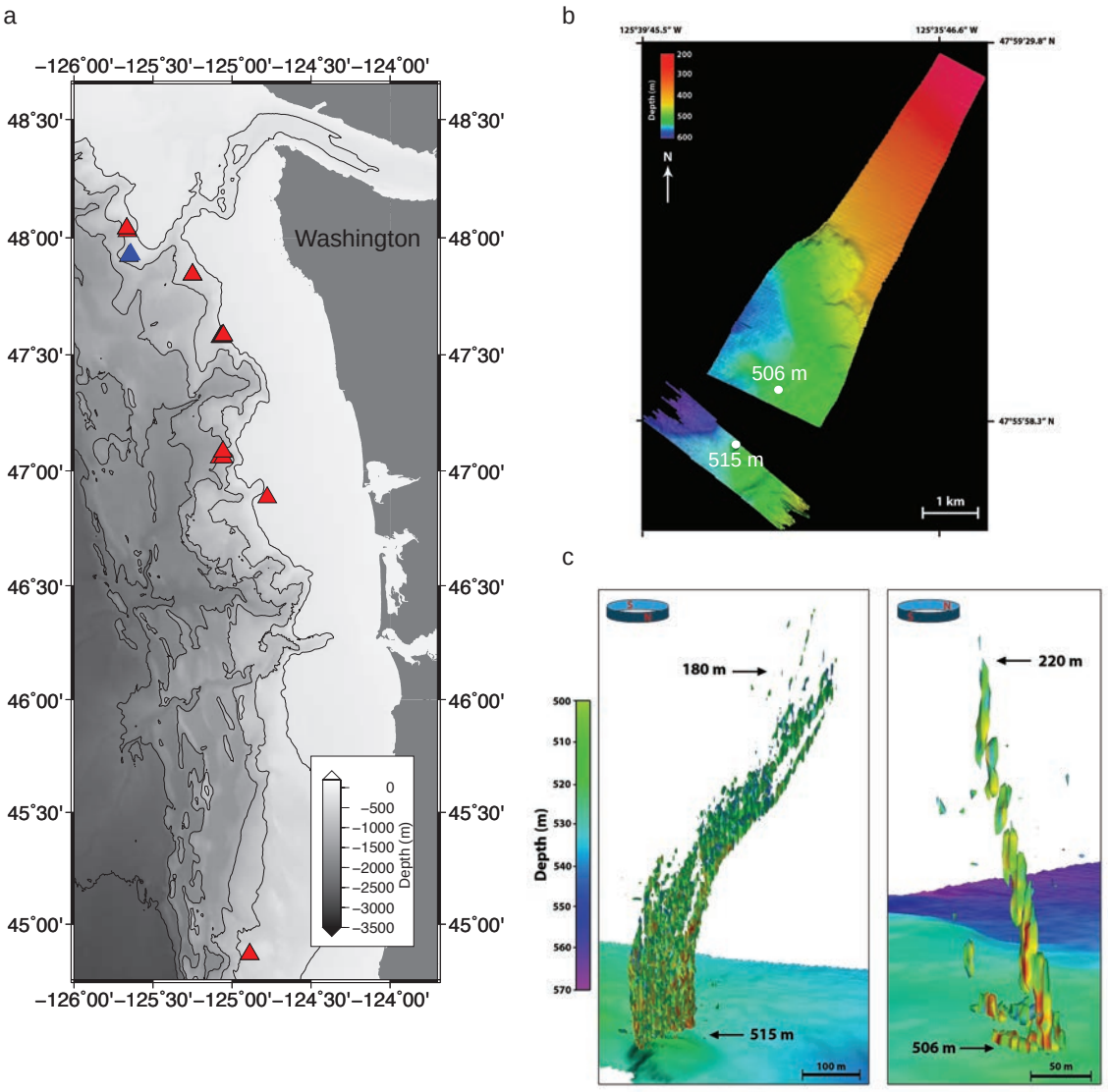

Supplementary Figure 5. Bubble plumes near the up-slope limit of gas hydrate stability offshore northern Washington. a. Location map showing locations of known methane seeps along from northern WA to northern OR. The bubble plumes imaged offshore northern Oregon are constrained to depths between 480-500 m. The blue triangle represents the location of the bubble plumes shown in b and c. b. Bathymetry at the location of two bubble plumes surveyed with the R/V Thompson in 2012. The multi-beam data was collected with a Konsberg EM302 echosounder and processed post-expedition with the Fledermaus FMMidwater module. c. Two distinct plumes were imaged with the largest sourced at 515 m and a less intense plume at 506 m water depth. Arrows show approximate rise height of each plume.

Projected gas hydrate dissociation through 2100

Projections of future seafloor warming along the Washington upper continental slope range from +0.88°C (linear extrapolation) to +2.4°C (AR4 high-emissions scenario) by the year 2100. This thermal disturbance will propagate an additional 68-75 m into the sediment column (Fig. 3 c-d, Supp. Fig. 1-2). This continued long-term warming will cause a horizontal downslope retreat of the gas hydrate stability zone that ranges from ~1.2 km (linear extrapolation) to 2.8 km (high-emissions). Using the same assumptions regarding the thickness of the sulfate reduction zone and the first occurrence of gas hydrate, an average of 0.72 to 1.86 Gg of methane hydrate would dissociate per meter of margin by 2100 (Table 1). Multiplying by the Washington margin length, ~470 Tg of gas hydrate is susceptible to warming-induced dissociation by 2100 in the high-emissions scenario. This rate (~0.5 Tg CH_4 yr^{-1}), represents the annualized release of a volume into the sediment column roughly quadruple the amount released to the water column during the *Deepwater Horizon* spill, and ~11% of the yearly flux of methane into the Black Sea [Reeburgh, 2007]. The amount of methane released that bypasses the microbial filter in the sediment column and is emitted to the water column is at present unconstrained, but would only be a fraction of the amount released from methane hydrate *in situ*.

Table 1. Model estimates and projections

Estimated area of gas hydrate stability zone affected by warming (m^2 per m of margin).			
Transect	1970 to 2013	1970 to 2100 linear	1970 to 2100 high-emissions
P1	4063	24378	65071
P2	4201	21125	46990
P3	5179	30310	82889
Estimated mass of methane hydrate dissociated in Gg per m of margin[a,b]			
Transect	1970 to 2013	1970 to 2100 linear	1970 to 2100 high-emissions
P1	0.116	0.696	1.86
P2	0.12	0.603	1.34
P3	0.148	0.865	2.37

Estimates consider upper 5 m of sediment column are initially devoid of gas hydrate as a result of the sulfate reduction zone.

[a]Assumes a porosity of 0.634 in the upper 15 mbsf based on results from IODP Site U1329 offshore Vancouver Island [Riedel et al., 2006] and an assumed average gas hydrate saturation of 5% of the pore space

[b]Calculated from the volume considering a methane hydrate density of 9×10^5 g/m^3

Conclusions

The dense historical water column data off the Washington margin strongly constrains our model of the impact of ocean warming on gas hydrate dissociation along its upper continental slope. The magnitude of warming at the source of NPIW [Itoh, 2007; Nakanowatari et al., 2007] suggests the Sea of Okhotsk hydrate reservoir is also affected. The environmental consequences of warming-induced hydrate dissociation along the Cascadia margin may be similar to recent models for the Arctic Ocean that show hydrate dissociation from contemporary bottom water warming playing a role in controlling seawater dissolved oxygen and pH in the coming decades [Biastoch et al., 2011]. Our results expand the portion of the gas hydrate reservoir susceptible to contemporary warming to lower latitude deposits and suggest a larger fraction of gas hydrate could dissociate along continental margins worldwide than previously recognized.

References

Becker, J. J., et al. (2009), Global bathymetry and elevation data at 30 arc second resolution: SRTM30 PLUS, Mar. Geodesy, 32, 355-371.

Berndt, C., et al. (2014), Temporal constraints on hydrate-controlled methane seepage off Svalbard, Science, 343, 284-287.

Biastoch, A., et al. (2011). Rising Arctic Ocean temperatures cause gas hydrate destabilization and ocean acidification. Geophys. Res. Lett., 38, doi:10.1029/2011GL047222.

Booth-Rea, G., D. Klaeschen, I. Grevemeyer and T. Reston (2008), Heterogeneous deformation in the Cascadia convergent margin and its relation to thermal gradient (Washington, NW USA), Tectonics, 27, doi:10.1029/2007TC002209.

Boswell, R., and T. S. Collett (2011), Current perspectives on gas hydrate resources, Energy Environ. Sci., 4, 1206-1215.

Davie, M. K. and B. A. Buffett (2001), A numerical model for the formation of gas hydrate below the seafloor, J. Geophys. Res., 106, 497-514.

Hickey, B. M. (1979), The California Current system - hypotheses and facts, Prog. Oceanogr., 8, 191–279.

Hyndman, R. D. and E. E. Davis (1992), A mechanism for the formation of methane hydrate and seafloor bottom simulating reflectors by vertical fluid expulsion, J. Geophys. Res., 97, 7025-7041.

Itoh, M. (2007), Warming of intermediate water in the sea of Okhotsk since the 1950s, J. Oceanogr., 63, 637–641.

Johnstone, J. A. and N. J. Mantua (2014), Atmospheric controls on northeast Pacific temperature variability and change, 1900-2012, Proc. Nat. Acad. Sci. 10.1073/pnas.1318371111.

Kennett, J. P., K. G. Cannariato, I. L. Hendy and R. J. Behl (2003), Methane Hydrate in Quaternary Climate Change: the Clathrate Gun Hypothesis, American Geophysical Union, Washington, DC.

Kouketsu, S., M. Fukusawa, D. Sasano, Y. Kunamoto, T. Kawano, H. Uchida and T. Doi (2010), Changes in water properties around North Pacific intermediate water between the 1980s, 1990s and 2000s, Deep-Sea Res. II, 57, 1177-1187, doi: 10.1016/j.dsr2.2009.12.007.

Nakanowatari, T., K. I. Ohshima and M. Wakatsuchi (2007), Warming and oxygen decrease of intermediate water in the northwestern North Pacific, originating from the Sea of Okhotsk, 1955–2004, Geophys. Res. Lett., 34, doi:10.1029/2006GL028243.

Mantua, N. J., S. R. Hare, Y. Zhang, J. M. Wallace and R. C. Francis (1997), A Pacific interdecadal climate oscillation with impacts on salmon production, Bull. Amer. Meteor. Soc., 78, 1069-1079.

McDougall, T. J. and P. M. Barker (2011), Getting started with TEOS-10 and the Gibbs Seawater (GSW) Oceanographic Toolbox, SCOR/IAPSO WG127, 28pp.

Meehl, G. A., et al. (2007), Global climate projections, in Climate Change 2007: The Physical Science Basis. Contribution of Working Group I to the Fourth Assessment Report of the

Intergovernmental Panel on Climate Change, edited by S. Solomon, S., et al., Cambridge University Press, Cambridge, UK and New York, USA.
Meinvielle, M. and G. C. Johnson (2013), Decadal water-property trends in the California Undercurrent, with implications for ocean acidification, J. Geophys. Res., 118, doi:10.1002/2013JC009299.
Phrampus, B. J. and M. J. Hornbach (2012), Recent changes to the Gulf Stream causing widespread gas hydrate destabilization, Nature, 490, 527-530.
Reagan, M.T., G. J. Moridis, S. M. Elliott and M. Maltrud (2011), Contribution of oceanic gas hydrate dissociation to the formation of Arctic Ocean methane plumes, J. Geophys. Res., 116, doi:10.1029/2011JC007189.
Reddy, C.M., et al. (2012), Composition and fate of gas and oil released to the water column during the *Deepwater Horizon* oil spill, Proc. Nat. Acad. Sci., 109, 20229-20234.
Reeburgh, W.S. (2007), Oceanic methane biogeochemistry, Chem. Rev., 107, 486-513.
Reid, J. L., Jr. (1965), Intermediate Waters of the Pacific Ocean. John Hopkins Oceanographic Studies No. 2, John Hopkins Press, Baltimore, 85pp.
Revelle, R.R. (1983), Methane hydrates in continental slope sediments and increasing atmospheric carbon dioxide, in Changing Climate: Report of the Carbon Dioxide Assessment Committee, National Academy Press, Washington, DC, pp. 252-261.
Rhein, M., et al. (2013), Observations: Ocean, in Climate Change 2013: The Physical Science Basis. Contribution of Working Group I to the Fifth Assessment Report of the Intergovernmental Panel on Climate Change, edited by T. F. Stocker, et al., Cambridge Univ. Press, Cambridge UK and New York USA.
Riedel, M., T. S. Collett, M. J. Malone and the Expedition 311 Scientists (2006), Proc. Int. Ocean Drill. Prog., Expedition 311, IODP, Washington DC.
Ruppel, C. D. (2011), Methane hydrates and contemporary climate change, Nature Ed. Knowledge, 3, 29.
Sandwell, D. T. and W. H. F. Smith (2009), Global marine gravity from retracked Geosat and ERS-1 altimetry: ridge segmentation versus spreading rate, J. Geophys. Res., 114, doi:10.1029/2008JB006008.
Solomon, E.A., M. Kastner, H. Jannasch, G. Robertson, and Y. Weinstein (2008), Dynamic fluid flow and chemical fluxes associated with a seafloor gas hydrate deposit on the northern Gulf of Mexico slope, Earth Planet. Sci. Lett., 270, 95-105.
Stocker, T. F. et al. (2013), Technical summary, in Climate Change 2013: The Physical Science Basis. Contribution of Working Group I to the Fifth Assessment Report of the Intergovernmental Panel on Climate Change, edited by T. F. Stocker, et al., Cambridge Univ. Press, Cambridge UK and New York USA.
Talley, L. D. (1993), Distribution and formation of North Pacific Intermediate Water, J. Phys. Oceanogr., 23, 517–537.
Thatcher, K. E., G. K. Westbrook, S. Sarkar, and T. A. Minshull (2013), Methane release from warming-induced hydrate dissociation in the West Svalbard continental margin: Timing, rates, and geologic controls, J. Geophys. Res., 118, 22-38, doi:10.1029/2012JB009605.
Thomson, R. E. and M. V. Krassovski (2010), Poleward reach of the California Undercurrent extension, J. Geophys. Res., 115, doi:10.1029/2010JC006280.
Tishchenko, P., C. Hensen, K. Wallmann, and C. S. Wong (2005), Calculation of the stability and solubility of methane hydrate in seawater, Chem. Geol., 219, 37–52.
Tryon, M. D. , K. M. Brown and M. E. Torres (2002), Fluid and chemical flux in and out of sediments hosting methane hydrate deposits on Hydrate Ridge, Or, II: hydrological processes, Earth Planet. Sci. Lett., 201, 541–557.
Ueno, H. and I. Yasuda (2003), Intermediate water circulation in the North Pacific subarctic and northern subtropical regions, J. Geophys. Res. Oceans, 108, 3348, doi:10.1029/2002JC001372.
Wang, K., R. D. Hyndman and M. Yamano (1995), Thermal regime of the Southwest Japan subduction zone: effects of age history of the subducting plate, Tectonophys., 248, 53-69.
Westbrook, G. K., et al. (2009), Escape of methane gas from the seabed along the West Spitsbergen

continental margin, Geophys. Res. Lett., 36, doi:10.1029/2009GL03191.
Whitney, F. A., H. J. Freeland, and M. Robert (2007), Persistently declining oxygen levels in the interior waters of the eastern subarctic Pacific, Prog. Oceanogr., 75, 179–199.
Zhang, Y., J. M. Wallace and D. S. Battisti (1997), ENSO-like interdecadal variability: 1900-93, J. Climate, 10, 1004-1020.

Compilation of Seep Sites Along the Washington and Oregon Margins

Preface

This work relates to Tasks 7 in the original proposal. The results described in this chapter were published in *Geochemistry, Geophysics, Geosystems*; the citation is below:

Johnson, H.P., Miller, U.K., Salmi, M.S., Solomon, E.A., 2015. Analysis of bubble plume distributions to evaluate methane hydrate decomposition on the upper continental slope, *Geophys. Geochem. Geosyst.*, 16, 3825-3839, doi:10.1002/2015GC005955.

Introduction

Methane emissions from the decomposition of gas hydrate reservoirs on continental margins can play an important role in the regional marine environment. In Paleogene paleoclimate records, methane hydrate dissociation provided a powerful amplification factor to global warming that was initiated by massive volcanic eruptions in the Atlantic Basin (Bowen et al., 2015; Wright and Schaller, 2013). During the Eocene, the massive release of methane from the sediment reservoir both decreased bottom water pH values (Zachos et al., 2005) and produced anoxia in the near-bottom water, which later propagated throughout the water column (Sluijs et al., 2006). These paleoclimate studies suggest that modern climate warming due to anthropogenic greenhouse gas emission may also have a similar impact on the gas hydrate inventory present in modern margin sediments (Bowen et al., 2006). Hautala et al (2014) have recently demonstrated that the North Pacific Intermediate Water that bathes the upper slope of the Washington State continental margin has undergone a systematic warming of +0.3°C over the past 44 years. Thermal models of the propagation of heat from this warming trend into the sediments of Washington continental slope indicate that the methane hydrate stability depth (MHSD) has increased by 20 meters vertically to its current depth at 500 meters and moved seaward by more than 1 kilometer over the past 4 decades. If the Hautala et al., (2014) thermal model is correct, Washington margin sediments should presently be releasing methane gas into the water column preferentially at depths near the upper hydrate stability depth of 500 meters, a hypothesis that is examined in the present study.

The accretionary wedge section of the Cascadia Subduction Zone (CSZ) in the NE Pacific Ocean extends along-strike for over 1000 km, from Cape Mendocino to central Vancouver Island. These accretionary margin sediments have been extensively studied due to the potential societal impact of a subduction megathrust earthquake on the populated coastal zone of western North America (Hyndman et al, 1993: Hyndman, 2013, Atwater et al., 2005; Satake and Atwater, 2007; Goldfinger et al., 2012; Atwater et al, 2014).

The upward migration of methane through Cascadia margin sediments has also been previously examined (Ritger et al., 1987; Trehu et al., 2004; Riedel et al., 2001; 2010; Liu and Flemings, 2006; Riedel, 2007; Daigle et al., 2011). Bottom Simulating Reflectors (BSRs) detected using multi-channel seismic profiles indicate the presence of abundant solid methane hydrate and methane gas within the pore spaces of the upper several hundred meters of margin sediments. These reflector horizons have been identified as hydrates on the Oregon (Torres et al., 2009; Trehu et al., 2004, 2006; Torres et al., 2004 ; Riedel et al., 2006), Washington (Booth-Rea et al., 2008, Holbrook et al., 2012) and Vancouver Island (Riedel et al., 2006; 2010; Malinverno et al., 2008) continental slopes. Extensive authigenic carbonate surface accumulations related to the anaerobic oxidation of methane on the Cascadia margin, inferred from regions of high acoustic backscatter intensity, indicate that large-scale methane emissions have been active over geological time scales

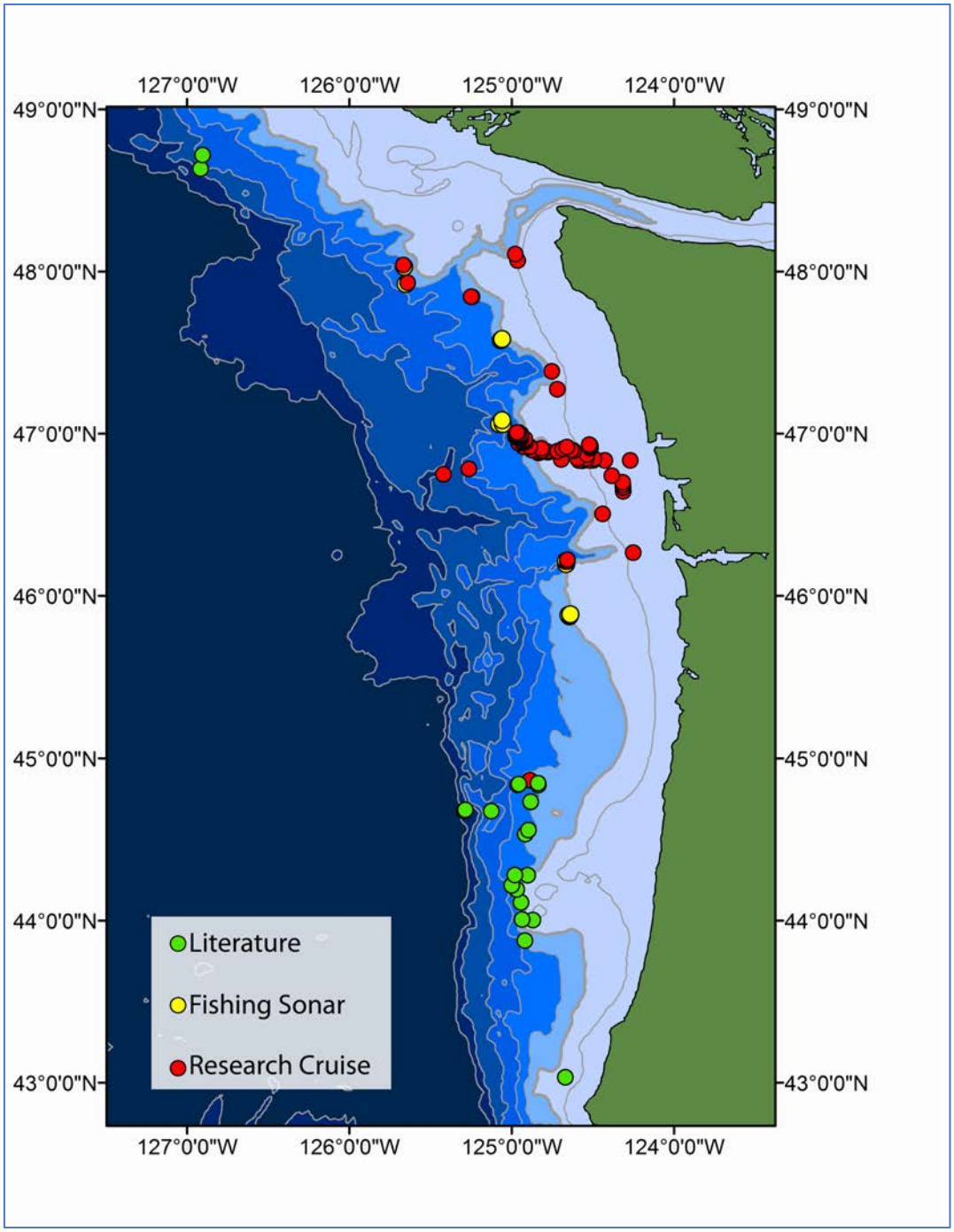

Figure 1. Methane emission sites on Cascadia Margin. Color of circles by data source. Red dots are sites from R/V Thompson and R/V Atlantis multibeam bathymetry surveys. Yellow dots are from reported fishing boat sonars. Green sites are taken from published literature. Total number of methane bubble streams (without clustering) is 168.

(Carson et al., 1994; Torres et al., 2009; He et al., 2007). In addition, isotopic studies of methane-specific foraminifera tests, bi-valve shells and authigenic carbonate deposits of Pliocene age on

the coastal Olympic Peninsula indicate that emissions have continued on this portion of the NE Pacific active margin for millions of years (Martin et al., 2007; Nesbitt et al 2013).

On the Oregon and Vancouver Island portions of the Cascadia margin, methane bubble plume emission have been observed and studied over the last decade (Suess et al., 1999; Torres et al., 2009; Trehu et al., 2004, 2006; Torres et al., 2004; Riedel et al., 2006), with similar studies on the Washington margin (Booth-Rea et al., 2009, Holbrook et al., 2012). Hydrate Ridge, a site of active methane plumes and exposed hydrate outcrops, has been the focus of multiple seismic surveys, several Deep Sea Drilling Project and Ocean Drilling Program drill holes, acoustic surveys of bubble plume emissions, submersible programs, and is the site of an Ocean Observatories Initiative cabled observatory (Suess et al., 1999; Torres et al., 2002; Bangs et al., 2005, 2011, Heeschen et al., 2005 Trehu et al., 2004, 2006; Borhmann et al., 2007, Crutchley et al., 2013). Similarly, three active methane plume sites off the western margin of Vancouver Island have been well-studied (Chapman et al., 2004; Riedel, et al., 2001; 2006; 2010; Riedel, 2007; Torres et al., 2008). Although fewer in number than on the Oregon and Washington segments of Cascadia, the Vancouver Island methane emission sites have also been the site of ODP and IODP drilling and are a node of the Canadian NEPTUNE fiber optic cable network (Barnes et al., 2008; Heesemann et al., 2013). Both the Vancouver Island and Hydrate Ridge sites are all located deeper than 600 meters water depth, where gas emissions are not likely to be the result of modern seawater warming at mid-slope depths.

On the Washington margin, previous acoustic signatures of methane flux have detected regions of extensive seafloor surface carbonate deposits (Salmi et al., 2011). Located on the continental shelf at 130 meters water depth, these methane emissions are too shallow to be related to contemporary hydrate decomposition. Recent Remotely Operated Vehicle (ROV) and ship based surveys on the deeper part of the Grays Harbor portion of the Washington margin have also detected large-scale seafloor carbonate deposits associated with long-term methane emissions, as well as water column methane gas plumes (Johnson et al., 2013) and prevalent BSRs in the sub-surface (Holbrook et al., 2012). During a 2013 heat flow survey of the Washington margin using the ROV Jason II and the R/V Atlantis, methane plumes at water depths of 1046 and 1988 meters were discovered proximal to active methane-specific bioherms (Johnson et al., 2013). However, these deeper bubble plume emission sites lie significantly below the upslope hydrate decomposition depth. For this study, we characterize methane emissions over the entire depth range of the Cascadia margin, including at the upper limit of methane hydrate stability. The calculated upper feather-edge of hydrate stability of 500 ± 4 meters for the Washington margin is taken from the Hautala et al. (2014) study, and is reported as deeper at the south and shallower at the north end of the margin. The upper stability depth at the northern Oregon margin has been reported to be ~510 m by other studies focused on the Hydrate Ridge region (Torres et al., 2009, Bangs et al., 2011; Kannberg et al., 2013).

Identification of Methane Plume Sites

Active methane gas emissions are detected through acoustic observations of bubble plumes in the water column (Figure 1 and Supplemental Figure S1). These acoustic reflectors are oriented vertically in the water column, have a characteristic plume-like shape, are often referred to as flares, and appear to be sourced directly from the seafloor. Although diameters of the individual gas bubbles with a size distribution centered at approximately 2-4 mm (Leifer and Culling, 2010; Römer et al., 2012a; Schneider von Deimling et al., 2011) are too small to be individually reflected by sonar acoustic frequencies which have wavelengths of tens of centimeters (Salmi et al., 2011),

the collective groups of rising bubble streams and associated entrained bottom water presents the strong impedance contrast required to acoustically image in the water column (Leifer and Patro, 2002; Greinert et al., 2006; Romer et al., 2012b, Schneider von Deimling et al., 2012; Salmi et al., 2011; Supplemental Figure S1). The installation of EM302 and EM122 Kongsberg swath bathymetry systems on the U.S academic research fleet have made it possible to routinely detect gas bubble plumes within the water column. These plume-like acoustic images have been confirmed as bubble streams using co-located ROV video images at a variety of sites (for Cascadia examples see Torres et al., 2009, Salmi et al., 2011, Riedel et al., 2007) and have been used extensively as an indicator of bubble plumes in other continental margin environments (Greinert et al., 2006; 2009, Sauter et al., 2006, Romer et al., 2012, Brothers et al., 2013, Skarke et al., 2014). Bubble plumes are also routinely detected by commercial fishing vessels, where sonar chirp frequencies range from 50 kHz to 200 kHz, depending on the water depth and required resolution.

A major uncertainty associated with any compilation of methane emissions on global continental margins is the caveat that the bubble streams are discontinuous in both space and time (Leifer et al., 2006, Greinert; 2009, Schneider von Deming et al; 2010). Some emission sites are long-lived, surrounded by large associated carbonate deposits that take thousands of years to form (Bayon et al., 2009; Berndt et al., 2014; Teichert et al., 2003). Methane emissions can also be intermittent over a wide range of time scales (Riedel, 2007, Bangs et al., 2011, Greinert, 2009, Kannberg et al., 2013). Where bubble plume emissions are episodic, they can sometimes be correlated with external tidal cycles or bottom water velocities (Suess et al., 2001, Thomsen et al., 2012). In time-series observations taken at methane emission sites, the bubble stream flows can appear randomly intermittent, with flow controlled by modifications such as blockage of sub-surface pathways by gas accumulation or mineral precipitation processes not readily visible to seafloor or shipboard based sensors (Tryon et al., 2002; Solomon et al., 2008; Lapham et al., 2013). Because of obvious limitations on logistics and resources, we ignore any potential temporal variations and make the simplistic assumption that the plume distributions are static and constant, at least over the past 10 years of data acquisition.

The 122 active methane gas emission sites in this study were compiled from both traditional and non-traditional sources (Figures 2 and 3). Most sites were discovered in the course of systematic geophysical surveys of relatively small areas of the margin. Many but not all of the bubble streams were later confirmed as methane gas by surface ship CTD casts, and submersible ALVIN and ROV water sampling. The majority of the methane plume sites identified on the Oregon portion of the Cascadia margin are from the compilation of Torres et al. (2009) using these methods. Three well-studied methane plume sites off the west coast of Vancouver Island are of a similar nature and are described in Riedel et al., (2010) and references within.

Included in the present compilation are 45 bubble plumes discovered and informally contributed by commercial fishermen using standard deep-water acoustic fish locating sonars. Modern commercial fish locating sonars are integrated with GPS navigation that can provide co-located seafloor depths, surface ship GPS location and images of plume-like reflectors in the water column. The photographic images of these reflectors were recorded by commercial fishermen using cell phone cameras, and were provided to the authors over a period of several years (Figure 3A; Supplemental Figure S1). An important sub-set of the plume sites detected by fisherman were later confirmed by subsequent scientific field programs using swath bathymetry and water column imaging of the EM302 system on the R/V Thomas G. Thompson (Figure 3C).

For the acoustic images obtained with fishing and other sonars to be identified as methane plumes, these reflectors were required to (1) be oriented sub-vertically, (2) extend at least 50

meters upward through the water column, (3) clearly originate at the seafloor, and (4) not match the criteria used to identify fish or other biological swarms including acoustic reflection lobes that spread horizontally at a given water depth (Figure Supplemental S1). Bubble plume locations derived from formal scientific expeditions on research vessels are also confirmed using swath water column imaging (Figures 3B and 3C) or ROV video images of bubbles when those systems have been available.

An issue in interpreting the present compilation is the confirmation that acoustically-imaged bubble plumes are actually composed solely of pure methane gas of microbial origin rather than a more complex organic gas of thermogenic origin, which would push the upper limit of gas hydrate stability to shallower depths. Torres et al. (2009) and Collier and Lilley (2005) show that most of the methane plumes in the Oregon margin compilation are composed primarily of methane gas, with only minor amounts of heavier hydrocarbons. These and other studies showed that many of the bubble streams off the Oregon coast are associated with surface exposures of solid methane hydrate (Johnson et al., 2003; Kannberg et al., 2013 and references within). However, many Oregon margin sites are located deeper than the upper limit of hydrate stability (Figure 4) and therefore unlikely to be derived from the decomposition of hydrate by contemporary warming of near-bottom seawater. The plume sites on the Vancouver Island segment of the Cascadia margin, also located below the hydrate stability depth, have been confirmed to be composed of both microbial and thermogenic methane gas, are associated with seafloor exposures of solid gas hydrate, and are proximal to extensive long-lived seafloor carbonate deposits (Riedel et al., 2010; Joseph et al., 2013; Lapham et al., 2013).

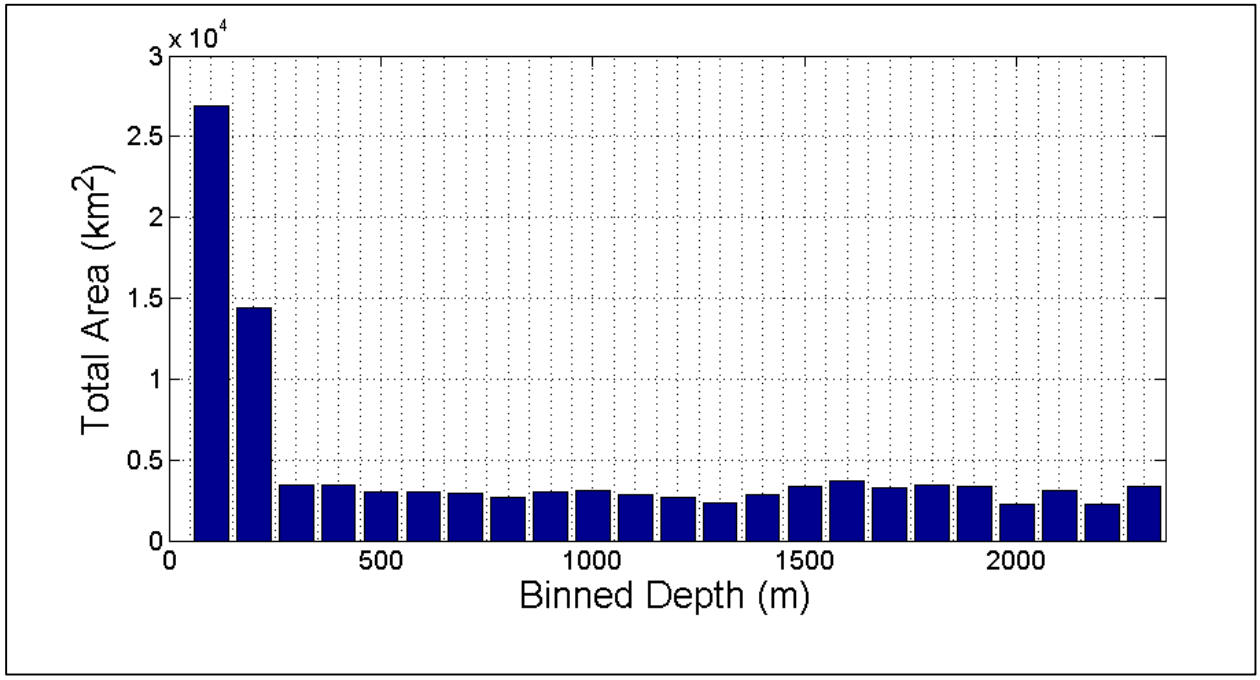

Supplemental Figure S2. Histogram showing the area of the individual depth bins for the Cascadia margin after partitioning into 100 meter depth intervals, beginning at 50 to 149 meters water depth. Note that the partition containing the shallow continental shelf between 50 and 149 meters has the largest area. Cascadia shelf break varies along-strike, but lies at approximately 180 to 200 meters water depth.

Depth Determination

Of the 194 total bubble stream emission sites, 129 sites have water depths extracted from the original fishing or research vessel acoustic sounder data, using the travel time of the acoustic return. These travel time depths could range in confidence from the fixed acoustic velocity values used for fishing sonars to the CTD-calibrated depths used during the research cruises. Each of these depths was tested by co-locating the methane emission site with a Cascadia Margin multibeam bathymetry compilation within GeoMapApp (http://www.geomapapp.org) and comparing it to the depth provided by the original bathymetric data. Of the 129 total sites compared using primary source depths and GeoMapApp depth, 96 locations agreed within 10 meters and 114 locations agreed within 50 meters. The GeoMapApp multiple resolution depth compilation includes both modern high resolution swath bathymetry that overlies a lower resolution NOAA multibeam bathymetry data set (Ryan et al., 2009). Three of the sites contributed by fishing sonar exceeded 100 meters depth disparity between reported primary source depths and GeoMapApp depths, but these corresponded to the low resolution portions of the compiled bathymetric data or could be due to using incorrect seawater velocity profiles. Depths provided by the primary reporting sources were used in all calculations in the study where available. However, 65 of the total 169 sites had only locations without original reported depths and were taken from the GeoMapApp bathymetric compilation. Figure S4 compares primary source depths with those depths given at the same location by the GeoMappApp bathymetry data. The high correlation lends confidence to the use of GeoMapApp depths where depth data is otherwise absent.

There are general increasing uncertainties associated with each of these depth assignments, where depths derived from submersible or ROV observations are assumed accurate within several meters. Depths from the R/V Thompson EM302 coverage have estimated accuracies of ± 5 meters, largely due to uncertainties in the horizontal positioning of the ship, and those depths from fishing sonars were assigned an uncertainty of ±10 meters due to the use of fixed factory-calibrated water velocity profiles. The uncertainties were estimated by comparing **c**ompares site depths obtained from GeoMapApp obtained using the latitude and longitude of the site locations to those original reported depths taken from research cruises, literature and fishing sonar images where there was overlap in coverage for the same bubble plume locations (Supplemental Figure 4).

Data Processing

Bubble Stream Clustering

Areas of methane emissions can consist of multiple individual gas streams that are partitioned in the shallow sub-surface just prior to entering the water column. As an example, a detailed survey of an emission site located on the Washington continental shelf shows approximately 20 individual bubble streams rising within the water column originating from what appears to be a single deeper sub-surface source of methane (Salmi et al., 2011; their Figure 1). In order to not overestimate sites composed of multiple but closely-related bubble streams, individual bubble plumes were grouped together in order to identify bubble streams that share a common sub-surface pathway. We applied a clustering strategy that consolidates all gas streams located within a fixed radius of 300 m, using the well-characterized Salmi et al (2011) site as our guide. A similar distribution of individual methane gas streams is present on the Vancouver Island Barkeley Canyon site, although the collection radius used there is somewhat larger than the 300 meter radius selected for this compilation (see Riedel, 2007). Some methane emission sites, particularly the

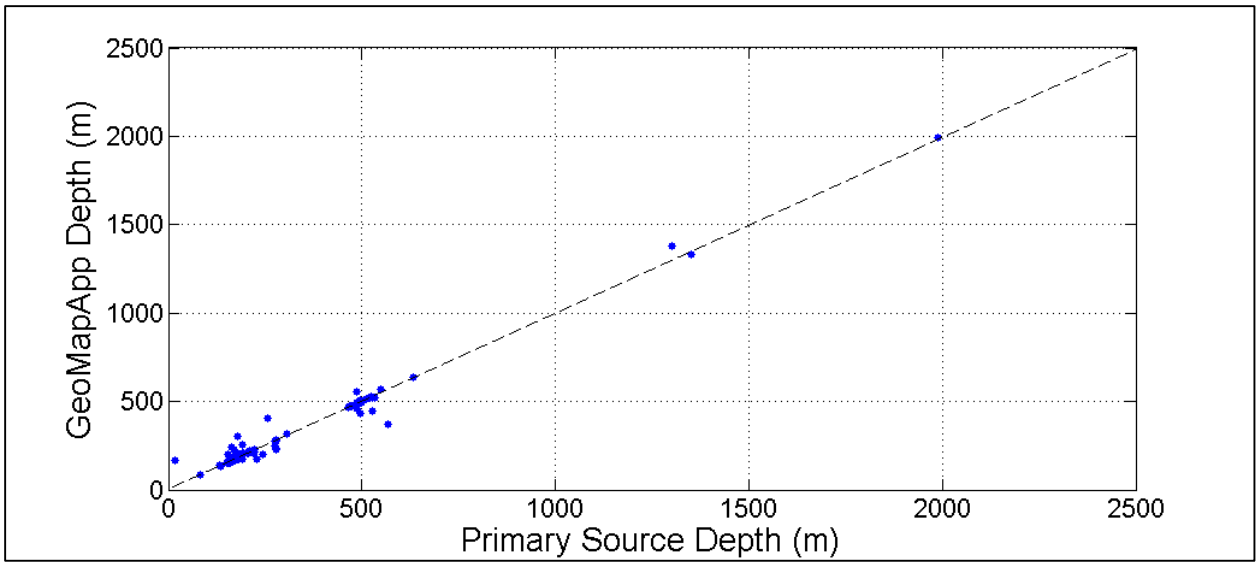

Supplemental Figure S4: Comparison of all primary source depths (fishing sonar, research sites, literature) with their equivalent depths obtained using the GeoMapApp database (multibeam bathymetry overlay data only). The R^2 value for a linear fit of a 1:1 slope is 0.9823. The strong linear correlation implies that most depths used are consistent with independent swath bathymetry depth sources and therefore likely to be reliable for this compilation.

quasi-linear distribution visible on the Washington shelf near Grays Canyon (Figure 1) appear controlled by listric fault traces that are not point sources (McNeill et al., 1997) and are therefore unlikely to have a characteristic clustering radius.

As an example of the clustering process, if there are distinct bubble streams identified within a clustering radius of 300 meters, it was still counted in this compilation as only one emission site. We arrived at a standard radius of 300 meters by testing clustered radii of 0, 150, 300 and 500 meters, to identify a characteristic length scale for emission sites where the number of total sites counted would become almost constant with increasing radii. Supplemental Figure 3S shows the number of plumes sites flattening with increasing clustering radii between 300 and 500 meters, suggesting that 300 meters is approaching but not yet reaching the full characteristic length scale for methane emission sites on the Cascadia margin.

Areal Normalization

The Cascadia margin is an active accretionary wedge where the bathymetric depth varies non-uniformly both across-strike and along-strike of the subduction zone convergence. This variation produces significant differences in the amount of area associated with each across-strike depth interval of the margin (Supplemental Figure 2S). For example, the entire Cascadia margin continental shelf between the depths of 50 and 149 meters has an area of 2.68×10^4 km^2, while the depth interval over the same 100 meter spacing between 450 and 549 meters has a much smaller surface area of 3.41×10^3 km^2. Without areal normalization, a uniform distribution of emission sites should produce a higher bubble stream count for depth intervals that have the largest exposed horizontal area, such as the continental shelf margin and mid-slope terraces which have larger horizontal areas. In order to compare methane plume density across depth intervals of varying areas, we normalized the observed plume density to area by using the following equation:

Normalized plume density at D = $N_p/(A)$

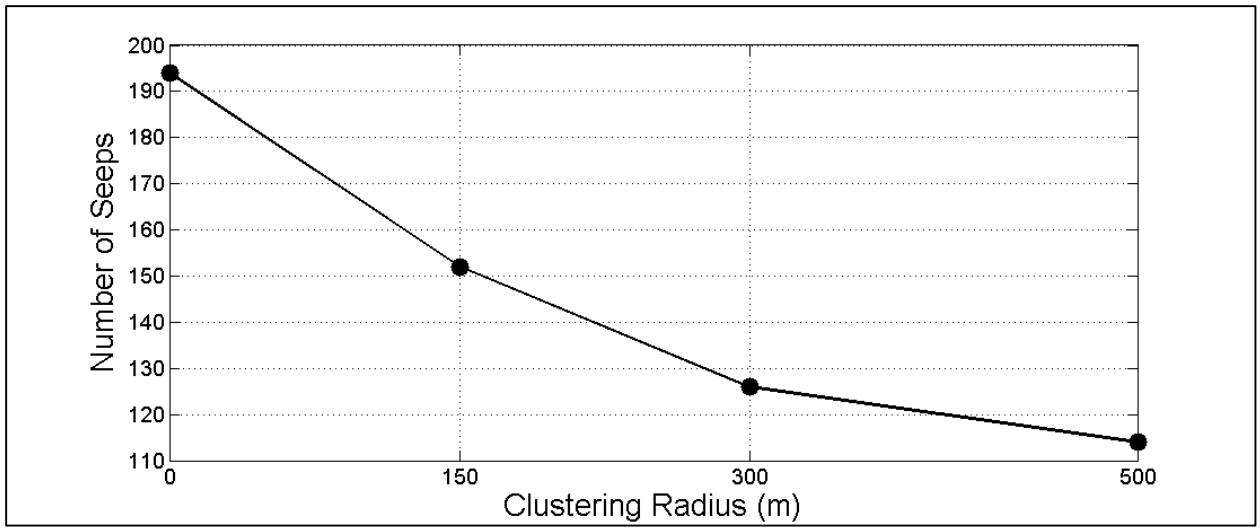

Supplemental Figure S3: Summary count of the total number of emission sites on the Washington and Oregon segments of the Cascadia margin after applying bubble stream clustering radii of 0, 150, 300 and 500 meters. A clustering radius of 0 meters would count every distinct individual bubble stream as an emission site. A clustering radius of 300 meters rather than 500 meters was used in Figures 3,4 and 5 since some sites on the continental shelf are associated with quasi-linear faults and do not show a characteristic clustering parameter (see Figure 1 in text)

where N_p is the plume site count, A is the area associated with each 100 meter depth interval along the entire margin, and D specifies the depth interval in meters (i.e., D = plumes/km^2 for a specific 100 meter wide depth bin).

Areal normalization provides a more accurate measure of bubble stream density with units of plumes/km^2 per depth interval than simple depth binning methods that have been used previously. For this normalization, we used the compiled margin bathymetry dataset available for Cascadia in GeoMapApp, sub-divided the margin depths into 100 meter depth bins for each of the depth intervals on the Cascadia margin (i.e., 50-149, 150-249, 250-349, …, in meters). We then calculated the areas for each depth interval using the geospatial processing program ArcMap. Plume densities are discussed in terms of these area-normalized units for the remainder of this report.

Non-Uniform Sampling Bias

Non-uniform and incomplete sampling of the entire Cascadia margin can produce a bias in a compilation of *ad hoc* emission sites. No complete systematic geophysical survey of methane emission sites of the entire Cascadia margin presently exists, although Torres et al (2009) have compiled many sites within a compact region of the Oregon coast near Hydrate Ridge, and the Grays Canyon area of Washington State has also had considerable coverage over a small area (Holbrook et al., 2012; Johnson et al., 2013). Scientific expeditions with goals other than methane bubble stream identification are non-uniformly distributed along the Cascadia margin, with many located at water depths deeper than the 500 meter upper limit of the MHSD for Cascadia. While useful in characterizing acoustic images associated with bubble streams and for confirming those fishing sonar anomalies, these focused scientific research expeditions have primarily targeted localized areas on the mid- and lower-slope of the Cascadia margin and do not provide uniform areal coverage.

Figure 3a shows that only a small number of the emission sites contributed from fishing sonars are located below 1000 meters. Any bias toward mid- to upper-slope depths by fishing sonar surveys on the Cascadia margin is difficult to quantify, since there is no estimate available of the time each fishing boat spends surveying at each depth interval. Fish catch reports indicate that the most completely sampled regions by the Cascadia margin commercial fishing fleet are the upper slope above 1000 meters depth (http://www.nwfsc.noaa.gov/research/divisions/fram/observation/data_products/index.cfm). The incomplete and non-uniformly sampled margin coverage for all data sources will limit confidence in any interpretation of our compilation, which must be viewed critically in this light. Since the primary hypothesis being tested is whether or not methane bubble plumes on the Cascadia margin have an unusual density in the range of depths that includes the upper limit of gas hydrate stability, an ideal compilation producing Figure 5 would require that all Cascadia continental slope depths would have been surveyed uniformly using a single methodology. Given the *ad hoc* and informal sources of some plume identifications in our compilation, this desired uniformity and completeness of spatial coverage is clearly not realized, and is further discussed below.

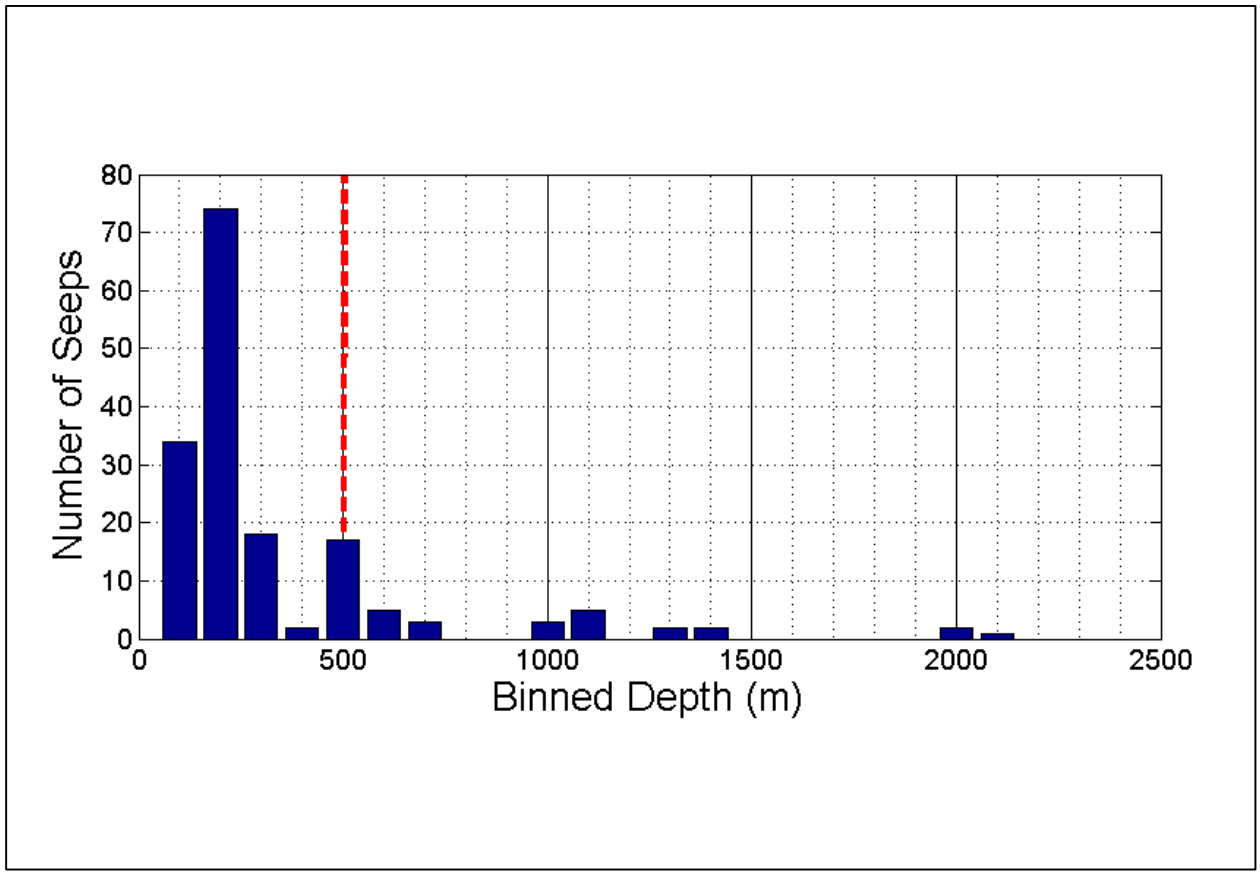

Figure 2. Histogram of all individual methane bubble streams observed in this study plotted as a function of site depth (meters), with no clustering or normalization by area applied. Depth bins are 100 meters wide, beginning at 50 meters water depth. Note the strong peak in the 150 to 249 meter depth bin where listric faults are present on the continental shelf edge between 150 and 249 meters water depth.

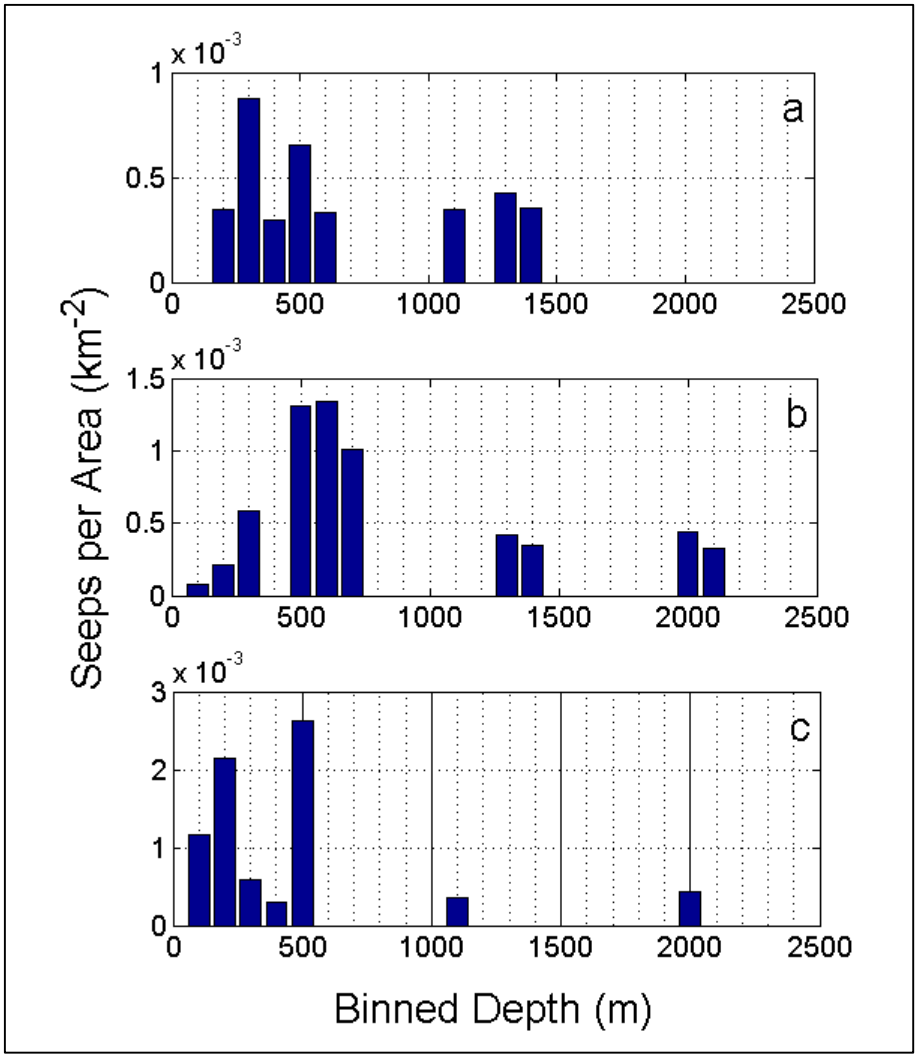

Figure 3a; Methane plumes identified using fishing sonars that have been normalized by area of depth bins and clustered using 300 m radii. **Figure 3b:** Methane plume sites taken from scientific literature normalized by area of depth bin and clustered using 300 m radii. **Figure 3c:** Methane plume sites taken from University of Washington research cruises on the R/V Thomas G. Thomson and R/V Atlantis and normalized by the area of each depth bin and clustered using 300 m radii.

Sensitivity Tests

We performed a series of sensitivity tests to test confidence in our interpretations based on the observed methane bubble plumes from this compilation. The first test is whether the anomalous plume densities shown in Figure 5 are due to only one of the data sources for the compilation, or are present independently in all three of the source sub-datasets. Figures 3a, 3b and 3c show the partitioning of the plume depth inventory by source, differentiating between plumes exclusively from fishing sonars, those from research cruises and those from published ROV and submersible studies. Examination of these histograms shows that a peak in plumes/km^2 at the depth bin for 500 (i.e., 450 to 549) meters is present in all subsets of the compilation (Figure S4), and is not dependent on the source of the identifications.

The plume density anomaly was also tested for along-strike geographical bias. Figures 4a and 4b shows plume distributions divided geographically into Washington and Oregon portions of the Cascadia margin. These two figures indicate that the plume sites for both geographic areas show an unusually high density of emission sites in the 500-meter depth interval that is associated with the upper hydrate stability depth. Figure 4 also shows that most of the Oregon emission sites are derived from published research expeditions rather than more recent fishing sonar observations. In contrast, the plume densities on the Washington segment have a broader mix of sources that include fishing sonar, R/V Thompson, R/V Atlantis and R/V Langseth swath bathymetry, and published methane plume sites (Figure 4). Even though the Washington and Oregon segments have a widely different mix of plume identification sources, comparison of the two geographical regions both show an anomalously high plume density near 500 meter water depths.

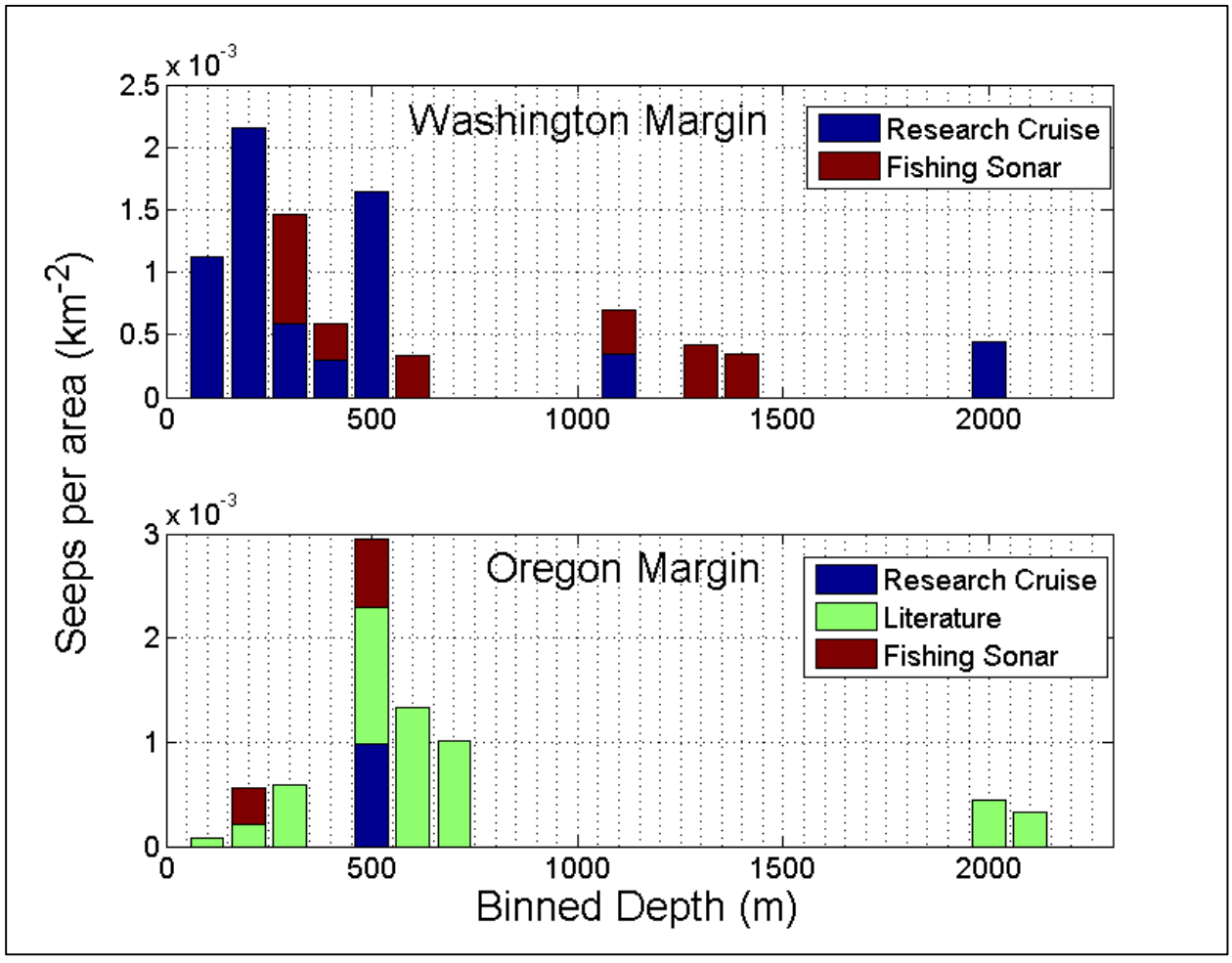

Figure 4. North-South geographic partitioning of methane plume sites, all with a clustering of 300 meter for individual bubble streams applied to the data and normalized by area for each 100 meter depth bin. **Top figure** shows the WA margin, from the Straits of Juan de Fuca to the Columbia River. **Bottom figure** is the Oregon margin from the Columbia River to the California state line. For both of these North-South segments of the Cascadia margin, the depth bins that include 500 meters water depth that are normalized by area has a high density of methane emission sites shown as peaks in the respective histograms.

Anomalous Plume Density for Cascadia

Using our preferred bubble stream clustering radius of 300 meters, Figure 5 represents our estimate of the depth distribution of the 113 high confidence methane plume sites detected by the data acquisition methods described above. The original large plume depth anomaly at the depths of less than 200 meters for un-clustered individual bubble streams for the shallow continental shelf in Figure 2 is reduced by applying the clustering process. Significantly, the peak plume density anomaly at the 500 meter depth interval persists after clustering. Of the total clustered 113 emission sites in this collection for the entire Cascadia margin at all depths, 14 sites lie within the narrow 450 to 549 meter depth range, which includes the upper hydrate stability depth of 500 meters.

Discussion and Interpretation

We approached this study with the goal of addressing the specific question: are there any plume density anomalies located across-strike the Cascadia Margin? If these density anomalies exist, are they located within the depth interval that contains the upper limit of hydrate stability? Logically, there are three possible alternative plume distributions that form the corresponding Null Hypotheses to this question. The first Null Hypothesis is that methane plume sites might have a uniform depth distribution along the Cascadia margin. However, even without the application of any filters, the bubble stream distributions shown in Figures 2 and 5 indicate that this Null Hypothesis is unlikely to be correct.

The second Null hypothesis is that any observed non-uniform distribution of methane emissions with depth would be controlled by tectonic and geological processes that are unrelated to changing sea water temperatures or hydrate decomposition and instead are controlled by sub-surface tectonic and bio-geochemical processes present. Figures 2 and 5 show a very non-uniform distribution for the bubble emission sites, with plume density anomalies associated with both the continental shelf (<200 m) and the depth of the upper limit of hydrate stability at 500 meters. In shallow water, the Washington continental shelf edge has been previously shown to be an extensional region with deep listric faults (McNeil et al., 1997**)**, and these fault traces are sites of both fluid and methane emissions (Salmi et al., 2011).

Previous tectonic models of fluid and gas migration for an active accretionary wedge predict observed plume emissions occurring near 2000 meters, 1000 meters, and on the shallow continental shelf region. In these models, the deeper sites near 2000 meters have been suggested to be due to sediment porosity reduction behind the deformation front (Hyndman et al., 1993; Wang et al., 1993; Wang, 1994; Shi and Wang, 1994; Riedel et al., 2010). In addition, the fluid/gas emissions occurring near 1000 meter depths have been proposed due to the development of late stage tectonic fault pathways that penetrate deeply into the middle portion of the accretionary sediment wedge (Wang et al., 1993; Moore et al., 1991; MacKay et al., 1992; Davie and Buffet, 2003; Bangs et al., 2011; Mandal et al., 2014; Hornbach et al., 2012; Li et al., 2014). In contrast to this model, observations using acoustic backscatter images of seafloor carbonate deposits suggest that the sub-surface fluid/methane vertical migration paths are strongly correlated with, and the locations primarily controlled by, the development of folded anticlinal ridges associated with the horizontal shortening of the accretionary wedge (Carson et al., 1991, 1994, Johnson et al., 2003).

At the critical minimum depth of gas hydrate stability near 500 meters in the North Pacific, we are not aware of any tectonic model that predicts a higher density of methane emission sites either below the shelf edge at 200 meters or above the near-1000 meter depth

interval where the emission anomaly shown in Figure 5 is located at 500 meters depth. However, we note that the lack of a currently published model does not indicate the absence of a yet-undescribed tectonic process.

The third possible Null Hypothesis is that if our plume compilation shows an anomalously high emission site density within the depth range that contains the upper hydrate stability depth of 500 meters, this density anomaly could still be solely the result of areal/depth sampling biases from incomplete survey coverage of the entire continental slope. Due to the *ad hoc* nature of our plume site sources, our data compilation may be fundamentally biased by spatially non-uniform survey tracklines that cannot be addressed quantitatively. Although difficult to verify, we assume that the fishing sonar observations of methane plumes may be more frequent on the shelf and upper margin mid-slope to 1000 meters water depth. In contrast, subduction zone-related research cruises and resultant emission sites taken from the reviewed scientific literature are likely to be surveying the lower mid-slope and deformation front on the deep margin rise. These opposing depth/spatial biases could partially compensate for the commercial fishing sonar observations, although this hopeful assumption may not be supported by more systematic geophysical surveys in the future.

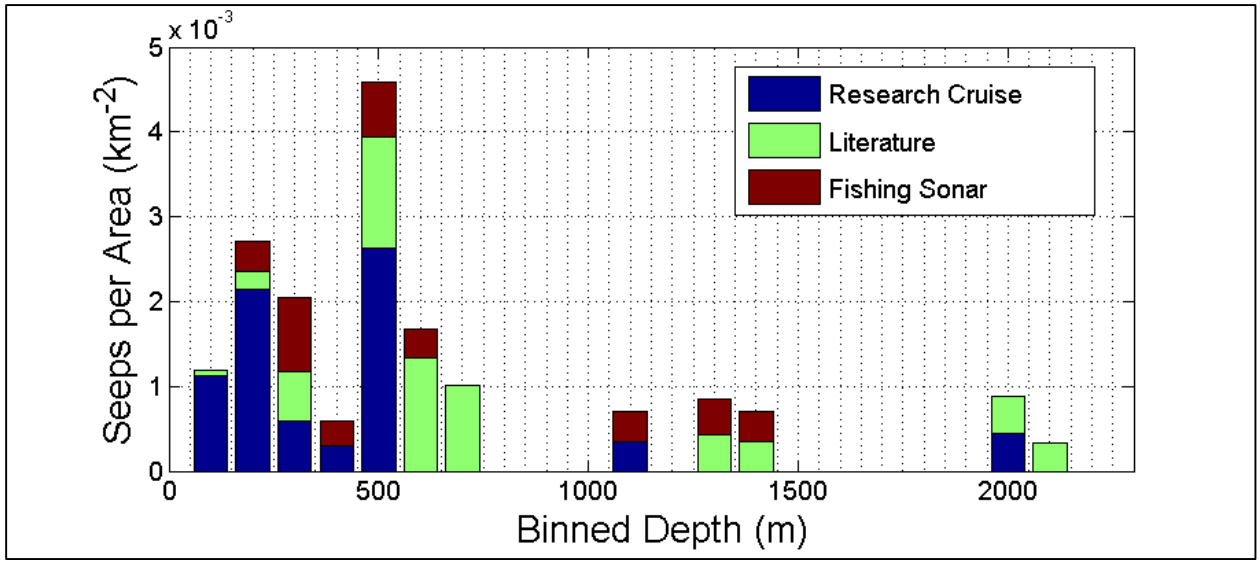

Figure 5. Histogram showing all methane emission sites on the Washington and Oregon segments of the Cascadia margin, with 300 meter clustering applied to the individual bubble streams and normalized by the area contained within each 100 meter depth bin. Color bar legend shows methane plume site data sources.

Results from Cascadia Margin

Whether partitioned by (1) bubble stream cluster radius, (2) plume identification method, (3) geographical region or (4) normalized for the area of each depth interval on the entire margin, the narrow 100 meter wide depth range that includes upper hydrate stability depth of 500 meters on the Cascadia margin appears to be an anomalously active region of methane plume emissions. Lacking any known alternative tectonic or geologic model that would produce anomalously high number of emission sites in this narrow depth range, and with new evidence that 44 years of seawater warming is also occurring at this depth, a plausible remaining explanation is that methane hydrates at the upslope feather edge of phase stability appear to be decomposing along the entire Cascadia margin.

This proposed hypothesis is consistent with a previous thermal model of the Cascadia upper continental slope that shows gas hydrates may have begun to dissociate in response to sea water warming observed in this depth interval and at this location (Hautala et al., 2014). That previous study used archived water temperature profiles to show that sea water in the Washington segment of Cascadia in the interval 400 to 700 meters has risen +0.007 °C/year over the past 45 years. Depending on local margin bathymetry, this warming is sufficient to cause the upper methane hydrate stability depth to migrate vertically 10 to 20 meters over this time period, releasing substantial quantities of methane gas (Hautala et al., 2014). If our assumptions and analyses are correct, the unusual density of methane plume emission sites at the upper stability limit for methane hydrate shown in Figure 5 is consistent with thermal models that show contemporaneously warming seawater is causing hydrates to decompose along the entire Cascadia margin, potentially from Northern California to Vancouver Island. While the above argument is plausible, it falls short of providing the confidence level that a uniform survey of the entire Cascadia margin, optimally using a single survey tool, would provide.

Conclusions

The present compilation of methane emission site densities along the Cascadia margin in the NE Pacific suggests that methane emission sites are preferentially located within depths represented by both the continental shelf and at the 500 meter depth on the margin, with the latter representing the depth interval that contains the upper limit of gas hydrate stability. However, this compilation includes non-traditional data acquisition methods and lacks the weight of a systematic geophysical survey with 100% areal coverage. The number of plumes within the 450 to 549 meter depth bin represents only 12% of the total emission sites from all depths over the entire Cascadia margin.

The area normalization for each of the 100-meter Cascadia depth bins and the persistence of the resulting emission peak at 500 meters after the application of several sensitivity tests adds weight to our proposed identification of the 14 emission sites as a substantial depth anomaly for methane emissions. Given this anomalous density of methane emission sites at the critical hydrate decomposition depth, the present Cascadia compilation is consistent with thermal models that show the observed warming of North Pacific seawater over the past several decades. This warming may be decomposing the previously stable hydrate reservoir along the entire Cascadia Margin (Hautala et al., 2014). If this hypothesis is correct, extensive decomposition of methane hydrate on the active Cascadia margin sediments has potential for major societal impact, including changes in near-bottom seawater chemistry including oxygen consumption and ocean acidification (pH) anomalies harmful to local near-bottom dwelling biota, possible tsunami-generating slope failures, and a potential positive feedback to atmospheric greenhouse gas emissions.

Extracting useful information from imperfect data sets has a strong tradition in oceanography, and with proper caveats, can be used to advance current models regarding critical processes to the next stage. The way forward is obvious; a systematic geophysical and geochemical examination of the entire Cascadia continental margin as well as other active and passive margins is required that includes the entire depth range from the continental shelf to the abyssal plain.

Supplemental Table S2. Methane Plume Inventory on the Washington and Oregon Segments of the Cascadia Subduction Zone.

Latitude, °N	Longitude. °E	Final Depth (m)	Source
3.0333	-124.6700	132	Collier et al (2005)
43.8760	-124.9190	493	Torres et al. (2009)
44.0033	-124.8700	83	Collier et al (2005)
44.0070	-124.9360	223	Torres et al. (2009)
44.1120	-124.9430	219	Torres et al. (2009)
44.1920	-124.9690	275	Torres et al. (2009)
44.2170	-125.0000	462	Torres et al. (2009)
44.2790	-124.9020	221	Torres et al. (2009)
44.2810	-124.9810	633	Torres et al. (2009)
44.5330	-124.9170	471	Torres et al. (2009)
44.5580	-124.8970	539	Torres et al. (2009)
44.6750	-125.1250	678	Carson et al. (1991)
44.6750	-125.2916	2017	Carson et al. (1990)
44.6830	-125.2850	2104	Carson et al. (1990)
44.7320	-124.8830	565	Torres et al. (2009)
44.7330	-124.8830	587	Torres et al. (2009)
44.8360	-124.8360	344	Torres et al. (2009)
44.8370	-124.9630	747	Torres et al. (2009)
44.8410	-124.9570	711	Torres et al. (2009)
44.8470	-124.8380	567	Torres et al. (2009)
44.8655	-124.8878	529	Torres Oregon Plume
45.8726	-124.6450	200	fishing sonar plumes
45.8770	-124.6456	199	fishing sonar plumes
45.8785	-124.6465	199	fishing sonar plumes
45.8805	-124.6500	200	fishing sonar plumes
45.8820	-124.6390	183	fishing sonar plumes
45.8825	-124.6470	199	fishing sonar plumes
45.8830	-124.6427	194	fishing sonar plumes
45.8830	-124.6420	190	fishing sonar plumes
45.8840	-124.6411	185	fishing sonar plumes
45.8850	-124.6386	182	fishing sonar plumes
45.8857	-124.6370	181	fishing sonar plumes
45.8860	-124.6380	181	fishing sonar plumes
45.8860	-124.6355	177.5765	fishing sonar plumes
46.1950	-124.6650	526.6944	fishing sonar plumes
46.2130	-124.6570	467	fishing sonar plumes
46.2145	-124.6660	548.64	fishing sonar plumes

46.2163	-124.6550	548.64	fishing sonar plumes
46.26523167	-124.251607	70	TN-177
46.50456617	-124.4406662	109	TN-207
46.64399183	-124.313437	66	TN-177
46.66629683	-124.3146268	66	TN-177
46.68335517	-124.315577	64	TN-177
46.69977517	-124.3164968	65	TN-177
46.7006035	-124.317252	65	TN-177
46.74022183	-124.382997	78	TN-177
46.7484	-125.4197	1988	August 2013 Cruise
46.7823	-125.26414	1027	August TGT 2013 Cruise
46.78243	-125.26348	1034	August TGT 2013 Cruise
46.78291	-125.26227	1068	August TGT 2013 Cruise
46.7830	-125.2642	1046	August TGT 2013 Cruise
46.7833	-125.26357	1051	August TGT 2013 Cruise
46.7840	-125.2617	1081	August TGT 2013 Cruise
46.83223683	-124.5639053	104.8	TN-177
46.83359017	-124.5851903	108.5	TN-177
46.83421017	-124.4989437	92	TN-177
46.83452517	-124.5212703	96	TN-177
46.8343335	-124.2698487	48.8	TN-177
46.83460183	-124.426177	78.3	TN-177
46.84064867	-124.6950912	135	TN-207
46.8457685	-124.493447	89.8	TN-177
46.8458035	-124.541202	98	TN-177
46.84592017	-124.5942737	108.4	TN-177
46.86965683	-124.5365737	95.2	TN-177
46.87982183	-124.8356628	157	TN-207
46.88116067	-124.8401718	156	TN-207
46.8813515	-124.8313675	157	TN-207
46.88135917	-124.8323212	158	TN-207
46.882515	-124.835823	160	TN-207
46.8850	-124.7770	154	Salmi et al plume
46.8851815	-124.7765198	154	TN-207
46.8852615	-124.7809317	152	TN-207
46.88584517	-124.776535	155	TN-207

46.88671117	-124.7778168	152	TN-207
46.89015583	-124.7851563	154	TN-207
46.89070133	-124.8447418	153	TN-207
46.8915185	-124.7173387	134	TN-177
46.8934885	-124.6180753	110	TN-177
46.89399717	-124.8124467	160	TN-207
46.898407	-124.8760452	180	TN-207
46.89974017	-124.6331537	112	TN-177
46.90524683	-124.6856587	123	TN-177
46.90913017	-124.8177643	162	TN-207
46.90996517	-124.5160503	88	TN-177
46.9155045	-124.89402	192	TN-207
46.91586517	-124.5150753	86	TN-177
46.9162635	-124.9029007	256	TN-207
46.91725683	-124.6611153	117	TN-177
46.91904833	-124.9265365	488	TN-207
46.91934967	-124.889183	171	TN-207
46.92648183	-124.5170303	84	TN-177
46.93190183	-124.5220803	83	TN-177
46.94059367	-124.955072	211	TN-207
46.9422263	-124.9574508	207	TN-207
46.944748	-124.9341355	193	TN-207
46.944973	-124.9338683	191	TN-207
46.9460945	-124.9168472	175	TN-207
46.9517135	-124.9161835	174	TN-207
46.9547996	-124.9203415	175	TN-207
46.955967	-124.9401932	205	TN-207
46.958908	-124.9442978	208	TN-207
46.96186067	-124.92099	175	TN-207
46.96381767	-124.9230118	177	TN-207
46.96704483	-124.9193343	169	TN-207
46.969952	-124.9413833	171	TN-207
46.97291183	-124.9643632	175	TN-207
46.97566	-124.9673615	184	TN-207
46.97640983	-124.9503173	170	TN-207
46.98126217	-124.970665	177	TN-207
46.983036	-124.9777527	245	TN-207
46.98417283	-124.961235	164	TN-207
46.98468783	-124.96241	164	TN-207
46.98811333	-124.948494	156	TN-207
46.98899083	-124.9443283	156	TN-207

46.989502	-124.941246	156	TN-207
46.99304583	-124.9636383	162	TN-207
46.9935875	-124.9745788	228	TN-207
46.993618	-124.9484787	154	TN-207
46.99165733	-124.9480515	154	TN-207
46.9942893	-124.9612732	159	TN-207
46.99447633	-124.943634	155	TN-207
46.99452583	-124.948288	154	TN-207
46.99496833	-124.9448472	154	TN-207
46.99518583	-124.9743652	191	TN-207
46.99518583	-124.9584275	156	TN-207
46.995369	-124.9658203	160	TN-207
46.99588017	-124.9485168	154	TN-207
46.99627683	-124.9391022	155	TN-207
46.9982033	-124.9443588	154	TN-207
46.998787	-124.9724578	173	TN-207
46.99883267	-124.9725265	173	TN-207
47.00130083	-124.971283	166	TN-207
47.00716517	-124.9574583	160	TN-207
47.007454	-124.966423	160	TN-207
47.0578	-125.0780	1396	fishing sonar plumes
47.0584	-125.0544	1253	fishing sonar plumes
47.0828	-125.0588	1113	fishing sonar plumes
47.0832	-125.0568	1111	fishing sonar plumes
47.2729635	-124.7195737	122	TN-177
47.38408517	-124.753087	133	TN-177
47.5763	-125.0677	306	fishing sonar plumes
47.5766	-125.0703	323	fishing sonar plumes
47.5772	-125.0706	320	fishing sonar plumes
47.5773	-125.0652	283	fishing sonar plumes
47.5774	-125.0720	328	fishing sonar plumes
47.5781	-125.0652	277	fishing sonar plumes
47.5788	-125.0662	285	fishing sonar plumes
47.5790	-125.0647	277	fishing sonar plumes
47.5791	-125.0660	277	fishing sonar plumes
47.5792	-125.0647	276	fishing sonar plumes
47.5792	-125.0647	274	fishing sonar plumes
47.5793	-125.0660	281	fishing sonar plumes
47.5828	-125.0588	235	fishing sonar plumes
47.5833	-125.0568	277	fishing sonar plumes
47.5840	-125.0544	277	fishing sonar plumes

47.8427	-125.2500	473	fishing sonar plumes
47.8437	-125.2497	470	fishing sonar plumes
47.8441	-125.2500	471	fishing sonar plumes
47.9220	-125.6532	560	fishing sonar plumes
47.9287	-125.6406	523	fishing sonar plumes
47.9298	-125.6393	533	fishing sonar plumes
47.9288	-125.6452	528	fishing sonar plumes
48.0278	-125.6627	402	fishing sonar plumes
48.0398	-125.6657	485	fishing sonar plumes
48.06697533	-124.9634803	98	TN-177
48.107377	-124.9781437	120	TN-177
48.6330	-126.9167	1300	Amnesiac Flare
48.7183	-126.9042	1350	Spinnaker Flare

References

Atwater, B.F., Musumi-Rokkaku, S., Satake, K., Tsuji, Y., Ueda, K., and Yamaguchi, D.K. (2005), The Orphan Tsunami of 1700, *U.S. Geol. Surv. Prof. Paper* 1707, 133 pp. 97, 7025-7041

Atwater, Brian F., Bobb Carson, Gary B. Griggs, H. Paul Johnson, and Marie S. Salmi. "Rethinking turbidite paleoseismology along the Cascadia subduction zone." *Geology* 42, no. 9 (2014): 827-830.

Bangs, N. L., Hornbach, M. J., & Berndt, C. (2011). The mechanics of intermittent methane venting at South Hydrate Ridge inferred from 4D seismic surveying. *Earth and Planetary Science Letters*, 310(1), 105-112.

Bangs, Nathan LB, Matthew J. Hornbach, and Christian Berndt. (2011) "The mechanics of intermittent methane venting at South Hydrate Ridge inferred from 4D seismic surveying." *Earth and Planetary Science Letters* 310, no. 1: 105-112.

Bayon, G., Henderson, G. M., & Bohn, M. (2009). U–Th stratigraphy of a cold seep carbonate crust. *Chemical Geology*, 260(1), 47-56.

Barnes, Chris R., Mairi MR Best, and Adam Zielinski. (2008) "The NEPTUNE Canada regional cabled ocean observatory." *Technology (Crayford, England)* 50: 3.

Berndt, C., Feseker, T., Treude, T., Krastel, S., Liebetrau, V., Niemann, H., ... & Steinle, L. (2014). Temporal constraints on hydrate-controlled methane seepage off Svalbard. *Science*, 343(6168), 284-287.

Bohrmann, Gerhard, Werner F. Kuhs, Stephan A. Klapp, Kirsten S. Techmer, Helmut Klein, M. Mangir Murshed, and Fritz Abegg. "Appearance and preservation of natural gas hydrate from Hydrate Ridge sampled during ODP Leg 204 drilling." *Marine Geology* 244, no. 1 (2007): 1-14.

Booth-Rea, G., Klaeschen, D., Grevemeyer, I., & Reston, T. (2008). Heterogeneous deformation in the Cascadia convergent margin and its relation to thermal gradient (Washington, NW USA). Tectonics, 27(4). Bottom-simulating reflectors by vertical fluid expulsion; *Journal of Geophysical Research* 1992;

Bowen, Gabriel J., Bianca J. Maibauer, Mary J. Kraus, Ursula Röhl, Thomas Westerhold, Amy Steimke, Philip D. Gingerich, Scott L. Wing, and William C. Clyde. (2015) "Two massive, rapid releases of carbon during the onset of the Palaeocene-Eocene thermal maximum." *Nature Geoscience* 8, no. 1: 44-47.

Bowen, Gabriel J., Timothy J. Bralower, Margareth L. Delaney, Gerald R. Dickens, Daniel C. Kelly, Paul L. Koch, Lee R. Kump et al. (2006) "Eocene hyperthermal event offers insight into greenhouse warming." *Eos, Transactions American Geophysical Union* 87, no. 17: 165-169.

Brothers, L. L., Van Dover, C. L., German, C. R., Kaiser, C. L., Yoerger, D. R., Ruppel, C. D., ... & Wagner, J. K. S. (2013). Evidence for extensive methane venting on the southeastern US Atlantic margin. *Geology*, 41(7), 807-810.

Carson, B., Holmes, M.L., Umstattd, K., Strasser, J.C., and Johnson, H.P., (1991). Fluid expulsion from the Cascadia accretionary prism: evidence from porosity distribution, direct measurements, and GLORIA Imagery. *Phi. Trans., R. Soc. London* 335, 331-340

Carson, B., Seke, E., Paskevich, V., and Holmes, M.L., (1994) Fluid expulsion site on the Cascadia accretionary prism: Mapping diagenetic deposits with processed GLORIA imagery: *Journal of Geophysical Research*, v. 99, no. B6, p. 11959–11969, doi: 10.1029/94JB00120.

Chapman, Ross, John Pohlman, Rick Coffin, Jeff Chanton, and Laura Lapham. (2004) "Thermogenic gas hydrates in the northern Cascadia Margin." *Eos, Transactions American Geophysical Union* 85, no. 38: 361-365.

Collier, R.W., and Lilley, M.D., (2005), Composition of methane seeps on the Cascadia continental margin: *Geophysical Research Letters*, v. 32, LO6609, doi: 10.1029 /2004GL022050.

Crutchley, Gareth J., Christian Berndt, Sebastian Geiger, Dirk Klaeschen, Cord Papenberg, Ingo Klaucke, Matthew J. Hornbach, Nathan LB Bangs, and Christine Maier. (2013) "Drivers of focused fluid flow and methane seepage at south Hydrate Ridge, offshore Oregon, USA." *Geology* 41, no. 5: 551-554.

Daigle, Hugh, Nathan L. Bangs, and Brandon Dugan. (2011) "Transient hydraulic fracturing and gas release in methane hydrate settings: A case study from southern Hydrate Ridge." *Geochemistry, Geophysics, Geosystems* 12, no. 12.

Davie, M. K., & Buffett, B. A. (2003). Sources of methane for marine gas hydrate: inferences from a comparison of observations and numerical models. *Earth and Planetary Science Letters*, 206(1), 51-63.

Goldfinger, Chris, Ann E. Morey, C. Hans Nelson, Julia Gutiérrez-Pastor, Joel E. Johnson, Eugene Karabanov, Jason Chaytor, Andrew Eriksson, and Shipboard Scientific Party. (2007) "Rupture lengths and temporal history of significant earthquakes on the offshore and north coast segments of the Northern San Andreas Fault based on turbidite stratigraphy." *Earth and Planetary Science Letters* 254, no. 1: 9-27.

Goldfinger, C., et al., 2012, Turbidite event history—Methods and implications for Holocene paleoseismicity of the Cascadia subduction zone: U.S. Geological Survey Professional Paper 1661-F, 170 p., http://pubs.usgs.gov/pp/pp1661f/.

Greinert, Jens, Yuriy Artemov, Viktor Egorov, Marc De Batist, and Daniel McGinnis. (2006) "1300-m-high rising bubbles from mud volcanoes at 2080m in the Black Sea: Hydroacoustic characteristics and temporal variability." *Earth and Planetary Science Letters* 244, no. 1: 1-15.

Greinert, Jens, and Daniel F. McGinnis. (2009) "Single bubble dissolution model–The graphical user interface SiBu-GUI." *Environmental Modelling & Software* 24, no. 8: 1012-1013.

Hautala, S. L., Solomon, E. A., Johnson, H. P., Harris, R. N., & Miller, U. K. (2014). Dissociation of Cascadia margin gas hydrates in response to contemporary ocean warming. *Geophysical Research Letters.*

He, T., Spence, G. D., Riedel, M., Hyndman, R. D., & Chapman, N. R. (2007). Fluid flow and origin of a carbonate mound offshore Vancouver Island: Seismic and heat flow constraints. *Marine Geology*, 239(1), 83-98.

Heeschen, Katja U., Anne M. Tréhu, Robert W. Collier, Erwin Suess, and Gregor Rehder. Distribution and height of methane bubble plumes on the Cascadia Margin characterized by acoustic imaging. *Geophysical Research Letters* 30, no. 12 (2003).

Heeschen, K.U., Collier, R.W., de Angelis, M.A., Suess, E., Rehder, G., Linke, P., and Klinkhammer, G.P., (2005), Methane sources, distributions, and fluxes from cold vent sites at Hydrate Ridge, Cascadia Margin: Global Biogeochemical Cycles, v. 19, GB2016, doi: 10.1029/2004GB002266.

Heesemann, Martin, Kim Juniper, Maia Hoeberechts, Marjolaine Matabos, Steven Mihaly, Martin Scherwath, and Richard Dewey. (2013) "Ocean Networks Canada: Live Sensing

of a Dynamic Ocean System." In *EGU General Assembly Conference Abstracts*, vol. 15, p. 6625.

Holbrook, W. S., Kent, G., Keranen, K., Johnson, H. P., Trehu, A., Tobin, H., ... & Beeson, J. (2012). Cascadia fore arc seismic survey: Open-access data available. Eos, Transactions American Geophysical Union, 93(50), 521-522.

Hornbach, Matthew J., Nathan L. Bangs, and Christian Berndt. "Detecting hydrate and fluid flow from bottom simulating reflector depth anomalies." (2012) *Geology* 40, no. 3: 227-230.

Hyndman, R. D., et al. "Tectonic sediment thickening, fluid expulsion, and the thermal regime of subduction zone accretionary prisms: The Cascadia margin off Vancouver Island." (1993) Journal of Geophysical Research: Solid Earth (1978–2012) 98.B12: 21865-21876.

Hyndman, Roy D. "Downdip landward limit of Cascadia great earthquake rupture." *Journal of Geophysical Research: Solid Earth* 118, no. 10 (2013): 5530-5549.

Johnson, H. P., Solomon, E. A., Harris, R. N., Salmi, M. S., & Berg, R. D. (2013). Heat Flow and Fluid Flux in Cascadia's Seismogenic Zone. *Eos, Transactions American Geophysical Union*, *94*(48), 457-458.

Johnson, J. E., Goldfinger, C., & Suess, E. (2003). Geophysical constraints on the surface distribution of authigenic carbonates across the Hydrate Ridge region, Cascadia margin. Marine Geology, 202(1), 79-120.

Joseph, C., Campbell, K. A., Torres, M. E., Martin, R. A., Pohlman, J. W., Riedel, M., & Rose, K. (2013). Methane-derived authigenic carbonates from modern and paleoseeps on the Cascadia margin: Mechanisms of formation and diagenetic signals. Palaeogeography, Palaeoclimatology, Palaeoecology, 390, 52-67.

Kannberg, P. K., Tréhu, A. M., Pierce, S. D., Paull, C. K., & Caress, D. W. (2013). Temporal variation of methane flares in the ocean above Hydrate Ridge, Oregon. Earth and Planetary Science Letters, 368, 33-42.

Lapham, L., Wilson, R., Riedel, M., Paull, C. K., & Holmes, M. E. (2013). Temporal variability of in situ methane concentrations in gas hydrate-bearing sediments near Bullseye Vent, Northern Cascadia Margin. *Geochemistry, Geophysics, Geosystems*, 14(7), 2445-2459.

Leifer, I., Culling, D., 2010. Formation of seep bubble plumes in the Coal Oil Point seep field. Geo-Marine Letters, 30, 339-353.

Leifer, Ira, Bruce P. Luyendyk, Jim Boles, and Jordan F. Clark. (2006) "Natural marine seepage blowout: Contribution to atmospheric methane." *Global Biogeochemical Cycles* 20, no. 3.

Leifer, I., & Patro, R. K. (2002). The bubble mechanism for methane transport from the shallow sea bed to the surface: A review and sensitivity study. *Continental Shelf Research*, 22(16), 2409-2428.

Li, H. L., He, T., & Spence, G. D. (2014). North Cascadia heat flux and fluid flow from gas hydrates: Modeling 3-D topographic effects. *Journal of Geophysical Research: Solid Earth*, 119(1), 99-11

Liu, Xiaoli, and Peter B. Flemings. (2006) "Passing gas through the hydrate stability zone at southern Hydrate Ridge, offshore Oregon." *Earth and Planetary Science Letters* 241, no. 1: 211-226.

MacKay, M. E., Moore, G. F., Cochrane, G. R., Casey Moore, J., & Kulm, L. D. (1992). Landward vergence and oblique structural trends in the Oregon margin accretionary prism: Implications and effect on fluid flow. *Earth and Planetary Science Letters*, 109(3), 477-491.

Malinverno, A., Kastner, M., Torres, M. E., & Wortmann, U. G. (2008). Gas hydrate occurrence from pore water chlorinity and downhole logs in a transect across the northern Cascadia margin (Integrated Ocean Drilling Program Expedition 311). *Journal of Geophysical Research: Solid Earth (1978–2012), 113*(B8).

Mandal, R., Dewangan, P., Ramprasad, T., Kumar, B. J. P., & Vishwanath, K. (2014). Effect of thermal non-equilibrium, seafloor topography and fluid advection on BSR-derived geothermal gradient. *Marine and Petroleum Geology.*

Martin, R. A., Nesbitt, E. A., & Campbell, K. A. (2007). Carbon stable isotopic composition of benthic foraminifera from Pliocene cold methane seeps, Cascadia accretionary margin. *Palaeogeography, Palaeoclimatology, Palaeoecology*, 246(2), 260-277.

McNeill, L.C., Piper, K.A., Goldfinger, C., Kulm, L.D., and Yeats, R.S., (1997), Listric normal faulting on the Cascadia continental margin: *Journal of Geophysical Research*, v. 102, no. B6, p. 12123–12138, doi: 10.1029 /97JB00728.

Moore, J. C., Brown, K. M., Horath, F., Cochrane, G., MacKay, M., & Moore, G. (1991). Plumbing accretionary prisms: effects of permeability variations. *Philosophical Transactions of the Royal Society of London. Series A: Physical and Engineering Sciences,* 335(1638), 275-288.

Moore, J. Casey, and Peter Vrolijk. (1992) "Fluids in accretionary prisms." *Reviews of Geophysics* 30, no. 2: 113-135.

Nesbitt, E. A., Martin, R. A., & Campbell, K. A. (2013). New records of Oligocene diffuse hydrocarbon seeps, northern Cascadia margin. *Palaeogeography, Palaeoclimatology, Palaeoecology,* 390, 116-129.

Orange, Daniel L., Brian G. McAdoo, J. Casey Moore, Harold Tobin, Elizabeth Screaton, Hank Chezar, Homa Lee, Mark Reid, and Rick Vail. (1997) "Headless submarine canyons and fluid flow on the toe of the Cascadia accretionary complex." *Basin Research* 9, no. 4: 303-312.

Phrampus, B. J., & Hornbach, M. J. (2012). Recent changes to the Gulf Stream causing widespread gas hydrate destabilization. *Nature*, 490(7421), 527-530.

Phrampus, B. J., Hornbach, M. J., Ruppel, C. D., & Hart, P. E. (2014). Widespread gas hydrate instability on the upper US Beaufort margin. *Journal of Geophysical Research: Solid Earth.*

Riedel, M. (2007). 4D seismic time-lapse monitoring of an active cold vent, northern Cascadia margin. *Marine Geophysical Researches*, 28(4), 355-371.

Riedel, Michael, Ivana Novosel, George D. Spence, Roy D. Hyndman, Ross N. Chapman, Richard C. Solem, and Trevor Lewis. (2006) "Geophysical and geochemical signatures associated with gas hydrate–related venting in the northern Cascadia margin." *Geological Society of America Bulletin* 118, no. 1-2: 23-38.

Riedel, M., Spence, G. D., Chapman, N. R., & Hyndman, R. D. (2001). Deep-sea gas hydrates on the northern Cascadia margin. *The Leading Edge*, 20(1), 87-109.

Riedel, M., Tréhu, A. M., & Spence, G. D. (2010). Characterizing the thermal regime of cold vents at the northern Cascadia margin from bottom-simulating reflector distributions, heat-probe measurements and borehole temperature data. *Marine Geophysical Researches,* 31(1-2), 1-16.

Ritger, S., Carson, B., and Suess, E., (1987), Methane-derived authigenic carbonates formed by subduction-induced pore-water expulsion along the Oregon/Washington margin:

Geological Society of America Bulletin, v. 98, p. 147–156, doi: 10.1130/0016-7606(1987)98<147MACFBS>2.0.CO;2.

Romer, M., Sahling, H., Pape, T., Bohrmann, G., Spiess, V., 2012. Quantification of gas bubble emissions from submarine hydrocarbon seeps at the Makran continental margin (offshore Pakistan). J. Geophys. Res.-Oceans, 117, doi:10.1029/2011JC007424.

Römer, Miriam, Heiko Sahling, Thomas Pape, André Bahr, Tomas Feseker, Paul Wintersteller, and Gerhard Bohrmann. (2012) "Geological control and magnitude of methane ebullition from a high-flux seep area in the Black Sea—the Kerch seep area." *Marine Geology* 319: 57-74.

Ryan, W.B.F., S.M. Carbotte, J.O. Coplan, S. O'Hara, A. Melkonian, R. Arko, R.A. Weissel, V. Ferrini, A. Goodwillie, F. Nitsche, J. Bonczkowski, and R. Zemsky (2009), Global Multi-Resolution Topography synthesis, *Geochem. Geophys. Geosyst.* 10, Q03014, doi: 10.1029/2008GC002332.

Saffer, D. M. "The permeability of active subduction plate boundary faults." *Geofluids* (2014).

Salmi, M. S., Johnson, H. P., Leifer, I., & Keister, J. E. (2011). Behavior of methane seep bubbles over a pockmark on the Cascadia continental margin. *Geosphere*, 7(6), 1273-1283.

Satake, K., & Atwater, B. F. (2007). Long-term perspectives on giant earthquakes and tsunamis at subduction zones. *Annu. Rev. Earth Planet. Sci.*, 35, 349-374.

Sauter, Eberhard J., Sergey I. Muyakshin, Jean-Luc Charlou, Michael Schlüter, Antje Boetius, Kerstin Jerosch, Ellen Damm, Jean-Paul Foucher, and Michael Klages. (2006) "Methane discharge from a deep-sea submarine mud volcano into the upper water column by gas hydrate-coated methane bubbles." *Earth and Planetary Science Letters* 243, no. 3: 354-365.

Schneider von Deimling, Jens, and Cord Papenberg. (2012) "Detection of gas bubble leakage via correlation of water column multibeam images." *Ocean Science* 8, no. 2: 175-181.

Schneider von Deimling,J., G. Rehder, J. Greinert, D.F. McGinnnis, A. Boetius, P. Linke, Quantification of seep-related methane gas emissions at Tommeliten, North Sea, Continental Shelf Research, Volume 31, Issues 7–8, 15 May 2011, Pages 867-878

Shi, Y., & Wang, C. Y. (1994). Model studies of advective heat flow associated with compaction and dehydration in accretionary prisms. *Journal of Geophysical Research: Solid Earth* (1978–2012), 99(B5), 9319-9325.

Skarke, A., C. Ruppel, M. Kodis, D. Brothers, and E. Lobecker. (2014) "Widespread methane leakage from the sea floor on the northern US Atlantic margin." *Nature Geoscience*.

Sluijs, Appy, Stefan Schouten, Mark Pagani, Martijn Woltering, Henk Brinkhuis, Jaap S. Sinninghe Damsté, Gerald R. Dickens et al. (2006) "Subtropical Arctic Ocean temperatures during the Palaeocene/Eocene thermal maximum." *Nature* 441, no. 7093: 610-613.

Solomon, E.A., Kastner, M., Jannasch, H., Weinstein, Y., Robertson, G., (2008). Dynamic fluid flow and chemical fluxes associated with a seafloor gas hydrate deposit on the northern Gulf of Mexico slope, *Earth and Planetary Science Letters,* 270 (1-2), 95-105.

Suess, E., Torres, M.E., Bohrmann, G., Collier, R.W., Greinert, J., Linke, P., Rehder, G., Trehu, A., Wallmann, K., Winkler, G., Zuleger, E., 1999. Gas hydrate destabilization: enhanced dewatering, benthic material turnover and large methane plumes at the Cascadia convergent margin. Earth Planet. Sci. Lett. 170, 1-15.

Suess, Erwin, M. E. Torres, G. Bohrmann, R. W. Collier, D. Rickert, C. Goldfinger, Peter Linke et al. (2001) "Sea floor methane hydrates at Hydrate Ridge, Cascadia margin." *Natural gas hydrates: occurrence, distribution, and detection*: 87-98.

Teichert, B.M.A., Eisenhauer, A., Bohrmann, G., Haase-Schramm, A., Bock, B., Linke, P. (2003). U/Th systematics and ages of authigenic carbonates from Hydrate Ridge, Cascadia convergent margin: recorders of fluid composition and sealevel changes. Geochimica et Cosmochimica Acta, 67, 3845-3857.

Thomsen, L., Barnes, C., Best, M., Chapman, R., Pirenne, B., Thomson, R., & Vogt, J. (2012). Ocean circulation promotes methane release from gas hydrate outcrops at the NEPTUNE Canada Barkley Canyon node. *Geophysical Research Letters*, 39(16).

Torres, M. E., Klaus Wallmann, A. M. Tréhu, Gerhard Bohrmann, W. S. Borowski, and H. Tomaru. (2004) "Gas hydrate growth, methane transport, and chloride enrichment at the southern summit of Hydrate Ridge, Cascadia margin off Oregon." *Earth and Planetary Science Letters* 226, no. 1: 225-241.

Torres, M. E., Ann M. Trehu, N. Cespedes, M. Kastner, U. G. Wortmann, J-H. Kim, P. Long et al. (2008) "Methane hydrate formation in turbidite sediments of northern Cascadia, IODP Expedition 311." *Earth and Planetary Science Letters* 271, no. 1: 170-180.

Torres, M.E., Embley, R.W., Merle, S.G., Trehu, A.M.,Collier, R.W., Suess, E., and Heeschen, K.U., (2009), Methane sources feeding cold seeps on the shelf and upper continental slope off central Oregon, USA:*Geochemistry Geophysics Geosystems*, v. 10, no. 11,Q11003, doi: 10.1029/2009GC002518.

Trehu, A. M., Long, P. E., Torres, M. E., Bohrmann, G. R. R. F., Rack, F. R., Collett, T. S., ... & Weinberger, J. L. (2004). Three-dimensional distribution of gas hydrate beneath southern Hydrate Ridge: constraints from ODP Leg 204. *Earth and Planetary Science Letters*, 222(3), 845-862.

Trehu, Anne Martine, Marta E. Torres, G. Bohrmann, and Frederick Colwell. " (2006) Leg 204 synthesis: Gas hydrate distribution and dynamics in the central Cascadia accretionary complex.".

Tryon, M.D., Brown, K.M., and Torres, M.E., (2002), Fluid and chemical flux in and out of sediments hosting methane hydrate deposits on Hydrate Ridge, OR, II: Hydrological processes*: Earth and Planetary Science Letters*, v. 201, p. 541–557, doi: 10.1016/S0012-821X (02)00732-X.

Wang, K. (1994). Kinematic models of dewatering accretionary prisms. *Journal of Geophysical Research: Solid Earth* (1978–2012), 99(B3), 4429-4438.

Wang, K., Hyndman, R. D., & Davis, E. E. (1993). Thermal effects of sediment thickening and fluid expulsion in accretionary prisms: Model and parameter analysis. *Journal of Geophysical Research: Solid Earth* (1978–2012), 98(B6), 9975-9984.9

Wright, James D., and Morgan F. Schaller. (2013) "Evidence for a rapid release of carbon at the Paleocene-Eocene thermal maximum." *Proceedings of the National Academy of Sciences* 110, no. 40: 15908-15913.

Zachos, James C., Ursula Röhl, Stephen A. Schellenberg, Appy Sluijs, David A. Hodell, Daniel C. Kelly, Ellen Thomas et al. (2005) "Rapid acidification of the ocean during the Paleocene-Eocene thermal maximum." *Science* 308, no. 5728: 1611-1615.

POST-EXPEDITION RESULTS

Preface

The work conducted pre-expedition provided the essential combination of high-resolution maps of the gas hydrate system with a clearly-defined edge of methane hydrate stability, strong constraints on the degree of bottom water warming along the upper continental slope of the Washington margin over the past 40 years, multi- and single-beam sonar evidence of enhanced methane seepage near the upper limit of methane hydrate stability, and numerical simulations of the downslope retreat of the methane hydrate stability zone over the period of historical warming, all of which were important in guiding the systematic geochemical and geophysical survey of methane seepage during the research expedition. The goal of the field program was to test and better understand the response of the upper limit of methane hydrate stability to contemporary warming of bottom water. We conducted the systematic survey of methane emissions along this climate-sensitive margin corridor during a 10-day field program from the 10-19 October 2014 on the *R/V Thompson*. The field program consisted of an along margin multi-beam sonar survey of methane seepage, traditional coring and pore water sampling, water column sampling, and heat flow measurements with the primary goal of characterizing the source of fluid and methane emissions and their relationship to contemporary intermediate bottom water warming along the margin.

The results of this field program and post-expedition geochemical and geophysical analyses are presented in this section. This work related to Tasks 7-12 in the original proposal, represents a significant portion of Theresa Whorley's M.Sc. thesis at the University of Washington, and has been published an is in preparation for publication in the following two citations:

Whorley, T.L.*, Solomon, E.A., Philip, B.T., Torres, M.E., Johnson, H.P., 2017. Investigating the response of methane hydrates to modern bottom water warming along the upper continental slope of the Cascadia margin, Paper, 9th International Conference on Gas Hydrates, Denver, CO, USA.

Whorley, T.L.*, Solomon, E.A., Philip, B.T., Johnson, H.P., *in prep*. Investigating the response of methane hydrates to modern bottom water warming along the upper continental slope of the Cascadia margin, *Earth Planet. Sci. Lett.*

Introduction

Gas hydrates are stable at moderate pressures and low temperatures, and are pervasive in sediments at continental margins worldwide. Estimates of methane carbon stored in the global gas hydrate reservoir vary by orders of magnitude (Kvenvolden, 1988; Macdonald, 1990; Holbrook et al., 1996; Milikov, 2004), with 1.7×10^3 Gt C near the low-end (Archer et al., 2009) and 6.4×10^4 Gt C at the high-end (Klauda and Sandler, 2005). In spite of the uncertainty in the absolute size of the global hydrate inventory, they represent one of the largest reservoirs of organic carbon on Earth. Globally, an estimated 99% of the hydrate reservoir is in continental margin sediments at water depths below 300-500 m, with the remaining 1% in high-latitude, permafrost-bearing sediments (Fig. 1; Collett et al., 2009; Ruppel, 2011). The majority of the marine gas hydrate reservoir occurs at mid- to low- latitudes at concentrations of ~1-5% of the pores of fine-grained clays, but can exceed 20-80% in some settings (e.g. sands and fractured clays; Boswell and Collett, 2006; 2011).

As a result of the positive seafloor geothermal gradient, gas hydrates are present only within the first few hundred meters of continental slope sediments. The upper limit of gas hydrate stability in the marine environment is governed by the prevailing pressure and temperature conditions and terminates on the upper continental slope at water depths of 300 to 500 meters worldwide. This up-slope limit of gas hydrate stability represents one of the most climate-sensitive boundaries in the global hydrocarbon reservoir. Compared to other climate-sensitive gas hydrate accumulations, including thinning permafrost in the Arctic, upper continental slope hydrates are located adjacent to actively circulating seawater. This close association permits hydrate dissociation over relatively short timescales in response to modest warming of seawater at intermediate depths; i.e., years vs 10^2 to 10^3 years for other climate sensitive deposits.

There has been a significant amount of recent work investigating the impact of ocean warming on methane hydrate reservoirs (e.g. Phrampus and Hornbach, 2012; Weinstein et al., 2016; Skarke et al., 2014; Berndt et al., 2014; Biastoch et al., 2011; Westbrook et al., 2009; Hautala et al., 2014), but these have mainly been modeling studies or based on the association of methane seeps with the upper limit of methane hydrate stability and have not documented active methane hydrate dissociation from direct sampling. Documenting the potential dissociation of upper continental slope methane hydrates as a result of contemporary bottom water warming is critical as these reservoirs may release methane to the overlying ocean where it is oxidized to CO_2, contributing to ocean acidification, and may potentially reach the atmosphere where methane is a potent greenhouse gas. The release of methane into the ocean and atmosphere has been posited as a potential feedback to modern climate change and invoked as a possible positive feedback to previous warming periods in Earth's history (Dickens et al., 1995; Kennett et al., 2003). Recent studies undertaken to examine the response of methane hydrate to modern ocean warming have focused primarily on the Arctic region (e.g. Reagan et al., 2011; Biastoch et al., 2011; Thatcher et al., 2013) with less attention given to intermediate latitude reservoirs (Phrampus and Hornbach, 2012; Weinstein et al., 2016; Skarke et al., 2014; Hautala et al., 2014).

A recent analysis of archive bottom water temperature data along the Washington margin collected over the past four decades shows a gradual warming trend at the upper limit of methane hydrate stability (Hautala et al., 2014). Thermal propagation simulations based on these bottom water records indicate that the MHSZ has retreated downslope by ~1-2 km (~40 m water depth) since the 1970s (Hautala et al., 2014). With global temperatures forecasted to continue rising (Zachos et al., 2008), it is critical to understand the current response of the marine methane hydrate reservoir to bottom water warming at the upper limit of stability, and the biogeochemical response to methane hydrate dissociation at this and other margins.

Retreat of the methane hydrate stability zone of the magnitude suggested by Hautala et al. (2014) has the potential to release a significant amount of methane into the sediment column and possibly the water column, but there is currently no direct evidence that methane hydrate dissociation is occurring. Johnson et al. (2015) documented 168 bubble plumes from archive sonar data spanning the length of the Cascadia margin to investigate whether seep distribution on the margin clusters at the depth of the current upper limit of hydrate stability. These data were compiled from a range of investigations including those identified by fishermen using single beam echosounders. Based on a statistical analysis of this incomplete dataset, bubble plumes are more concentrated along the predicted upper limit of hydrate stability, though other natural mechanisms of fluid and gas expulsion could not be disregarded. In addition, an Ocean Exploration Trust Expedition in 2016 on the *R/V Nautilus* conducted a water column sonar survey spanning Astoria

Canyon to northern California and documented an additional >400 bubble plumes near the upper limit of methane hydrate stability (Embley et al., 2016).

Since the Washington margin has experienced bottom water warming at the upper limit of methane hydrate stability over the past ~40 years and there is circumstantial evidence for enhanced methane emissions within this depth interval, the Washington margin is an ideal location to better understand the effects of modern bottom water warming on the upper limit of methane hydrate stability, specifically the flux and sinks of methane associated with active hydrate dissociation and the significance of contemporary hydrate dynamics to marine biogeochemical cycles. This study seeks to constrain the extent of active methane hydrate dissociation along the vulnerable upper limit of stability along the Washington (WA) sector of the Cascadia margin through the use of geochemical tracers and to work toward an understanding of the regional biogeochemical impacts of methane hydrate dissociation in response to modern and future ocean warming.

Geochemical Tracers of Methane Hydrate Dynamics and Sediment Diagenesis

Chloride is a conservative element in low temperature pore water and can be used to trace the addition and removal of water within the shallow sediment column. The formation of gas hydrate and clays will remove water from the surrounding pore space and increase the chloride concentration in the residual pore water. Addition of water from dissociation of hydrate, clay dehydration at depth, and deeper metamorphic reactions, serve to decrease the concentration of chloride in pore water. Chloride concentrations alone cannot distinguish what process is driving the addition or removal of water, therefore other solutes and isotope ratios must be investigated. The formation of the hydrate structure fractionates water isotopes and preferentially incorporates the heavier isotopes of oxygen and hydrogen into the structure (Heese and Harrison, 1981). This process leaves the surrounding pore water depleted of ^{18}O and ^{2}H (or deuterium, D). Hydrate dissociation releases these heavier isotopes back into the surrounding pore space, increasing $\delta^{18}O$ and δD values with respect to seawater (Figure 1). Clay dehydration releases heavy oxygen and light hydrogen, thus decreasing the δD value and increasing $\delta^{18}O$ in pore water. By examining both chloride concentrations and the stable isotopes of oxygen and hydrogen, methane hydrate formation and dissociation can be distinguished from clay formation and dehydration.

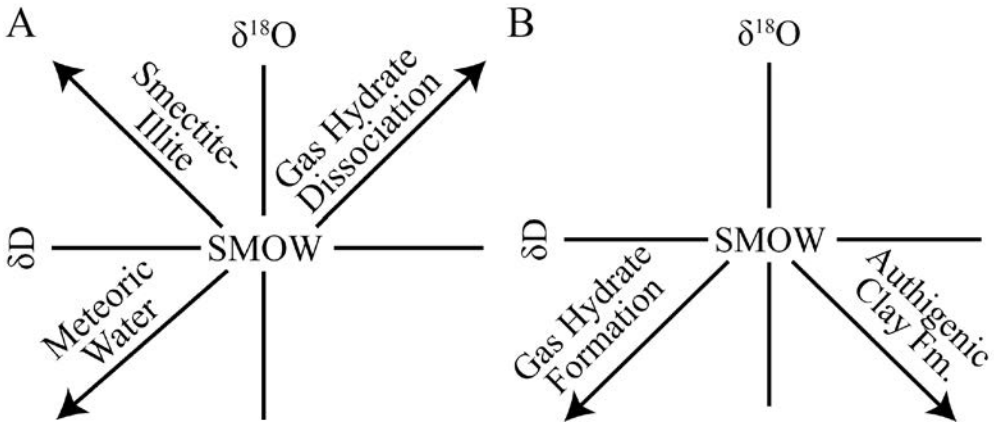

Figure 1. Schematic diagrams of expected pore water trends in $\delta^{18}O$ and δD when chloride concentrations (A) increase and (B) decrease with respect to seawater.

Pore water sulfate (SO_4^{2-}) is another important chemical parameter that provides insight into methane dynamics. Dissolved sulfate is a major electron acceptor for the oxidation of particulate organic carbon (POC) (reaction 1). Methane is microbially produced through fermentation of POC and CO_2 -reduction after sulfate has been consumed in the sediment column (Claypool and Kaplan, 1974). This shift in dominant microbial metabolism is referred to as the sulfate-methane transition zone (SMTZ). The anaerobic oxidation of methane (AOM) is a microbially-mediated reaction that occurs in the zone where downward diffusing sulfate meets upward diffusing methane according to the relationship shown in reaction 2.

$$CH_2O + SO_4^{2-} \rightarrow 2HCO_3^- + H_2S + H_2O \quad (1)$$
$$CH_4 + SO_4^{2-} \rightarrow HS^- + HCO_3^- + H_2O \quad (2)$$

The production of bicarbonate (HCO_3^-) through reactions 1 and 2 contributes to alkalinity and DIC of the pore water and can react with dissolved calcium and magnesium to precipitate authigenic carbonate minerals. Tracking the δ^{13}C-DIC values in combination with SO_4, DIC, NH_4, and alkalinity can help constrain the distribution and rates of sulfate reduction through POC oxidation, AOM, and methanogenesis. Pore water SO_4 gradients, and in particular kinked profiles, can be used to indicate non-steady state system behavior. Kinked sulfate profiles can be the results of a variety of factors including changes in sedimentation rates or changes in methane fluxes. Thus, numerical modeling of the solute profiles combined with knowledge of the sedimentation history at a particular site can be used to constrain past changes in methane fluxes.

The concentrations of major and minor elements of seawater are informative of several *in situ* diagenetic reactions that commonly occur in margin settings, including ion exchange, volcanic ash alteration, microbial metabolic reactions, carbonate precipitation/dissolution, and silicate weathering as well as deep-sourced fluid production through clay dehydration. In addition, the concentrations of Li, K, and B are useful tracers of fluid-rock reactions and geothermometers, with each having a specific range in threshold temperatures of partitioning into the solid or fluid. Dissolved Si concentrations provide information on fluid-rock equilibria and fluid sources.

Noble gases preferentially fractionate upon entering the hydrate structure (Barrer and Edge, 1967). Experimental studies have shown that heavier noble gases, such as Kr and Xe, are preferentially incorporated into the hydrate structure while lighter noble gases are rejected (Barrer and Edge, 1967) and may serve as a means of distinguishing methane released to the ocean from hydrate dissociation (e.g. Hunt et al., 2013). Field-based studies to examine the usefulness of this relationship on natural gas hydrate samples from Blake Ridge (Dickens and Kennedy, 2000) and Hydrate Ridge (Winckler et al., 2002) have been plagued by contamination, among other issues. However, the formation and dissociation of hydrate should measurably alter the ratios of each of these gases in the expelled seep fluid, acting as a conservative chemical tracer for gas hydrate dynamics.

The 2014 Field Program and Sampling

We conducted a 10-day research expedition on the *R/V Thompson* from 10-19 October 2014 to test whether there is active methane hydrate dissociation within the predicted depth range of methane hydrate retreat from the numerical thermal propagation simulations based on the historical record of bottom water warming along the upper continental slope of the Washington margin (Hautala et al., 2014). An along-margin multi-beam sonar survey was conducted using a Kongsberg EM 302 on the *R/V Thompson* from 48°N to 46°N (Figure 2). The survey focused on

cataloguing bubble plumes between 470 – 520 meters below sea level (mbsl) to adequately capture the upper limit of hydrate stability where methane hydrate should be dissociating in response to bottom water warming (Hautala et al., 2014). We imaged 18 bubble plumes from 7 newly discovered active seep sites within this predicted depth range (Figure 3). Plumes commonly rose approximately 200 meters above seafloor, with at least one extending to within 50 meters of the sea surface. A description of each of the seep sites including new seafloor bathymetry is provided in Appendix I.

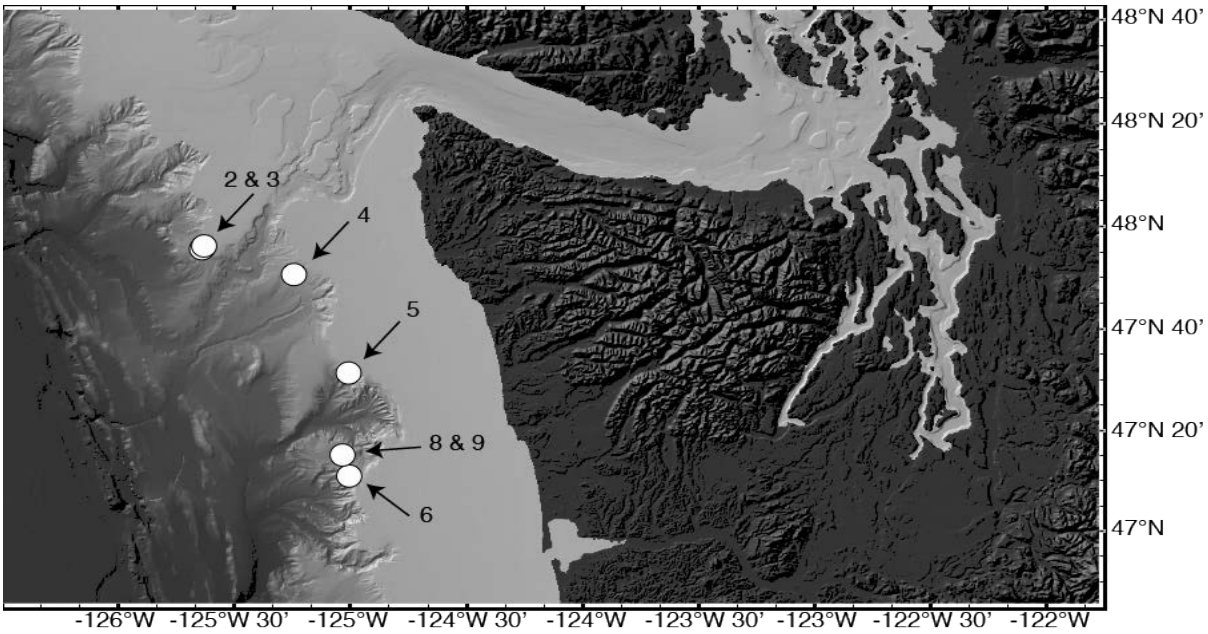

Figure 2. Locations of sampled seep sites along the WA margin within the upper limit of methane hydrate stability.

Twenty-two gravity cores and 20 CTD/hydrocasts were collected at active seep sites and background locations for geochemical analysis. A summary of the locations of gravity core and CTD deployments at each site is presented in Appendix I, and a full desciription of the subseafloor temperature and thermal conductivity measurements is presented in Appendix II. Gravity cores (GC) were sectioned into 5-10 cm lengths immediately after recovery. Pore water was extracted with titanium squeezers under hydraulic press and passed through disposable 0.45 μm syringe filters before being portioned into sampling vials appropriate for various analyses. A 3 cm^3 sediment plug was collected from each pore water whole-round, and the sediment plug was placed into a 20 cm^3 headspace vial that was pre-flushed with ultra-high purity N_2 and filled with 10 ml of degassed KCl solution and glass beads. After placing the sediment plug into the bottle, it was capped with a butyl rubber stopper and sealed with an Al crimp cap and stored inverted until shore-based analysis.

Analytical Methods

Salinity and alkalinity were measured immediately after pore water extraction by means of optical refractometry and Gran titration with 0.1 M HCl, respectively. Chloride concentrations were evaluated onshore via Mohr titration with silver nitrate and sample concentrations reported are based on no fewer than duplicate analysis with a precision <0.2%. Concentrations were

evaluated by comparison to International Association of Physical Sciences of the Ocean (IAPSO) standard seawater. Pore water aliquots for sulfate analyses were portioned into centrifuge tubes and preserved with a zinc acetate solution to precipitate any present sulfide as zinc-sulfide. These samples were analyzed on a Metrohm 882 Compact Ion Chromatograph with sample concentrations compared to dilutions of IAPSO. The precision of sulfate analyses was <1.5%.

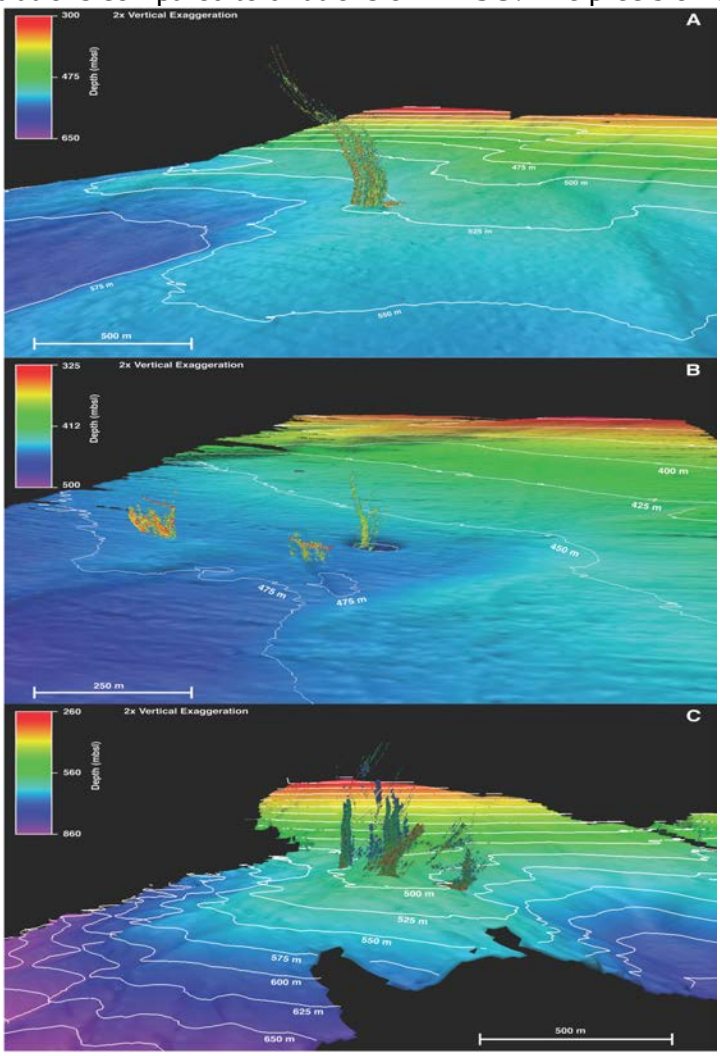

Figure 3. Multi-beam sonar images of (A) Site 2, (B) Site 4, and (C) Site 6.

Pore water oxygen and hydrogen stable isotope samples were preserved immediately on board in flame-sealed 2-mL glass ampules. These samples were analyzed on a Picarro cavity ring-down spectrometer water analyzer. Results are reported in standard δ notation relative to Vienna Standard Mean Ocean Water (VSMOW), where

$$\delta(‰) = \left[\frac{R_{sample} - R_{standard}}{R_{standard}}\right] * 1000$$

and R represents the ratio of $^{18}O/^{16}O$ and D/H ratios of samples and standards. The precision of analysis of $\delta^{18}O$ and δD was <1.8% and <2.6%, respectively. Aliquots for analysis of the stable carbon isotope ratio of dissolved inorganic carbon ($\delta^{13}C$-DIC) were first poisoned shipboard with

mercuric chloride and analyzed via isotope-ratio mass spectrometry (IRMS) on a Delta V Mass Spec/Gas Bench at Oregon State University. All stable isotope data is reported in the standard δ notation relative to Vienna Pee Dee Belemnite (VPDB) with an analytical precision of <2.2%.

Pore water samples for major and minor elemental analysis were pre-acidified shipboard with trace metal grade HNO_3. Samples for major element analysis were prepared in a 1:100 dilution with a 1% HNO_3 solution and measured via inductively-coupled plasma optical-emission spectrometry (ICP-OES) on a Perkin-Elmer 8300 ICP-OES at the University of Washington. Precision of the Ca, Mg, K, and Na analyses were <1%, <1%, <1.8%, and <2%, respectively. Minor element analysis was performed at Oregon State University using a Leeman Labs Prodigy ICP-OES. Samples were prepared as 1:20 and 1:100 dilutions using a 1% HNO_3 solution. Precision of Li, B, and Sr were <3%, <3.3%, and <1.8%, respectively.

The sediment headspace samples were analyzed for acetylene, n-butane, ethane, ethylene, methane, methyl acetylene, propane, and propylene on an SRI 8610 gas chromatograph equipped with a flame ionization detector. The headspace gas samples were passed through a Restek MXT-1 pre-column and a Restek RT Alumina analytical column, and calibration was based on dilutions of Air Liquide calibration gas standards. Only the n-alkane data is presented here. The percent precision of the methane, ethane, propane, and n-butane analyses, based on repeated analysis of multiple check standards was <2.5%. The accuracy of the analyses based on the percent difference of the measured concentrations of multiple check standards was <3%. The detection limit for n-alkanes was 0.3 ppmv and the quantification limit was 0.5 ppmv.

Water column samples for noble gas analysis were collected directly above active vent locations during CTD/hydrocasts in an effort to capture the purest unaltered fluid. These samples were sub-sampled under a vacuum and preserved in duplicate. The analysis of Ne, Kr, and Xe were conducted at the University of Washington following the methods of Emerson et al. (1999). Values presented here are percentages of *in situ* saturation for Ne, Kr, and Xe with respect to Ar.

Site	Sample ID	methane (ppmv)	ethane (ppmv)	propane (ppmv)	n-butane (ppmv)
6	H200	9767	-	-	0.90
2	H17	8036	-	-	<0.5
4	H118	6797	3.95	<0.5	<0.5
4	H120	6911	2.46	<0.5	<0.5
4	H122	7357	2.71	<0.5	<0.5
4	H138	7782	4.37	<0.5	<0.5
4	H139	4627	2.40	<0.5	0.70
4	H141	2880	1.85	<0.5	<0.5
5	H158	11447	3.36	0.7	<0.5
5	H160	12811	4.71	<0.5	<0.5
5	H162	22264	2.17	<0.5	<0.5
8	H273	4538	<0.5	<0.5	-
8	H275	9157	<0.5	<0.5	-
8	H286	6535	0.85	<0.5	-
8	H284	6708	0.44	<0.5	-

Table 1. Headspace methane, ethane, propane, and n-butane concentrations from gravity core pore water whole rounds collected below the sulfate-methane transition zone at each site. Methane comprises >99% of the hydrocarbons present at each of the seep sites. A dash indicates the component was not detected.

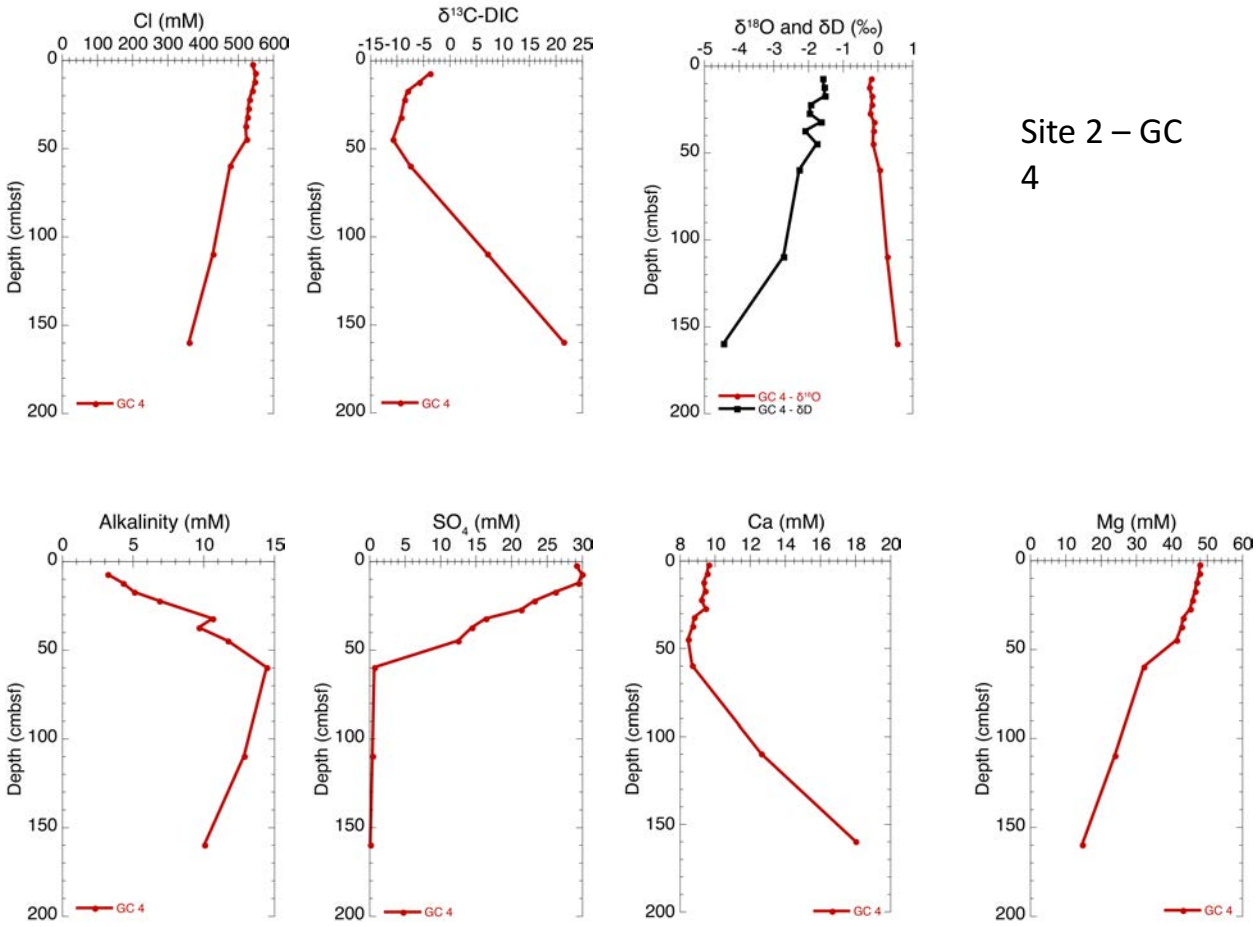

Site 2 – GC 4

Figure 4. Pore water Cl, δ^{13}C-DIC, δ^{18}O, δD, alkalinity, SO_4, Ca, and Mg from Gravity Core 4 at Site 2. For location of gravity cores at each site, refer to Appendix I.

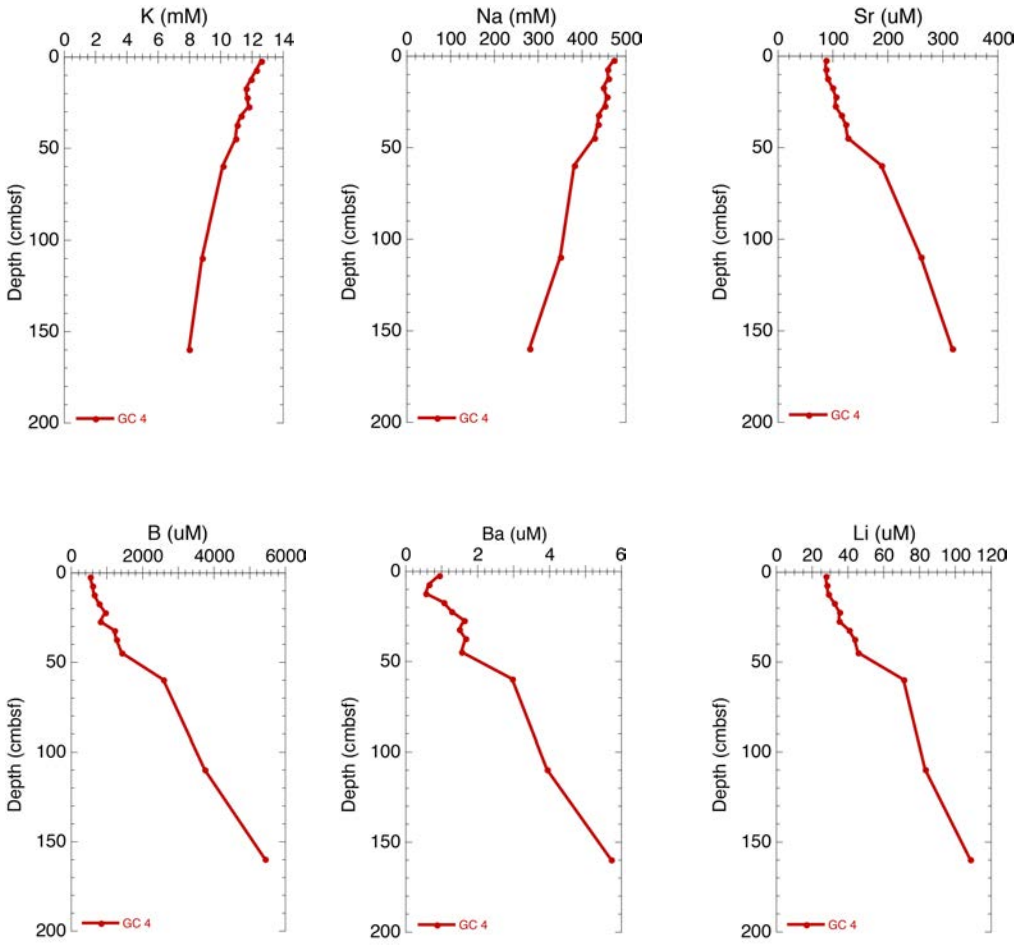

Site 2 – GC 4

Figure 5. Pore water K, Na, Sr, B, Ba, and Li from Gravity Core 4 at Site 2. For location of gravity cores at each site, refer to Appendix I.

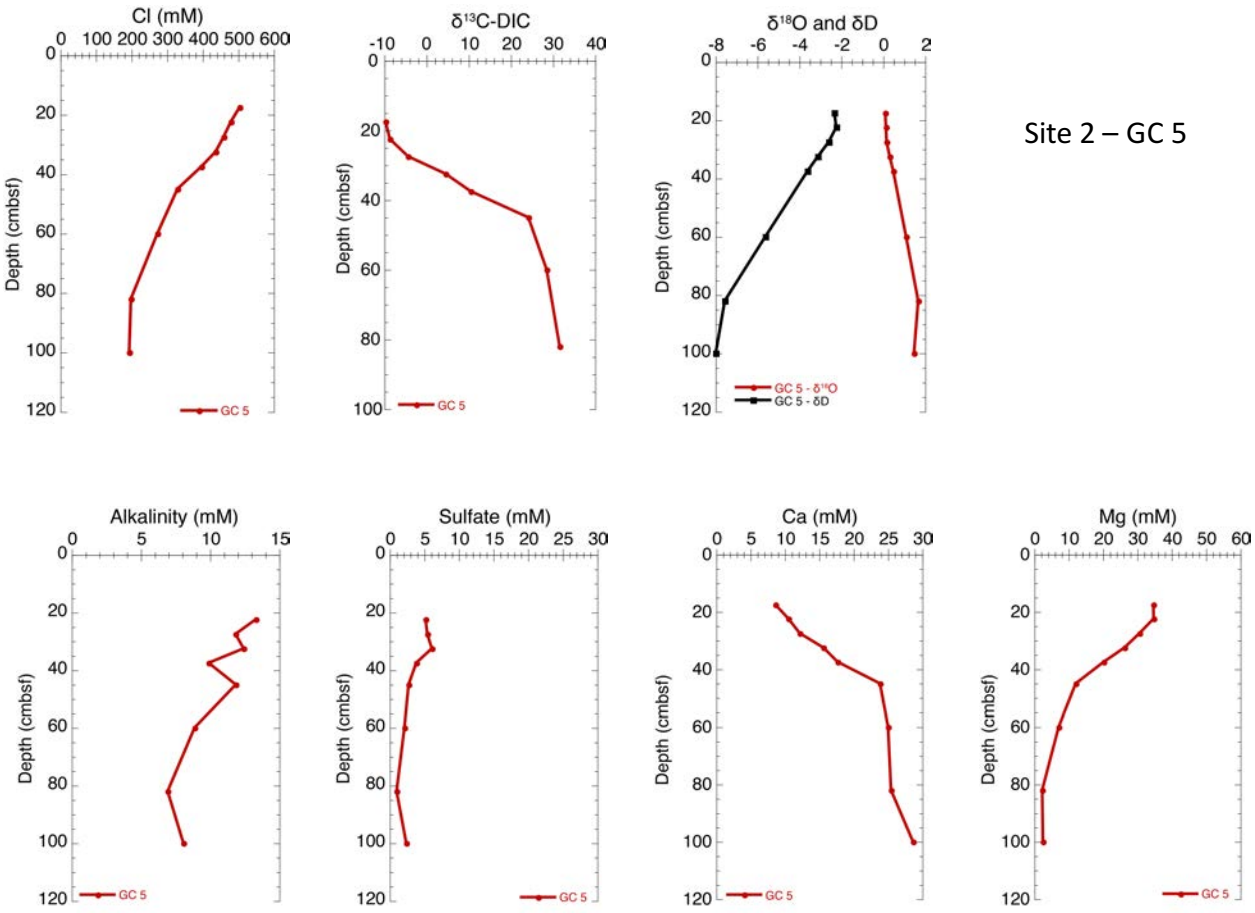

Figure 6. Pore water Cl, δ^{13}C-DIC, δ^{18}O, δD, alkalinity, SO_4, Ca, and Mg from Gravity Core 5 at Site 2. For location of gravity cores at each site, refer to Appendix I.

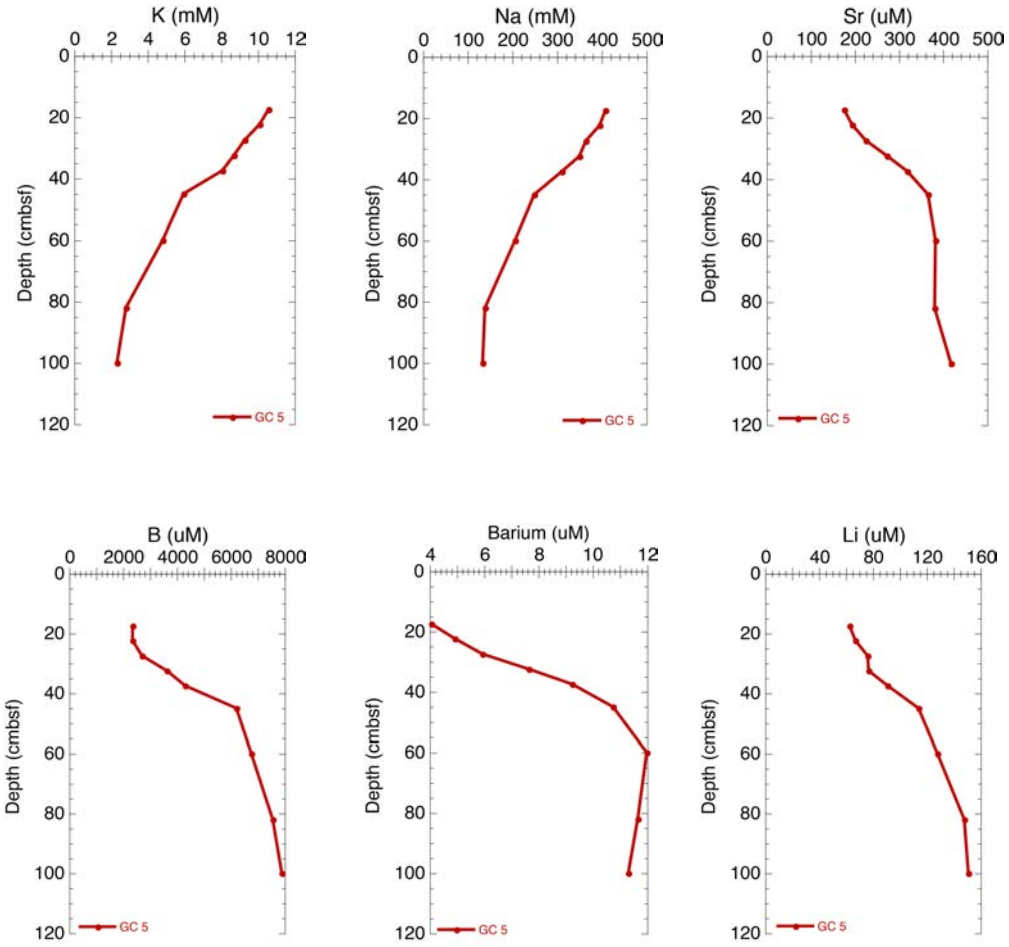

Site 2 – GC 5

Figure 7. Pore water K, Na, Sr, B, Ba, and Li from Gravity Core 4 at Site 2. For location of gravity cores at each site, refer to Appendix I.

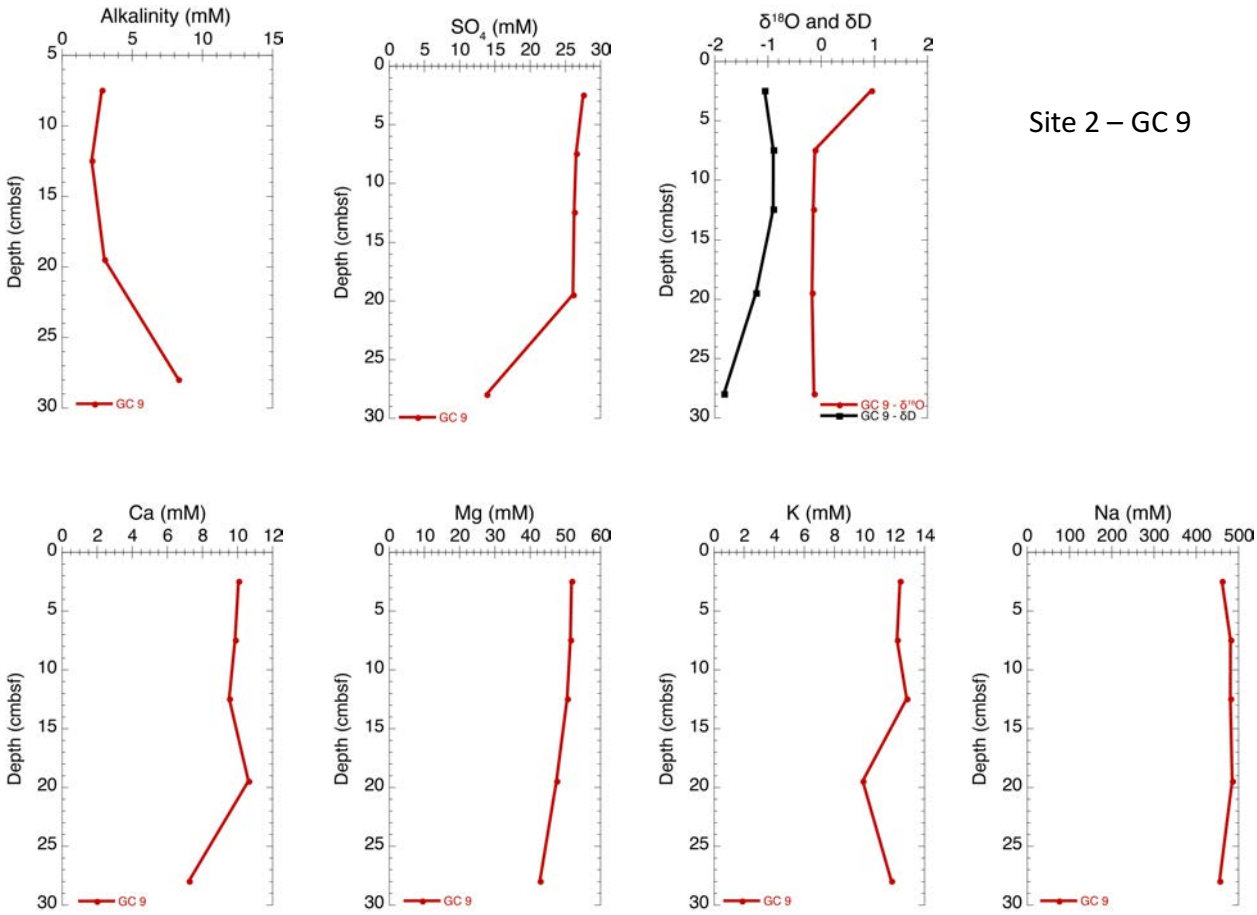

Figure 8. Pore water alkalinity, SO_4, $\delta^{18}O$, δD, Ca, Mg, K, and Na from Gravity Core 9 at Site 2. For location of gravity cores at each site, refer to Appendix I.

Site 2 – GC 10

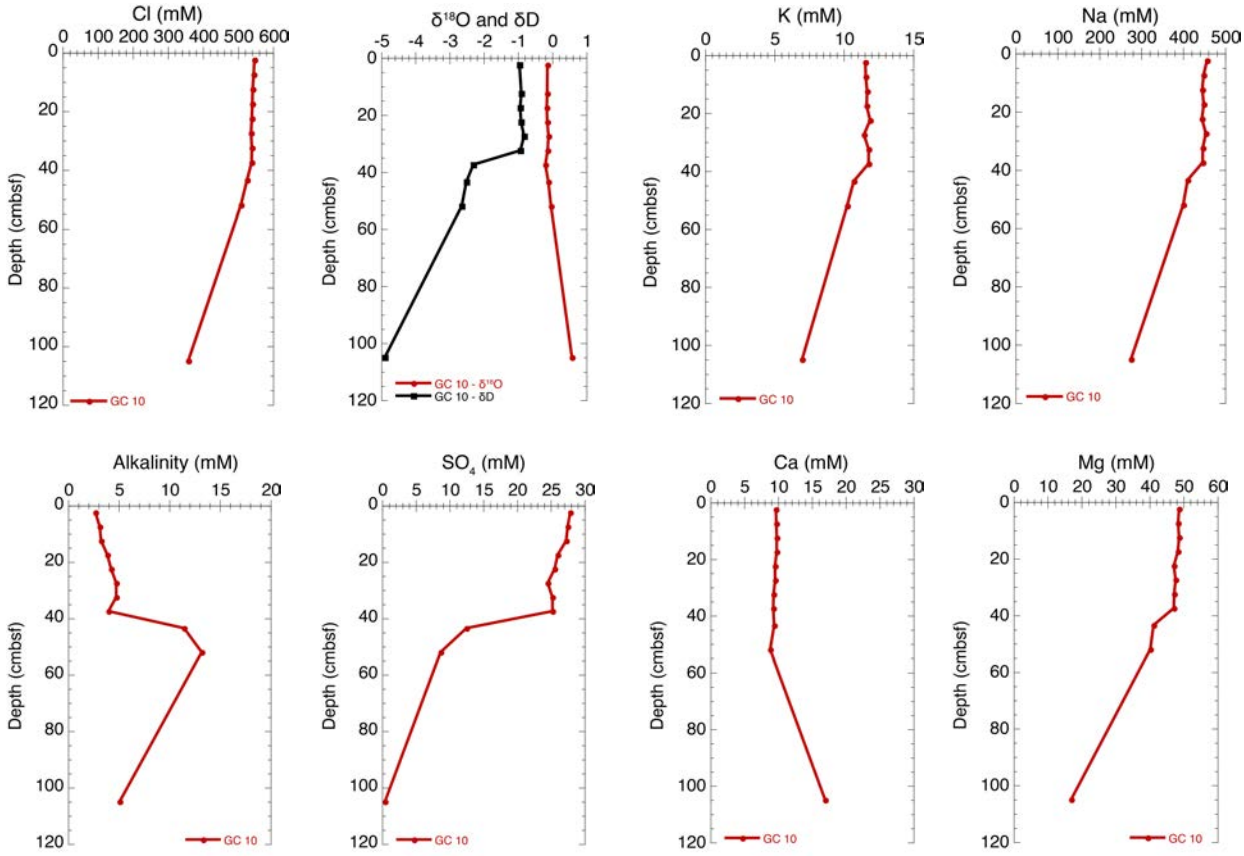

Figure 9. Pore water Cl, $\delta^{18}O$, δD, K, Na, alkalinity, SO_4, Ca, and Mg from Gravity Core 10 at Site 2. For location of gravity cores at each site, refer to Appendix I.

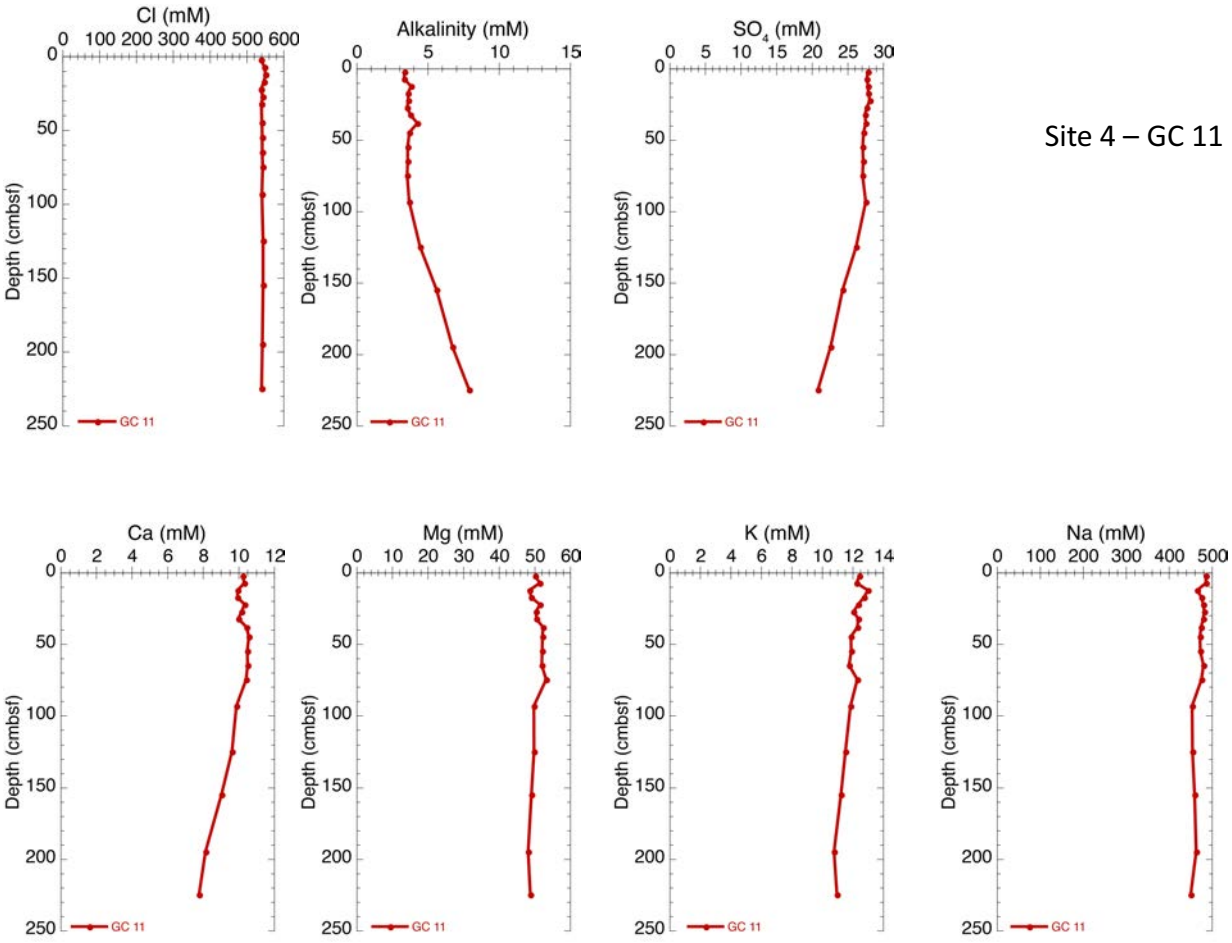

Site 4 – GC 11

Figure 10. Pore water Cl, alkalinity, SO_4, Ca, Mg, K, and Na from Gravity Core 11 at Site 4. For location of gravity cores at each site, refer to Appendix I.

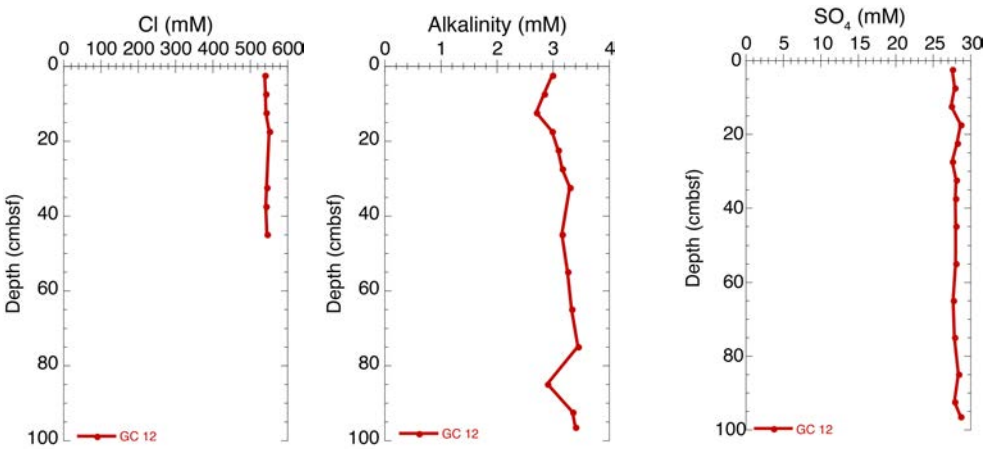

Figure 11. Pore water Cl, alkalinity, and SO_4 from Gravity Core 12 at Site 4. For location of gravity cores at each site, refer to Appendix I.

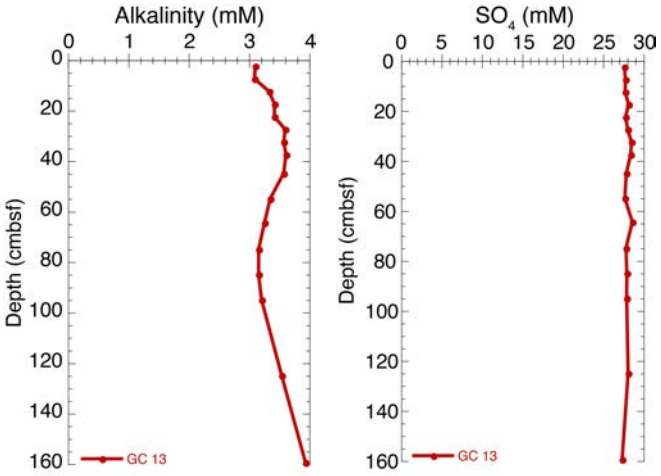

Figure 12. Pore water alkalinity and SO_4 from Gravity Core 13 at Site 4. For location of gravity cores at each site, refer to Appendix I.

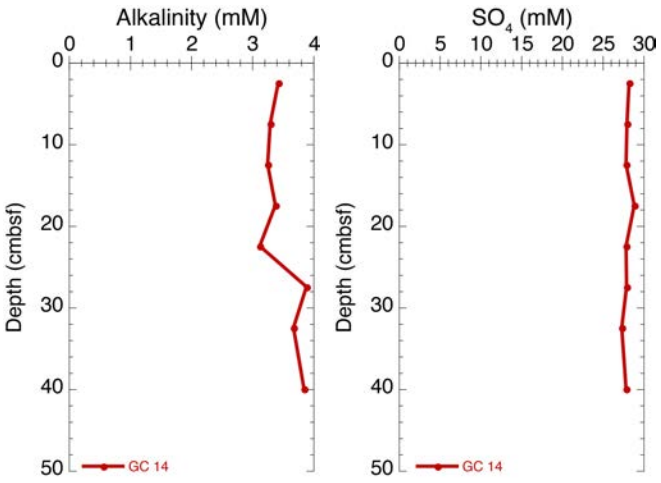

Figure 13. Pore water alkalinity and SO_4 from Gravity Core 14 at Site 4. For location of gravity cores at each site, refer to Appendix I.

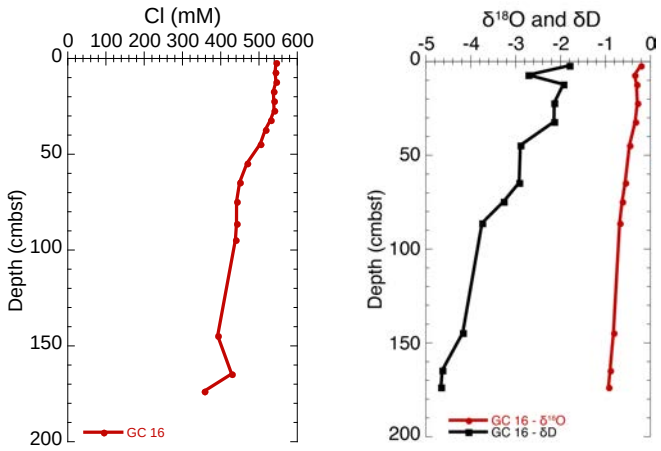

Figure 14. Pore water Cl, $\delta^{18}O$, and δD from Gravity Core 16 at Site 4. For location of gravity cores at each site, refer to Appendix I.

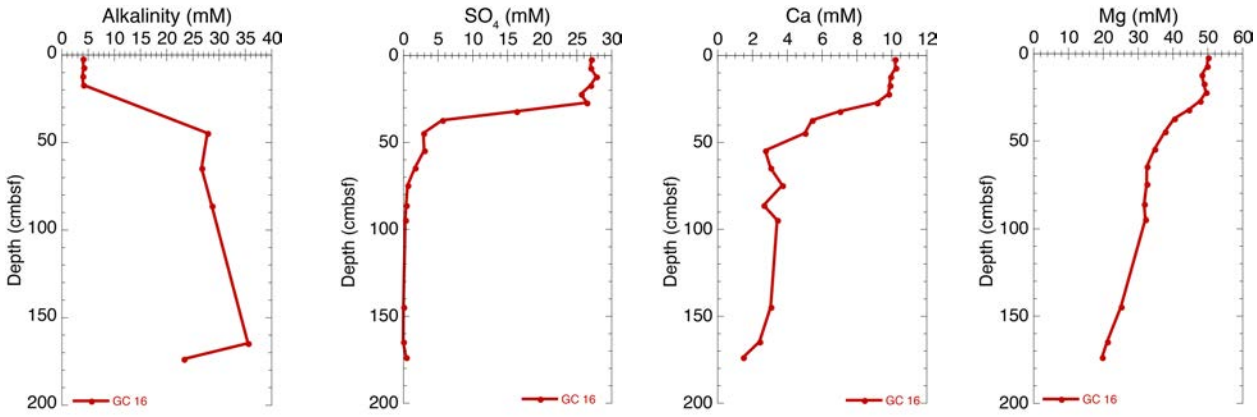

Figure 15. Pore water alkalinity, SO_4, Ca, and Mg from Gravity Core 16 at Site 4. For location of gravity cores at each site, refer to Appendix I.

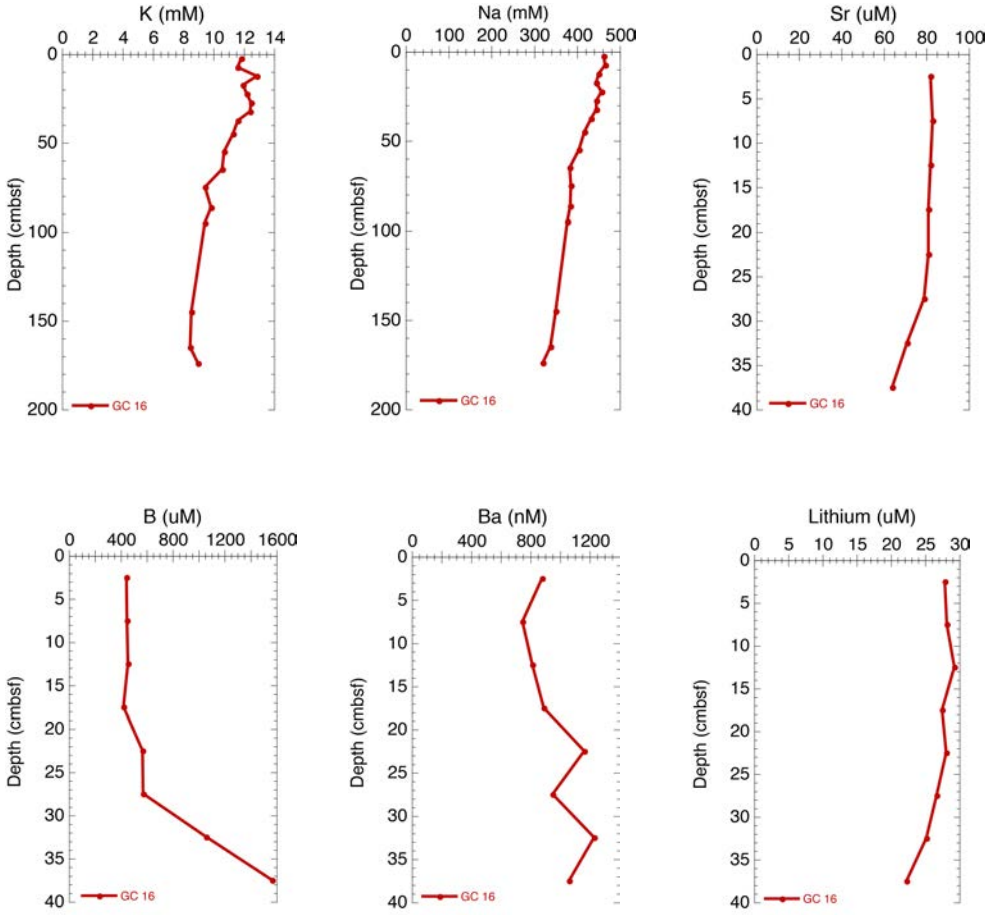

Figure 16. Pore water K, Na, Sr, B, Ba, and Li from Gravity Core 16 at Site 4. For location of gravity cores at each site, refer to Appendix I.

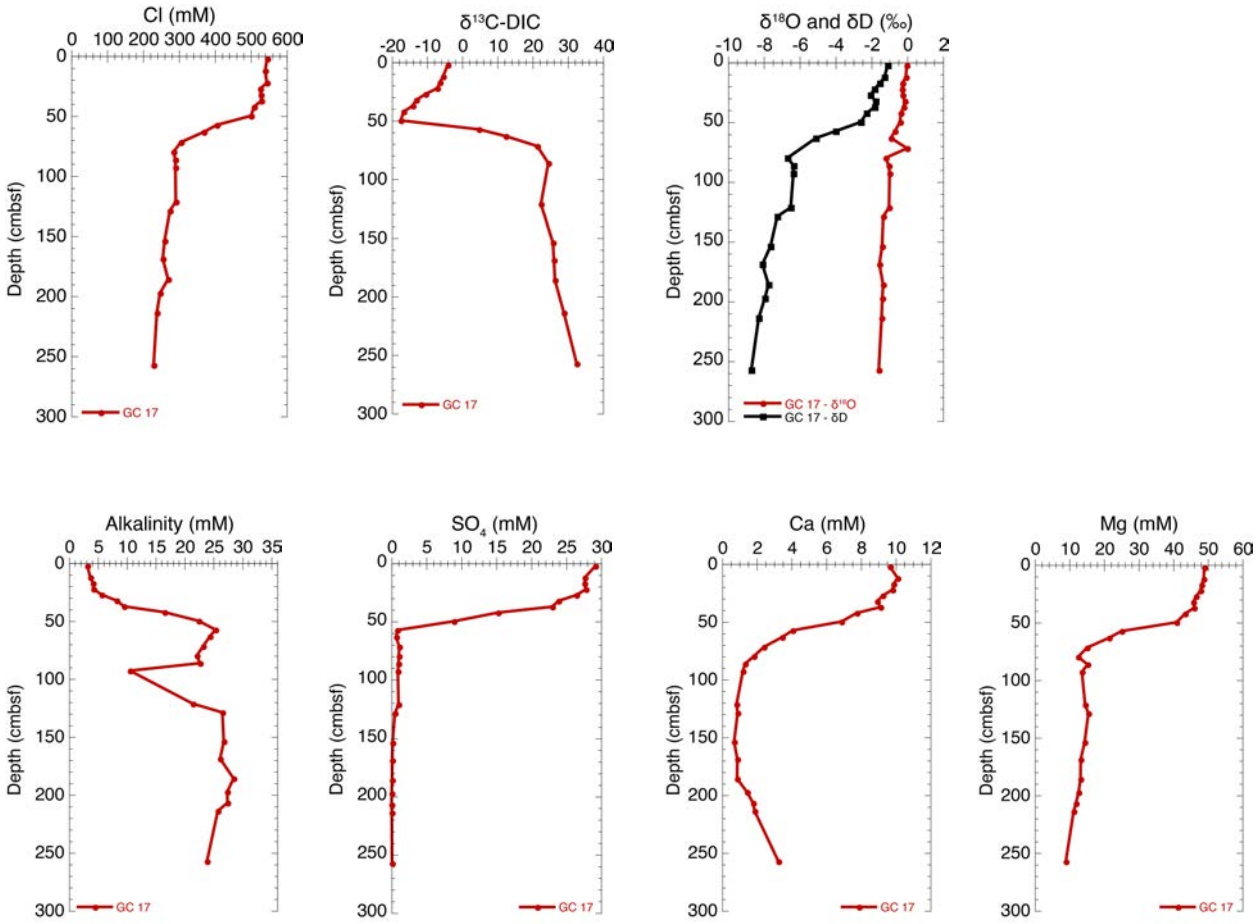

Figure 17. Pore water Cl, $\delta^{18}O$, δD, $\delta^{13}C$-DIC, alkalinity, SO_4, Ca, and Mg from Gravity Core 17 at Site 4. For location of gravity cores at each site, refer to Appendix I.

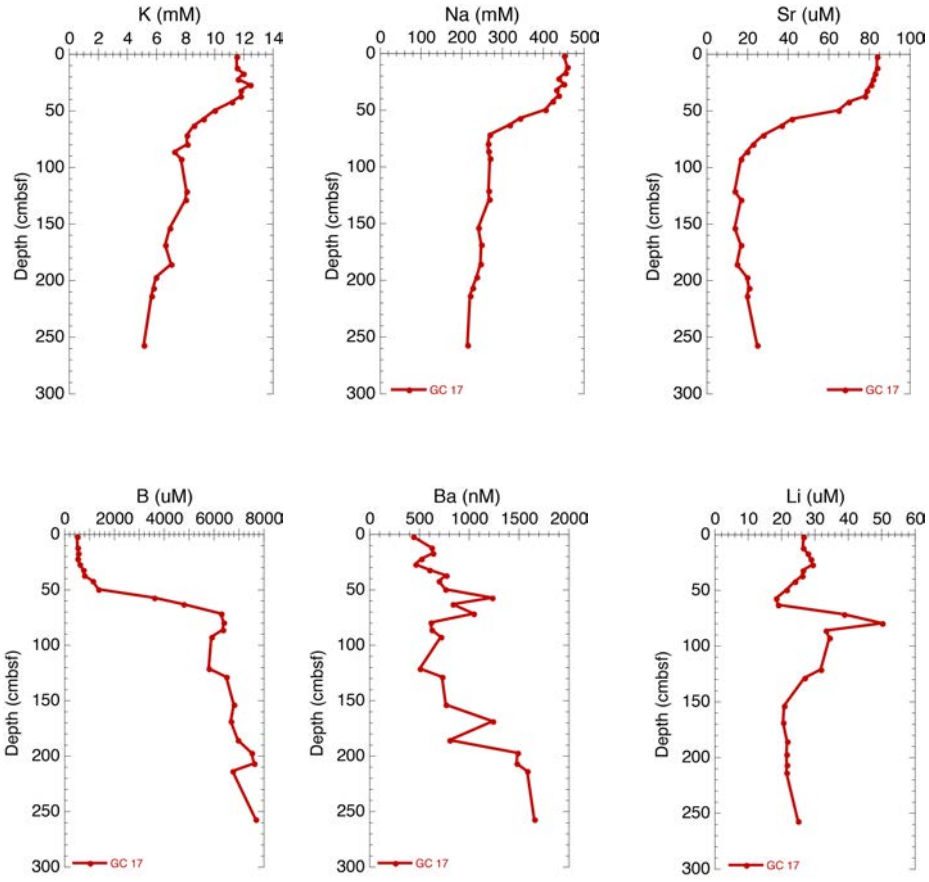

Figure 18. Pore water K, Na, Sr, B, Ba, and Li from Gravity Core 17 at Site 4. For location of gravity cores at each site, refer to Appendix I.

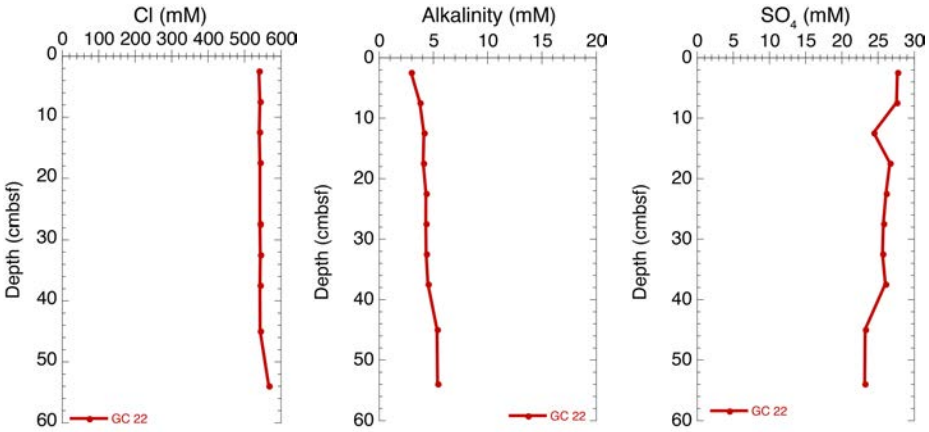

Figure 19. Pore water Cl, alkalinity, and SO_4 from Gravity Core 22 at Site 5. For location of gravity cores at each site, refer to Appendix I.

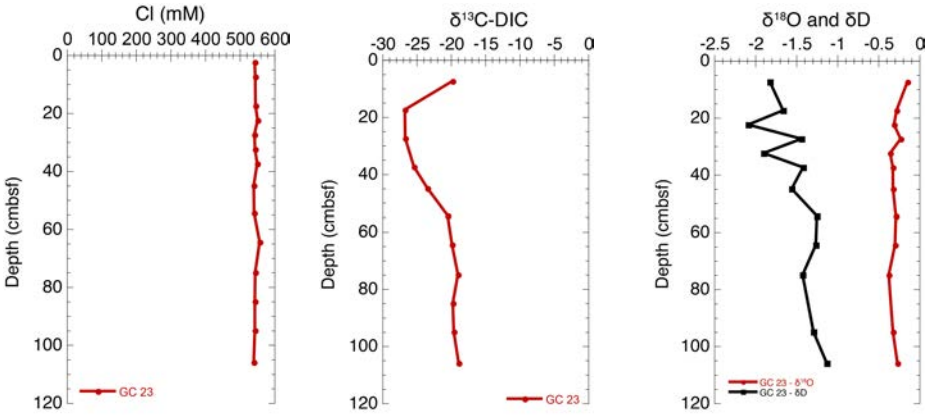

Figure 20. Pore water Cl, $\delta^{18}O$, δD, and $\delta^{13}C$-DIC from Gravity Core 23 at Site 5. For location of gravity cores at each site, refer to Appendix I.

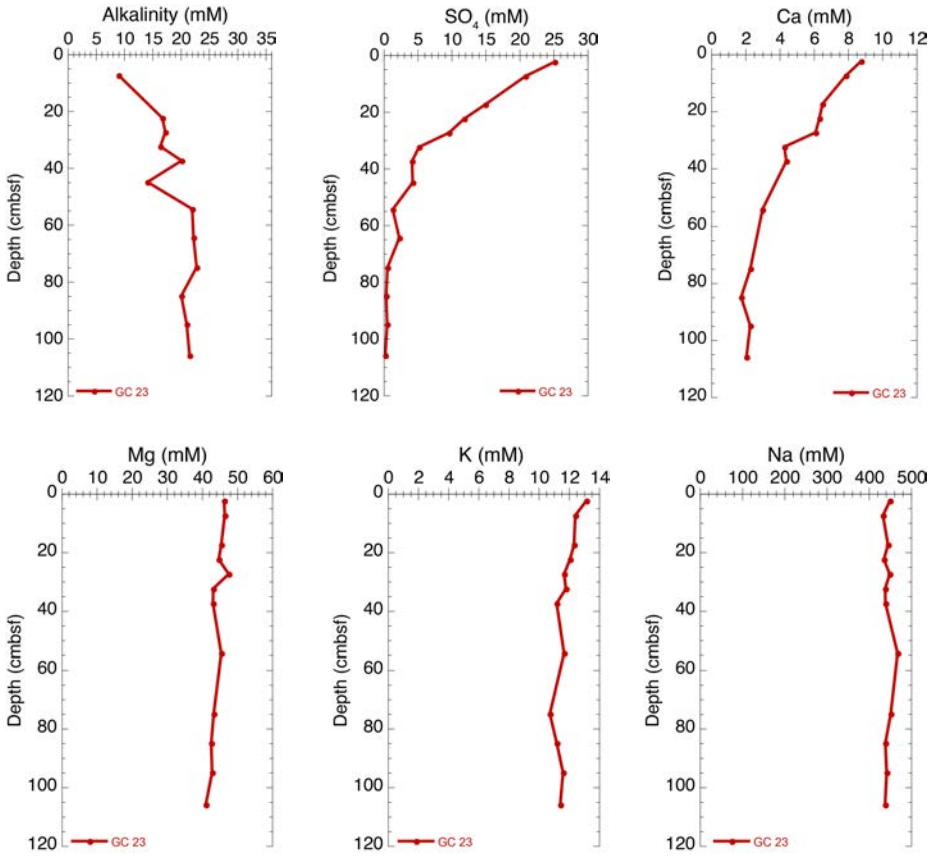

Figure 21. Pore water alkalinity, sulfate, Ca, Mg, K, and Na from Gravity Core 23 at Site 5. For location of gravity cores at each site, refer to Appendix I.

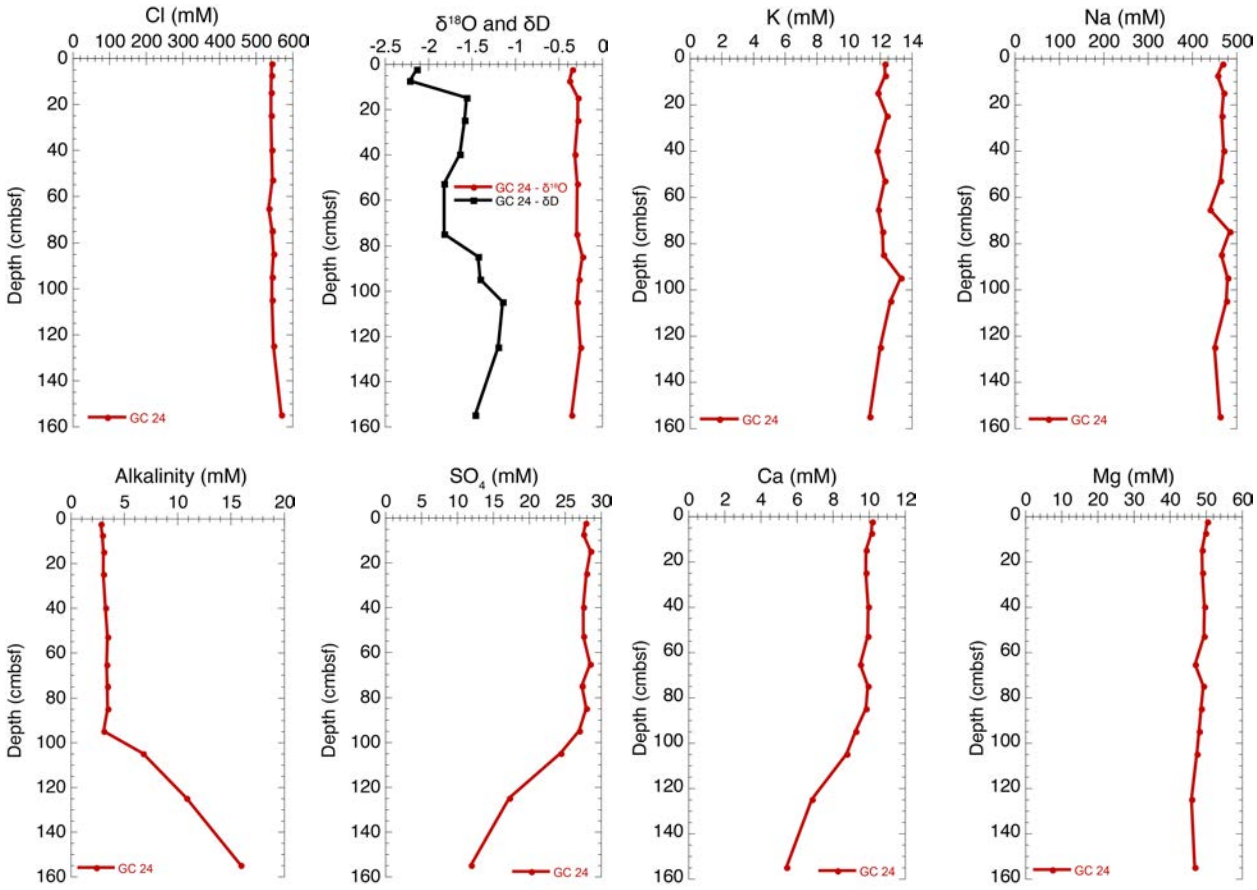

Figure 22. Pore water Cl, $\delta^{18}O$, δD, K, Na, alkalinity, sulfate, Ca, and Mg from Gravity Core 24 at Site 5. For location of gravity cores at each site, refer to Appendix I.

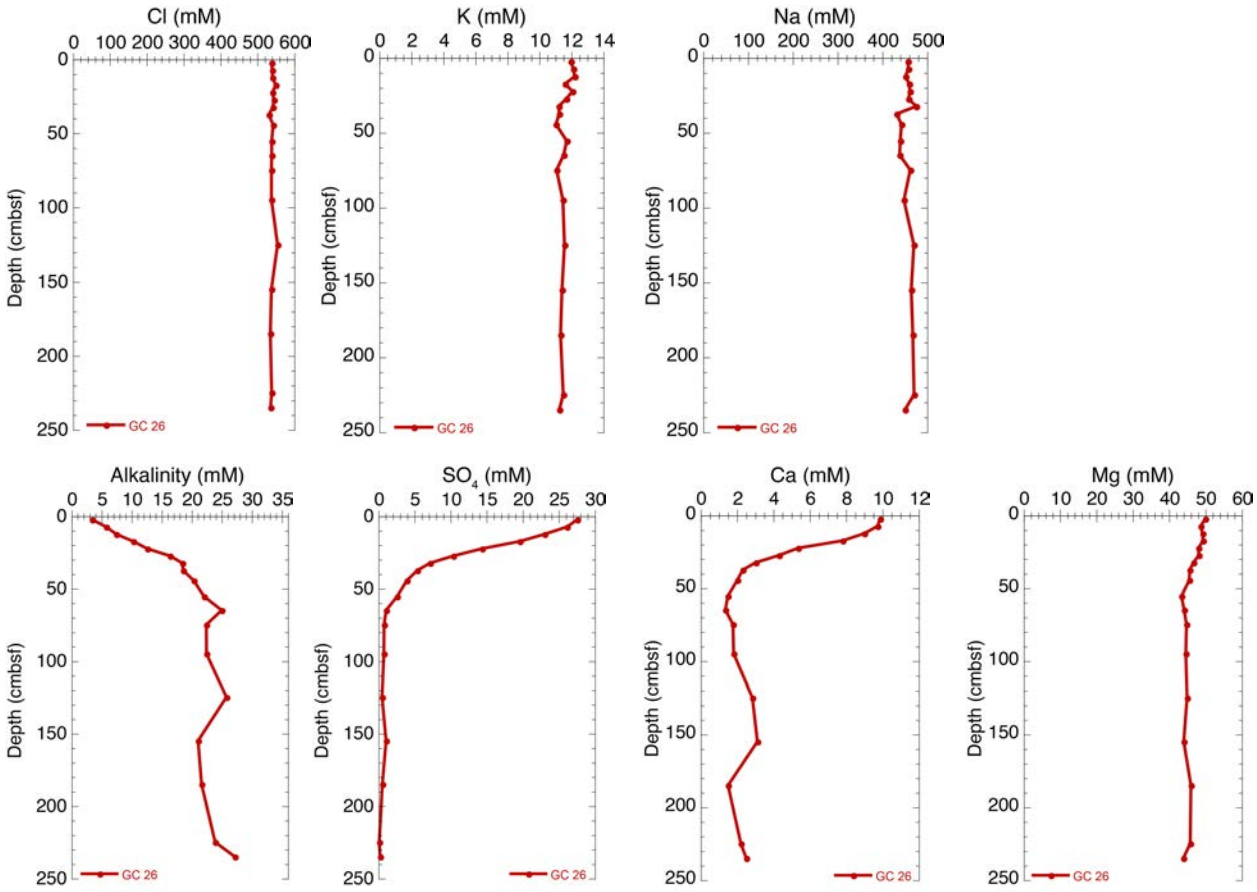

Figure 23. Pore water Cl, K, Na, alkalinity, sulfate, Ca, and Mg from Gravity Core 26 at Site 6. For location of gravity cores at each site, refer to Appendix I.

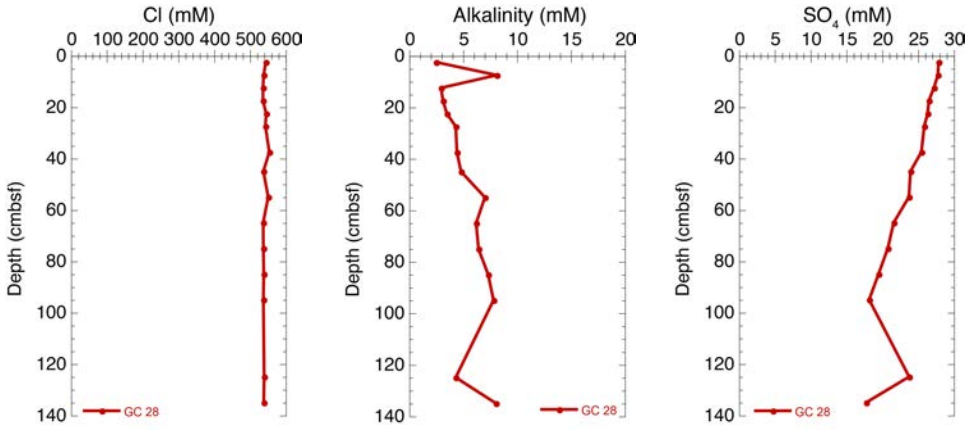

Figure 24. Pore water Cl, alkalinity, and sulfate from Gravity Core 28 at Site 6. For location of gravity cores at each site, refer to Appendix I.

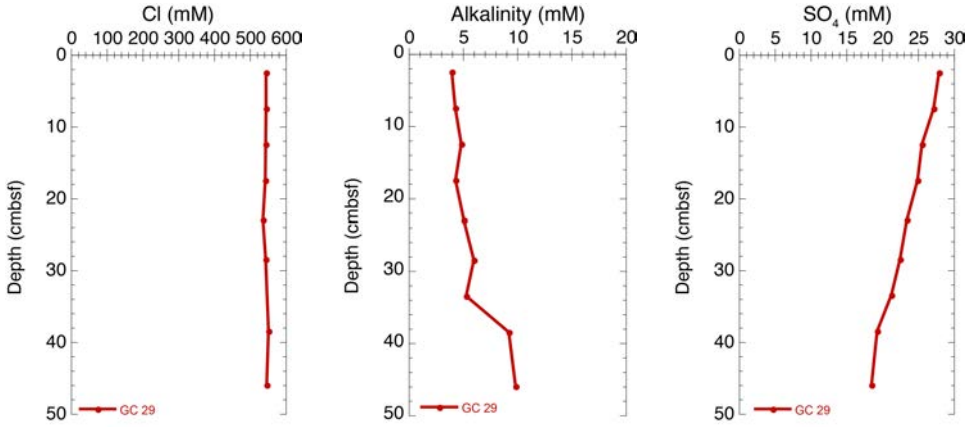

Figure 25. Pore water Cl, alkalinity, and sulfate from Gravity Core 29 at Site 6. For location of gravity cores at each site, refer to Appendix I.

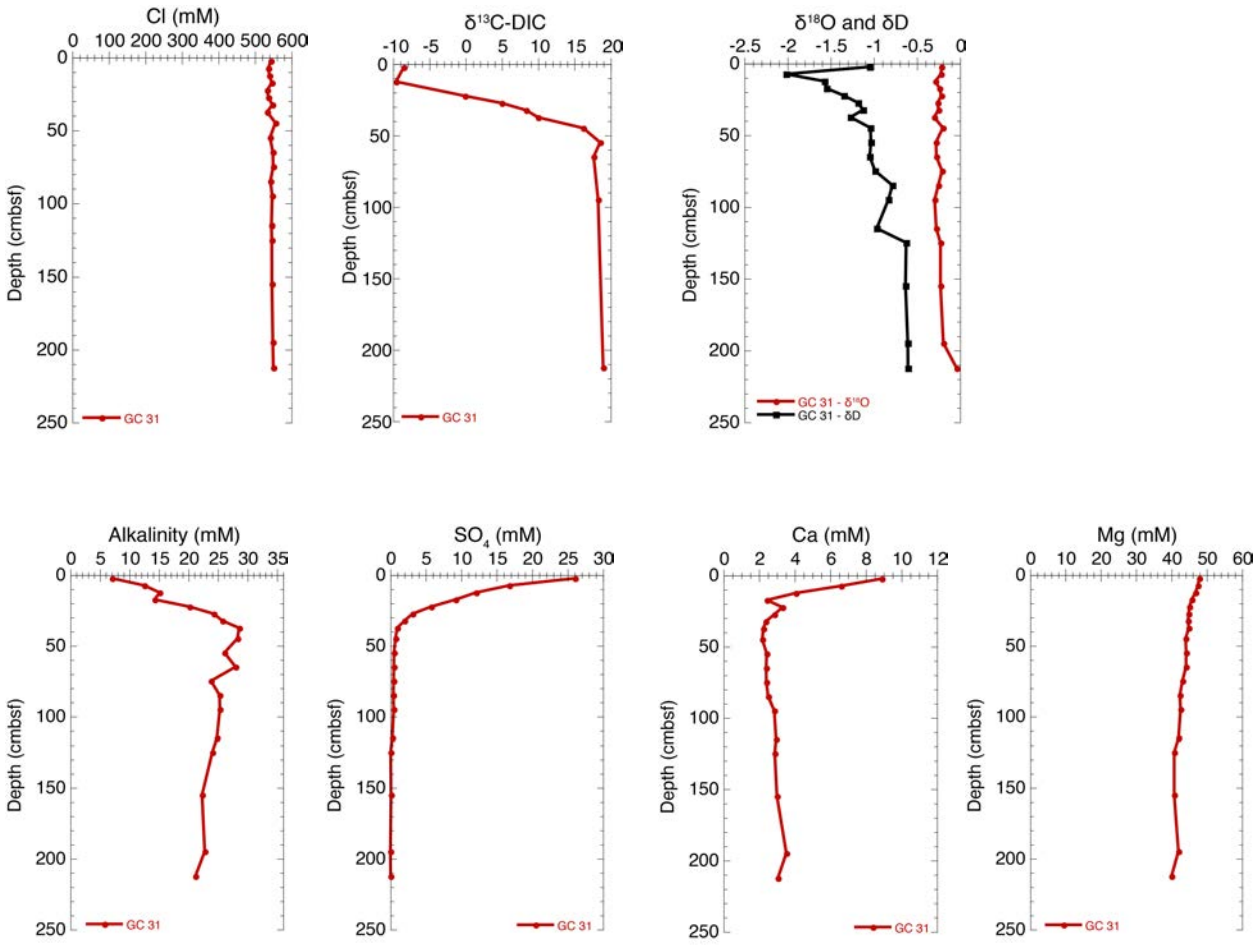

Figure 26. Pore water Cl, $\delta^{18}O$, δD, $\delta^{13}C$-DIC, alkalinity, sulfate, Ca, and Mg from Gravity Core 31 at Site 6. For location of gravity cores at each site, refer to Appendix I.

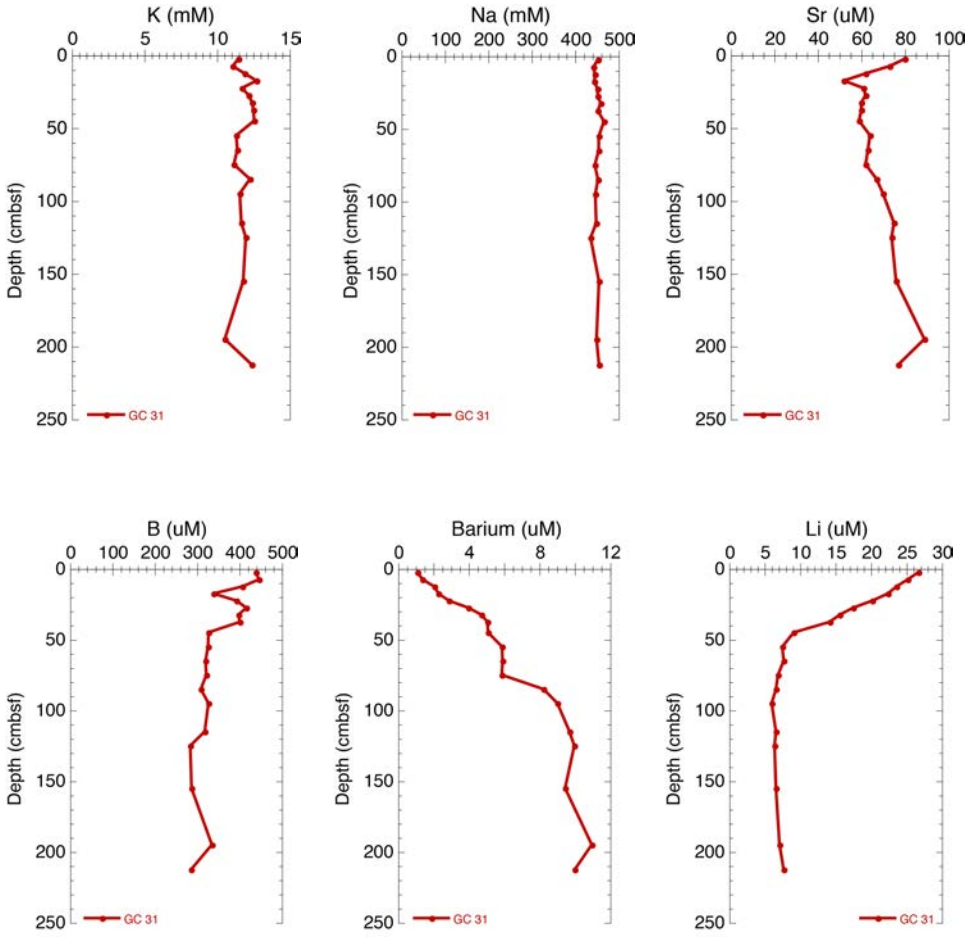

Figure 27. Pore water K, Na, Sr, B, Ba, and Li from Gravity Core 31 at Site 6. For location of gravity cores at each site, refer to Appendix I.

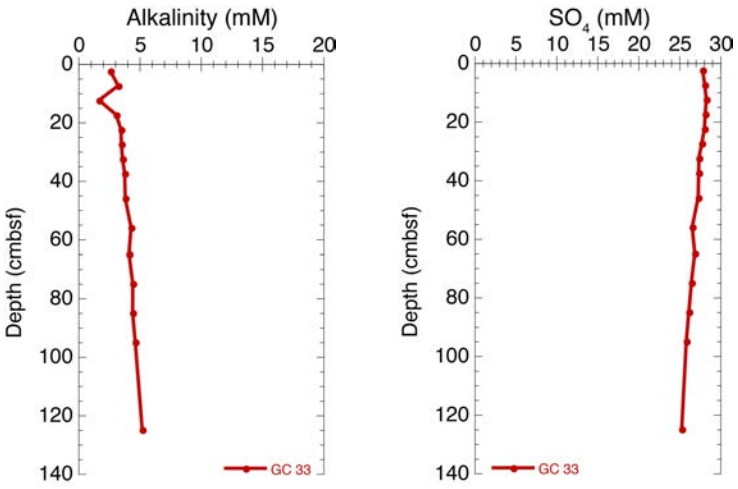

Figure 28. Pore water alkalinity and sulfate from Gravity Core 33 at Site 8. For location of gravity cores at each site, refer to Appendix I.

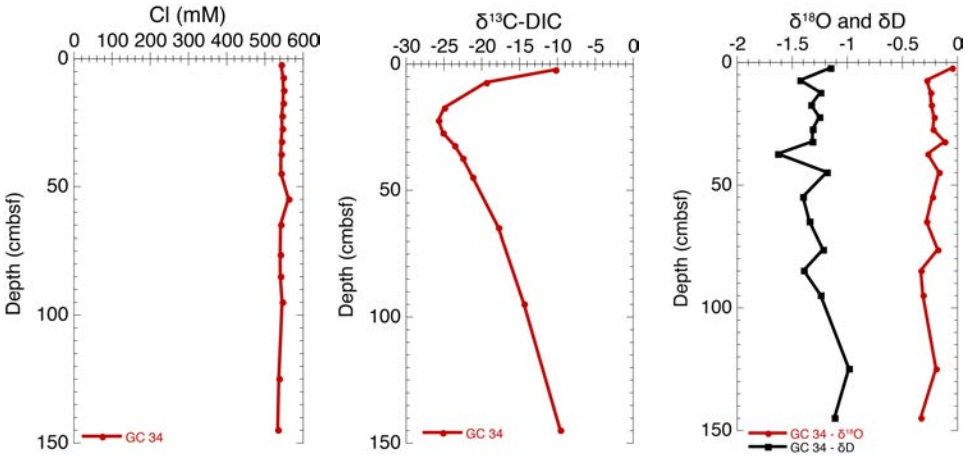

Figure 29. Pore water Cl, $\delta^{18}O$, δD, and $\delta^{13}C$-DIC from Gravity Core 34 at Site 8. For location of gravity cores at each site, refer to Appendix I.

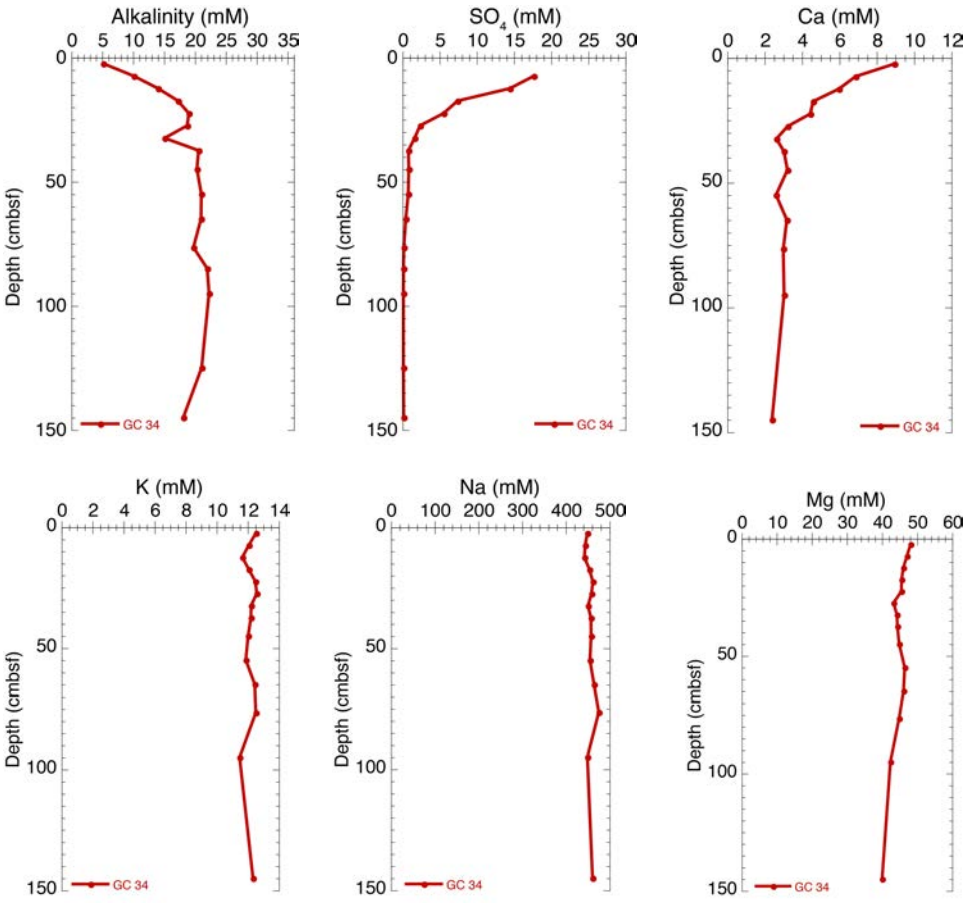

Figure 30. Pore water alkalinity, sulfate, Ca, Mg, K, and Na from Gravity Core 34 at Site 8. For location of gravity cores at each site, refer to Appendix I.

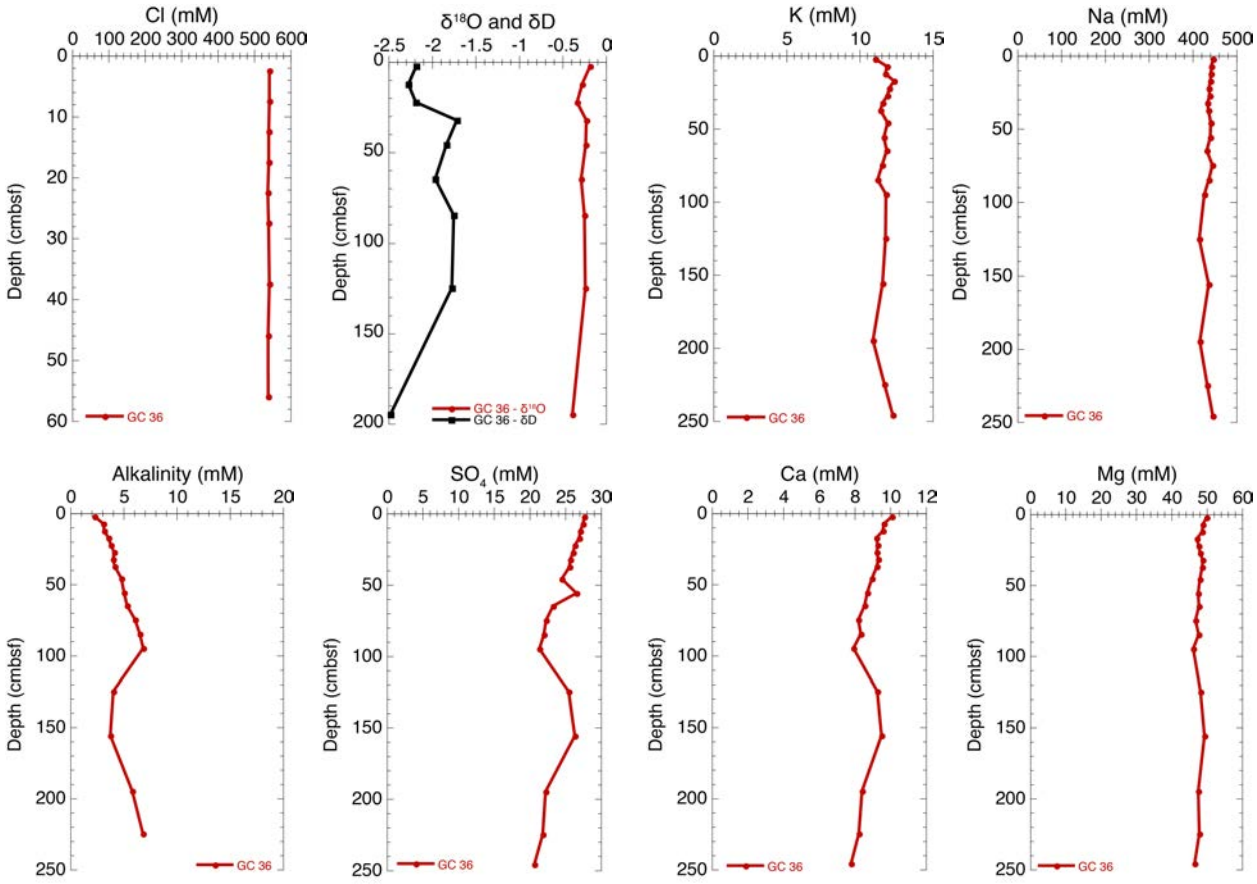

Figure 31. Pore water Cl, $\delta^{18}O$, δD, K, Na, alkalinity, sulfate, Ca, and Mg from Gravity Core 36 at Site 8. For location of gravity cores at each site, refer to Appendix I.

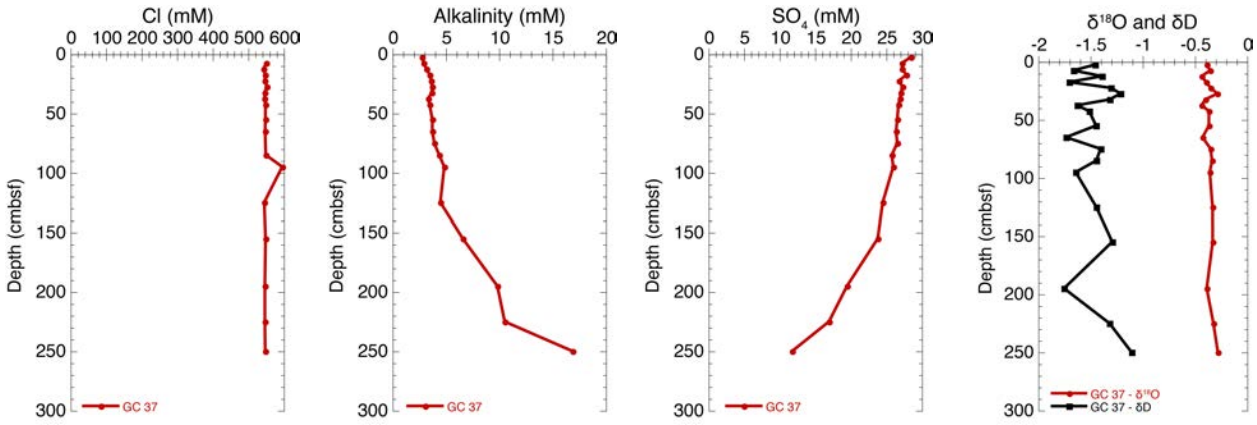

Figure 32. Pore water Cl, $\delta^{18}O$, δD, alkalinity, and sulfate from Gravity Core 37 at Site 9. For location of gravity cores at each site, refer to Appendix I.

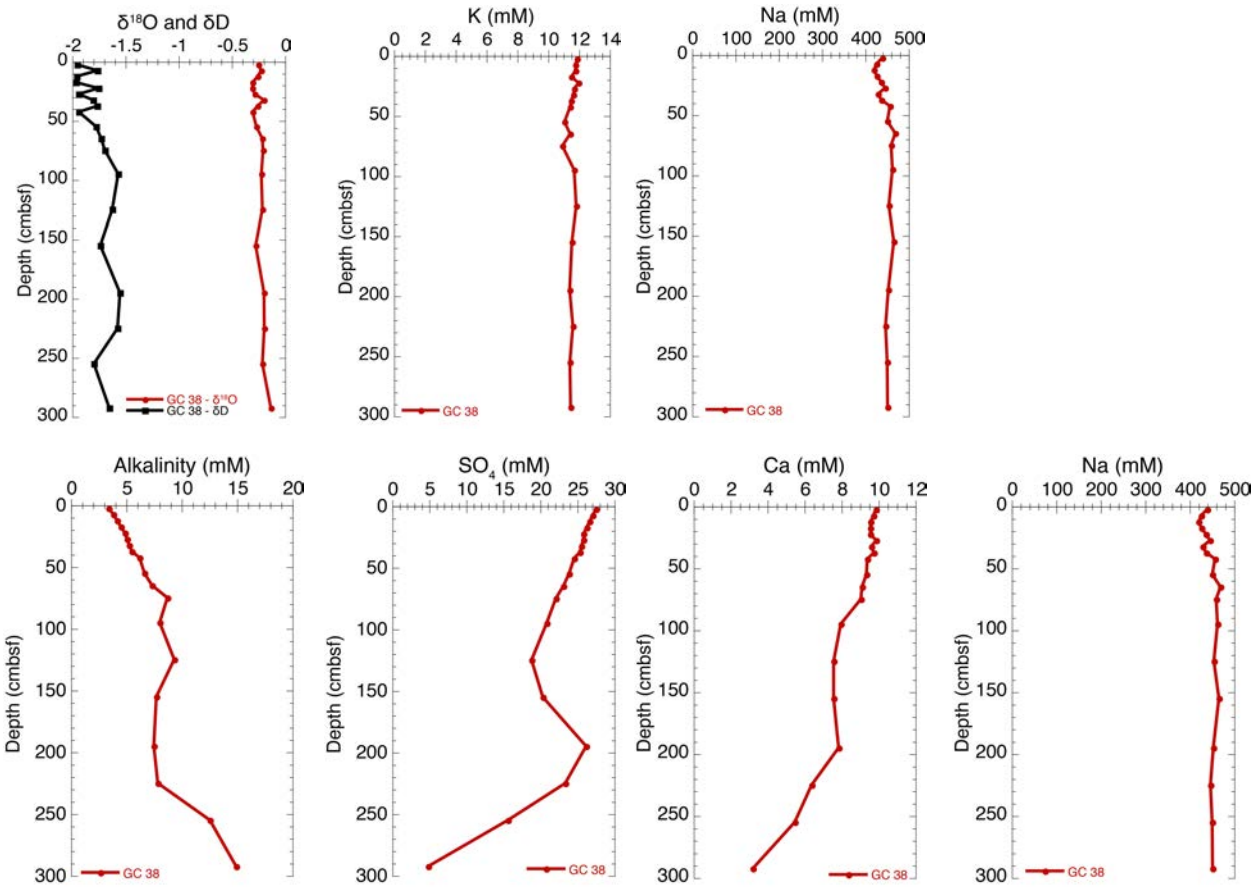

Figure 33. Pore water $\delta^{18}O$, δD, alkalinity, sulfate, Na, K, Ca, and Mg from Gravity Core 38 at Site 9. For location of gravity cores at each site, refer to Appendix I.

Results

In the preceding figures, we present the geochemical results from all the sites cored, but in the subsequent discussion we focus on three of the seven studied seep sites characterized by chloride concentrations lower than seawater value. Sites 2 and 4 display unique pore water geochemistry indicating deeper-sourced fluid advection. Site 6 is characterized by upward pore water advection but from much shallower depths than Sites 2 and 4. We further discuss data from background locations for comparison of geochemical data.

Site 2 – Soft Sediment Mud Mound

Site 2 is a soft sediment mound surrounded by authigenic carbonates and chemosynthetic communities within the MHSZ at a depth of 520 m. Two cores recovered from the location of active venting at Site 2 are discussed here. GC 4 was taken at a depth of 521 mbsl and had the greatest penetration with 170 cm total core recovery. GC 5 was taken adjacent to GC 4 at a water depth of 519 m and penetrated 105 cm into the sediment. The upper 15 cm was fluid-dominated with a moussey-texture and subsequently lost upon recovery on board, leaving a total of 90 cm of core to process for chemistry.

Pore water from these cores show significant freshening downcore (Figures 4-7). The Cl depletions correspond to a 35% dilution of seawater in GC 4 and a 65% dilution in GC 5. The sulfate-methane transition zone (SMTZ) generally occurs between 50-100 cmbsf. Alkalinity inversely mirrors these sulfate concentration-depth profiles. Oxygen isotope values become more positive with depth while δD values simultaneously become more negative by as much as 3‰ for GC 4 and 5‰ for GC 5. δ^{13}C-DIC values for GC 4 decrease to a minimum value of -10.68‰ at the SMTZ, then increase to a maximum value of +21.52‰ at the base of the core. Due to the loss of the top 15 cm of GC 5, a potentially similar initial lightening trend in δ^{13}C-DIC values is lost though the same positive increase in the carbon isotope ratio is present.

Each of these cores show depleted K concentrations with depth. The most significant decrease in concentration is seen in GC 5, where concentrations decrease to 77.8% less than seawater within 1 m. Magnesium concentrations decrease dramatically in both GC 4 and GC 5 to minimum values of 15.2 mM and 2.5 mM, respectively. These equate to a 71.9% dilution from seawater value in GC 4 and a 95.2% dilution in GC 5. Alternatively, Ca concentrations generally increased in both cores. GC 4 Ca concentrations decrease slightly in the upper 60 cm, then increase to 18 mM by 170 cmbsf, or a 72% total increase from seawater values. Calcium concentrations in GC 5 did not show this same kink, potentially due to the loss of the upper portion of the core, and increased to a maximum concentration of 28.7 mM.

Measurements of water column samples collected directly above active venting at Site 2 show a Ne/Ar ratio greater than background. Kr/Ar and Xe/Ar values are both lower than background values (Figure 34).

Site 4 – Pockmark Location

Site 4 is a location of active venting just shallower than the upper limit of the MHSZ between 473 and 489 m water depth. Plumes at this location emanate from within a 120-meter wide, 20 m deep pockmark bifurcated by extensional faults and authigenic carbonate is scattered throughout the area. Pore water data from two gravity cores are discussed here.

GC 16 and 17 were acquired adjacent to each other within the pockmark at a water depth between 470 and 480 meters. Recovery for GC 16 was 178 cm while the recovered length of GC 17 was 262 cm. Several gas pockets were seen in this latter core, with each pocket measuring 2 to 10 cm in length within the core liner. Pore water Cl concentrations for both cores are notably

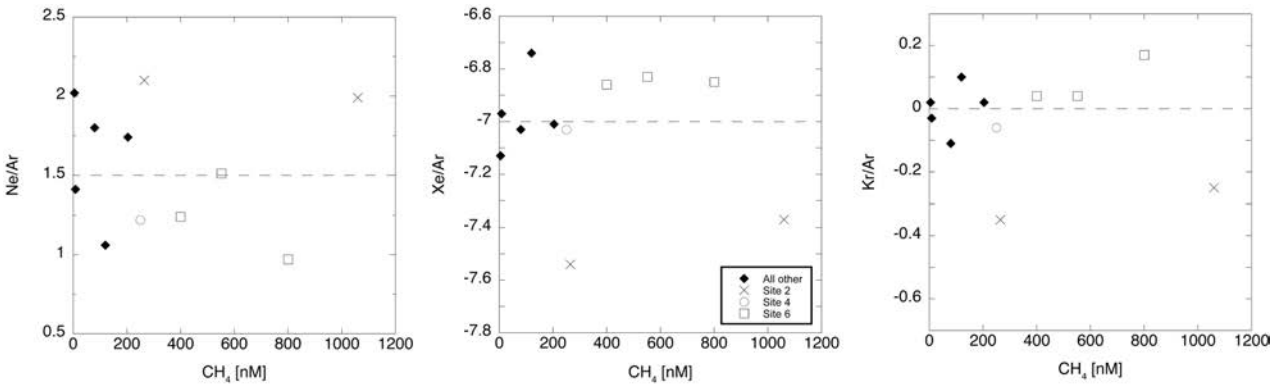

Figure 34. Plotted noble gas ratios represent the percent in situ saturation of Ne/Ar, Kr/Ar, and Xe/Ar. Site 2 samples are plotted as an "X", open circles are Site 4, open squares are site 6, and filled diamonds are all other sampled sites.

depleted downcore by 34% for GC 16 and 58% for GC 17 with respect to seawater (Figures 15-18). The SMTZ depth for GC 16 is approximately 80 cmbsf, whereas SO_4^{2-} concentrations in GC 17 decrease to <1 mM at 55 cmbsf then increase to above 1 mM at 67 cmbsf before persisting at <1 mM concentrations below 127 cm. This pattern is reflected in the alkalinity data for GC 17.

Stable oxygen and hydrogen isotopes become lighter with depth in both cores. δD for GC 17 becomes -7‰ lighter over the 2.6 m core length. δ^{13}C-DIC values for GC 17 reach a minimum value of -17.4‰ at 55 cmbsf. These isotope ratios become increasingly positive over the rest of the core. This inflection point from increasingly negative to increasingly positive values begins at the same depth when SO_4^{2-} concentrations first decrease below 1 mM.

Potassium concentrations in GC 16 show a minimal decrease of 14% compared to seawater, and a 51% decrease in GC 17, the latter being approximately equal to the percent dilution seen in Cl concentrations. Magnesium concentrations decrease dramatically in both cores, by 63% for GC 16 and 83% for GC 17, each greater than the Cl decrease and resembling the Mg decrease seen in Site 2 cores. Unlike Site 2 cores, Ca concentrations decrease from near seawater values at the surface to less than 1 mM at depths below 116 cm where SO_4^{2-} concentrations also decrease to below 1 mM. Ratios of Ne/Ar, Kr/Ar, and Xe/Ar are all within the error of the measurements (Figure 34).

Site 6 – Astoria Canyon

Site 6 is the southernmost site surveyed during this cruise. Plumes at this site emanated from the walls of Astoria Canyon at depths between 484 and 504 m. These plumes are within the depth range of predicted retreat of the MHSZ. Cores recovered from site 6 contained disseminated authigenic carbonates and exhibit pore water chemistry representative of the majority of seeps that were sampled on this cruise except sites 2 and 4.

As a representative core, GC 31 displays little pore water freshening, with the largest deviation in Cl concentrations from standard seawater of only 4.4% (Figures 26-27). Sulfate concentrations decrease from 26 mM at the surface to less than 1 mM at 35 cmbsf. These SO_4^{2-} concentrations are mirrored by an opposite trend in alkalinity, which increases before decreasing below 35 cm. Unlike sites 2 and 4, the δ^{18}O and δD values are relatively constant with depth (Figure 26). δ^{13}C-DIC values become lighter within the upper 15 cm before becoming heavier with

depth to a maximum value of +18.99‰. This inflection point is approximately 20 cm shallower than the SMTZ.

Pore water potassium concentrations are slightly elevated compared to average seawater. Magnesium concentrations are less than seawater at the surface of the core and decrease with depth by 7.9 mM. This decrease is greater than the observed dilution seen in Cl values. Calcium decreases from 8.9 mM at the top of the core and decrease to a minimum concentration of 2.2 mM at 50 cm before increasing slightly to 3.0 mM by 215 cmbsf. The Ne/Ar value for this site is less than background values (Figure 34). Kr/Ar and Xe/Ar values are slightly elevated from background values but within the error of the analyses.

Non-Steady State Profiles

Sulfate profiles from several sites have kinks that are indicative of non-steady state behavior. GC 10 from Site 2 (Figure 35), cored in between GC 4 and GC 5, shows minimal decrease in SO_4^{2-} concentrations in the upper 40 cm before decreasing rapidly to <1 mM; the concave-down shape of the profile indicates fluid advection. At site 8, GC 36 sulfate concentrations are variable with several kinks in the profile. The sulfate profile for GC 38 from site 9 is S-shaped, with two maxima and two minima in concentration. GC 36 and 38 were specifically taken away from active seeps to serve as references for background chemistry at Sites 8 and 9, respectively.

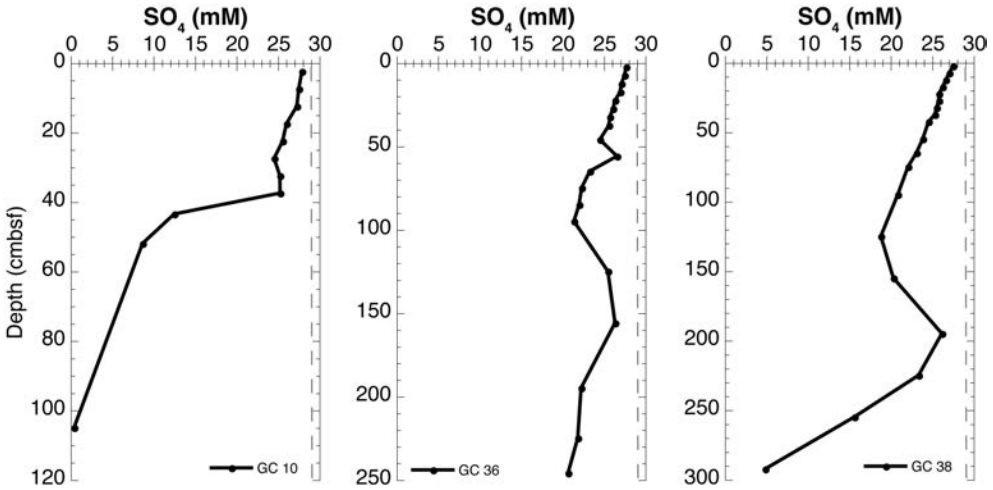

Figure 35. Examples of non-steady state pore water sulfate profiles. The profiles above are just a subset of those profiles that exhibit non-steady state conditions. GC 10 is from Site 2, GC 36 is from Site 8, and GC 38 is from Site 9. Gray dashed lines indicate seawater concentration.

Discussion

The goal of this study was to evaluate whether there is geochemical evidence for contemporary methane hydrate dissociation at the upper edge of stability along the Washington margin in response to bottom water warming along the upper continental slope over the past 40 years (Hautala et al., 2014; Johnson et al., 2015). Multi-beam acoustic imaging and pore water geochemistry results presented here confirm that areas of active fluid and gas discharge are indeed present on the WA margin at the predicted upper limit of methane hydrate stability. However, authigenic carbonate minerals both disseminated and as nodules were sampled at Sites 2, 4, and 6, suggesting that these are long-lived seep systems. Likewise, the geochemical analyses of pore fluid show that each seep site is likely fed by a variety of fluid sources. However, the gas composition

at each site was >99% methane, suggesting any gas hydrate present at these sites would be Structure I methane hydrate (Table 1).

Pore water chemical profiles varied strongly along the margin with different fluid sources contributing to observed discharge at the sampled seeps. At site 2, vigorous venting and strong depletion of Cl concentrations with respect to seawater indicate some process is actively adding fluid and gas to the system. If dissolution of methane hydrates were contributing to this signal there should be an increase in both $\delta^{18}O$ and δD as the heavier isotopes are released from the hydrate structure in addition to this Cl anomaly. Instead, $\delta^{18}O$ values increase and δD values decrease. This is the geochemical signal expected for the dehydration of clay minerals at depth (Figure 1). The process of clay dehydration releases fresh water, heavy oxygen isotopes, and light hydrogen isotopes.[26] Smectite is a dominant clay mineral on the Cascadia margin (Underwood, 2007) and begins to dehydrate at approximately 60°C (Pytte and Reynolds, 1989; Kastner et al., 2014) with peak fluid production from the smectite-illite transition occurring between ~80-150 ^{o}C (e.g. Saffer and Tobin, 2011), suggesting that the fluid sampled from this seep is sourced at a temperature of at least 60°C. Indeed, the strong depletion in potassium in the fluids sampled at Site 2 in comparison to the other seeps sampled in this study suggests fluid production from the smectite-illite transition. We applied chemical geothermometers, including stable oxygen and hydrogen isotopes (Yeh, 1980; Capuano, 1992; Sheppard and Gilg, 1996), Mg/Li ratios (Kharaka and Mariner, 1989), and Na/Li ratios (Fouillac and Michard, 1981), to bracket the temperature of deeper-sourced fluid production at this site between 70-150°C. This temperature range is well within the range of peak smectite to illite transition (Kastner et al., 1991). The significantly increased Ca and decreased Mg in pore water further suggest volcanic ash alteration along the fluid flow path or incongruent weathering of detrital silicates.

The increase in Ne/Ar and decrease in Kr/Ar and Xe/Ar within the site 2 sample suggests that methane hydrate may be forming at this location. Methane hydrate preferentially incorporates Kr and Xe into the lattice structure and excludes Ne. When hydrate is forming within the pore spaces of sediment, the gas will become enriched in Ne and depleted in Kr and Xe with respect to background values. Based upon these relationships, the water collected from site 2 shows a signal of methane hydrate formation below the surface. This site is located within the predicted MHSZ, but only the upper few meters of the sediment column are within the stability field with respect to hydrate. Indeed, the upper 15 cm of several of the sediment cores had a moussey-texture, indicative of the presence of methane hydrate *in situ*, that dissociates during core recovery. This indicates that advection of the deep-sourced fluid carrying methane promotes active methane hydrate formation in the very shallow subsurface at this site. Though this was unexpected, given that the seep was just inside the methane hydrate stability field, it is a reasonable outcome at this particular site.

Pore water from site 4 displays similarly strong variations from background seawater composition. As in site 2 cores, fluid at this seep was significantly fresher than seawater. Unlike what would be expected for clay dehydration or gas hydrate dissociation, $\delta^{18}O$ and δD values become lighter with depth. This relationship in conjunction with decreased chloride concentrations suggests that at least some component of the fluid emitted may be from a meteoric source. This submarine groundwater discharge may be modern or relict from the last glacial maximum or other Quaternary glaciations. The modern local meteoric water line (LMWL) for the Olympic Peninsula of WA (Sidle and Cvetic, 2011) is the closest resource available to compare the pore water isotope values to regional meteoric groundwater. If the fluid sampled at Site 4 is from a purely meteoric source originating on the Olympic Peninsula the isotope ratios would be significantly more

negative than the observed values and should be consistent with the LMWL (Sidle and Cvetic, 2011) Therefore, the fluid feeding this seep must be mixed with at least one other fresh water source in order to create a positive shift in the oxygen and hydrogen isotope values with respect to the LMWL. At the time of this writing we are not aware of studies that have found meteoric groundwater discharge on the upper slope of the WA margin. However, Michael et al. (2016) posit that it is likely there is more fresh groundwater discharge further offshore along continental margins than currently budgeted. Collectively, the pore water composition suggests the other component of fresh water is from clay dehydration at depth (Table 1). This deeper-sourced fluid is the dominant component of fresh water and potentially mixes with the meteoric water source along the two faults that bisect this seep location. Based on the data, we cannot rule out a minor component of methane hydrate dissociation at this site, but, if present, it was not enough to impact the noble gas ratios of the seeping fluid. This is in contrast to the signature in the bottom water noble gas ratios related to methane hydrate precipitation at Site 2.

Site	Depth (mbsl)	In/Out MHSZ	SMTZ depth (cmbsf)	Evidence of Deep Fluid Source?
2	520	In	50-100	Yes
4	473-489	Out	80-127	Yes
6	484-504	Out	35	No

Table 2. Compilation of seep site, water depth in meters below sea level, whether the seep is inside or outside of the MHSZ, the SMTZ depth within gravity cores, and whether fluid emitted at this location is dominantly from a deep source.

Pore water chemistry from GC 31 recovered at Site 6 is more representative of the majority of cores collected at the other sites. In sharp contrast to cores from sites 2 and 4, chloride concentrations do not deviate by more than 4.4% from seawater concentrations. In addition, pore water $\delta^{18}O$ values remain fairly constant with depth and δD values increase slightly by 1.4‰. This is the only site where noble gas ratios indicate hydrate dissociation (Figure 5), however the values fall within the uncertainty of the measurements. Thus, the combination of these data provide no clear signal of gas hydrate dissociation feeding these bubble plumes.

Though the geochemistry varies widely by location, and even among cores from the same site, some observations remain consistent. The kinks in sulfate profiles observed at multiple seeps and at background locations show that non-steady state behavior is pervasive along the margin, though the variation in profile shapes suggests that the processes responsible for creating each profile are not necessarily the same. The upper portion of the sulfate profile for GC 10 (Figure 8), GC 16, and GC 17 (Figure 15-18), could be due to rapid sedimentation events that quickly buried seawater, thus accounting for the near constant seawater values. Another potential explanation for this linearity could be from shallow bubble irrigation circulating seawater through the upper ~20-50 cm of the sediment column.

Pore water $\delta^{13}C$-DIC from these three seep locations show the same pattern of increasing ratios with depth. This trend indicates that these seeps are fed by a methane source where a significant fraction of the CO_2 produced through fermentation has been reduced to produce CH_4. Methanogens preferentially metabolize lighter carbon out of the available carbon pool thereby making the residual carbon pool heavier over time. In order for biological production to make the

pool as heavy as +30‰ at sites 2 and 4, specifically, the system would need to be closed for some time and likely deep. This lends support to the conclusion that deep-sourced fluids are being advected to the surface at sites 2 and 4 (Table 2).

The majority of noble gas ratios cluster within the noise of the analysis with the exception of one sample that indicates methane hydrate precipitation at Site 2. It is likely we would have seen clearer results with *in situ* sampling of interstitial water or more direct sampling of vent gases via an ROV. Future work is needed to test the feasibility of noble gas fractionation as a tracer of gas hydrate dynamics.

Conclusions

Hautala et al. [7] showed that bottom water has been warming on the upper slope of the WA margin over the last 40 years. The authors projected that a sizable quantity of methane hydrate at the upper limit of the MHSZ may be destabilized and released into the sediment and water columns in direct response to this contemporary warming. The current investigation sought to directly test these model results through the sampling of geochemical tracers of methane and methane hydrate dynamics. The results show no strong signal of methane hydrate dissociation at seep sites within the predicted depth interval of contemporary methane hydrate dissociation based on bottom water warming. There is, however, an abundance of active fluid and gas seepage along the entire span of the WA slope at the predicted upper limit of hydrate stability that are fed by a variety of fluid sources. While methane hydrate dissociation may be occurring today, it is not the most dominant signal seen in cores from the sampled seeps.

Various potential reasons may exist for why we did not see a clear signal of methane hydrate dissociation. Our sampling mainly focused on locations of active venting within the predicted depth range of the MHSZ with collection of only a few background cores. In this regard, we may have captured only well-developed, long-lived seeps. The presence of authigenic carbonate at some of the seeps supports this possibility. It is also possible that the concentration of methane does not reach saturation with respect to hydrate within the methane hydrate stability field at the upper edge of stability at these seep sites. However, with the evidence of components of deep-sourced fluid feeding various seeps it is unlikely that methane is undersaturated with respect to hydrate formation in the shallow sediment column. Thus, at the seep sites, any signal of methane hydrate dissociation is diluted by other fluid sources. Outside of seep sites, methane concentrations may not be at methane hydrate saturation within the methane hydrate stability zone near the upper limit of stability. Most modeling studies of microbial methane production predict the first occurrence of methane hydrate at depths greater than 20 mbsf. This is also likely the case for the Washington margin outside of active seep sites. This would suggest that methane hydrate did not exist within the depth range of the predicted downslope retreat of the methane hydrate stability field over the past 40 years (Hautala et al., 2014). However, if long-term bottom water warming persists into the future, the upper limit of the methane hydrate occurrence zone would begin to dissociate.

While the present study did not find unequivocal evidence of hydrate dissociation as the main driver of fluid and gas discharge at these seep locations, it is clear the WA margin is host to a dynamic biogeochemical system that requires further study to better inform our understanding of fluid movement through active margins, the significance of methane hydrate dynamics to marine biogeochemical systems, and the response of mid-latitude methane hydrate reservoirs to past and present bottom water warming.

References

Barrer, R.M., A.V.J. Edge, "Selective Clathration during the Formation of Gas Hydrates", *Separation Science*, 1967

Biastoch, A., T. Treude, L.H. Rüpke, U. Riebesell, C. Roth, E.B. Burwicz, W. Park, M. Latif, C.W. Böning, G. Madec, K. Wallmann, "Rising Arctic Ocean temperatures cause gas hydrate destabilization and ocean acidification", *Geophysical Research Letters*, 2011

Boetius, A., K. Ravenschlag, C.J. Schubert, D. Rickert, F. Widdel, A. Gieseke, R. Amann, B.B. Jørgensen, U. Witte, O. Pfannkuche, "A marine microbial consortium apparently mediating anaerobic oxidation of methane", *Nature*, 2000

Boswell, R., T.S. Collett, "Current perspectives on gas hydrate resources", *Energy and Environmental Science*, 2011

Capuano, R.M. "The temperature dependence of hydrogen isotope fractionation between clay minerals and water: Evidence from a geopressured system", *Geochimica et Cosmochimica Acta*, 1992

Claypool, G.E., I.R. Kaplan, "The origin and distribution of methane in marine sediments", *Natural Gases in Marine Sediments*, 1974

Collett, T.S., A.H. Johnson, C.C. Knapp, R. Boswell, "Natural gas hydrates: a review", *Natural gas hydrates: energy resource potential and associated geologic hazards*, 2009

Dickens, G.R., B.M. Kennedy, "Noble gases in methane hydrate from the Blake Ridge", *Proceedings of the Ocean Drilling Program, Scientific Results*, 2000

Dickens, G.R., J.R. O'Neil, D.K. Rea, R.M. Owen, "Dissociation of oceanic methane hydrate as a cause of the carbon isotope excursion at the end of the Paleocene", *Paleoceanography*, 1995

Embley, R.W., S.G. Merle, N. Raineault, T. Baumberger, S.A. Seabrook, H.P. Johnson, A.M. Trehu, J.E. Lupton, A.R. Thurber, S.R. Hammond, E.A. Solomon, M. Salmi, "Numerous bubble plumes mapped and new seeps characterized on the Cascadia margin", *AGU Fall Meeting*, 2016

Emerson, S., C. Stump, D. Wilbur, P. Quay, "Accurate measurement of O_2, N_2, and Ar gases in water and the solubility of N_2", *Marine Chemistry*, 1999

Fouillac, C., G. Michard, "Sodium/Lithium ratio in water applied to geothermometry of geothermal reservoirs", *Geothermics*, 1981

Gieskes, J.M., T. Gamo, H. Brumsack, "Chemical Methods for Interstitial water Analysis Aboard *Joides Resolution*", *Ocean Drilling Program Texas A&M University*, 1991

Hautala, S.L., E.A. Solomon, H.P. Johnson, R.N. Harris, U.K. Miller, "Dissociation of Cascadia margin gas hydrates in response to contemporary ocean warming", *Geophysical Research Letters*, 2014

Hesse, R., W.E. Harrison, "Gas hydrates (clathrates) causing pore-water freshening and oxygen isotope fractionation in deep-water sedimentary sections of terrigenous continental margins", *Earth and Planetary Science Letters*, 1981

Hunt, A.G., L. Stern, J.W. Pohlman, C. Ruppel, R.J. Moscati, G.P. Landis, "Mass fractionation of noble gases in systematic methane hydrate: Implications for naturally occurring gas hydrate dissociation", *Chemical Geology*, 2013

Johnson, H.P., U.K. Miller, M.S. Salmi, E.A. Solomon, “Analysis of bubble plume distributions to evaluate methane hydrate decomposition on the continental slope”, *Geochemistry, Geophysics, Geosystems*, 2015
Kastner, M., E.A. Solomon, R.N. Harris, M.E. Torres, “Fluids Origins, Thermal Regimes, and Fluid and Solute Fluxes in the Forearc of Subduction Zones”, *Developments in Marine Geology: Earth and Life Processes Discovered from Subseafloor Environments*, 2014
Kastner, M., H. Elderfield, J.B. Martin, “Fluids in convergent margins: what do we know about their composition, origin, role in diagenesis and importance for oceanic chemical fluxes?”, *Philosophical Transactions of the Royal Society of London*, 1991
Kennett, J.P., K.G. Cannariato, I.L. Hendy, R.J. Behl, “Methane hydrates in Quaternary climate change: The clathrate gun hypothesis”, *Methane Hydrates in Quaternary Climate Change: The Clathrate Gun Hypothesis*, 2003
Kharaka, Y.K., R.H. Mariner, “Chemical geothermometers and their application to formation waters from sedimentary basins”, *Thermal History of Sedimentary Basins: Methods and Case Histories*, 1989
Michael, H.A., K.C. Scott, M. Koneshloo, X. Yu, M.R. Khan, K. Li, “Geologic influence on groundwater salinity drives large seawater circulation through the continental shelf”, *Geophysical Research Letters*, 2016
Phrampus, B., M. Hornbach, “Recent changes to the Gulf Stream causing widespread gas hydrate destabilization”, *Nature*, 2012
Pytte, A.M., R.C. Reynolds, “The Thermal Transformation of Smectite to Illite”, *Thermal History of Sedimentary Basins: Methods and Case Histories*, 1989
Reagan, M.T., G.J.Moridis, S.M. Elliott, M. Maltrud, “Contribution of oceanic gas hydrate dissociation to the formation of Arctic Ocean methane plumes”, *Journal of Geophysical Research*, 2011
Ruppel, C.D., “Methane Hydrates and Contemporary Climate Change”, *Nature Education Knowledge*, 2011
Sheppard, S.M.F., H.A. Gilg, “Stable isotope geochemistry of clay minerals”, *Clay Minerals*, 1996
Sidle, W.C., V. Cvetic, “Stable water isotope climate archives in springs from the Olympic Mountains, Washington”, *Environmental Earth Sciences*, 2011
Skarke, A., C. Ruppel, M. Kodis, D. Brothers, E. Lobecker, “Widespread methane leakage from the sea floor on the northern US Atlantic margin”, *Nature Geoscience*, 2014
Thatcher, K.E., G.K. Westbrook, S. Sarkar, T.A. Minshull, “Methane release from warming-induced hydrate dissociation in the West Svalbard continental margin: Timing, rates, and geological controls”, *Journal of Geophysical Research: Solid Earth*, 2013
Underwood, M.B., “Sediment inputs to subduction zones: Why lithostratigraphy and clay mineralogy matter”, *The Seismogenic Zone of Subduction Thrust Faults*, 2007
Weinstein, A., L. Navarrete, C. Ruppel, T.C. Weber, M. Leonte, M.Y. Kellermann, E.C. Arrington, D.L. Valentine, M.I. Scranton, J.D. Kessler, “Determining the flux of methane into Hudson Canyon at the edge of methane clathrate hydrate stability”, *Geochemistry, Geophysics, Geosystems*, 2016
Westbrook, G.K., K.E. Thatcher, E.J. Rohling, A.M. Piotrowski, H. Pälike, A.H. Osborne, E.G. Nisbet, T.A. Minshull, M. Lanoisellé, R.H. James, V. Hühnerbach, D. Green, R.E. Fisher, A.J. Crocker, A. Chabert, C. Bolton, A. Beszczynska-Möhller, C. Berndt, A. Aquilina,

"Escape of methane gas from the seabed along the West Spitsbergen continental margin", *Geophysical Research Letters*, 2009
Winckler, G., W. Aeschbach-Hertig, J. Holocher, R. Kipfer, I. Levin, C. Poss, G. Rehder, E. Suess, P. Schlosser, "Noble gases and radiocarbon in natural gas hydrates", 2002
Yeh, H.W., "D/H ratios and late-stage dehydration of shales during burial", *Geochimica et Cosmochimica Acta*, 1980
Zachos, J.C., G.R. Dickens, R.E. Zeebe, "An early Cenozoic perspective on greenhouse warming and carbon-cycle dynamics", *Nature*, 2008

CONCLUDING REMARKS

This project constitutes one of the first field programs focused on the response of a methane hydrate system at the upper limit of gas hydrate stability to environmental change outside the Arctic environment. Using detailed pre-expedition analysis and modeling of archive and recently collected data, we (1) provided an inventory of bottom simulating reflectors and methane hydrate along the Washington margin, (2) provided a characterization of temporal variations in bottom water temperature (both short and long-term) at the upper continental slope, and (3) estimated how the upper limit of methane hydrate stability responds to this long-term environmental change. Our systematic geophysical and geochemical field survey of methane seepage along the upper continental slope provided: (1) a margin-wide characterization of seep sites and their relationship to the up-slope limit of hydrate stability, and (2) a rigorous geochemical evaluation of the origin of methane emissions as dissociating hydrates.

The primary results of this project are:

1. Bottom simulating reflector-derived heat flow values decrease from 95 mW/m^2 10 km east of the deformation front to ~60 mW/m^2 60 km landward of the deformation front, with anomalously low values of ~25 mW/m^2 on a prominent mid-margin terrace off central Washington.
2. The temperature of the incoming sediment/ocean crust interface at the deformation front ranges between 164-179 ^oC off central Washington, and the 350 ^oC isotherm at the top of the subducting ocean crust occurs 95 km landward of the deformation front. Differences between BSR-derived heat flow and modeled conductive heat flow suggest mean upward fluid flow rates of 0.4 cm/yr across the margin, with local regions (e.g. fault zones) exhibiting fluid flow rates up to 3.5 cm/yr.
3. A compilation of 2122 high-resolution CTD, glider, and Argo float temperature profiles spanning the upper continental slope of the Washington margin from the years 1968 to 2013 show a long-term warming trend that ranges from 0.006-0.008 ^oC/yr. Based on this long-term bottom water warming, we developed a 2-D thermal model to simulate the change in sediment temperature distribution over this period, along with the downslope retreat of the methane hydrate stability field. Over the 43 years of the simulation, the thermal disturbance propagated 30 m into the sediment column, causing the base of the methane hydrate stability field to shoal ~13 m and the upper limit of stability in the sediments to move ~1 km downslope.
4. A preliminary analysis of seafloor observations and mid-water column acoustic data to detect bubble plumes was used to characterize the depth distribution of seeps along the Cascadia margin. These results indicate high bubble plume densities along the continental shelf at water depths <180 m and at the upper limit of methane hydrate stability along the Washington margin. This analysis, however, was based on a limited archive dataset and additional analysis of new and other sources of archive single- and multi-beam sonar data is needed to test these results.
5. The goal of the 2014 research expedition on the *R/V Thompson* was to test whether there is active methane hydrate dissociation along the upper continental slope of the Washington margin in response to contemporary warming. Sampling focused on the depth range of simulated retreat of the methane hydrate stability field based on the record of bottom water warming. The majority of the seeps cored during the field program contained abundant authigenic carbonate indicating that they are locations of long-lived seepage rather than

emergent seep systems related to contemporary methane hydrate dissociation. Despite the evidence for enhanced methane seepage at the upper limit of methane hydrate stability along the Washington margin, we found no unequivocal evidence for active methane hydrate dissociation as a source of fluid and gas at the seeps surveyed. The pore fluid and bottom water chemistry shows that the seeps are fed by a variety of fluid and methane sources, but that methane hydrate dissociation, if occurring, is not widespread and is only a minor source (below the detection limit of our methods).

6. Reasons for a lack of a geochemical signal of active methane hydrate dissociation in response to bottom water warming along the Washington margin include: 1) the flux of fluid and methane associated with this source is diluted by the other fluid sources, 2) at the high upward fluid advection rates observed at many of the seep sites, any signal of gas hydrate dissociation at the seeps (though localized and small in magnitude compared to the reservoir disseminated in margin sediments outside of the seeps) would have been flushed out of the system over the past few decades, 3) methane concentrations in the sediment column outside of active seep sites do not reach saturation with respect to methane hydrate within the narrow pressure-temperature window for methane hydrate stability at the feather-edge, thus methane hydrate did not occur in the depth interval of methane hydrate stability zone retreat over the past few decades.

Collectively, these results provide a significant advance in our understanding of the thermal structure of the Cascadia subduction zone and the fluid and methane sources feeding seeps along the upper continental slope of the Washington-sector of the Cascadia margin. This detailed study of a mid-latitude margin that is susceptible to modern environmental change is relevant to recent priorities for research focused on documenting the stability of methane hydrate systems outlined by the scientific community (e.g. *IODP Science Plan for 2013-2023, Building US Strategies for 2013-2023 Scientific Ocean Drilling workshop report, COL/NETL Methane Hydrate Field Program* workshop report). Though we did not find unequivocal evidence for methane hydrate dissociation as a source of water and methane at the upper pressure-temperature limit of methane hydrate stability at present, continued warming of North Pacific Intermediate Water in the future has the potential to impact the methane hydrate reservoir in sediments at greater depths along the slope. Thus, this study provides a strong foundation and the necessary characterization of the background state of seepage at the upper limit of methane hydrate stability for future investigations of this important process.

APPENDIX I: SEEP SITES IDENTIFIED AND SAMPLED DURING RESEARCH EXPEDITION

In this appendix, we present the EM 302 multibeam bathymetry collected at each of the survey sites on the *R/V Thompson* along with the locations of gravity core and CTD deployments at each site. Archive pore water and water column samples are preserved and housed in Dr. Evan Solomon's laboratory at the University of Washington, and available to the broader research community.

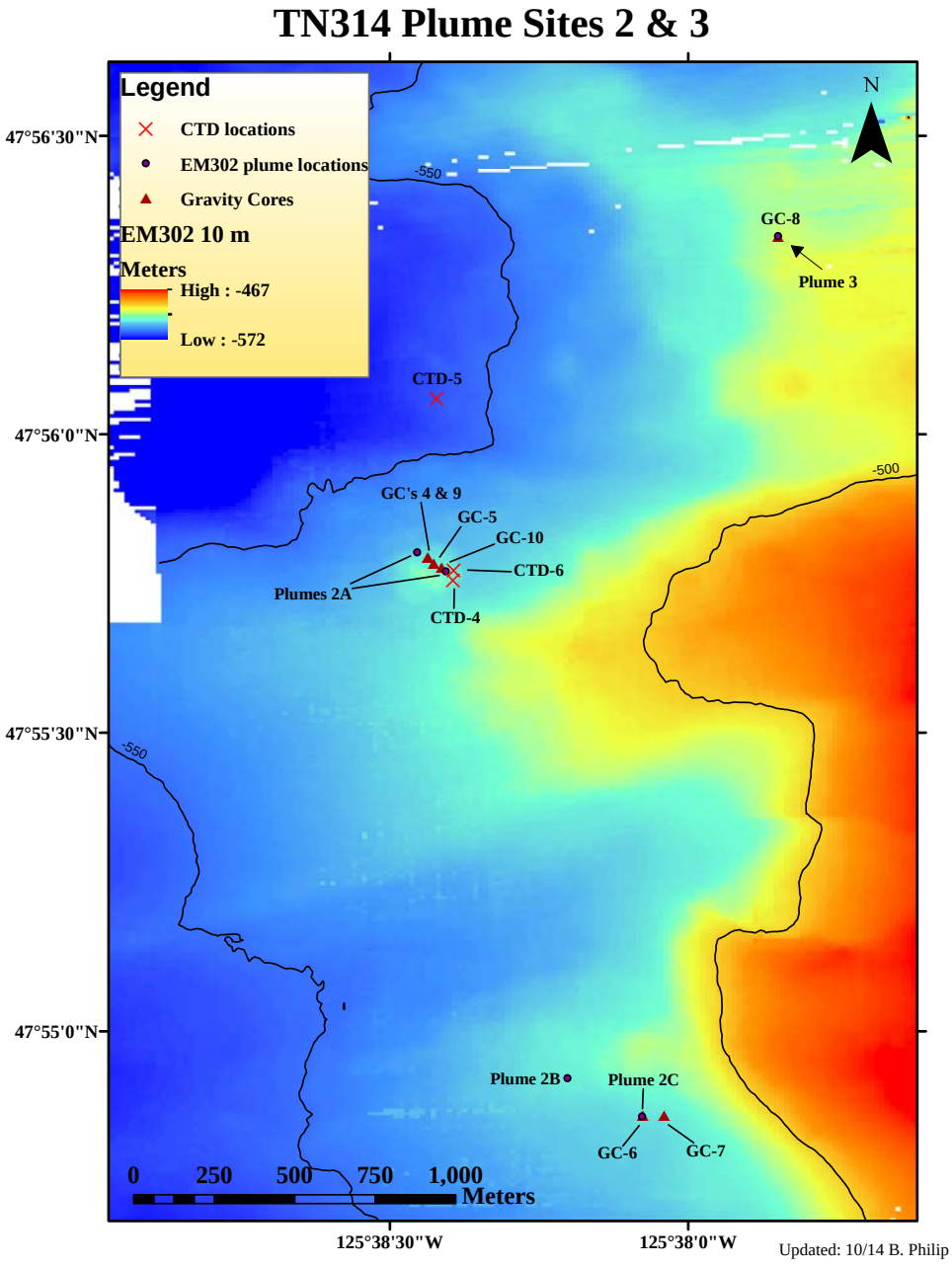

Bubble plume locations

ID	Lat	Long	depth
2A_1	47.9295	-125.64	-519
2A_2	47.93003	-125.641	-528.4
2B	47.91535	-125.637	-521.4
2C	47.91428	-125.635	-523.6
3	47.93886	-125.631	-510.9

Site 2 - Gravity core locations

ID	Lat	Long
GC-4	47.9299	-125.6406
GC-5	47.92961	-125.640218
GC-6	47.9143	-125.6346
GC-7	47.9143	-125.634
GC-8	47.938862	-125.630818
GC-9	47.9299	-125.6406
GC-10	47.929733	-125.640443

Site 2 - CTD cast locations

ID	Lat	Long
CTD-4	47.92926	-125.6399
CTD-5	47.93434	-125.64036
CTD-6	47.92954	-125.63988

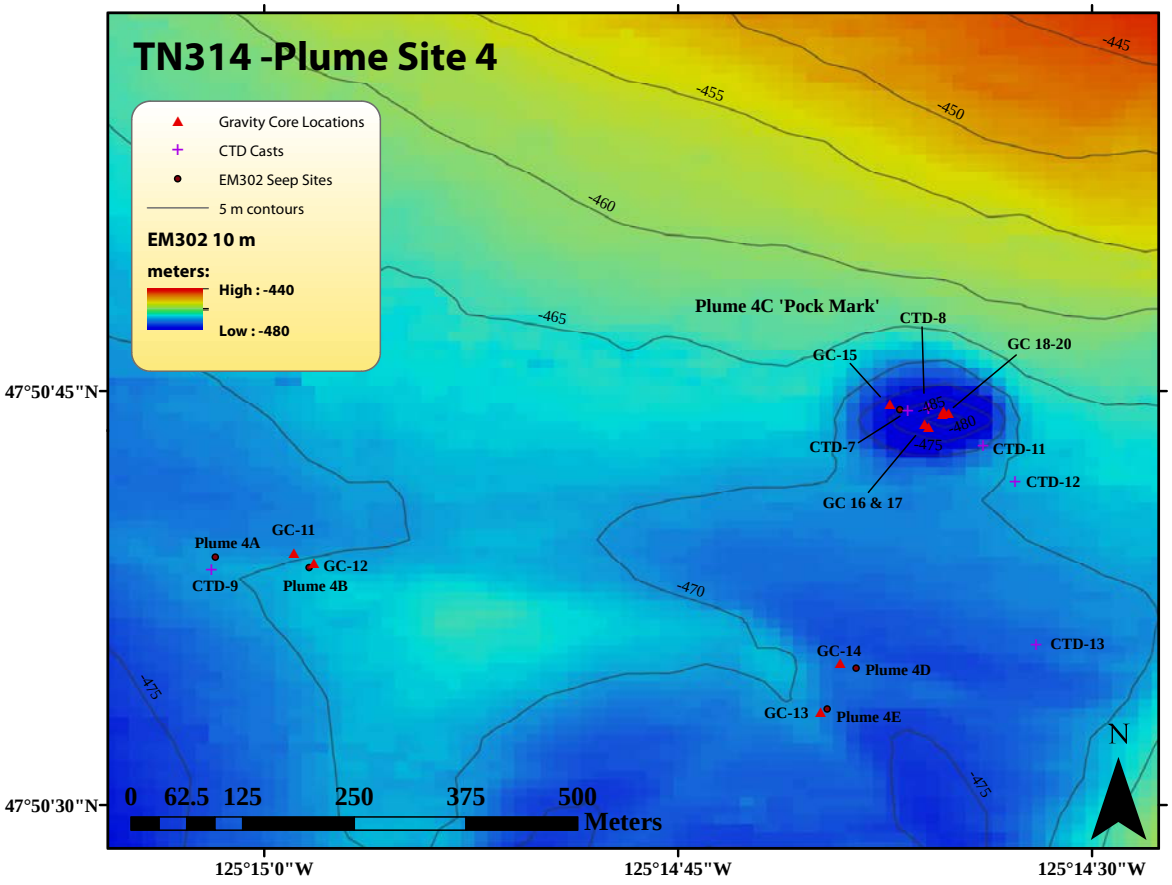
TN314 -Plume Site 4
Gravity Core Locations
CTD Casts
EM302 Seep Sites
5 m contours
EM302 10 m
meters:
High : -440
Low : -480
Plume 4C 'Pock Mark'
CTD-8
GC 18-20
GC-15
CTD-7
CTD-11
CTD-12
GC 16 & 17
Plume 4A
GC-11
GC-12
CTD-9
Plume 4B
GC-14
Plume 4D
CTD-13
GC-13
Plume 4E
-445
-450
-455
-460
-465
-470
-475
-480
-485
47°50'45"N
47°50'30"N
125°15'0"W
125°14'45"W
125°14'30"W
0 62.5 125 250 375 500
Meters
N

Site 4 - Bubble plume locations

ID	Lat	Long	Depth
4A	47.844161	-125.25049	-470.1
4B	47.844056	-125.249547	-468.2
4C	47.845644	-125.2436	-481.2
4D	47.843042	-125.24404	-472.7
4E	47.842631	-125.24433	-471.8
	47.8295	-125.319	Eastern Pockmark
	47.8214	-125.3223	Western Pockmark

Site 4 - Gravity core locations

ID	Lat	Long
GC-11	47.8442	-125.2497
GC-12	47.8441	-125.2495
GC-13	47.8426	-125.2444
GC-14	47.8431	-125.2442
GC-15	47.8457	-125.2437
GC-16	47.84547	-125.24331
GC-17	47.8455	-125.24335
GC-18	47.84563	-125.24316
GC-19	47.8456	-125.24317
GC-20	47.84561	-125.24311

Site 4 - CTD Cast Locations

ID	Lat	Long
CTD-7	47.84564	-125.24352
CTD-8	47.84566	-125.24331
CTD-9	47.84404	-125.25053
CTD-10	47.8481	-125.2502
CTD-11	47.84528	-125.24276
CTD-12	47.84492	-125.24244
CTD-13	47.84328	-125.24223

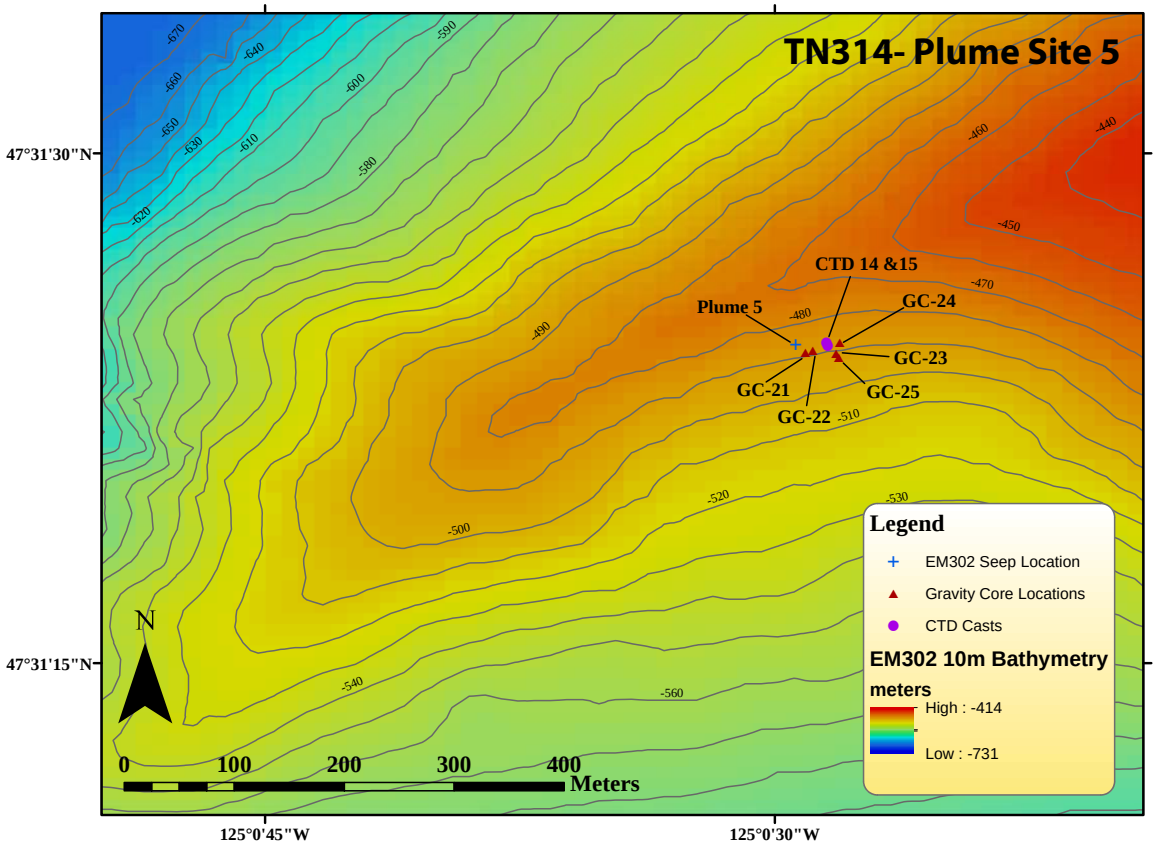
TN314- Plume Site 5
47°31'30"N
47°31'15"N
125°0'45"W
125°0'30"W
CTD 14 &15
Plume 5
GC-24
GC-23
GC-21
GC-25
GC-22
N
0
100
200
300
400
Meters
Legend
EM302 Seep Location
Gravity Core Locations
CTD Casts
EM302 10m Bathymetry
meters
High : -414
Low : -731

Site 5 - Bubble plume locations

ID	Lat	Long	Depth
Plume5	47.523433	-125.00816	-485.1

Site 5 - Gravity core locations

ID	Lat	Long
GC-21	47.52337	-125.00808
GC-22	47.52339	-125.00802
GC-23	47.52336	-125.00783
GC-24	47.52345	-125.0078
GC-25	47.52333	-125.00781

Site 5 - CTD Locations

ID	Lat	Long
CTD-14	47.52343	-125.0079
CTD-15	47.52345	-125.00791

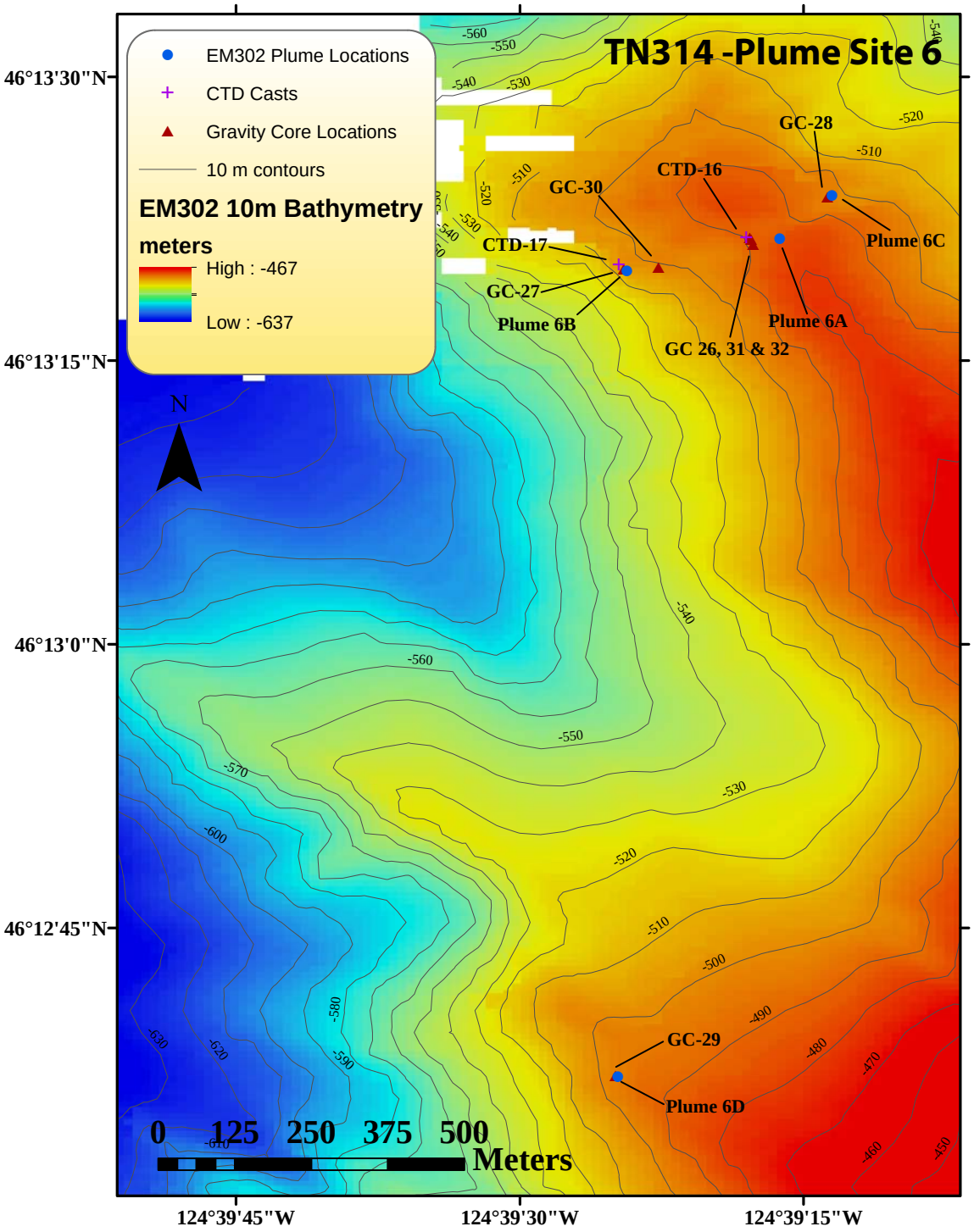

Edited: B. Philip 18 Oct 2014

Site 6 - Plume locations

ID	Lat	Long	Depth (m)
6A	46.222628	-124.65452	-484.6
6B	46.222155	-124.65676	-504.6
6C	46.2232556	-124.65375	-499
6D	46.2103167	-124.65689	-497.1

Site 6 - Gravity core locations

ID	Lat	Long
GC-26	46.22254	-124.65491
GC-27	46.22217	-124.65681
GC-28	46.22323	-124.65382
GC-29	46.21033	-124.65693
GC-30	46.2222	-124.6563
GC-31	46.22261	-124.65494
GC-32	46.22264	-124.65496

Site 6 - CTD locations

ID	Lat	Long
CTD-16	46.22264	-124.65501
CTD-17	46.22225	-124.65688

Site 7 - Plume locations, note we did not collect gravity cores and CTD casts at this site

ID	Lat	Long	Depth	line #
Plume 7a	46.47822	-124.538122	487	132
Plume 7b	46.40784	-124.580719	500	131
Plume 7c	46.35819	-124.615147	306	130
Plume 7d	46.31938	-124.647142	496	129

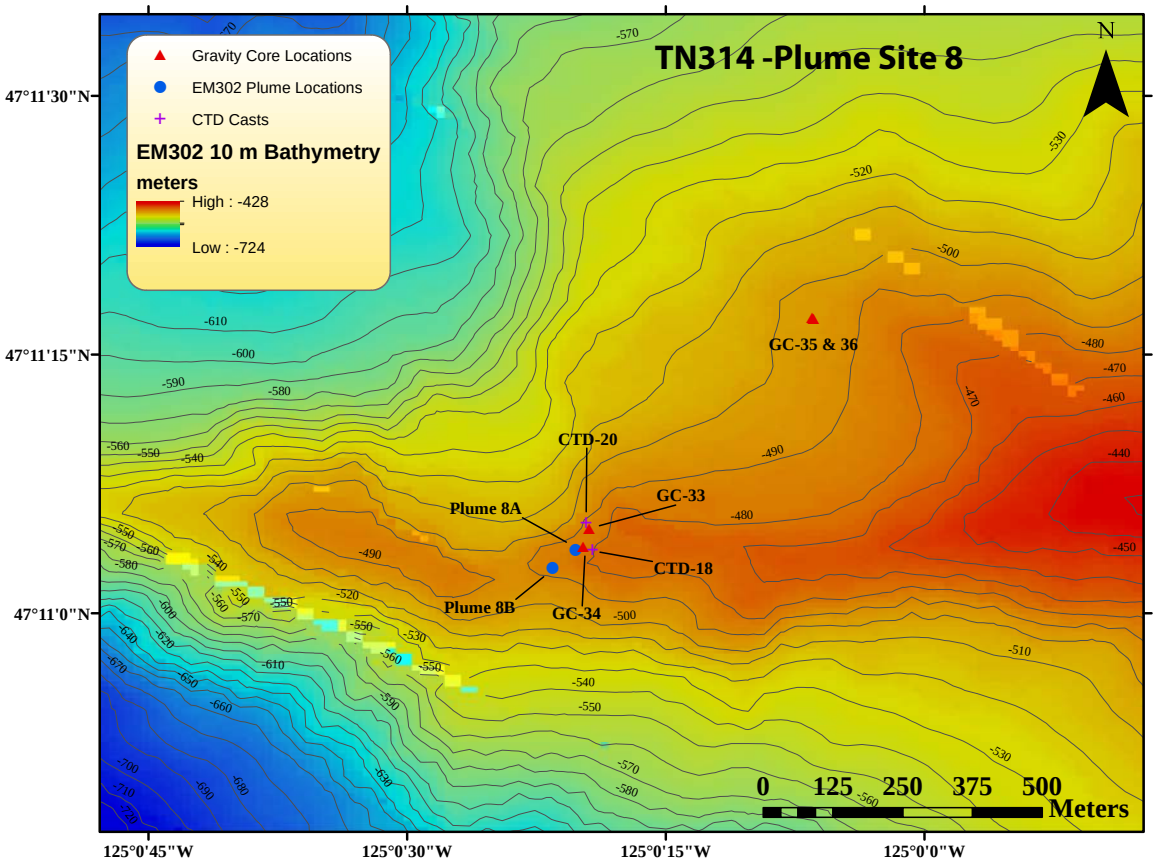

Edited: B. Philip 18 Oct 2014

Site 8 - Plume locations

ID	Lat	Long	Depth
8A	47.184347	-125.00562	-485.1
8B	47.184067	-125.00599	-485.8

Site 8 - Gravity core locations

ID	Lat	Long
GC-33	47.1847	-125.0054
GC-34	47.1844	-125.0055
GC-35	47.1881	-125.00181
GC-36	47.18808	-125.00179

Site 8 - CTD locations

ID	Lat	Long
CTD-18	47.18436	-125.00535
CTD-20	47.18479	-125.00545

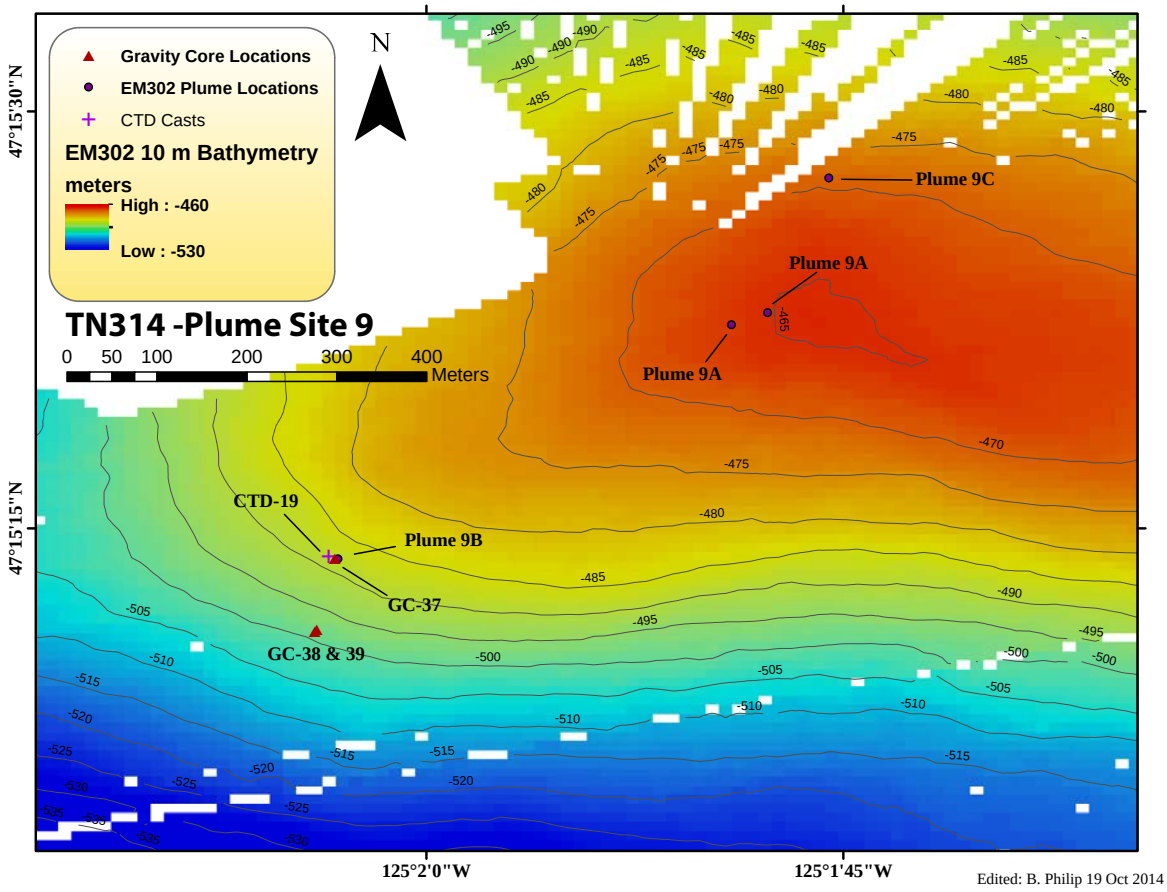

Edited: B. Philip 19 Oct 2014

Site 9 - Plume locations

ID	Lat	Long	Depth
9A	47.2562	-125.030283	-466
9A	47.25632	-125.029922	-465
9B	47.25374	-125.034283	-490
9C	47.25779	-125.029278	-472

Site 9 - Gravity core locations

ID	Lat	Long
GC-37	47.25386	-125.03425
GC-38	47.25313	-125.03445
GC-39	47.25315	-125.03443

Site 9 - CTD cas location

ID	Lat	Long
CTD-19	47.25389	-125.03431

APPENDIX II: HEAT FLOW DATA FROM RESEARCH EXPEDITION

Overview

Heat flow measurements were collected on TGT313 using a combination of piston and gravity cores with outriggers able to hold Antaries thermistors securely attached to the outside of the core barrel. Heat flow was determined by knowing the length of the core, temperature sensor (outrigger) position along the core length, and sediment thermal conductivity determined on board the ship with a needle thermal conductivity probe. While deploying the gravity or piston cores for heat flow measurements, the core was hung for 5 minutes above the seafloor and then deployed into the sediments for 20 minutes to allow the thermistors to come into equilibrium with the geothermal gradient. Heat flow was calculated by finding the slope of a Bullard plot, which consists of thermal resistance plotted against temperature.

During TGT-313, cores with temperature outriggers were deployed at 6 gravity core locations offshore and two deployments of a piston core off North Seattle.

Washington Margin Piston/Gravity Cores

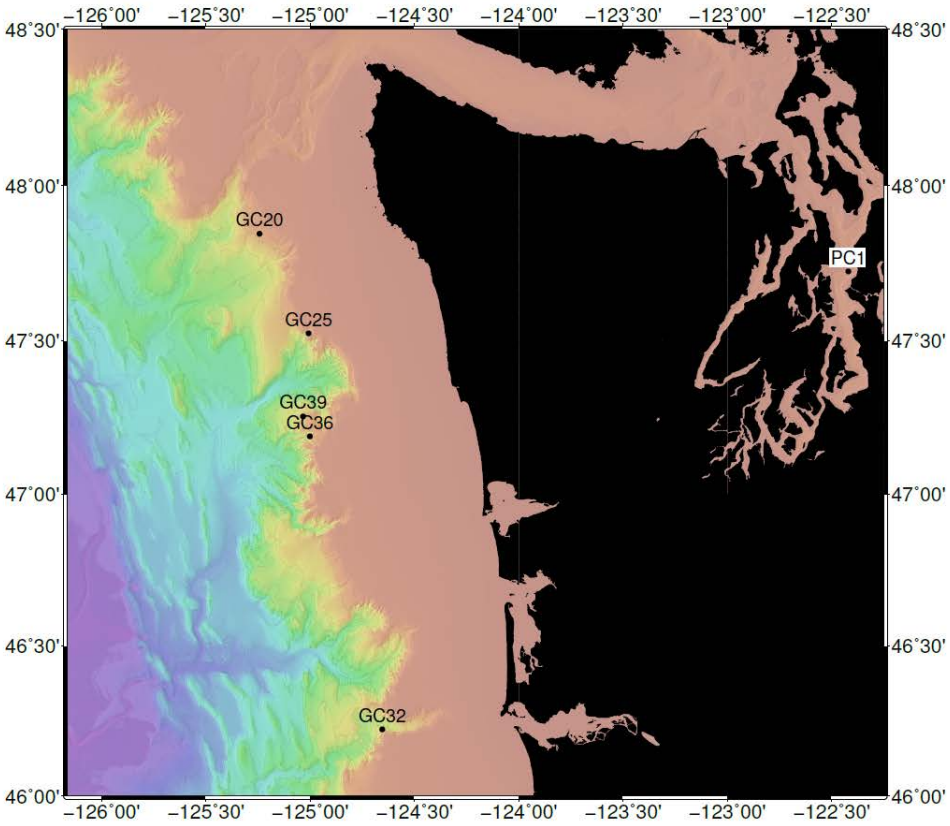

Name	Type of Core	Date	Latitude	Longitude	Depth (meters)	Comments
GC-20	Gravity	10/14/2014	47.84561	-125.24311	490	No sensors penetrated sediments
GC-25	Gravity	10/15/2014	47.52333	-125.00781	495	No sensors penetrated sediments Core bounced off seafloor
GC-32	Gravity	10/16/2014	46.22264	-124.65496	490	3 of 6 sensors entered the sediments
GC-35	Gravity	10/18/2014	47.1881	-125.00181	497	No sensors penetrated sediments
GC-36	Gravity	10/18/2014	47.18808	-125.00179	496	5 of 6 Sensors in sediment Background location ~170m from GC-35
GC-39	Gravity	10/19/2014	47.25315	-125.03443	498	6 Sensors in sediment

Temperature records

Example of fully inserted core temperature profile:

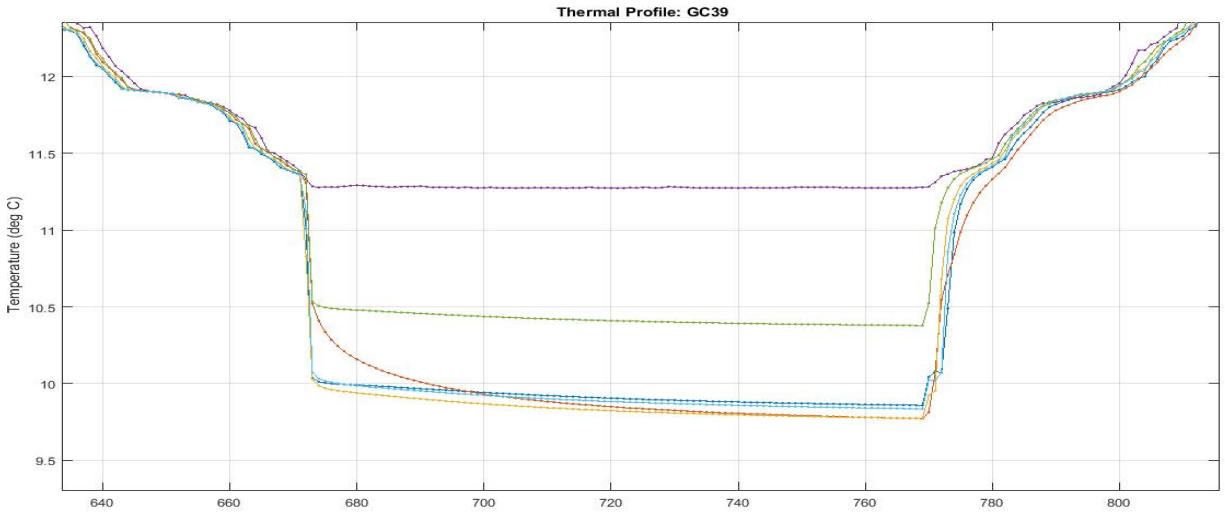

Example of partially inserted core temperature profile:

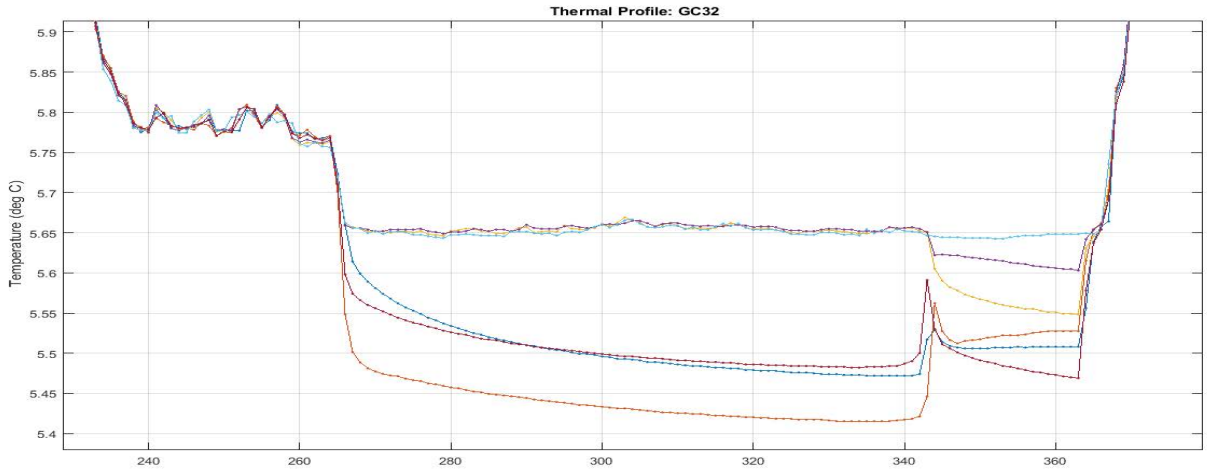

Example of a failed insertion temperature profile:

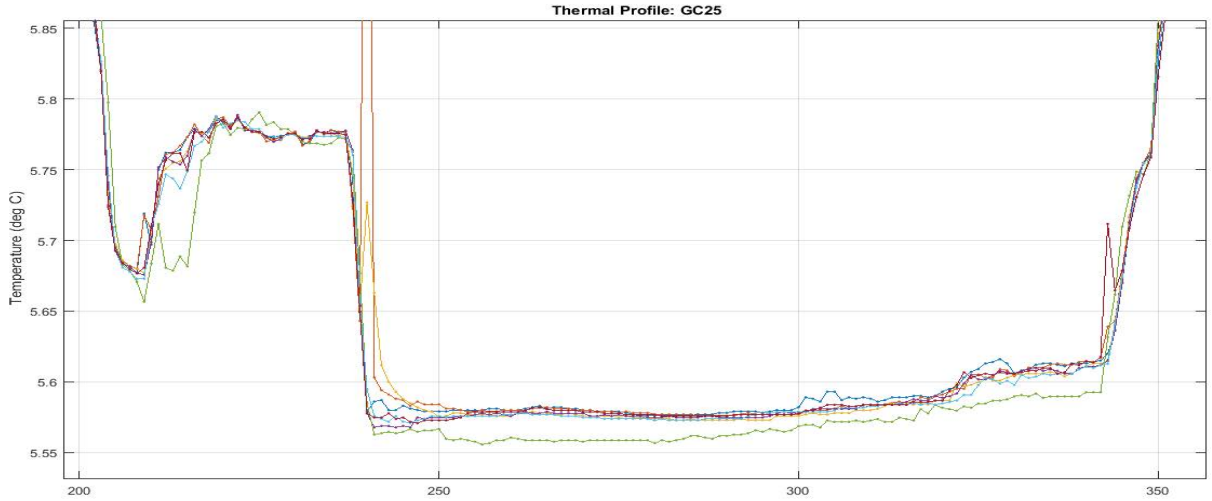

Geothermal gradient for gravity cores GC32 (left) and GC36 (right):

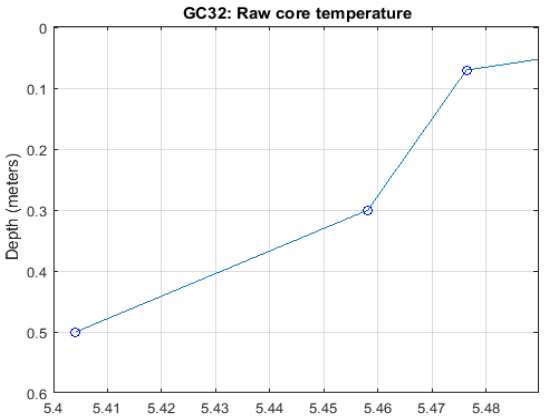

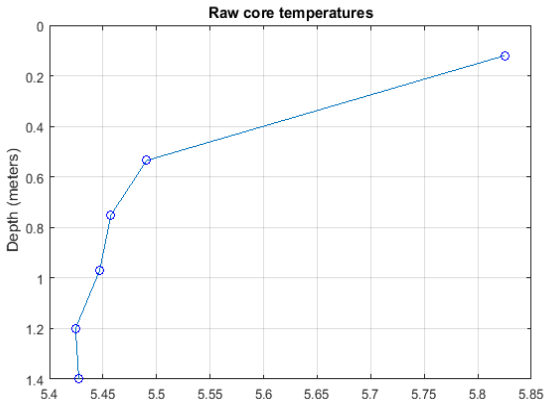

Thermal Conductivity

Thermal Conductivity measurements exist for the following gravity cores:

Core Name	Depth (cm)	Thermal Conductivity (W/m/K)	RMSE (W/m/K)
GC35	47	0.92	0.0002
GC35	100	1.1	0.0002
GC32	24	1.5	0.0007

Depth of each measurement is from the bottom of the collected core upwards.

Heat Flow

Of the six gravity cores rigged for heat flow measurements, three bounced off the hard ground, failing to collect a geothermal gradient. Sediment thermal conductivity was collected from one of the three successful cores (GC-32) providing enough data to calculate a heat flow

values of -206 mW/m^2. Gravity core 36 did not have any thermal conductivity measurements but GC-35, 170m away did have one measurement and was used to calculate a heat flow of -263mW/m^2.

Variations in bottom water temperature due to seasonal storms or shifting currents that propagate warmer temperature into the sediment likely explain the measured negative heat flow. Without a long-term seafloor temperature record, we cannot rule out other environmental factors that could lead to abnormally low heat flow.

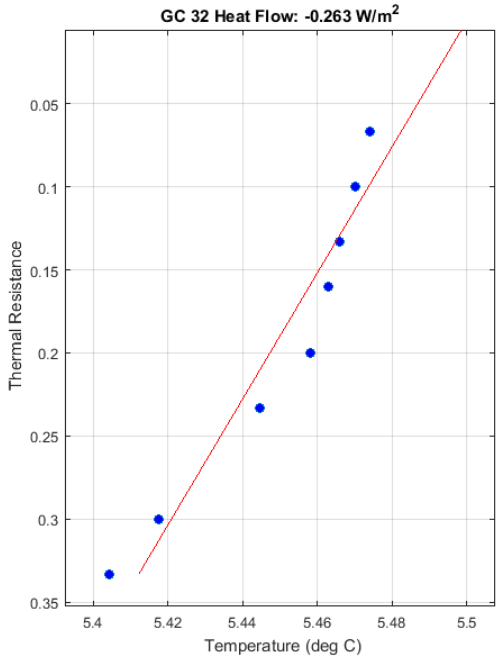

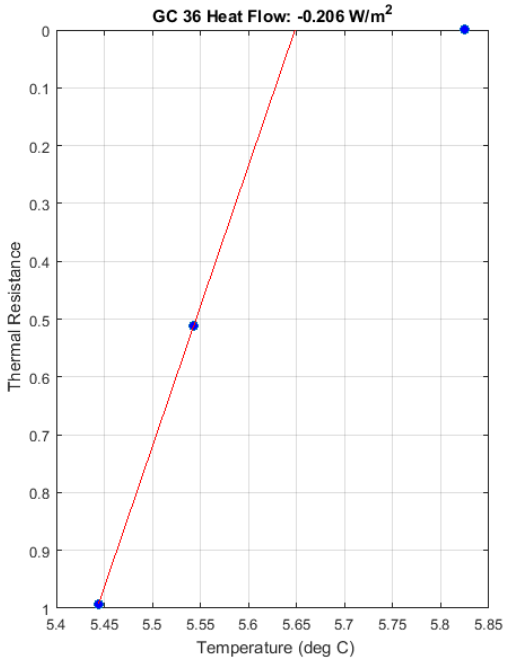

Puget Sound Piston Cores

Two cores were collected with the Puget Sound with the goals of testing the piston core system and to collect a heat flow measurement in a heavily sediment location.

Name	Type of Core	Date	Latitude	Longitude	Depth (meters)	Comments
PC1	Piston	10/10/2014	47.7242	122.4204	208	5 Sensors in sediment
PC2	Piston	10/28/2014	47.7242	122.4204	208	5 Sensors in sediment

Temperature Record

(Below) PC1 Temperature record over time

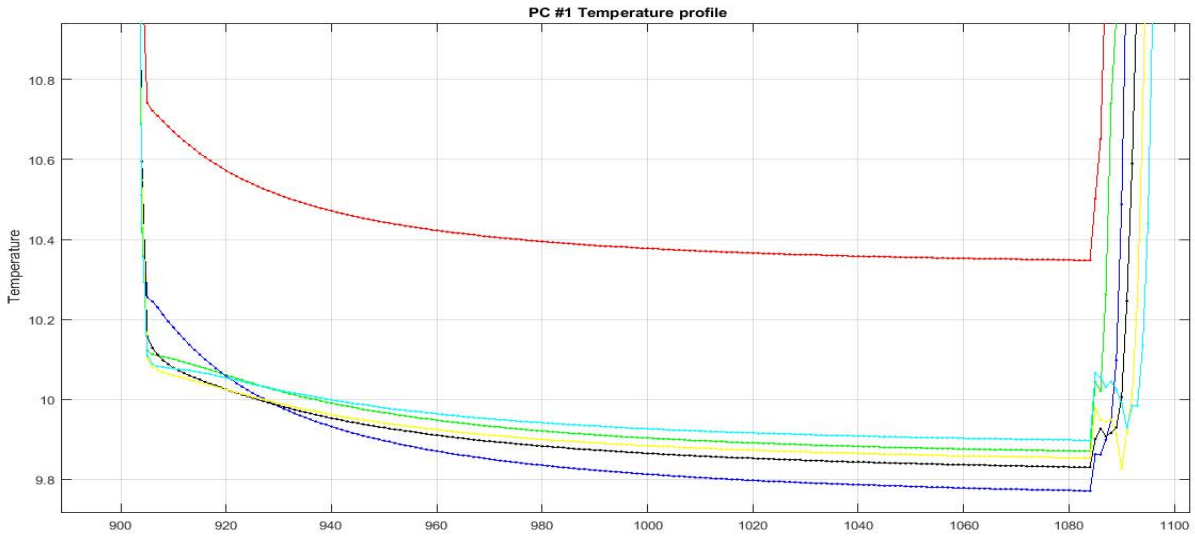

(below) The thermal gradient for both Piston Core deployments

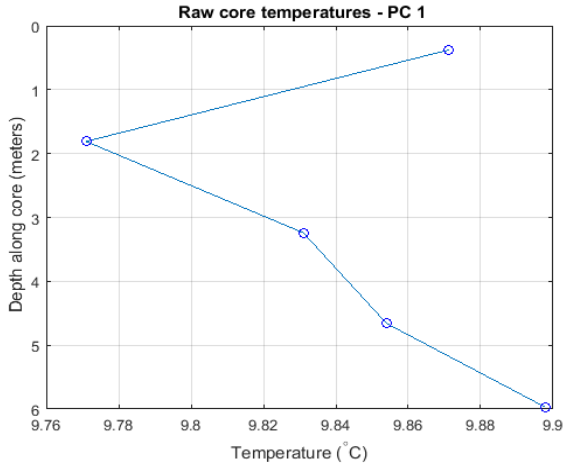

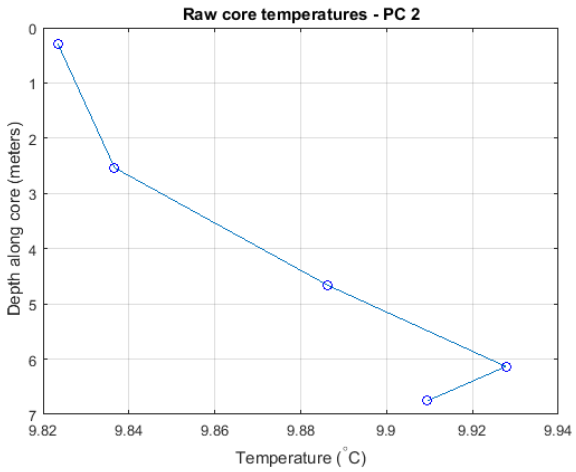

Thermal Conductivity

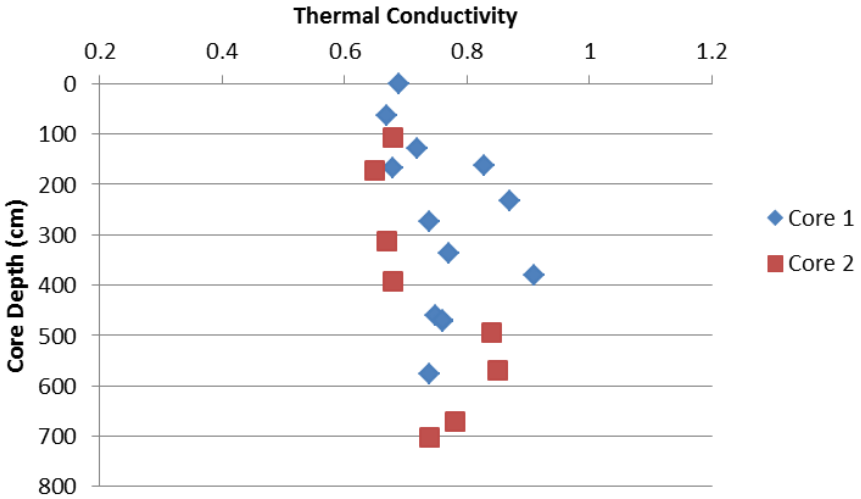

The thermal conductivity was sampled at fairly high intervals within the long piston cores. The low thermal conductivity argues for low consolidation and high porosity within the Puget Sound sediments. Data within this graph can be found in the tables below.

Core Name	Depth (cm)	Thermal Conductivity (W/m/K)	RMSE (W/m/K)
PC-1	64	0.67	0.00001
PC-1	162	0.829	0.0002
PC-1	129	0.72	0.0002
PC-1	275	0.74	0.0001
PC-1	380	0.91	0.0005
PC-1	473	0.76	0.0001
PC-1	576	0.74	0.0001
PC-1	167	0.68	0.0002
PC-1	232	0.87	0.0002
PC-1	337	0.77	0.0001
PC-1	460	0.75	0.0002
PC-1	471	0.76	0.0001

Core Name	Depth (cm)	Thermal Conductivity (W/m/K)	RMSE (W/m/K)
PC-2	173	0.65	0.0001
PC-2	108	0.68	0.0001
PC-2	494	0.84	0.0001
PC-2	312	0.67	0.0001
PC-2	393	0.68	0.0001
PC-2	569	0.85	0.0001
PC-2	672	0.78	0.0001
PC-2	703	0.74	0.0001

1.1. Heat Flow

See map above for location, marked PC1.

Deviations in the bottom water temperature variations brought on by seasonal changes in the Puget Sound circulation can potentially alter the geothermal gradient. To account for this, more than 10 years of monthly CTD based temperature at station LSNT01 (Fauntleroy/Vashon) were downloaded from the Puget Sound Marine Monitoring department within King County, Washington (http://green2.kingcounty.gov/marine/Monitoring/OffshoreCTD). The LSNT01 CTD station was specifically used as it had the longest continuous data and based on comparison with other stations, the monthly temperature swings were roughly consistent within the Puget Sound Basin and are appropriate to use for correcting heat flow data slightly north. This CTD data was subsampled to only the deepest temperature measurement on the downcast at roughly 197 m water depth.

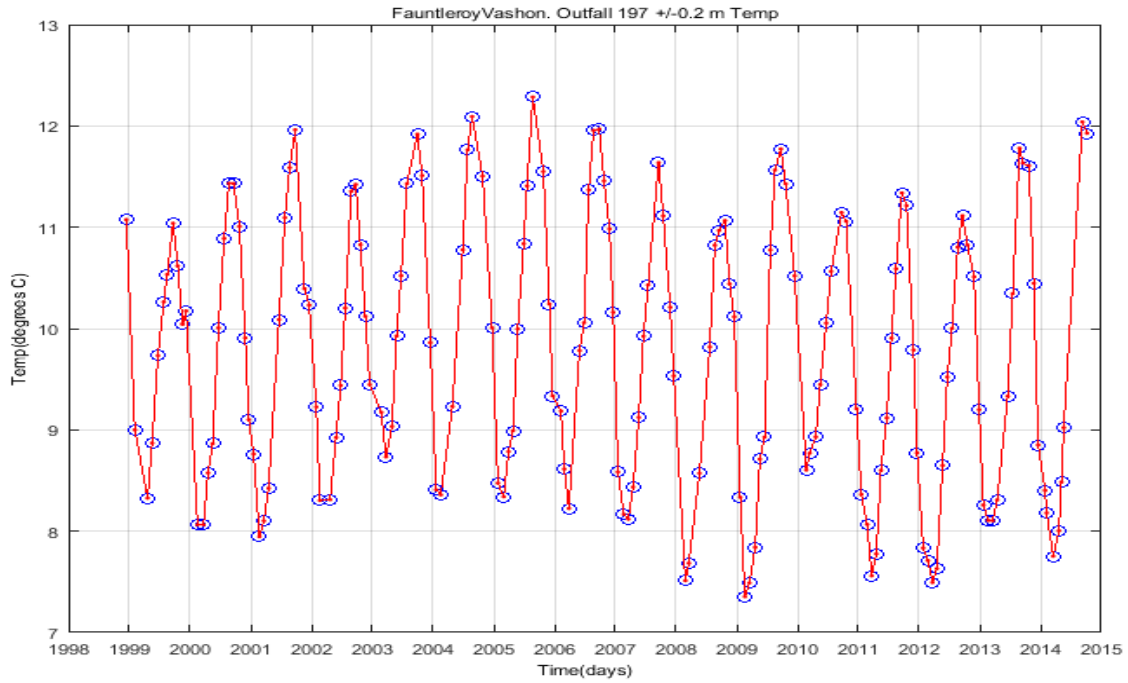

The bottom water temperature record was propagated into the sediment using the thermal conductivity from the Piston cores. The resulting thermal gradient was then removed from the Piston core data to prove a 'corrected' heat flow value.

Core Name	Thermal Gradient (°C/m)	Uncorrected Heat Flow (W/m^2)	Corrected Heat Flow (W/m^2)
PC1	0.0096	-2.9	-10.73
PC2	0.0178	14.62	-13.2

As the corrected heat flow shows consistently negative heat flow, it appears the water correction didn't account for varying temperature well enough. The low seafloor temperature sampling rate could potentially be low enough to thwart this correction effort and higher seafloor temperature sampling rate could distinguish sub-monthly temperature swings not resolved in this data. The uncorrected PC2 heat flow measurement appears to be moderately close to the roughly 20 mW/m^2 background geothermal gradient for this area due to the subduction zone geometry. The uncorrected PC1 measures roughly 0 mW/m^2 heat flow.

Washington Margin BSR derived Heat Flow

To provide another view on the offshore heat flow along the Washington Margin, we analyzed the total of 74 Multi-Channel Seismic lines provided by Western-Geco. The data was acquired from USGS National Archive of Marine Seismic Surveys.

Heat flow was calculated by tracing the Bottom Simulating Reflectors (BSRs), which represent a thermal boundary that marks the transition from methane hydrate to gas transition. The temperature at the BSR was determined using the relationship found in Tishchenko et al., 2005 assuming normal salinity of 32.5 PSU and a mixed hydrostatic to lithostatic pressure.

Seafloor temperatures were assumed using a CTD collected in summer 2012 directly west of the Cascadia deformation front, offshore Washington.
Surveys with detectable BSRs include:

- 1975 Survey (w-8-75-np and w-18-75-np): 3 of the 5 Washington Lines
    - WR-52/WR-48/WR-46
- 1980 Survey (w-29-80-wo): 1 of the 13 Washington Lines
    - WO-44
- 1985 Survey (w-39-85-wo): 9 of the 56 Washington Lines
    - WO-4034/ WO-4036/ WO-4040/ WO-4042/ WO-4044/WO-4046/ WO-4060/WO-4068/ WO-4070/

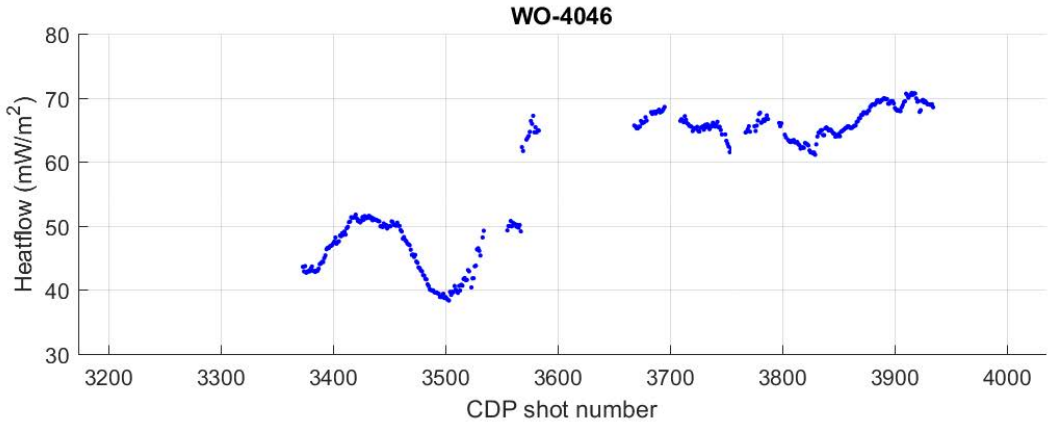

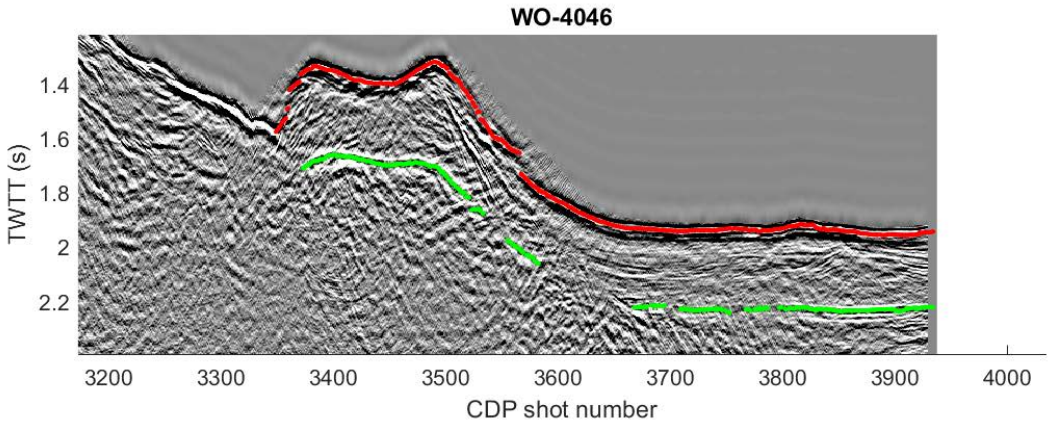

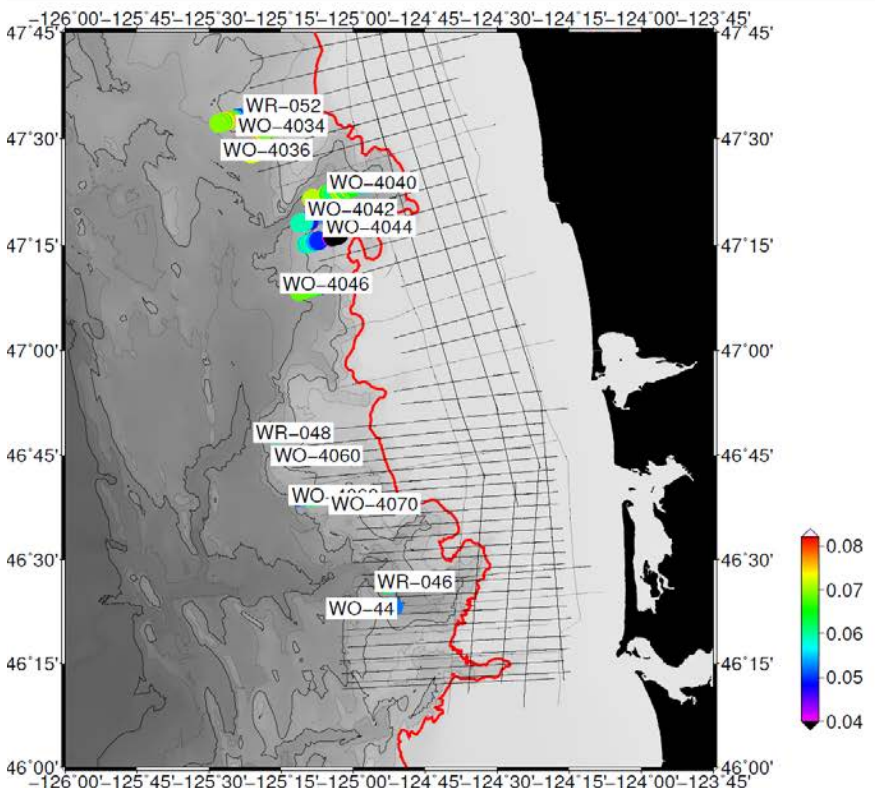
−126°00'−125°45'−125°30'−125°15'−125°00'−124°45'−124°30'−124°15'−124°00'−123°45'
47°45'
47°30'
47°15'
47°00'
46°45'
46°30'
46°15'
46°00'
WR−052
WO−4034
WO−4036
WO−4040
WO−4042
WO−4044
WO−4046
WR−048
WO−4060
WO−4070
WR−046
WO−44
0.08
0.07
0.06
0.05
0.04

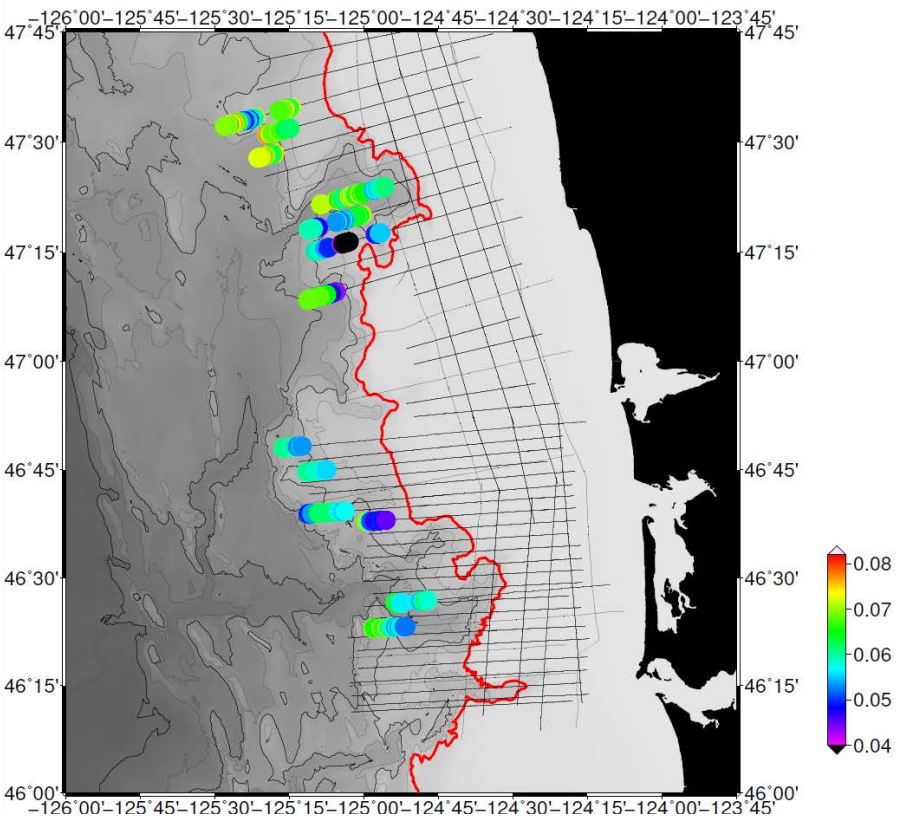
−126°00'
−125°45'
−125°30'
−125°15'
−125°00'
−124°45'
−124°30'
−124°15'
−124°00'
−123°45'
47°45'
47°30'
47°15'
47°00'
46°45'
46°30'
46°15'
46°00'
0.08
0.07
0.06
0.05
0.04

(Below) Heat flow in comparison with locations of methane emission sites (Johnson et al., 2015). The red contour line marks the 500 isobath which represents the upper limit of the hydrate stability zone.